Developing a Framework for Sensitivity and Comparative Analysis in Real Driving Data-Based Vehicle Parameter Extraction

Entwicklung eines Frameworks für Sensitivitäts- und Vergleichsanalysen bei der Fahrzeugparameterextraktion auf Basis von Realdaten

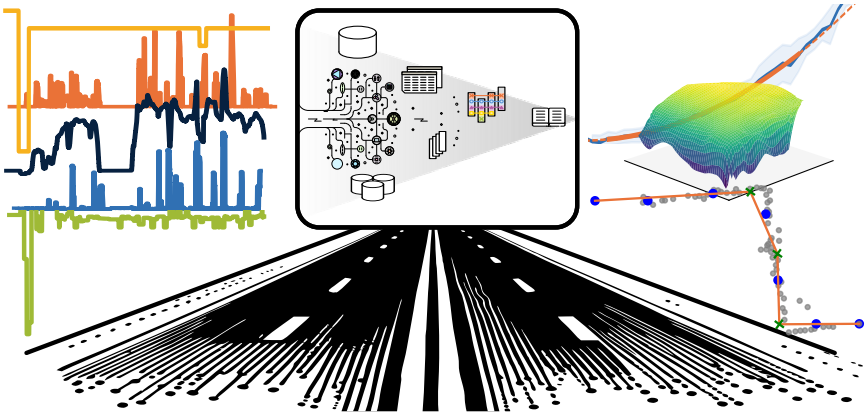

Scientific work for obtaining the academic degree
Master of Science (M.Sc.)
at the Department Mobility Systems Engineering
of the TUM School of Engineering and Design
at the Technical University of Munich

Supervised by	Prof. Dr.-Ing. Markus Lienkamp Nico Rosenberger, M.Sc. Chair of Automotive Technology
Submitted by	Till Zacher, B.Sc. Logenweg 4 85276 Hettenshausen
Submitted on	February 21, 2025

Chair of Automotive Technology
TUM School of Engineering and Design
Technical University of Munich

Project description

Developing a Framework for Sensitivity and Comparative Analysis in Real Driving Data-Based Vehicle Parameter Extraction

Der Fokus der Automobilindustrie verschiebt sich zunehmend auf die Elektromobilität. Über milliardenschwere Investitionen in Forschung und Entwicklung im Bereich der Elektromobilität streben Automobilhersteller an sich einen Vorsprung zu sichern und sich damit langfristig auf dem Markt zu etablieren. Dabei sind unterschiedlichste Konzepte entstanden, deren Charakteristika extrem stark gehütete Geheimnisse darstellen. Über sogenannte Benchmarkuntersuchungen werden die Konzepte der Konkurrenz untersucht und es wird analysiert, welche Konzepte der eigenen überlegen sind und welche das größte Potential bieten. Diese Untersuchungen sind aktuell sowohl mit einem enormen zeitlichen als auch finanziellen Aufwand verbunden, daher wird angestrebt diese Untersuchungen zu optimieren.

In dieser Abschlussarbeit soll eine Methode weiterentwickelt werden, die diesen Aufwand reduziert und das gesamte Vorgehen optimiert. Basierend auf Realfahrdaten besteht das Ziel in der Entwicklung eines Ansatzes zur Identifikation von sowohl Gesamtfahrzeug- als auch Komponentenparametern, welche in der Bereitstellung der Fahrwiderstandsparameter und der Erstellung eines Wirkungsgradkennfelds des Motors- bzw. des Antriebsstrangs resultiert. Diese Identifikation soll für eine bestehende Methode in Python weiterentwickelt und optimiert werden. Der zugrundeliegende Datensatz wird über Realfahrdaten aus dedizierten Testfahrten nach einem Versuchsplan bereitgestellt. Zur Validierung der Ergebnisse werden die aus spezifischen Komponentenversuchen entwickelten Parameter herangezogen. Als Versuchsfahrzeug kommt ein Porsche Taycan zum Einsatz.

Folgende Arbeitspakete umfasst die zu vergebende Studienarbeit:

- Literaturrecherche und Aufzeigen des Stands der Technik von Fahrzeugparameteridentifikations- & Realfahrdatenanalysen sowie aktueller Forschung.
- Untersuchung des vorhandenen Datensatzes auf Quantität, Qualität und Relevanz für die geplante Analyse.
- Weiterentwicklung einer Methode zur Identifikation der Schaltstrategie, des Effizienzkennfelds und der Straßenlastkoeffizienten aus Realfahrdaten.
- Analyse unterschiedlicher Einflussfaktoren auf den Identifikations- und Optimierungsprozess, um die Robustheit und Übertragbarkeit der Methode zu erhöhen.
- Validierung bzw. Plausibilisierung der Ergebnisse anhand Literatur- und realer, am Lehrstuhl erhobener Referenzwerte.
- Einordnung der Resultate in den Kontext der Benchmarkuntersuchungen.
- Umfassende schriftliche Dokumentation und kritische Reflexion der Ergebnisse.

Die Ausarbeitung soll die einzelnen Arbeitsschritte in übersichtlicher Form dokumentieren. Der Kandidat verpflichtet sich, die Masterarbeit selbständig durchzuführen und die von ihm verwendeten wissenschaftlichen Hilfsmittel anzugeben.

Die eingereichte Arbeit verbleibt als Prüfungsunterlage im Eigentum des Lehrstuhls.

Announcement date: November 04, 2024

Submission date: February 21, 2025

Prof. Dr.-Ing. Markus Lienkamp

Nico Rosenberger, M.Sc.

Chair of Automotive Technology
TUM School of Engineering and Design
Technical University of Munich

Geheimhaltungsverpflichtung

Herr: **Zacher, Till**

Gegenstand der Geheimhaltungsverpflichtung sind alle mündlichen, schriftlichen und digitalen Informationen und Materialien die der Unterzeichner vom Lehrstuhl oder von Dritten im Rahmen seiner Tätigkeit am Lehrstuhl erhält. Dazu zählen vor allem Daten, Simulationswerkzeuge und Programmcode sowie Informationen zu Projekten, Prototypen und Produkten.

Der Unterzeichner verpflichtet sich, alle derartigen Informationen und Unterlagen, die ihm während seiner Tätigkeit am Lehrstuhl für Fahrzeugtechnik zugänglich werden, strikt vertraulich zu behandeln.

Er verpflichtet sich insbesondere:

- derartige Informationen betriebsintern zum Zwecke der Diskussion nur dann zu verwenden, wenn ein ihm erteilter Auftrag dies erfordert,
- keine derartigen Informationen ohne die vorherige schriftliche Zustimmung des Betreuers an Dritte weiterzuleiten,
- ohne Zustimmung eines Mitarbeiters keine Fotografien, Zeichnungen oder sonstige Darstellungen von Prototypen oder technischen Unterlagen hierzu anzufertigen,
- auf Anforderung des Lehrstuhls für Fahrzeugtechnik oder unaufgefordert spätestens bei seinem Ausscheiden aus dem Lehrstuhl für Fahrzeugtechnik alle Dokumente und Datenträger, die derartige Informationen enthalten, an den Lehrstuhl für Fahrzeugtechnik zurückzugeben.

Eine besondere Sorgfalt gilt im Umgang mit digitalen Daten:

- Für den Dateiaustausch dürfen keine Dienste verwendet werden, bei denen die Daten über einen Server im Ausland geleitet oder gespeichert werden (Es dürfen nur Dienste des LRZ genutzt werden (Lehrstuhllaufwerke, Sync&Share, GigaMove).
- Vertrauliche Informationen dürfen nur in verschlüsselter Form per E-Mail versendet werden.
- Nachrichten des geschäftlichen E-Mail Kontos, die vertrauliche Informationen enthalten, dürfen nicht an einen externen E-Mail Anbieter weitergeleitet werden.
- Die Kommunikation sollte nach Möglichkeit über die (my)TUM-Mailadresse erfolgen.

Die Verpflichtung zur Geheimhaltung endet nicht mit dem Ausscheiden aus dem Lehrstuhl für Fahrzeugtechnik, sondern bleibt 5 Jahre nach dem Zeitpunkt des Ausscheidens in vollem Umfang bestehen. Die eingereichte schriftliche Ausarbeitung darf der Unterzeichner nach Bekanntgabe der Note frei veröffentlichen.

Der Unterzeichner willigt ein, dass die Inhalte seiner Studienarbeit in darauf aufbauenden Studienarbeiten und Dissertationen mit der nötigen Kennzeichnung verwendet werden dürfen.

Datum: 21. Februar 2025

Unterschrift: T. Zacher

Chair of Automotive Technology
TUM School of Engineering and Design
Technical University of Munich

Erklärung

Ich versichere hiermit, dass ich die von mir eingereichte Abschlussarbeit selbstständig verfasst und keine anderen als die angegebenen Quellen und Hilfsmittel benutzt habe.

Garching, den 21. Februar 2025

T. Zacher

Till Zacher, B.Sc.

Chair of Automotive Technology
TUM School of Engineering and Design
Technical University of Munich

Declaration of Consent, Open Source

Hereby I, Zacher, Till, born on June 29, 1998, make the software I developed during my Semester Thesis available to the Institute of Automotive Technology under the terms of the license below.

Garching, February 21, 2025

T. Zacher

Till Zacher, B.Sc.

Contents

List of Abbreviations

AC	Alternating Current
ANOVA	Analysis of Variance
BEV	Battery Electric Vehicle
CAN	Controller Area Network
CoC	Certificate of Conformity
DBSCAN	Density Based Spatial Clustering of Applications with Noise
DC	Direct Current
DoE	Design of Experiments
EMA	Exponential Moving Average
EPA	Environmental Protection Agency
FTM	Future Transport Mobility
FTP	Federal Test Procedure
GPS	Global Positioning System
GSA	Global Sensitivity Analysis
HWFET	Highway Fuel Economy Test
ID	Identification Number
IDW	Inverse Distance Weighting
IMU	Inertial Measurement Unit
IQR	Interquartile Range
KDD	Knowledge Discovery in Databases
kwarg	Keyword Argument
LSA	Local Sensitivity Analysis
LSTM	Long Short Term Memory
ML	Machine Learning
MS	Mean Square
OBD	On-Board Diagnostics
PCA	Principal Component Analysis
PMSM	Permanent Magnet Synchronous Motor
RF	Random Forest
RLC	Road Load Coefficient
RMSE	Root Mean Square Error
SAE	Society of Automotive Engineers
SOC	State of Charge
SS	Sum of Squares
VW	Volkswagen
WLTC	Worldwide harmonized Light-duty vehicles Test Cycle
WLTP	World Wide Harmonized Light Vehicle Test Procedure

Formula Symbols

Formula Symbols	Unit	Description
A_{front}	m^2	Frontal area of the vehicle
E_{elec}	$\mathrm{kW\,h}$	Electrical energy
F_N	N	Normal force on the tire
F_{acc}	N	Acceleration force
F_{air}	N	Aerodynamic drag force
F_{climb}	N	Climbing resistance force
$F_{\text{drag}}(v)$	N	Drag force model
F_{roll}	N	Rolling resistance force
F_{trac}	N	Traction force
I_{hv}	A	High-voltage bus current
J	-	Distortion Measure
J_{rot}	kgm^2	Generic rotational inertia of a component
$J_{\text{rot,M}}$	kgm^2	Rotational inertia of the motor
$J_{\text{rot,W}}$	kgm^2	Rotational inertia of one wheel
$M_{\text{motor},i}(t)$	$\mathrm{N\,m}$	Time-dependent motor torque for segment i
M_{wheel}	$\mathrm{N\,m}$	Wheel torque
N	-	Number of samples in a dataset
P_{aux}	W	Auxiliary power
P_{battery}	W	Electrical power from battery
P_{in}	W	Input power to the drivetrain
P_{out}	W	Output power from the drivetrain
P_{trac}	W	Traction power
U_{hv}	V	High-voltage bus voltage
a	$\mathrm{m/s}^2$	Vehicle acceleration
$a_{\text{climb},i}(t)$	$\mathrm{m/s}^2$	Time-dependent climb-induced acceleration for segment i

c_w	-	Aerodynamic drag coefficient
f_0	N	Road load coefficient (constant term)
f_1	$\mathrm{N\,s\,m^{-1}}$	Road load coefficient (linear term)
f_2	$\mathrm{Ns^2/m^2}$	Road load coefficient (quadratic term)
f_r	-	Rolling resistance coefficient
$f_{r,0}$	-	Rolling resistance polynomial coefficient (constant)
$f_{r,1}$	-	Rolling resistance polynomial coefficient (linear term)
$f_{r,4}$	-	Rolling resistance polynomial coefficient (quartic term)
g	$\mathrm{m/s^2}$	Gravitational acceleration
i	-	Index
j	-	Gear ratio
k	-	Number of clusters
m_{acc}	kg	Additional equivalent mass due to rotating components
$m_{\text{acc,M}}$	kg	Additional equivalent mass due to rotating motor
$m_{\text{acc,W}}$	kg	Additional equivalent mass due to rotating wheels
m_v	kg	Vehicle mass
$n_{M,\text{base}}$	$\mathrm{rad\,s^{-1}}$	Base motor speed
n_{min}	-	Minimum number of samples in a cluster
n_{window}	-	Number of samples in a moving window
p	-	Power Parameter
r_{wheel}	m	Wheel radius
v	$\mathrm{m\,s^{-1}}$	Vehicle velocity
$\dot{v}(t)$	$\mathrm{m\,s^{-1}}$	Numerically approximated vehicle acceleration at time t
$v_{\text{corr},i}(t)$	$\mathrm{m\,s^{-1}}$	Time-dependent slope-corrected vehicle velocity for segment i
w_i	-	Weight at index i
x_i	-	Data point x at index i
y_i	-	Data point y at index i
α	rad	Road inclination angle
$\alpha(t)$	rad	Time-dependent road inclination (pitch angle)
α_{ema}	-	Exponential moving average smoothing factor
$\Delta v_{\text{climb},i}(t)$	$\mathrm{m\,s^{-1}}$	Time-dependent climb-induced velocity correction for segment i
ε	-	Proximity Radius
$\eta_{\text{drivetrain}}$	-	Drivetrain efficiency

μ_i	-	Cluster center at index i
ρ_{air}	$\mathrm{kg/m^3}$	Air density

1 Introduction

1.1 Motivation

The Volkswagen (VW) emissions controversy, commonly referred to as "dieselgate," began in September 2015 after VW was officially accused of breaking US emissions regulations by the US Environmental Protection Agency (EPA) [1]. VW later acknowledged that 11 million diesel-powered cars globally had a "defeat device" placed in them [1]. These gadgets had the ability to recognize when a vehicle was being tested in a lab and turn on the emissions control system to ensure that NOx emissions regulations were met [1]. However, when the car was on the road, the emissions control system was turned off, allowing the vehicle to emit up to 40 times the legal limit of NOx [1]. This scandal made shortcomings in the regulatory process apparent [1]. Environmental protection agencies and type-approval authorities often relied heavily on laboratory testing provided by manufacturers themselves as the primary method for determining vehicle emissions and fuel consumption [1]. This reliance on lab tests has been criticized for not accurately reflecting real-world driving conditions, leading to a lack of transparency and accountability in the automotive industry [1]. This example illustrates the importance of independent vehicle benchmarking to ensure that manufacturers' claims are accurate and that vehicles comply with regulatory standards. Finding novel methods to benchmark vehicles using real-world driving data is crucial in overcoming the cost and time limitations of traditional laboratory testing while simultaneously emulating the real driving process better. Empowering independent researchers and stakeholders to accurately characterize vehicles could help keep manufacturers accountable and accelerate automotive research by cutting costs and complexity of the testing process.

Furthermore, in the realm of autonomous driving research, the need for accurate vehicle models is highly relevant [2]. To enable the accurate modeling of vehicles, it is essential to have precise knowledge of the vehicle's behavior under various driving conditions [2]. These models have to be parametrized to simulate real vehicles accurately. These models' parametrization is often done using data from laboratory tests [3]. Real-driving data-based benchmarking methods could provide a cost-effective and quick way to obtain the necessary data to parametrize these models.

1.2 Research Objectives

This research aims to develop an automated, end-to-end methodology for extracting three key vehicle parameters, efficiency maps, road load coefficients, and gear shift strategies, directly from real-world driving data recorded on public roads. While certain aspects of these estimations have been demonstrated individually, the overarching goal here is to unify them in a generalizable process that can be applied to a range of vehicles under varied driving conditions. By reducing dependence on specialized facilities, costly equipment, and time-consuming procedures, the proposed approach seeks to cut both material and time investments in vehicle benchmarking.

To illustrate, test, and develop this approach, the research focuses on a high-performance two-gear Battery Electric Vehicle (BEV), with the Porsche Taycan serving as the principal case study. The core research question is:

How can existing data-driven benchmarking methods be adapted for two-gear BEVs to enable accurate drivetrain efficiency mapping, road load coefficient estimation, and gear strategy determination, all using real-world driving data?

To address this question, a modular framework will be developed. This framework allows for systematic testing, comparison, and refinement of various algorithmic components and subfunctions, with a particular focus on process robustness. By integrating Global Sensitivity Analysis (GSA) and evaluating multiple approaches under diverse conditions, the study aims to identify the most effective methodologies for comprehensive drivetrain characterization.

Ultimately, this work aspires to establish a cost-effective, scalable, and reliable end-to-end process that streamlines vehicle benchmarking, broadens its applicability to different powertrain architectures, and facilitates rapid simulation model parametrization—all while offering a means to independently validate manufacturer claims.

1.3 Thesis Structure

This thesis is organized to progressively build the reader's understanding from foundational principles to comprehensive experimental validations. The first section, State of the Art, discusses the fundamentals of electric vehicle drivetrains, outlines the key vehicle dynamics concepts required for subsequent analyses, and reviews existing laboratory-based and on-road benchmarking techniques, identifying gaps that motivate this work. Methodologies then establish the overarching knowledge discovery approach, incorporating global sensitivity analysis, design of experiments, and statistical significance testing, and introduce the three core algorithms: road load coefficient estimation, drivetrain efficiency mapping, and gear shift strategy determination, which recur throughout the thesis. Next, Vehicle and Data Logging describes the Porsche Taycan's two-gear architecture and explains how real-world data was collected. Building on this, the Modular Framework and Experimental Architecture elaborates on how different algorithmic configurations are systematically tested and evaluated, detailing the measures used to assess performance. Then, each algorithm's precise data processing and parameter settings are examined, including results from grid searches and sensitivity analyses that refine and validate the chosen methods. Validation and Results compare the new on-road approaches with traditional, laboratory-derived parameters by simulating multiple driving cycles and evaluating how closely each method predicts vehicle energy consumption. Finally, the Conclusion and Outlook summarize the key findings, highlight limitations, and provide recommendations for further improvement and effort reduction. Additional supporting material, including extended plots and intermediate data processing examples, is available in the Appendix.

2 State of the Art

This chapter introduces all relevant technical background alongside the current state of the art in electric vehicle drivetrains and benchmarking. The overview of the main components of an BEV drivetrain introduces essential concepts for the subsequent chapters. The acting forces section formalizes the relevant variables and their interdependencies for the mechanics of a vehicle model. Then, the traditional lab-based and the on-road driving data-based benchmarking methods are introduced. The efficiency map estimation, road load coefficient estimation, and shift strategy estimation are outlined for both methods. The main achievements and limitations of previous research are summarized. Concepts of used filtering and data processing techniques are also introduced. Lastly, the Knowldepedge Discovery in Databases (KDD) process is introduced as a methodological approach to derive knowledge from large amounts of data.

2.1 Battery Electric Vehicle Drivetrain

The drivetrain of a BEV is a system that converts chemical energy saved in the battery into kinetic energy of the vehicle [4, p. 110]. Figure 2.1 gives an overview of the main components involved in this process while also providing information about in what form the energy is passed between the components. The drivetrain starts with the high voltage battery pack, which provides Direct Current (DC) power to the inverter [5, p. 84]. The inverter converts the DC power into Alternating Current (AC) power which is required to drive the electric motor [4, p. 111]. The electric motor converts the electrical energy into mechanical energy, which is then transmitted to the wheels via the transmission [5, p. 69]. The transmission adapts the electric motor's operating area to the vehicle's operating area while simultaneously providing functionality like reverse gear, neutral gear, and differential drive [5, p. 71]. This chain of energy-converting components builds a typical BEV drivetrain [5, p. 69].

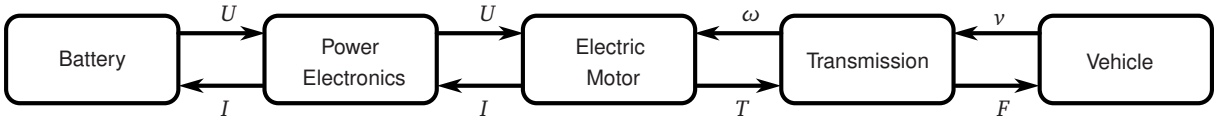

Figure 2.1: System Model of a BEV adapted from [5, p. 69].

The arrows connecting the components in Figure 2.1 represent the directionality of causality in a dynamical modeling approach [5, p. 69]. In this context, causality defines the computational dependencies within the system, ensuring that each variable is correctly assigned as an input or output based on physical principles [5, p. 69]. For instance, the high-voltage battery dictates the available DC power, which the inverter processes into AC power for the electric motor [5, p. 69]. Similarly, the motor's rotational speed influences the torque output, which propagates through the transmission to the wheels [5, p. 69]. This structured representation of causality allows for accurate modeling of energy conversion dynamics, facilitating control and optimization strategies for BEV powertrains [5, p. 69].

2.1.1 Battery

The traction battery supplies the necessary electrical energy for the propulsion of the vehicle and the required power for auxiliary devices [6, p. 118]. When the vehicle is in use, the battery is discharged to provide the necessary power for the electric motor and auxiliary high-voltage systems, while the battery is recharged during regenerative braking or when the vehicle is plugged into a charging station [6, p. 118]. As these batteries typically operate above $60\,\mathrm{V}$, they are typically classified after ISO 6469-3 as high-voltage systems [6, p. 118]. Common voltage levels include $400\,\mathrm{V}$, and $800\,\mathrm{V}$ [6, p. 118]. The latter is growing in adoption, as it brings advantages in terms of efficiency and power delivery, but simultaneously also needs more complex power electronics [6, p. 118]. The increasing electrification of commercial vehicles, like trucks and buses, is driving demand in higher energy capacity traction batteries, which in turn require higher charging powers and thus higher voltage levels [6, p. 118].

A portion of the energy is lost due to chemical side reactions and aging effects, which consume part of the current flowing through the battery without contributing to the active electrochemical processes [4, p. 66]. During charging and discharging, additional losses occur due to the difference between the battery's terminal voltage and its open-circuit voltage. The product of this voltage difference and the current represents the energy losses associated with overvoltage effects, which primarily manifest as heat generation within the battery cells [4, p. 67]. This heat dissipation is a key factor in battery thermal management, as excessive temperatures can degrade battery performance and lifespan [4, p. 67]. Aging further exacerbates these losses by reducing the active surface area of the battery electrodes, which increases the required overvoltage for a given current. This results in higher voltage drops during discharge and increased voltage requirements during charging, negatively impacting overall efficiency [4, p. 67]. As a consequence, older batteries exhibit greater energy losses and require stronger thermal management to maintain performance [4, p. 67].

2.1.2 Inverter

The inverter is responsible for converting the DC voltage from the battery into an AC voltage to power the electric motor [6, p. 115]. It supplies variable voltage, current, and frequency, enabling motor and generator operation [6, p. 116]. The Voltage Source Inverter is the dominant topology in automotive applications due to its cost efficiency and effectiveness [6, p. 196]. It uses pulse-width modulation to create sinusoidal voltages for the motor [6, p. 196]. Another inverter type, the Current Source Inverter, differs by utilizing a DC-link inductor instead of a capacitor but is less common due to higher costs and lower efficiency [6, p. 196]. The inverter structure is typically based on a three-phase bridge circuit, known as the B6C topology, also depicted in Figure 2.2 [6, p. 197]. This consists of power semiconductor switches and freewheeling diodes, allowing efficient AC output from a DC input [6, p. 197]. A disadvantage of the B6C topology is that it only provides two voltage levels for modulation, resulting in higher Total Harmonic Distortion, which increases iron losses in the electric drive [6, p. 197].

Switching losses occur in power electronics because semiconductors like IGBTs and MOSFETs do not switch instantaneously [6, p. 190]. Both voltage and current overlap briefly during each switching event, leading to power dissipation in the form of heat [6, p. 190]. These losses increase linearly with switching frequency, making high-frequency operation a trade-off between efficiency and control precision [6, p. 190]. Conduction losses occur when semiconductor switches are conducting [6, p. 190]. Even in their "on" state, they exhibit a small resistance, causing voltage drops that dissipate power as heat [6, p. 190]. These losses are proportional to the square of the current flowing through the switch [6, p. 190]. Ripple current losses are associated with the pulsating nature of power conversion [6, p. 190]. Filters and capacitors are used to smooth out voltage and current fluctuations, but the ripple currents they manage cause additional resistive losses in passive components [6, p. 190]. Transformer and inductor losses arise in magnetic components such as transformers and inductors used in filtering and energy storage [6, p. 190]. These include core

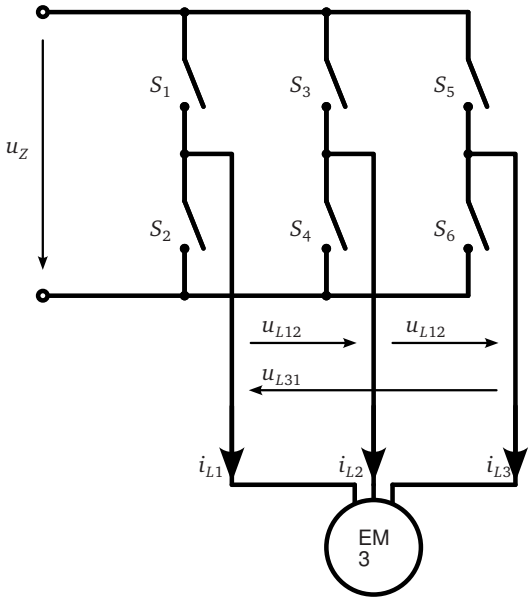

Figure 2.2: Bridge Circuit based on [4, p. 55].

losses, which depend on the magnetic material properties and frequency of operation, and winding losses, which result from resistance in the coil wires and are influenced by the skin effect at higher frequencies [6, p. 190]. Higher switching frequencies allow for smaller passive components but increase switching losses [6, p. 190]. Optimizing the inverter design requires balancing these factors to minimize overall losses while maintaining compactness [6, p. 190].

2.1.3 Motor

BEVs typically use either DC or AC motors, which include synchronous and asynchronous types [7, p. 199]. With synchronous motors, the rotor always has the same rotational speed as the electric field. In contrast, asynchronous motors have a rotor that lags behind the electric field, creating slip [7, p. 201]. While asynchronous motors can bring benefits in terms of robustness and cost [7, p. 209], the synchronous Permanent Magnet Synchronous Motor (PMSM) is most commonly used in BEVs due to their high efficiency and torque density [7, p. 210]. As the name implies, PMSM contain permanent magnets embedded in the rotor, which provide the excitation field for the outer magnetic field to interact with, removing the need for an additional current-induced excitation system [8, p. 192]. This magnetic field, which is fixed to the rotor, is then dragged along by the rotating magnetic field of the stator, creating torque [8, p. 191]. The stator field frequency, alongside the number of pole pairs, determines the engine speed [8, p. 191].

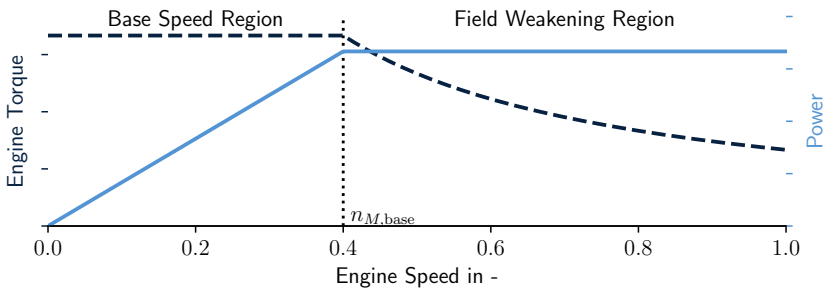

Figure 2.3: Typical Power and Torque Characteristics of a PMSM based on [7, p. 194].

Figure 2.3 provides a qualitative overview of the power and torque characteristics of a PMSM. Both the available torque and power depend on the engine's rotational speed [7, p. 195]. The base speed $n_{M,base}$ partitions the engine characteristics into two regions, the *base speed region* and the *field weakening region* [7, p. 195]. The available motor torque remains constant for rotational speeds up to the base speed, while the power output increases linearly with the rotational speed [7, p. 195]. The power output remains constant for engine speed above the base speed, which means that with increasing engine speed, the available torque drops hyperbolically [7, p. 195].

The efficiency of the motor, which is qualitatively shown in Figure 2.4, is not uniform across all speeds and torques, with the highest efficiency regions typically found in the mid-speed, mid-torque range [8, p. 48]. Different factors at different regions dominate the motor's efficiency [7, p. 200]. At low torque, efficiency is mainly determined by core losses and mechanical friction [7, p. 200]. At high engine speeds, the limiting factors include field-weakening losses and iron losses [7, p. 200].

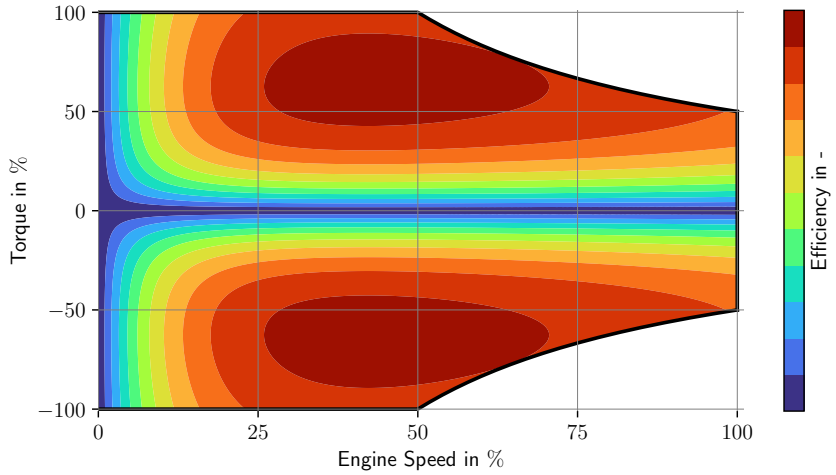

Figure 2.4: Qualitative Efficiency of a PMSM based on [8, p. 48].

2.1.4 Transmission

The main function of a transmission is to convert the rotational speed and torque of the electric motor in a way that matches the requirements at the wheels [4, p. 117]. This ensures that the electric motor operates within an efficient range while providing the right performance to handle various driving conditions [4, p. 117]. Unlike internal combustion engine vehicles, which require multi-speed transmission to function as intended due to the narrow optimal operating range of combustion engines, electric motors have a much broader speed range and generally a higher and more constant torque availability starting from standstill, allowing BEVs to function with just a single-speed reduction gear [4, p. 117]. Only when it comes to high-performance vehicles or vehicles with specialty speed or torque requirements a two-speed transmission is used to optimize acceleration at lower speeds while allowing higher top speeds without sacrificing efficiency [8, p. 57].

Figure 2.5 illustrates how a two-speed transmission transforms the basic torque curve of an electric motor. It can be seen that a speed reduction always comes with an increase in torque, which allows the transformation of the engine's point of maximum efficiency into different points of vehicle operation [8, p. 57]. While single-speed transmissions usually use spur-gear systems due to their high efficiency and minimal maintenance requirements, two-speed transmissions often use planetary gear systems for their short disruption of torque during shifting and their compactness [8, p. 54].

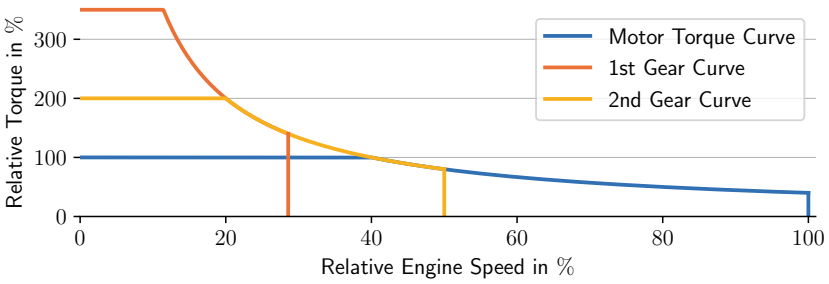

Figure 2.5: Gear Torque Curves based on [8, p. 57].

2.2 Vehicle Kinetics

This section introduces the forces acting on a vehicle during the driving process. It also establishes a foundation for the subsequent algorithms, formalizing variable names and their interdependencies. It is assumed that the vehicle always has traction with the street. This assumption allows neglecting vertical forces and the torque around the center of gravity induced by them. The sum of forces is, therefore, done in the vehicle's longitudinal direction. [8, p. 99] As outlined by Doppelbauer [8, p. 99], the traction force always opposes the sum of all resistive forces:

$$F_{\text{trac}} = F_{\text{air}} + F_{\text{roll}} + F_{\text{climb}} + F_{\text{acc}}. \tag{2.1}$$

The traction force F_{trac} is the force that is applied by the vehicle's drivetrain to the road [8, p. 99]. The air resistance F_{air} is the force that opposes the vehicle's movement due to the air drag [8, p. 100]. The rolling resistance F_{roll} is the force that opposes the vehicle's movement due to the tire movement [8, p. 101]. The climbing resistance F_{climb} is the force that opposes the vehicle's movement due to the road's inclination [8, p. 101]. The acceleration force F_{acc} is the inertial force that opposes the vehicle's movement due to acceleration or deceleration [8, p. 102]. The sum of forces acting on a vehicle in equation 2.1 is also illustrated in Figure 2.6.

In short, that means that if the traction force F_{trac} is greater than the sum of the air, rolling, and climb resistance forces, the acceleration force F_{acc} is positive and the vehicle accelerates. If the traction force is smaller than the sum of the resistive forces, the acceleration force is negative, and the vehicle decelerates. If the traction force is equal to the sum of the resistive forces, the vehicle moves at a constant speed. [8, p. 100-102]

2.2.1 Traction Force

As the traction force is the force that is applied by the vehicle's drivetrain to the road via the wheel torque M_{wheel}, it is directly proportional to the wheel torque and inversely proportional to the wheel radius r_{wheel} [8, p. 100]:

$$F_{\text{trac}} = \frac{M_{\text{wheel}}}{r_{\text{wheel}}}. \tag{2.2}$$

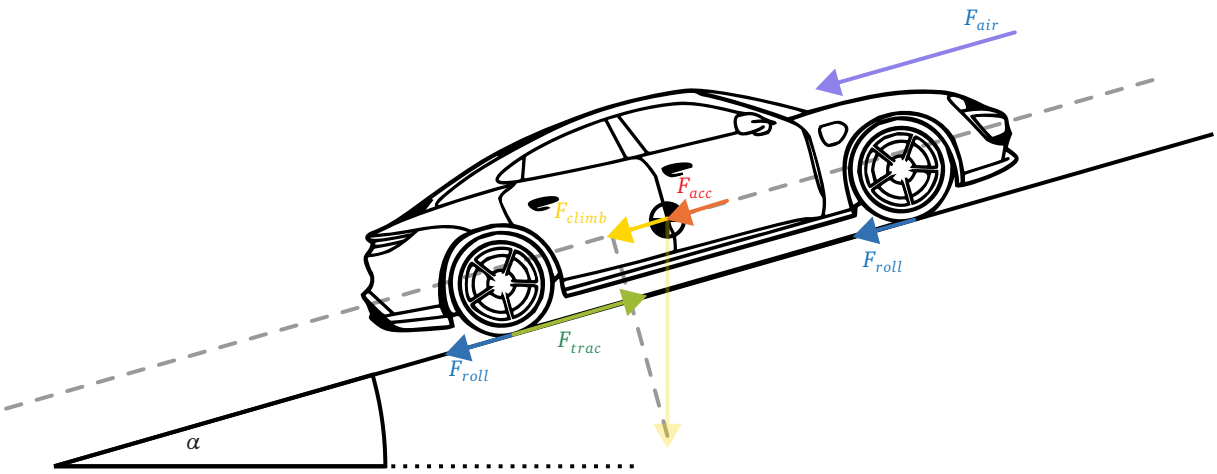

Figure 2.6: Free Body Diagram of a moving vehicle based on [9, p. 50].

In conjunction with the vehicle velocity v, the traction force can be used to calculate the power P_{trac} that is required to move the vehicle [8, p. 100]:

$$P_{\text{trac}} = F_{\text{trac}} v \tag{2.3}$$

If the neutral gear is engaged, the wheel torque is zero, which means the traction force is zero. The vehicle is coasting, and the power applied to or from the drivetrain is zero. Otherwise, the traction force can either be negative or positive to accelerate or decelerate the vehicle. [5, p. 20]

2.2.2 Air Resistance

The air resistance is a collection of all forces that must be overcome to move the vehicle through the air [10, p. 121]. Multiple factors contribute to the air resistance, such as the force applied through atmospheric pressure, boundary layer friction-induced drag, and inner flow drag [10, p. 121]. Induced drag arises from vehicle-generated turbulence, which can be attributed to pressure drag [10, p. 121]. This turbulence often results from pressure differences between the top and underside of the vehicle, creating crossflows [10, p. 121]. As not all incoming air is deflected by the vehicle, but some of the air is channeled inside the vehicle for cooling of components or the air conditioning system, the inner drag is also to be considered [10, p. 122]. This inner drag depends on the vehicle state and dependent on the setting of the air conditioning system and the cooling system can vary and contributes typically 3 % to 11 % of the total air resistance [10, p. 122]. All these contributors to the total resistance are usually quantified by the dimensionless drag coefficient c_w [10, p. 122]. The air resistive force furthermore depends on the air density ρ_{air}, the frontal area A_{front} and lastly also the vehicle velocity [8, p. 100]. The equation gives the air resistance force:

$$F_{\text{air}} = \frac{1}{2} c_w \rho_{\text{air}} A_{\text{front}} v^2 \tag{2.4}$$

[8, p. 100]. Notably, the air resistance force is proportional to the square of the vehicle velocity. This means that the air resistance force increases quadratically with the vehicle velocity. This is a significant factor in the energy consumption of a vehicle, as the air resistance force is the dominant force at higher speeds [11, p. 57].

2.2.3 Rolling Resistance

Modeling the tire-induced resistive force is a complex task as it has many contributing factors, among others, the material of the tire, the tire pressure, the tire temperature, the tire wear, the vehicle mass and velocity, and the road surface [11, p. 12]. The most obvious and largest contributors are the deformation losses [11, p. 30]. As the tire is a non-rigid body, it deforms when it is loaded and can be modeled as a spring-dampener system [11, p. 30].

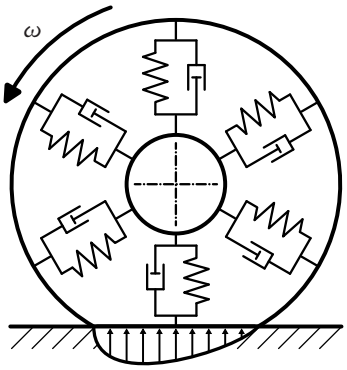

Figure 2.7: Tire Model based on [11, p. 30].

Figure 2.7 illustrates this deformation alongside the force distribution and contact patch. Influenced by the tire's rotation, the center of pressure is not in the center of the contact patch but rather slightly in front of it. This offset creates a moment around the center of the tire, which opposes the driving direction as a result of the deformation [11, p. 30]. This constant deformation creates energy losses due to internal friction within the rubber material, known as hysteresis losses [11, p. 12]. As the tire moves out of the contact patch, the energy does not completely recover, resulting in rolling resistance [11, p. 12]. Caused by the deformation, the contact patch is not a perfect line but rather a small area. If the tire is rotated along this flat contact patch, it means that some contact areas are not rolling perfectly but are rather always sliding, which creates additional energy losses [11, p. 79]. Schütz models deformation losses [12, p. 15] as a function of the normal force F_N acting on the tire combined with a tire-specific rolling resistance coefficient f_r, which capture the tire-specific properties, like pressure, material, and temperature [12, p. 15]. With the vehicle mass m_v, the inclination α, and the acceleration due to gravity g, the rolling resistance force is given by the equation:

$$F_{\text{roll}} = f_r F_N = f_r m_v g \cos(\alpha) \tag{2.5}$$

[12, p. 15]. This model captures the velocity-independent tire deformation resistance well enough for most applications [12, p. 15], but with increased velocity, more complex dynamic effects, mainly wave formation around the circumference of the tire, have to be considered [11, p. 79]. With sufficiently high velocities, this wave-induced resistance and thus heating of the tire becomes the dominant factor and ultimately limits the vehicle's top speed [11, p. 79]. Mitschke and Wallentowitz [11, p. 79] therefore introduce a velocity-dependent rolling resistance coefficient, which is a function of the vehicle velocity v:

$$f_r(v) = f_{r,0} + f_{r,1} \frac{v}{100\,\mathrm{km\,h^{-1}}} + f_{r,4} \left(\frac{v}{100\,\mathrm{km\,h^{-1}}} \right)^4. \tag{2.6}$$

2.2.4 Climbing Resistance

The climbing force is a force that opposes the vehicle's movement when the road is inclined [8, p. 101]. If the road goes downhill, the climbing force is negative, and the force accelerates the vehicle. In the flat case,

the vehicle's weight is perpendicular to the road and has as such noch influence on the forces acting in the longitudinal direction of the vehicle [8, p. 101]. As can be seen in Figure 2.6, if the road is inclined by an angle, the vehicle's weight $m_v g$ is not perpendicular to the road anymore and has, as such, a component in the longitudinal direction of the vehicle [8, p. 101]. The climbing force can, therefore, be computed as

$$F_{\text{climb}} = m_v g \sin(\alpha) \tag{2.7}$$

[8, p. 101]. It is notable that the climbing resistance is no dissipative force but rather a force that is converted into potential energy [12, p. 15], which in turn allows the backconversion of potential energy into kinetic energy when the vehicle goes downhill [12, p. 15].

2.2.5 Acceleration Force

The acceleration force is the force that overcomes the inertia to accelerate or decelerate the vehicle [8, p. 102]. With the assumption that the vehicle is always in traction with the road, not only the inertia of the vehicle mass in lateral direction has to be considered, but as change of vehicle velocity always also involves a change in the rotational speed of drivetrain components, the inertia of the drivetrain components must also be considered [8, p. 102]. To account for the inertia of the rotating components, an equivalent mass m_{acc} can be found for each rotating component that captures the inertial effects of the rotation and gives an equivalent longitudinal internal mass [8, p. 103]. The equivalent mass for the rotating components is given by

$$m_{\text{acc}} = \frac{J_{\text{rot}} j^2}{r_{\text{wheel}}^2} \tag{2.8}$$

[11, p. 80]. With J_{rot} being the rotational inertia of the rotating component, j being the transmission ratio between the pre-transmission side rotating components and wheel-side rotating components [11, p. 80]. Using this equation, the equivalent mass $m_{\text{acc,W}}$ can be expressed as

$$m_{\text{acc,W}} = 4\frac{J_{\text{rot,W}}}{r_{\text{wheel}}^2} \tag{2.9}$$

[8, p. 102]. In this case, j is equal to one, as the wheel rotates with wheel speed. The transmission ratio between the motor and wheel speed has to be considered for the motor inertia. The equivalent mass $m_{\text{acc,M}}$ for the motor is given by

$$m_{\text{acc,M}} = \frac{J_{\text{rot,M}} j^2}{r_{\text{wheel}}^2} \tag{2.10}$$

[8, p. 102]. Using the actual vehicle mass and the sum of the equivalent masses, the acceleration force can be calculated as

$$F_{\text{acc}} = (m_v + m_{\text{acc}})a, \tag{2.11}$$

with a being the acceleration or deceleration in longitudinal direction of the vehicle [8, p. 102]. The World Wide Harmonized Light Vehicle Test Procedure (WLTP) standard [13] also provides a formalized approach to estimate the rotating mass equivalents. Because the number of components for two-wheel and all-wheel drive vehicles can vary, the WLTP standard differentiates between two-wheel and all-wheel drive vehicles [13]

$$m_{\text{acc}} = \begin{cases} 0.03 m_{\text{v}} + 25\,\text{kg} & \text{for 4WD vehicles,} \\ 0.015 m_{\text{v}} & \text{for 2WD vehicles.} \end{cases} \tag{2.12}$$

2.3 Drivetrain Efficiency

The overall efficiency $\eta_{\text{drivetrain}}$ of the drivetrain is the ratio of the output power P_{out} to the input power P_{in} [7, p. 197]. In this case, the incoming power is the power that is provided by the battery P_{battery} and the outgoing power is the power that is applied the traction power applied to the road by the wheels

$$\eta_{\text{drivetrain}} = \frac{P_{\text{out}}}{P_{\text{in}}} = \frac{P_{\text{trac}}}{P_{\text{battery}}} = \frac{F_{\text{trac}} v}{U_{\text{hv}} I_{\text{hv}} - P_{\text{aux}}}. \tag{2.13}$$

To remove the influence from additional consumers of electrical power, the auxiliary power consumption P_{aux}, with the high voltage battery current I_{hv} and the high voltage battery voltage U_{hv} is subtracted from the power provided by the battery.

2.4 Automotive Benchmarking

Benchmarking in the automotive industry is a common practice to evaluate the characteristics of a vehicle [14]. Driven by the need to compare vehicles with each other, benchmarking is used to evaluate how to position a vehicle in the market among continuous monitoring of the development status [14]. But benchmarking is not only used by vehicle manufacturers and legislators to quantify vehicles in multiple aspects [14], but also to parametrize vehicle models for simulation purposes [15]. The following section will introduce how previous research uses benchmarking to determine efficiency maps, aerodynamic and rolling resistance, and the gear shift strategy of a vehicle, both under laboratory conditions and with real driving data.

2.4.1 Laboratory Supported Benchmarking

All methods that utilize special facilities to provide a controlled environment for the vehicle are considered laboratory-supported benchmarking for this investigation. Therefore, measurements done on a closed test track are considered laboratory-supported benchmarking among dynamometer and wind tunnel tests. The following section will outline previous approaches to obtain efficiency maps, aerodynamic and rolling resistance coefficients, and the gear shift strategy from laboratory-supported benchmarking.

Efficiency Map Determination from Laboratory Tests

The efficiency map of a BEV drivetrain is commonly determined using a rolling dynamometer. This specialized test system enables controlled assessment of the drivetrain's performance under various operating conditions [16]. A rolling dynamometer consists of a set of rollers that simulate road conditions by allowing the vehicle to remain stationary while its driven wheels rotate on the rollers [17, p.201]. The rolling dynamometer provides for precise control of test conditions, enabling measurements across a full torque-speed plane [16]. This is achieved by setting specific torque and speed points and recording efficiency at each operating point [16]. The efficiency map is then constructed by plotting the efficiency values against the torque and speed points

[16]. Rosenberger et al. used a rolling dynamo to build efficiency maps for the VW ID.3 and the Porsche Taycan [3, 18].

Road Load Coefficient Determination from Laboratory Tests

When measuring the drag forces of the vehicle, it is common practice to measure the combined drag forces of the vehicle as a function of velocity [13, 19–21]. As outlined in the WLTP standard [13], the drag characteristics of a vehicle are captured by fitting a quadratic function of the form

$$F_{\text{drag}(v)} = f_0 + f_1 v + f_2 v^2 \tag{2.14}$$

[13]. The drag force model $F_{\text{drag}}(v)$ is the sum of the air resistance and the rolling resistance [13]. The coefficients f_0, f_1, and f_2 (Road Load Coefficients (RLCs)), are determined by fitting the drag force measurements to the quadratic function [13]. These RLCs allow thus to quantify the drag characteristics of a vehicle agnostic of the vehicle's drivetrain or any specific tire and air resistance models [19, 20]. A commonly used method to determine these coefficients under laboratory conditions is the coastdown test, where the vehicle is accelerated to a specific speed and then allowed to decelerate freely in neutral gear on a closed test track with as many controlled parameters as possible [17, p. 206]. By analyzing the recorded velocity-time profile, the RLCs can be derived [17, p. 206]. The rolling resistance is more dominant at lower speeds, while the aerodynamic drag becomes increasingly significant at higher velocities [17, p. 206]. To accurately represent real-world conditions, coastdown tests are typically conducted in both directions multiple times to minimize the influence of wind and road inclination [17, p. 207]. The derived resistance parameters can then be transferred to a chassis dynamometer, where the vehicle is subjected to a controlled environment replicating real-world drag forces [17, p. 207]. Rosenberger et al. determined the RLCs for the VW ID.3 and the Porsche Taycan using a coastdown test under laboratory conditions [3, 18].

Shift Strategy Determination from Laboratory Tests

A review of the existing literature reveals that there is a scarcity of studies that have analyzed and derived a vehicle's gear shift strategy under laboratory conditions, such as on a rolling dynamometer. Despite the widespread use of dynamometer testing for efficiency mapping, no references that specifically investigate shift strategy determination for internal combustion engine vehicles in such a controlled setting could be found.

For BEVs, the lack of research in this area may be attributed to the fact that the vast majority of BEVs employ a single-speed transmission, rendering a shift strategy analysis unnecessary. The only identified study conducting such an analysis under laboratory conditions is Rosenberger et al. (2025), who examined the shift strategy of the Porsche Taycan, one of the few BEVs equipped with a multi-speed gearbox [18]. This highlights a potential research gap in the field of shift strategy determination for vehicles with multi-gear transmissions, particularly in controlled laboratory environments.

2.4.2 On-Road Driving Data Supported Benchmarking

In recent years, data-driven approaches have become increasingly prevalent in deriving vehicle parameters from real-world driving data [15, 19, 22–41]. This trend highlights the growing intersection between data science and automotive research. Unlike laboratory-based benchmarking, real driving data-supported benchmarking uses data collected during public road driving to derive vehicle parameters, aiming to achieve comparable data quality with lower effort and cost. The following subsections review prior approaches, their findings, and identified limitations.

Efficiency Map Determination from On-Road Data

Dépature et al. [33] addressed the challenge of deriving efficiency maps from real-world driving data, motivated by the need to model BEVs without prior knowledge of detailed parameters or the use of intrusive and costly instrumentation. They calculated drivetrain efficiency across various operating points by measuring the battery's power and the wheels' mechanical output power. Validation was performed by predicting vehicle energy consumption over an actual driving cycle, achieving an accuracy within $5\,\%$ of the actual reported energy consumption. The authors acknowledged that future accuracy improvements could incorporate additional environmental parameters like road slope and expand driving condition coverage.

Building on this work, Dépature et al. [32] extended their research by comparing on-road data methods with dynamometer-based experiments. They refined the methodology by integrating wheel torque measurements into output power calculations. Comparative analysis revealed an absolute difference of less than $6\,\%$ across most torque-speed regions. The authors concluded that the on-road method is a viable alternative to dynamometer-based approaches but noted limitations, including errors in estimated wheel torque. They recommended closed-loop wheel torque measurements for future studies. Additionally, the inherent transient states of real-world driving necessitated data filtering, which may introduce inaccuracies.

Kropiwnicki and Gawlas [39] developed a method to evaluate the energy efficiency of BEV drivetrains under real-world urban operating conditions, with a particular focus on the impact of regenerative braking. Their approach uniquely examines how varying operating conditions influence drivetrain efficiency. Utilizing Global Positioning System (GPS) speed and elevation data, they estimated energy consumption and recovery through regenerative braking. Their findings indicate that regenerative braking efficiency varies significantly, primarily influenced by vehicle speed and battery State of Charge (SOC). The study demonstrates that GPS logger data provides a viable means of estimating energy consumption. Moreover, the results underscore the critical role of SOC in regenerative braking efficiency, suggesting that integrating SOC into efficiency map algorithms could enhance accuracy. While the authors provide efficiency ranges for specific test vehicles, their methodology does not extend to constructing a comprehensive efficiency map across all operating conditions. This limitation could impact broader applicability.

Road Load Coefficient Determination from On-Road Data

Batra et al. [41] follow the same overarching motivation of leveraging data from on-road tests to minimize costs and time consumption. The authors developed a method to derive essential vehicle parameters such as the aerodynamic drag coefficient, rolling resistance coefficient, center of gravity, frontal area, and wheel inertia from data collected during tests of a Toyota Rav4EV. Coast-down tests were performed to gather road load data, involving vehicle acceleration to $80\,\mathrm{km\,h^{-1}}$ followed by coasting in neutral until a standstill. The recorded data included wheel torque, vehicle speed, GPS position, acceleration, and brake pedal positions. Additionally, a weather station was deployed to measure wind speed. The parameter estimation utilized a nonlinear least-squares estimator implemented in MATLAB, with validation conducted through comparisons to experimental measurements obtained from lab-based tests. Despite its advantages, the proposed method exhibits notable limitations. The dependency on accurate wind speed measurements introduces potential sources of error, especially in uncontrolled environments. The tire model employed assumes linear rolling resistance below $70\,\mathrm{km\,h^{-1}}$, which oversimplifies real-world behavior and may affect the accuracy of derived parameters. Furthermore, the methodology was restricted to closed-off roads and a maximum speed of $80\,\mathrm{km\,h^{-1}}$, limiting the generalizability of the results to more diverse driving scenarios.

Šarkan et al. [36] are primarily motivated by improving the accuracy, reliability, and practicality of driving resistance measurements, which are critical for WLTP and UNECE test procedures. They applied the coast-down method to estimate the total resistance acting on vehicles. The methodology involved accelerating the

vehicle to $110\,\mathrm{km\,h^{-1}}$, shifting it into neutral, and allowing it to coast to a standstill. The authors calculated the average deceleration within $20\,\mathrm{km\,h^{-1}}$ speed segments to determine the resistance forces. Atmospheric data, including wind speed and air temperature, was recorded using a weather station. The tests were conducted on a closed-off test track, isolating the vehicle from public road conditions. However, several limitations were identified in their approach. Notably, the effects of track slopes exceeding the $1\,\%$ limit mandated by WLTP standards were not accounted for, which could introduce significant errors in the resistance force calculations. Furthermore, their exclusive use of a closed-off test track limits the generalizability of the results to diverse real-world driving scenarios. Future work could address these shortcomings by incorporating slope correction techniques and expanding testing conditions to include public road environments, enhancing the robustness and applicability of their findings.

Komnos et al. [31] introduce a method for quantifying rolling resistance and aerodynamic drag using on-road measurements without the need for specialized facilities or expensive equipment. Their approach fundamentally differs from traditional coast-down experiments, where the vehicle is accelerated and then allowed to coast in neutral, measuring the velocity decrease over time. Instead, Komnos et al. maintain the vehicle at constant speeds over a range of different velocities. By measuring the torque required to keep the vehicle at a steady speed, they calculate the forces acting on the vehicle and subsequently determine the road load coefficients. This constant-speed methodology allows for the direct measurement of the power needed to sustain motion, offering a practical alternative to the deceleration-based coast-down method. The results of their approach showed a deviation of less than $5.8\,\%$ compared to manufacturer-provided target values, demonstrating its potential accuracy. A notable advantage of this method is its applicability on public roads, eliminating the need for controlled testing environments. Additionally, maintaining constant speed segments enables the averaging of minor errors, enhancing data reliability. However, the authors acknowledge that inaccuracies in GPS data, particularly for elevation correction, occasionally impacted the precision of their results. Komnos et al.'s approach presents an innovative alternative to coast-down testing by leveraging steady-state conditions to directly measure rolling and aerodynamic drag forces. While the method demonstrates promising accuracy and broader applicability, addressing GPS-related limitations would further strengthen its robustness and reliability for widespread use.

Another team of researchers that tackled the data-driven road load coefficient estimation problem is Singh et al. [40]. The authors aim to contribute to the field by focusing on residual road load that exists between lab-measured and track-measured road loads. Data from on-road coast tests, mainly velocity, and wheel torque, were used alongside data from lab tests, which included wind tunnel aerodynamic tests as well as rolling resistance measurements (Society of Automotive Engineers (SAE) J2352). They also used wind speed, temperature, and pressure data from a weather station to minimize variability from environmental factors. Using two multinomial regression models, they fit polynomials of third degree to the data. Employing Spearman correlation and the Analysis of Variance (ANOVA) f-statistic, they identified relevant predictive features from the dataset. The authors acknowledge that a lot of data is required for their machine-learning approach, such that their model was probably overfitted, which may have led to limited generalizability. They also acknowledge that with higher amounts of data, it would be possible to more closely resolve non-linearities in the tire model. Like others that did coast-down tests, these authors also mention the complexity of real-world testing as the environmental conditions frequently vary widely.

Shift Strategy Determination from On-Road Data

Ngo [30] demonstrated the ability to build shift maps from driving data. Since most shift strategies follow distinct upshift and downshift rules, Ngo initially extracted all shift-up and shift-down moments from the driving data. He effectively reduced the scattered data into gear change thresholds by combining hierarchical clustering to identify outliers with non-hierarchical clustering to determine cluster means. This approach

successfully enabled the determination of gear change strategies directly from driving data. However, the study primarily focused on static clustering methods and internal combustion engine vehicles and did not evaluate the sensitivity of the results to varying clustering parameters.

Wang et al. [29] were motivated by the need to automate gear change strategies for mining trucks to minimize errors and inefficiencies in mining operations. Their approach involved collecting data from manually driven trucks via the Controller Area Network (CAN)-bus. The data underwent preprocessing to eliminate outliers and normalize the features. The authors predicted gear shifts using a Bi-LSTM network, which considers sequential data from both past and future states. Key features for training included accelerator pedal position, driver-requested torque, actual engine percent torque, engine speed, actual gear ratio, transmission current range, transmission sump oil temperature, and output shaft speed. Among several architectures evaluated, the Bi-LSTM performed best, achieving $95.8\,\%$ accuracy on the test dataset. While promising, their approach relied heavily on predefined feature engineering and did not explore potential variations in data patterns across different vehicle types or driving environments, which could impact generalizability.

Feng et al. [28] sought to develop an adaptive gear shift strategy to enhance fuel efficiency and drivability, addressing the limitations of traditional strategies that lack adaptability to diverse driving behaviors and environmental conditions. The authors collected naturalistic driving data using onboard diagnostics and CAN-bus across various scenarios and preprocessed it with a low-pass filter to remove noise. Long-term driving behavior was classified into categories (mild, normal, aggressive) using fuzzy C-means clustering, while short-term intentions (e.g., rapid acceleration) were identified with an Long Short Term Memory (LSTM) network. Road slope estimation was achieved through a combination of dynamic and kinematic models. While their methodology demonstrated significant potential, key shortcomings included a lack of sensitivity analysis for clustering and network parameters and reliance on heuristic assumptions. Furthermore, like many other studies, their approach still depended on controlled conditions on test tracks, limiting its applicability to real-world driving scenarios. Moreover, their machine-learning-based approach necessitates substantial amounts of data, which was feasible as they gathered information from a fleet of mining vehicles. However, this contradicts the goal of reducing effort.

The reviewed studies demonstrate diverse methods for deriving shift strategies from driving data. While clustering-based approaches, such as those proposed by Ngo [30], effectively condense scattered data into actionable thresholds, machine learning methods like those in Wang et al. [29] and Feng et al. [28] offer enhanced adaptability to varying driving conditions.

Summary of Previous Work

A review of existing studies on data-driven benchmarking for efficiency map derivation, road load coefficient determination, and shift strategy analysis reveals a variety of promising approaches. On-road data collection methods have demonstrated considerable potential in minimizing the cost and effort associated with traditional laboratory or test-track measurements. In particular, researchers have successfully obtained drivetrain efficiency maps [32, 33, 39] and vehicle road load coefficients [31, 36, 40, 41] under real-world driving conditions by leveraging readily available data (e.g., GPS, CAN-bus signals, and weather station measurements). While these methods generally achieve accuracy levels of around $5\,\%$ to $6\,\%$ deviation from established baselines, they frequently encounter challenges related to data quality and the complexity of uncontrolled environmental conditions.

For efficiency map estimation, some researchers [32, 33] employed battery power outputs alongside wheel power measurements to model BEVs, achieving good alignment with dynamometer experiments. However, these studies noted that capturing highly transient states under real driving conditions can necessitate significant data filtering, potentially impacting the fidelity of the results. Others [39] have underscored the

relevance of regenerative braking and SOC on efficiency but did not extend their analysis to a complete operating map, limiting broader applicability.

Road load coefficient estimation from on-road measurements has similarly evolved from coast-down methods [36, 40, 41] to constant-speed testing [31], aiming to reduce reliance on specialized facilities. Despite notable progress, most studies underscore the influence of factors such as wind speed, road slope, and GPS-related elevation uncertainties. Moreover, many of these experiments still relied on controlled or partially controlled settings (e.g., closed test tracks), restricting their generalizability to broader real-world conditions.

In terms of deriving shift strategies, approaches have ranged from clustering-based threshold extraction [30] to machine learning methods leveraging CAN-bus data [28, 29]. While these techniques have demonstrated high prediction accuracy (over $95\,\%$ in some cases), they typically require extensive datasets and often focus on particular vehicle types or applications (e.g., mining trucks). Furthermore, existing studies do not explicitly address scenarios involving passenger vehicles equipped with multi-speed gearboxes beyond the limited investigations carried out by Rosenberger et al. [18]. Consequently, none of these methods precisely match the requirements of our use case, where a flexible, data-driven, and broadly applicable shift strategy derivation is desired.

A consistent issue across nearly all areas is the limited scope of sensitivity analyses. Although many authors acknowledge the impact of parameter assumptions and filtering steps, explicit quantification of how these choices affect final accuracy remains scarce. In addition, many studies rely on test-track environments or closed roads to control for confounding factors, which curtails their real-world applicability. These constraints illustrate the need for further research that rigorously evaluates model sensitivities, minimizes cost-intensive instrumentation, and broadens the scope to find a solution that applies to a wide range of vehicles and driving conditions.

While previous work provides a solid foundation for data-driven automotive benchmarking, a gap remains in developing robust, widely generalizable, and cost-effective methods, particularly for multi-gear transmissions and comprehensive real-world parameter estimation. Addressing these gaps is crucial for advancing the state of the art and enabling more accurate, scalable benchmarking solutions.

2.5 Knowledge Discovery in Databases

The KDD process was first described by Fayyad et al. [42] and provides a methodological approach to extract valid, novel, useful, and understandable patterns from data [42, 43]. It was designed to tackle the problem of ever-increasing amounts of data in the digital age, which necessitates the integration of statistical, Machine Learning (ML), and database techniques [42]. In contrast to traditional data analysis, KDD emphasizes an end-to-end process, removing the need for manual intervention at each step [42]. KDD has gained widespread adoption in domains such as marketing, finance, healthcare, and scientific research, where large datasets require systematic analysis to derive actionable insights [43]. The KDD process consists of several steps, as illustrated in Figure 2.8.

Initially, the process begins with forming a clear understanding of the domain and the application goals [42]. This includes researching existing and relevant knowledge, including existing models, trends, and challenges [42]. Additionally, it is of high importance to clarify what "useful knowledge" means in the context of the application to have a clearly defined goal [43]

The next step is to select the right target data from the whole pool of available data [42]. This may include identifying and gathering data sources relevant to the defined goals while also ensuring that data is integrated, if necessary, to ensure a cohesive and unified representation of relevant data [43]. It must be noted that

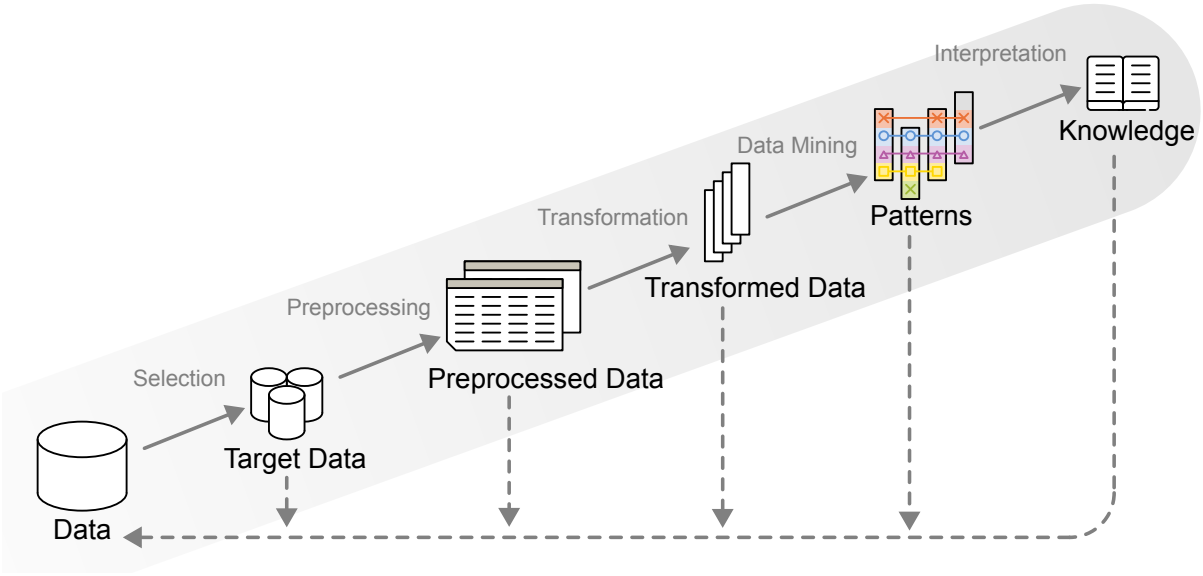

Figure 2.8: Knowledge Discovery in Databases based on [42].

incomplete or biased data can lead to invalid results, so careful attention must be given to the data coverage [43].

The target data is then algorithmically cleaned and preprocessed to increase the quality of the data [42]. This includes the removal of noise and outliers, handling missing values by imputation or interpolation, and accounting for inconsistencies in data representation, such as mixed units or different length scales [43]. This step frequently consumes the majority of project time but is mission-critical as the quality of the results depends on the quality of the data [43].

The preprocessed and prepared data is subsequently transformed into a representation that can be fed into data-mining algorithms [43]. This step could include dimensionality reduction techniques like Principal Component Analysis (PCA) or feature selection to focus on the most relevant features [43]. Domain transformations like discretization variables or representing in a different basis are also common [43]. Domain knowledge is crucial to guide this step [42]. Additionally, iterative exploration of transformed data may reveal additional insights [43].

The data mining step is the core of the KDD process, where algorithms are applied to the transformed data to extract patterns [42]. Initially, the data mining task has to be well-defined. Whether the goal is predictive or descriptive is to be aligned with the task description from the first step [43]. Another key step is to decide on a success metric that can be used to quantify the quality of the results, which could be accuracy for predictive tasks or interpretability for descriptive tasks [43]. With known goals, a suiting algorithm can be selected and applied [43]. This may often include experimentation with different model types and hyperparameters to iteratively refine the results [43]. This step is highly iterative as adjustments to the data mining process frequently rely on the findings of intermediate results [42, 43]. Visualizations are essential to understand the results and to guide the iterative process [42].

When patterns of acceptable quality have been obtained from the data-mining step, the results have to be evaluated for validity, novelty, and utility regarding the project's goals [42]. Again, visualizations are key to understanding the results and communicating them to stakeholders while simultaneously providing transparency [43]. The final step is to integrate the discovered knowledge into new applications or to refine existing ones [42].

This proven methodology to discover robust and systematic insights from raw data is chosen as a backbone for the data-driven approach to derive vehicle parameters from real-world driving data. The interdisciplinary

domain-agnostic nature of the KDD process [42, 43] makes it a suitable framework for deriving vehicle parameters from real-world driving data. Also, the iterative nature of the KDD process [42, 43] allows for revisiting different techniques. Another great alignment of the KDD process with the problem at hand is the focus on practical utility, which ensures that the results are actionable and meaningful [42, 43], which aligns perfectly to improve cost-effective benchmarking of vehicle parameters to both inform simulations while also providing tools to validate manufacturer claims. The inherent consideration of complex, multi-dimensional, and heterogeneous data [42, 43] is also an excellent fit for the problem at hand. The emphasis on preprocessing [42, 43] further aligns well, as the data at hand is recorded data from driving on public roads, which means that it is likely noisy and incomplete.

2.6 Algorithmic Methods

This section presents fundamental algorithmic methods that support the data-driven techniques discussed later in this thesis. Essential filtering techniques include the Moving Average, Exponential Moving Average, Savitzky-Golay, Inverse Distance Weighting, and Gaussian filters, all crucial for preprocessing noisy and irregular data. Additionally, key machine learning algorithms for regression and clustering, such as Random Forest (RF), k-Means, and Density Based Spatial Clustering of Applications with Noise (DBSCAN), are reviewed. These standard techniques establish the theoretical and practical basis for the subsequent data-driven approaches in the following chapters.

2.6.1 Filters

Time series data collected from real-world driving scenarios often contain noise and outliers that may distort the accuracy of derived vehicle parameters [44]. Filtering techniques are commonly employed to remove unwanted noise and enhance the quality of the data [43]. The following subsections introduce filtering methods that are used to preprocess driving data for subsequent analysis.

Moving Average

The Moving Average filter, sometimes also called Simple Moving Average, is a commonly used filtering technique belonging to the family of smoothing methods [44]. The smoothing is achieved by averaging a fixed number of previous data points, known as the window size n_{window}, to generate a new data point y_i [44]:

$$y_i = \frac{1}{n_{\text{window}}} \sum_{j=0}^{n_{\text{window}}-1} x_{i-j}. \tag{2.15}$$

The Moving Average filter is effective in reducing high-frequency noise and outliers, making it suitable for preprocessing driving data with erratic fluctuations [44]. Other benefits include its computational efficiency and ease of implementation, making it a popular choice for real-time applications [44]. Drawbacks include its tendency to introduce lag in the data, which may impact the accuracy of time-sensitive applications [44]. Additionally, the window size has to be tuned carefully to find a balance between noise reduction and data distortion [44].

Exponential Moving Average

The Exponential Moving Average (EMA) filter is an extension of the Moving Average filter that assigns exponentially decreasing weights to previous data points [44]. The EMA filter is defined as:

$$y_i = \alpha_{\text{ema}} x_i + (1 - \alpha_{\text{ema}}) y_{i-1}, \tag{2.16}$$

where y_i is the filtered data point, x_i is the raw data points, and α_{ema} is the smoothing factor [44]. The smoothing factor determines the weight assigned to the current data point relative to the previous filtered data point [44]. A large α_{ema} produces a more responsive filter, analogous to using a smaller window size in the Moving Average filter, while a small α_{ema} results in a more stable filter, similar to a larger window size [44]. As the influence of the weights is exponentially decaying with increased distance from the current data point, the EMA filter is less prone to lag compared to the Moving Average filter and typically provides a better tradeoff between noise reduction and signal distortion [44]. The computational efficiency is less than the Moving Average filter because it requires recursive calculations [44]. Nevertheless, the computational overhead is minimal and does not significantly impact real-time applications [44].

Savitzky-Golay

The Savitzky-Golay filter is, as the moving average based methods, a smoothing filter and was first introduced in 1964 by Savitzky and Golay [45]. The idea is to combat the problem of signal distortion by using a local least-squares polynomial fit to the data [45]. Unlike the moving average-based filters, the Savitzky-Golay filter does not blur signal features but preserves fine detail like peaks while still reducing noise [46]. The Savitzky-Golay filter is parametrized by the polynomial order N and the window size $2M + 1$, with M being the number of data points to be considered for the local polynomial environment fit on each side of the current data point [45]. A polynomial of the form

$$p(n) = \sum_{k=0}^{N} a_k n^k \tag{2.17}$$

is fitted to the data points in the window, with the coefficients a_k being determined by least-squares fitting [45]:

$$E_{ls} = \sum_{n=-M}^{M} \left(\sum_{k=0}^{N} a_k n^k - x(n) \right)^2. \tag{2.18}$$

This results in a set of $N + 1$ equations, which can be solved for the coefficients a_k using this equation system [45]:

$$a = (A^T A)^{-1} A^T x, \tag{2.19}$$

where A is the design matrix containing powers of n and x is the vector of data points [45, 46]. Once the coefficients a_k are determined, the smoothed data point is obtained by evaluating the polynomial at the center of the window, which leads to a discrete convolution with a fixed set of weights [46]:

$$y(n) = \sum_{m=-M}^{M} h(m) x(n-m), \tag{2.20}$$

where $h(m)$ are the precomputed filter coefficients derived from the least-squares polynomial fitting process [45]. These coefficients depend solely on the polynomial order N and window size $2M+1$ and are determined as:

$$h = \left(A^T A\right)^{-1} A^T e, \tag{2.21}$$

where e is the unit impulse vector used to extract the polynomial coefficient corresponding to the center point [46].

The primary advantage of the Savitzky-Golay filter over moving average-based filters is its ability to smooth noisy data while preserving important signal features, such as peaks and valleys [45]. Unlike the Moving Average and Exponential Moving Average filters, which tend to flatten peak structures, the Savitzky-Golay filter maintains local maxima and minima, making it particularly useful for applications in which shape preservation is crucial, such as spectral analysis and vehicle dynamics research [46]. Another advantage is that the Savitzky-Golay filter can also be used to compute numerical derivatives, as the polynomial coefficients allow for direct differentiation of the smoothed signal [45]. This makes it a suitable choice for applications requiring both noise reduction and feature extraction. However, the filter has some limitations. Compared to simple moving average methods, it is computationally more intensive, as it requires solving a least-squares system to derive the filter coefficients [46]. While these coefficients can be precomputed for a given polynomial order and window size, the computational cost may still be higher for real-time applications with dynamically varying window sizes. Another drawback is its sensitivity to the choice of parameters. Selecting an inappropriate polynomial order N or window size $2M+1$ can lead to overfitting or under-smoothing, potentially amplifying noise instead of reducing it [46]. Additionally, the filter is less effective when dealing with non-uniformly sampled data, as it relies on fixed-width convolution windows. Despite these challenges, the Savitzky-Golay filter remains a powerful tool for processing real-world driving data, particularly when it is essential to preserve the integrity of peaks and other localized features while reducing noise [46].

Inverse Distance Weighting

Inverse Distance Weighting (IDW) is a deterministic spatial interpolation method that can be applied for spatial data analysis [47]. The basic idea is that points closer to the location of interest have a larger influence on the interpolated value than points further away [47]. By assigning weights to know data points that are inversely proportional to their distance from the location of interest, this assumption can be implemented with $z(x_0)$ being the interpolated value at location x_0 and $z(x_i)$ being the known value at location x_i [47]:

$$z(x_0) = \frac{\sum_{i=1}^{N} w_i z(x_i)}{\sum_{i=1}^{N} w_i}. \tag{2.22}$$

Further, the weights w_i are defined as

$$w_i = \frac{1}{d(x_0, x_i)^p}, \tag{2.23}$$

with $d(x_0, x_i)$ being the distance between the location of interest and the known data point [47]. The power parameter p is the only design parameter that has to be set for this method, which determines the influence of the distance on the weight [47]. A higher p leads to a more local interpolation, while a lower p leads to a

more global interpolation [47]. IDW is particularly useful when the spatial distribution of data points is irregular. However, its limitations include its inability to extrapolate data as well as the tendency to create "bull's eye" artifacts around data points in sparse regions [47].

Gaussian Filter

The Gaussian Filter is a smoothing filter that has its origins in image processing, where it was mostly used for its ability to reduce noise [48, p. 165]. It works by convoluting the input data with a Gaussian function, resulting in a weighted average that emphasizes central values [48, p. 164-165]. The Gaussian function is defined as:

$$G(s,t) = K \exp\left(-\frac{s^2+t^2}{2\sigma^2}\right), \tag{2.24}$$

with K being a normalization constant and σ being the standard deviation of the Gaussian, which controls the extent of smoothing [48, p. 167]. The application of the Gaussian kernel to the data involves its convolution with the input data [48, p. 167]:

$$f'(s,t) = \sum_{m=-a}^{a} \sum_{n=-b}^{b} f(s-m, t-n) G(m,n), \tag{2.25}$$

with $f'(s,t)$ being the smoothed data, $f(s,t)$ being the input data and $G(m,n)$ being the Gaussian kernel [48, p. 167].

2.6.2 Machine Learning

Mitchell (1997) defines machine learning as: "A computer program is said to learn from experience E with respect to some class of tasks T and performance measure P, if its performance at tasks in T, as measured by P, improves with experience E [49, p. 2]." This fundamental principle of algorithmically improving performance through experience (data) rather than explicit programming underpins the field of machine learning. Machine learning is broadly categorized into supervised and unsupervised learning, each serving distinct purposes in data analysis and pattern recognition [50, p. 3]. Supervised learning involves training the model on labeled data, where the input features are paired with corresponding output labels [50]. Regression and classification tasks are common applications of supervised learning [50, p. 137]. In contrast, unsupervised learning operates on unlabeled data, seeking to identify patterns and relationships within the data without predefined output labels [50, p. 3]. Clustering and dimensionality reduction are typical unsupervised learning tasks [50, p. 3].

Regression

Regression involves training a model to predict one or more continuous output variables based on input features [50, p. 3]. A versatile architecture that can do both regression and classification is the RF architecture, which is used in this work and thus described in more detail in the following paragraph.

Random Forest

As the name Random Forest (RF) implies, it consists of a collection of randomized decision trees [51]. It is thus called an ensemble method, as it combines multiple models to improve prediction accuracy [51]. It can be used for classification and regression [51]. Each tree in the forest is trained on a random subset of

the data and a random subset of the features [51]. This added randomness helps to prevent overfitting and increases the robustness of the model [51]. The final prediction is then the average of all predictions of the individual trees, with a majority vote for classification tasks and an averaging of the predictions for regression tasks [51]. It is also efficient with large datasets, is agnostic to feature scaling, and has the inherent capability to handle missing values [51].

A unique characteristic of the RF algorithm is its ability to provide feature importance scores [51]. It is determined by assessing how much each variable contributes to prediction accuracy. During the construction of the forest, data that is not used in training specific trees is used to estimate the misclassification rate [51]. The mechanism, consisting of random permutation, impact assessment, and relative importance calculation, allows us to give a percentage of how much each feature contributes to the prediction accuracy [51]. The ensemble nature of the RF algorithm makes it possible to independently evaluate predictions using numerous subsets of data [51].

Clustering

Clustering, part of the unsupervised learning regime, groups data points into distinct clusters based on similarity [50, p. 3]. Both the k-means and DBSCAN algorithms are employed for various functions in this work. Both have unique characteristics that make them suitable for different clustering tasks.

k-Means

The k-means algorithm, first described by Macqueen (1967) [52], is a clustering algorithm that divides a set of n data points into k clusters [50, p. 424]. Through an iterative optimization process, the algorithm minimizes the sum of the squared Euclidian distances between data points $x_1, x_2, ..., x_n$ and their corresponding cluster centers $\mu_1, \mu_2, ..., \mu_k$ [50, p. 424]. This optimization objective J also called the *distortion measure* is expressed as:

$$J = \sum_{n=1}^{N} \sum_{k=1}^{K} r_{nk} \|x_n - \mu_k\|^2. \tag{2.26}$$

[50, p. 425]. r_{nk} can be assigned one if x_n belongs to cluster k and zero if otherwise [50, p. 426]. The cluster mean μ_k is then updated as the mean of all data points assigned to cluster k [50, p. 426]:

$$\mu_k = \frac{\sum_n r_{nk} x_n}{\sum_n r_{nk}}. \tag{2.27}$$

By iteratively first assigning each data point to its respective closest cluster centroid and then updating the cluster centroids, the algorithm converges with a monotonically decreasing objective function J to a local minimum [50, p. 428]. Macqueen showed that the algorithm under specific assumptions converges to a specific set of unbiased centroids [52]. It was also shown that specific unstable configurations exist, where centroids oscillate indefinitely [52]. The quality of the clustering is highly dependent on the initial randomly assigned cluster centroids, which means that the algorithm is sensitive to the initial conditions [50, p. 428]. This clustering method is computationally efficient, scalable, and interpretable. Still, it simultaneously has limitations, like its sensitivity to outliers and the need to specify the number of clusters k manually and beforehand [50, p. 428]. Also, the cluster shape is always convex, which limits the applicability to data that forms non-convex clusters [52].

Density-Based Spatial Clustering of Applications with Noise

Another clustering method that has particular differences compared to the k-means method is the DBSCAN algorithm, first introduced by Ester et al. (1996) [53]. It also groups data points into clusters, but it does not require the number of clusters k to be specified beforehand but rather uses density connectivity to arrive at a number of clusters of arbitrary shape while simultaneously identifying outliers as noise [53]. The algorithm required two key parameters: the ε-radius and the minimum number of points n_{min}. The ε-radius defines a set of points $N_\varepsilon(p)$ within a radius around a point p [53]:

$$N_\varepsilon(p) = \{q \in D \mid \text{dist}(p, q) \leq \varepsilon\}. \tag{2.28}$$

The algorithm categorizes the points into three categories: core points, border points, and noise points [53]. The minimum number of points n_{min} defines the minimum number of points that have to be within the ε-radius to consider the point in question as a core point [53]:

$$|N_\varepsilon(p)| \geq \text{MinPts}. \tag{2.29}$$

Border points are identified as points that are within the ε-radius of a core point but do not have enough points within their ε-radius to be considered a core point themselves [53]. Lastly, noise points are points that are neither core points nor border points [53]. The procedure starts by randomly selecting an unvisited point before checking if it fulfills the conditions to be a core point. If so, its cluster is expanded by iteratively adding density-reachable points [53]. If it is not a core point, it is preliminarily labeled as noise, which may be overwritten later when another core point is found and its cluster is expanded [53]. This process is repeated until every data point is visited at least once [53]. One of the main differences to the previously introduced k-means algorithm is its convergence properties. First of all, it does not depend on random initialization, which means that DBSCAN always produces the same result. Additionally, it can converge to clusters of arbitrary shape, which includes elongated and non-convex clusters [53]. It is also highly robust to noise and outliers, as it can identify them as noise points [53]. However, it is still sensitive to its design parameters, as choosing the right ε-radius and a minimum number of points n_{min} is crucial to prevent over-merging or fragmentation [54].

2.7 Parameter Tuning and Sensitivity Analysis

As parameters of data-driven analysis models usually come with a set of design parameters that can not be optimized mathematically, it is crucial to tune these parameters to achieve the best possible performance. In data-driven vehicle benchmarking, these design parameters could include filter sizes, thresholds, or other hyperparameters. As Montgomery (2017) points out, parameter tuning is a key aspect of experimental design, as it helps to investigate the effect of parameter settings on model performance while controlling for interactions between variables [55, p. 3].

Design parameters that can not be trivially determined using optimization techniques must be adjusted empirically to arrive at a robust, reliable, and generalizable model [55, p. 17]. To avoid heuristical guesswork, a systematic approach to parameter tuning is required, ensuring that arbitrary selections are avoided while possible parameter interactions are counted for [55, p. 258]. Traditional Design of Experiments (DoE) techniques provide a systematic way to tune parameters while controlling confounding effects and have widely been applied in engineering to manage high-dimensional parameter spaces [55, p. 180]. Montgomery

suggests using a factorial design of experiments to systematically investigate the effect of multiple parameters on the experiment outcome [55, p. 258]. The ultimate goal in the parameter tuning is robustness, which means that the model should perform consistently across different datasets, generalizing well to unseen data [50, p. 284].

The following paragraphs introduce the specific approach suitable to tune the design parameters of the data-driven vehicle benchmarking models, including the concepts of grid search, sensitivity analysis, and ANOVA.

2.7.1 Grid Search and Design of Experiments

Grid search is a brute-force parameter tuning method that systematically evaluates all possible parameter combinations in a predefined grid [56]. In DoE terms, this approach could be considered analogous to a full-factorial experimental design, where all parameter levels are tested [55, p. 330]. This approach has the advantage that all possible interactions between parameters can be analyzed [55, p. 334]. Bergstra and Bengio (2012) mention the shortcomings of a full, exhaustive grid search approach, as it can quickly become computationally expensive, especially for high-dimensional parameter spaces, and when parameter influence is highly non-linear [56]. The depth of a parameter search must be balanced with computational feasibility. As domain knowledge about the given parameters can be considered a priori, the parameter ranges can be constrained effectively, reducing the number of parameter combinations to be tested to a feasable amount.

2.7.2 Sensitivity Analysis

To understand the influence of design parameters on model performance, two main approaches exist: Local Sensitivity Analysis (LSA) and GSA [57].

LSA investigates how small perturbations in a single parameter affect the model output while all other parameters are held constant [57, p. 11]. This approach assumes low interactions and linearity between parameters, which is often not the case in real-world applications [57, p. 11]. GSA, on the other hand, investigates the effect of parameters over their entire range, providing a round view of the parameter influence on the model output [57, p. 11]. Variance-based methods allow to investigate the influence of each parameter on the model output, as well as the interactions between parameters [57, p. 157]. Due to the expected non-linearities that, for example, smoothing factors or filter thresholds can introduce, alongside the expected interactions that may take place between parameters, a global sensitivity analysis is more suitable for the data-driven vehicle benchmarking models. To quantify the influence of each parameter on the model output, variance-based approaches can be used, like the ANOVA method [57, p. 162].

2.7.3 Analysis of Variance

ANOVA is the most popular method for hypothesis testing currently in use [58]. The general idea of the ANOVA method is to partition the total variability in the dependent variable into contributions from each factor [58]. For each factor, four key values are calculated when conducting an ANOVA analysis: the Sum of Squares (SS), the Mean Square (MS), the F-statistic, and the p-value [58]. The SS quantifies the variation due to each factor [58]. The MS is the SS normalized by the degrees of freedom [58]. The ratio of unexplained variance is expressed by the F-statistic, with the F statistic always being a positive value which, if exceeded 1.0, indicates a difference between tested means [58]. The p-value indicates the statistical significance of the factor, with the limit for significance being set at usually $p = 0.05$ [58]. In the context of parameter tuning, ANOVA can be used to investigate the effect of each parameter on the model output because it allows the ranking of factors based on their statistical significance [58]. The tested hypothesis for each parameter is

whether it influences the results. In interpretation terms, the F-value signifies the degree of influence of a parameter on the model output, while the p-value indicates the statistical significance of the parameter [58]. The sum of squares proportion indicates how much of the total variation is explained by that factor [58]. Using this method, the GSA can be quantified, and the most influential parameters can be identified [58].

2.7.4 Robustness and Generalizability

Overfitting is a central concern in parameter tuning because if the combination is chosen that provides the absolute lowest loss, the algorithm might fail to generalize well to new data [59, p. 111]. To prevent this, a robust approach to design parameter tuning accounts not only for the minimization of the loss but also for maintaining a low variance across different subsets of parameters and datasets [59, p. 122]. Evaluating the Interquartile Range (IQR) of loss scores across multiple runs allows for identifying parameter settings that lead to more stable performance rather than ones that achieve the absolute lowest loss. This aligns with the findings of Bergstra and Bengio (2012), who emphasize that small changes in parameter values can cause significant variations in test performance, particularly in high-dimensional search spaces [56, p. 285].

Another way to improve robustness is to select hyperparameters that work well across different datasets or data subsets rather than just on one dataset. Probst et al. (2019) introduce the concept of tunability, where the goal is not only to minimize loss but also to ensure that the chosen hyperparameters perform consistently in different cases [60, p. 3]. It is, therefore, decided to tune the parameters on the dataset from the vehicle under study before evaluating the performance on a different dataset from another vehicle.

A practical approach is iterative tuning, where first, a broad search is done to find promising parameter regions, and then a more detailed search is performed in these areas. This method helps avoid wasting resources on bad configurations while still making sure the best ones are explored properly [59, p. 432].

Instead of choosing the hyperparameters with the lowest loss, it is better to pick ones that have stable performance, shown by low IQR [56, 60]. Also, robustness can be improved by checking performance across datasets, using visual analysis, and applying iterative search instead of just running one full grid search [60].

3 Vehicle Parameter Estimation from Driving Data

This chapter first introduces the vehicle under study, the Porsche Taycan, and then describes the recorded driving data. Additionally, the algorithms used to estimate the RLCs, the efficiency map, and the gear strategy are introduced alongside the overarching framework to perform the sensitivity analysis of the process parameters, which is then used to investigate the influence of the process parameters on the estimated vehicle parameters. This insight is then used to select robust and functional parameter combinations to estimate the vehicle parameters.

3.1 Vehicle under Study

The Porsche Taycan was chosen as the vehicle for this investigation due to its unique drivetrain configuration, featuring a two-speed transmission on the rear axle [61]. This makes it one of the few BEVs with a multi-speed gearbox [62], providing an ideal platform to extend real driving data-based benchmarking methods to vehicles with multiple gears. Additionally, it's advanced engineering, including high-performance motors, an $800\,\mathrm{V}$ electrical architecture, and comprehensive aerodynamic optimization, ensures that the vehicle's design is representative of cutting-edge BEV technology [63].

Table 3.1 summarizes the relevant technical specifications of the Porsche Taycan, including drivetrain characteristics, aerodynamic properties, and vehicle dimensions.

Table 3.1: Technical Specifications of the Porsche Taycan.

Category	Parameter	Value	Source
General Information	Manufacturer	Porsche	
	Model Year	2022	
	Model / Variant	Y1A / JA12 / 1051000	
Drivetrain	Drive Type	Rear-wheel drive	[62]
	Motor Type	PMSM	[62]
	Transmission	Two-speed gearbox	[62]
	Gear Ratios	15.56 (1st), 8.16 (2nd)	[61]
	Max Engine Torque	$357\,\mathrm{N\,m}$	[62]
	Max Power (Overboost)	$350\,\mathrm{kW}$	[62]
	Max Speed	$230\,\mathrm{km\,h^{-1}}$	[62]
Energy System	Battery Capacity (Gross/Net)	$93.4\,\mathrm{kW\,h}$ / $83.7\,\mathrm{kW\,h}$	[63]
	Battery Type	Lithium-ion, NMC721 chemistry	[63]
	Voltage Architecture	$800\,\mathrm{V}$	[62]
Aerodynamics and Weight	Drag Coefficient (c_w)	0.22	[62]
	Frontal Area (A)	$2.33\,\mathrm{m^2}$	[62]
	Curb Weight	$2282\,\mathrm{kg}$	[62]
	Gross Vehicle Weight	$2795\,\mathrm{kg}$	[62]

Figure 3.1 illustrates the two-speed transmission used in the Porsche Taycan, a key feature that differentiates this vehicle from most other BEVs. Including multiple gears allows for optimized torque delivery and efficiency over a broader operating range, particularly to enable high-speed capabilities while keeping good acceleration at low speeds, which would otherwise challenge single-speed transmissions.

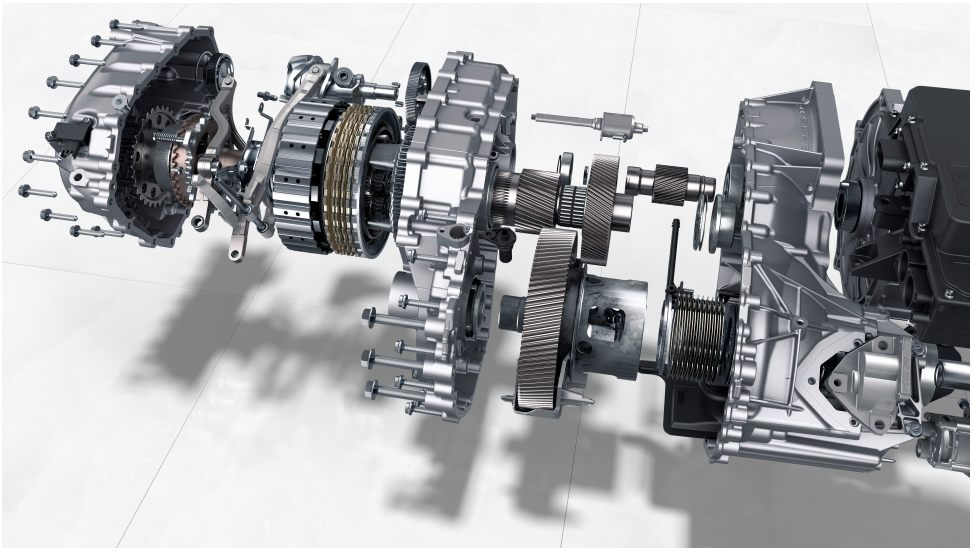

Figure 3.1: Porsche Taycan Two-Speed Transmission [62].

3.2 Characterization of Driving Data

To conduct this investigation, driving data was collected from a Porsche Taycan using a logging device inserted into the vehicle's On-Board Diagnostics (OBD) port. This setup enabled access to the vehicle's CAN bus, allowing real-time recording of various signals. The logger was configured to capture relevant data at specified frequencies, balancing the trade-off between the number of recorded signals and the available bandwidth. Table 3.2 summarizes the recorded signals, their descriptions, and their respective sampling frequencies.

Table 3.2: Recorded Signals.

Signal Name	Description	Unit	Sampling Freq (Hz)
accelerator_pedal	Accelerator pedal position	%	10
air_intake_level_1	Position of air intake flap 1	%	1
air_intake_level_2	Position of air intake flap 2	%	1
brake_pedal_activated	Brake pedal activation	Boolean	10
engine_rpm	Motor speed	min^{-1}	10
gear_selected	Selected gear	-	10
gear_selected_neutral	Neutral gear selected	Boolean	10
hv_battery_current	High voltage battery current	A	10
hv_battery_voltage	High voltage battery voltage	V	10
hv_battery_soc	High voltage battery SOC	%	10
dcdc_power_hv	Power of the HV DCDC converter	W	10
rear_motor_torque	Torque of rear motor	$\mathrm{N\,m}$	10
spoiler_level	Spoiler position	-	1
suspension_level	Suspension level	-	1
steering_wheel_angle	Steering wheel angle	°	10
vehicle_speed	Velocity of the vehicle	$\mathrm{km\,h}^{-1}$	10

To supplement the CAN-data, an Oxford Technical Solutions Inertial Measurement Unit (IMU) was employed to record additional signals, including GPS data, vehicle acceleration, and inclination. This data was resampled to a common time base to enable seamless integration with the CAN-data. However, due to a time delay between the two data sources, the offset was corrected by aligning the vehicle speed from the CAN data with the GPS speed from the IMU. This preprocessing step ensures synchronization and accuracy in the combined dataset. It is performed automatically to adhere to the KDD process's emphasis on reducing manual intervention and promoting an end-to-end approach.

Table 3.3: Summary of driving data used for each experiment.

Description	Duration	Distance	Average Velocity
RLC Coastdown			
Very Low Suspension	6.65 h	364.47 km	54.81 km h^{-1}
Low Suspension	2.75 h	212.65 km	77.25 km h^{-1}
Medium Suspension	3.34 h	117.65 km	35.25 km h^{-1}
Normal, Pitch Correction	8.18 h	528.36 km	64.61 km h^{-1}
Total	20.94 h	1223.13 km	58.41 km h^{-1}
RLC Constant Speed			
Total	7.20 h	485.72 km	67.47 km h^{-1}
Efficiency Map			
Gear One	3.95 h	134.25 km	33.97 km h^{-1}
Gear Two	8.28 h	952.02 km	115.04 km h^{-1}
Total	12.52 h	1086.38 km	86.76 km h^{-1}
Gear Strategy			
Normal Mode	0.74 h	35.36 km	47.75 km h^{-1}
Sport Mode	1.30 h	58.69 km	45.02 km h^{-1}
Total	2.04 h	94.05 km	46.10 km h^{-1}

For the RLC estimation, the vehicle was repeatedly accelerated and then placed into neutral to allow it to coast, enabling the collection of free-rolling deceleration data. These tests were conducted on both the Autobahn and country roads to cover a wide range of operating conditions. Measurements were performed at all suspension levels to analyze the influence of suspension settings on resistive forces. A total of $6.65\,\mathrm{h}$ of data was recorded over a distance of $364.47\,\mathrm{km}$ for the very low suspension level, $2.75\,\mathrm{h}$ over a distance of $212.65\,\mathrm{km}$ for the low suspension level, and $3.34\,\mathrm{h}$ over a distance of $117.65\,\mathrm{km}$ for the medium suspension level. Some tests were performed in normal drive mode, where the suspension level automatically adjusts based on speed with the IMU sensor active to evaluate the pitch correction methodology. For these tests, $8.18\,\mathrm{h}$ of data over a distance of $528.36\,\mathrm{km}$ was recorded.

Data was also collected to assess road load coefficients via the constant speed method during everyday driving on city roads and highways. Cruise control was engaged wherever possible to maintain steady speeds. This resulted in $7.20\,\mathrm{h}$ and $485.72\,\mathrm{km}$ of recorded driving data.

For efficiency map estimation, the vehicle was driven under real-world conditions, covering a variety of operating points encountered in everyday driving. A total of $12.52\,\mathrm{h}$ of driving data was recorded over $1086.38\,\mathrm{km}$. During the data collection phase, gaps in operating point coverage were periodically reviewed, and subsequent test drives were planned to address any uncovered areas. This iterative approach ensured comprehensive coverage of both gears' operating range. Additionally, data from all other test rides was utilized in creating the efficiency map, as all recorded data qualifies to estimate it.

Data was also collected to estimate the gear change strategy while driving on public roads. To maximize the number of gear changes captured, the driver performed multiple passes of steady acceleration with distinct accelerator pedal positions until the vehicle engaged the second gear, followed by steady deceleration until the threshold to switch back to the first gear was reached. As the vehicle's handbook mentions a difference

in gear strategy between different drive modes, this routine was performed in both Normal and Sport drive modes. A total of $94.05\,\mathrm{km}$ of driving data was recorded over $2.04\,\mathrm{h}$ for this analysis.

It has to be noted, that the durations and distances given in Table 3.3 are represent the amount of data that is used for each part of the analysis. This is technically not the same as the total amount of data recorded, which is lower, because some data was used in multiple parts of the analysis.

3.3 Vehicle Parameter Estimation Methodology

A modular software architecture is implemented to effectively evaluate the performance of various solutions and combinations of design parameters, as illustrated in Figure 3.2. The core concept involves breaking down the three primary pipelines, the efficiency map, the road load, and the gear strategy algorithm, into distinct subfunctions. Each function receives input data, processes it, and then forwards the processed data to the following function in a standardized format. This modular design allows for the easy replacement of functions with different implementations. Furthermore, a key feature of the software architecture is its parametric nature, meaning that no process design parameters are hardcoded or fixed. Instead, when the pipeline is executed, the function caller must specify the design parameters. A parent function is designated to handle the pipeline calling and parameter assignment. This parent function also facilitates the specification of different ranges of possible input values for each parameter, generating a list of various parameter combinations. These combinations are then assigned to a thread pool executor, enabling the algorithm to run multiple instances in parallel with different parameter combinations from the search space. Various metrics are collected throughout the process to determine the optimal combinations and assess the sensitivity of the process to specific parameters. These metrics include loss values, which are calculated against results derived from different lab tests, providing insights into how closely the measurements based on driving data match the data obtained from lab tests.

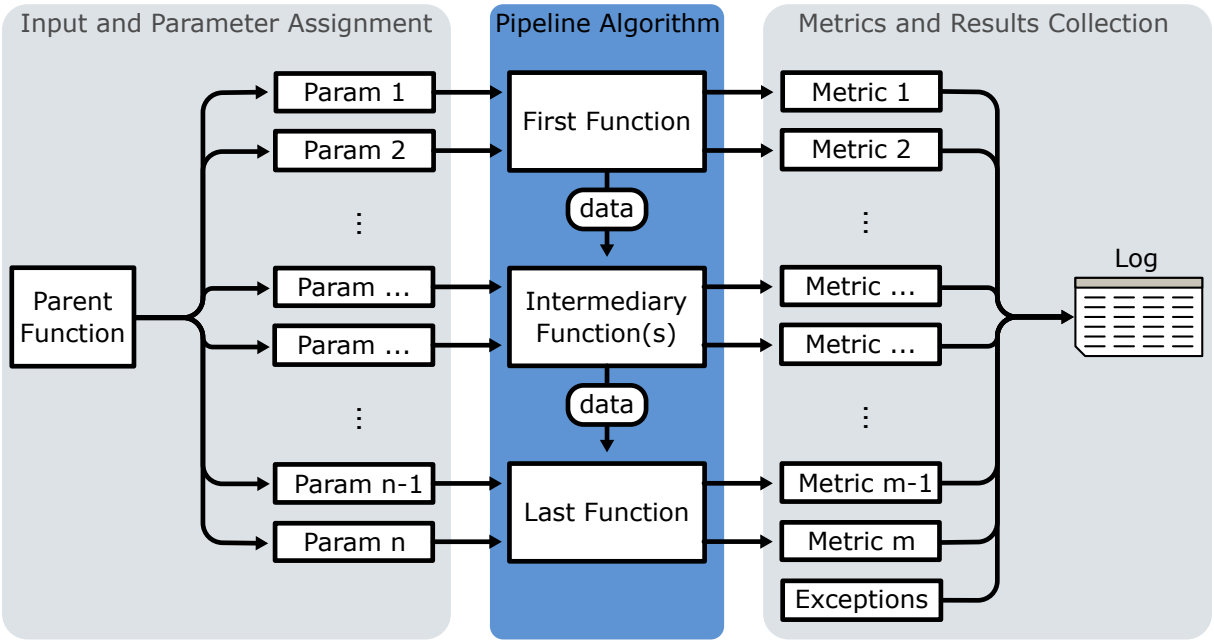

Figure 3.2: Modular Software Architecture.

The log files, which contain the evaluation metrics alongside the used parameter combination, are then analyzed to understand which design parameter influences the results in what way. At the same time, it also provides insights into the interactions of different design parameters. As this exhaustive grid search approach

is in DoE terms equivalent to a full-factorial experiment, standard evaluation methods like ANOVA will be used to assess the significance of design parameters and to quantify the GSA. Boxplots and pair plots are used to gain insight into the high dimensional results space and identify possible parameter interactions. It is emphasized that the parameters won't be optimized for the lowest loss but rather for robustness by understanding how and why the parameters influence the results.

3.3.1 Road Load Coefficient Estimation

This algorithm aims to model the resistive forces of the driving process in dependence on the vehicle's velocity. As outlined in the WLTP procedure to measure a vehicle's aerodynamic and rolling resistance, a combined model is used to describe the resistive forces acting on the car. The model used to describe the resistive forces in dependence of vehicle velocity in the WLTP cycle is a polynomial of degree two specified by the coefficients f_0, f_1, and f_2 [13]. As other research has also adopted this methodology of modeling the resistive forces [3, 18, 31, 36, 40, 41], the same model is used in this investigation. The road load coefficient estimation algorithm thus aims to determine the coefficients of this quadratic model. Previous works have used two approaches to estimate the road load coefficients from on-road driving data: the coast-down approach [36, 40, 41], and the constant speed approach [31]. Both methods are implemented in this investigation to determine the most suitable method for estimating the road load coefficients.

Road Load Coefficient Estimation using Coast Down Approach

The coast-down approach, as described in the WLTP procedure [13], involves accelerating the vehicle to a high speed before enabling the neutral gear setting and letting the vehicle coast. Putting the car into neutral forces the traction force to become zero. The sum of forces introduced in Equation 2.1 hence becomes

$$0 = F_{\text{air}} + F_{\text{roll}} + F_{\text{climb}} + F_{\text{acc}} \tag{3.1}$$

[64, p.203]. The recording of the vehicle speed is then used to determine the decelerating force F_{acc}. By approximating F_{climb} using a pitch correction method, the equation can be solved for the resistive forces. Figure 3.3 provides an overview of the parametric data processing pipeline used to estimate the road load coefficients from the driving data using this methodology. If a function requires parametrization, the parameter Identification Number (ID) is indicated as a number in a circle. This pipeline fits into the general KDD procedure model. It is emphasized that none of the design parameters are fixed to allow for performing a sensitivity analysis to determine how much and how the design parameters influence the road load coefficient estimation results before selecting a robust parameter combination. This may also include the selection of different methods for the same step in the pipeline or whether to include a step at all. Table 3.4 summarizes the road load coefficient estimation design parameters using the coast-down approach.

As a first step, the relevant target data is selected from the pool of raw driving data. This includes filtering for the coast-down segments, indicated by the vehicle being in neutral gear and the vehicle speed being above a certain threshold. As the coast-down measurements could be skewed if the car follows a curved path, the data is filtered to only include sections where the steering is within a specific range around the neutral position. Similarly, sections where the driver engaged the brake pedal are also removed from the data. Lastly, as the test vehicle features an adaptive suspension, which can be set to different levels and affect the resistive forces acting on the car, the data can be filtered to only include sections where the suspension is set to the exact specified setting. This also allows estimating a separate set of RLCs for each suspension level.

The target data is then preprocessed by applying a time-domain smoothing filter to the coast segments to remove noise from the data. This step employs either a moving average, an exponential moving average, or

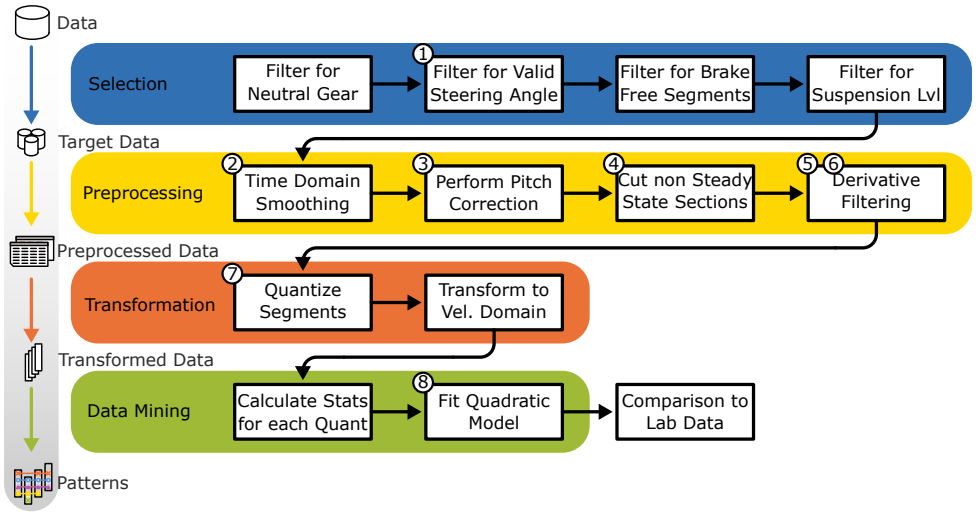

Figure 3.3: Road Load Coefficient Estimation Coast Down Pipeline.

a Savitzkly-Golay filter. As the data recorded is from public roads, it can not be guaranteed that the road inclination is negligibly low. Thus, the road's inclination should also be considered to estimate the resistive forces accurately. The following model is used to correct the velocity data based on the influence of the slope. The IMU sensor measures the road's inclination. As this is continuous time-series data, the inclination is given as a function of time $\alpha(t)$. The index i is used to denote the i-th coast segment. Using the inclination time-series measurements $\alpha_i(t)$ with equation 2.7, the climbing resistance $F_{\text{climb},i}(t)$ is calculated with the vehicle mass and the acceleration due to gravity:

$$F_{\text{climb},i}(t) = m_v g \sin \alpha_i(t). \tag{3.2}$$

The now-known time series of forces $F_{\text{climb},i}(t)$ on the center of gravity can be used to calculate the climbing-induced acceleration $a_{\text{climb},i}(t)$ using Equation 2.11:

$$a_{\text{climb},i}(t) = \frac{F_{\text{climb},i}(t)}{m_v + m_{acc}}. \tag{3.3}$$

Integrating the climbing-induced acceleration $a_{\text{climb},i}(t)$ over time gives the effective change in velocity $\Delta v_{\text{climb},i}(t)$ due to the slope:

$$\Delta v_i(t) = \int a_{\text{climb},i}(t)\, dt. \tag{3.4}$$

By combining the effective change in velocity $\Delta v_{\text{climb},i}(t)$ with the measured velocity $v_i(t)$ a velocity signal with the influence of the slope removed $v_{\text{corr},i}(t)$ is obtained:

$$v_{\text{corr},i}(t) = v_i(t) + \Delta v_i(t). \tag{3.5}$$

As for these coast-down segments, the influence of the slope is removed, and it can be assumed that $F_{\text{climb},i}(t) = 0$ and the sum of forces acting on the vehicle, therefore, reduces to

$$F_{\text{acc}} + F_{\text{air}} + F_{\text{roll}} = 0. \tag{3.6}$$

Figure 3.4 depicts this pitch correction procedure using an example dataset. The recorded pitch angle $\alpha_i(t)$ is shown in Figure 3.4a, the resulting velocity change $\Delta v_{\text{pitch},i}(t)$ is shown in Figure 3.4b. The corresponding

raw coast down velocity profile $v_i(t)$ is shown in Figure 3.4c, with the corrected velocity profile $v_{\text{corr},i}(t)$ shown in Figure 3.4d.

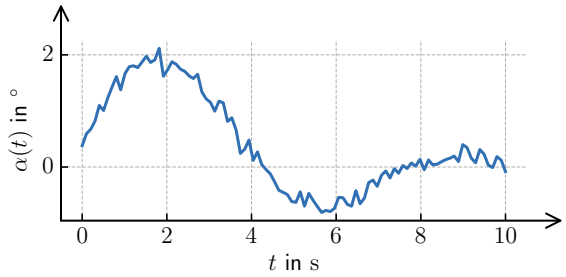

(a) Pitch Angle Measurement $\alpha_i(t)$.

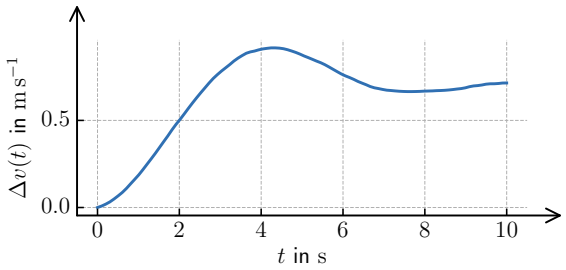

(b) Pitch Induced Velocity Change $\Delta v_{\text{climb},i}(t)$.

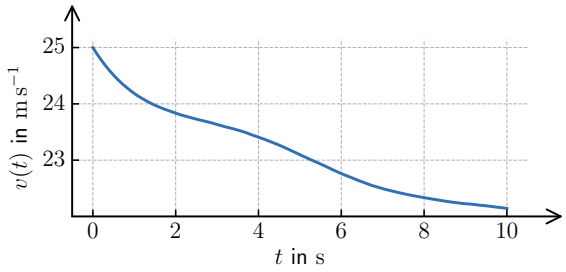

(c) Raw Coastdown Velocity Measurement $v_i(t)$.

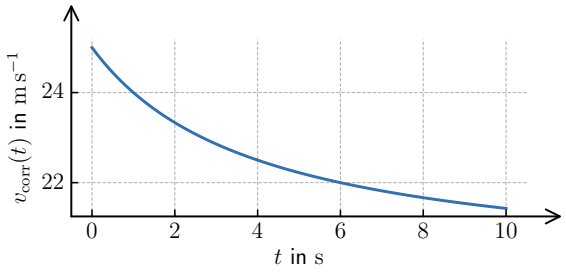

(d) Cleaned Coastdown Velocity Measurement $v_{\text{corr},i}(t)$.

Figure 3.4: Pitch Correction Example.

The subsequent preprocessing step involves cutting a specific amount of samples from the beginning and end of each coast-down segment, as a visual exploration of the data has shown that these sections may include non-steady state segments. For example, if the vehicle was accelerated before being put into neutral, its inertia could still influence its dynamic behavior.

The preprocessing is concluded by a last filtering step, which filters the segments based on their numerical derivative. By doing so, segments that contain non-coasting behavior can be removed from the dataset alongside segments that contain jumps caused by faulty measurements or other disturbances.

As the coast-down segments are measured in the time domain, but the target is to obtain the resistive forces in the velocity domain, a domain transformation has to be performed. The full range of vehicle velocity is divided into equally sized bins. Afterward, each coast segment can be divided into subsegments covering one bin completely. The mean deceleration for each subsegment is calculated and saved to the corresponding bin. Overall coast segments, statistics can be aggregated for each bin, such that the mean and standard deviation of the deceleration are known for each bin in the velocity domain.

This method has transformed the data into data points that provide the mean deceleration over the range of driving velocities. Finally, a quadratic model is fitted to the data to obtain the road load coefficients f_0, f_1, and f_2. The fitting of the quadratic model allows for the commission of outliers by setting a threshold for the number of standard deviations a data point can deviate from the model to be considered an outlier. Comparison to the results from the lab tests is done by calculating the deviation of both fitted curves using the Root Mean Square Error (RMSE) over the velocity range where both tests have been executed.

Table 3.4: Design Parameters for Road Load Coefficient Estimation using Coast Down Approach.

ID	Design Parameter	Description	Unit
1	Max Steering Angle	Outer limit of allowed steering angle range	°
2	Smoothing Keyword Arguments (kwargs)	Method and parameters for time domain smoothing	-
3	Speed Signal	Signal to use for velocity data	-
4	Trim Length	Amount of Data to cut from beginning and end	s
5	Derivative Lower Limit	Lower limit for derivative to consider as coasting	$\mathrm{km\,h^{-1}\,sample^{-1}}$
6	Derivative Upper Limit	Upper limit for derivative to consider as coasting	$\mathrm{km\,h^{-1}\,sample^{-1}}$
7	Bucket Size	Number of bins to divide velocity range into	-
8	Outlier Threshold	Number of standard deviations to consider as outliers	Std Dev

Road Load Coefficient Estimation using Constant Speed Approach

An alternative way to obtain the road load coefficients from driving data is laid out by Komnos et al. [31], and other than the coast-down methodology, it doesn't involve accelerating the vehicle before coasting in neutral. Instead, the vehicle is driven at a constant speed to measure the torque required to maintain this speed. The resistive forces can then be calculated from the measured torque required to maintain a certain constant vehicle speed. Working with the main equation of driving forces 2.1, the accelerating force F_{acc} is zero as the vehicle is driven at a constant speed

$$F_{\text{trac}} = F_{\text{air}} + F_{\text{roll}} + F_{\text{climb}}. \tag{3.7}$$

The traction force F_{trac} which can be measured from driving data, is then equal to the sum of the resistive forces F_{air}, F_{roll}, and F_{climb}. Using a pitch correction method, the resistive forces can be calculated by eliminating the climbing force F_{climb}. The parametric data processing pipeline used to estimate the road load coefficients from the driving data using this methodology is depicted in Figure 3.5. The road load coefficient estimation design parameters using the constant speed approach are summarized in Table 3.5.

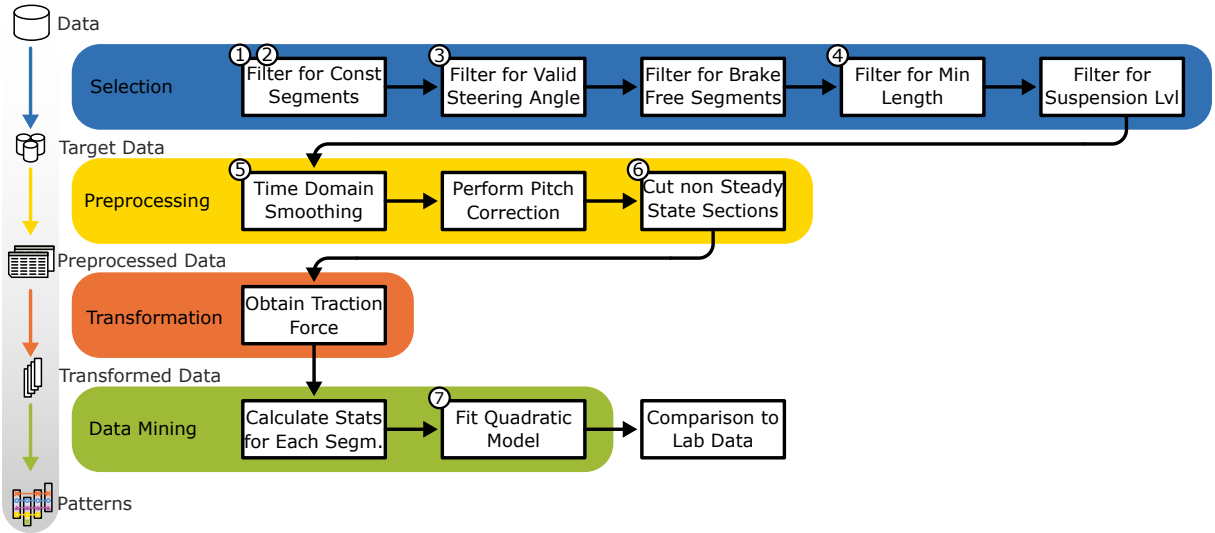

Figure 3.5: Road Load Coefficient Estimation Constant Speed Pipeline.

To obtain the relevant target data from the raw measurements, segments of constant speed are initially selected by filtering for consecutive sections within a given velocity range. Similarly to the coast-down approach, the selected segments are also filtered to be below a specific steering angle range while having no brake pedal activations. One addition is the functionality of choosing segments longer than a given minimum

of samples to ensure a minimum amount of data points in each segment for further processing. Lastly, the target data for a given suspension level is selected to enable individual evaluation of the road load coefficients over all suspension levels.

The preprocessing involves time series smoothing before using the recorded pitch data $\alpha_i(t)$ from the IMU to account for the climbing force in the main equation 3.7. Using Equation 2.7, recalling equation 2.7, the climbing force $F_{\text{climb},i}(t)$ is calculated for each segment i using the vehicle mass and the acceleration due to gravity:

$$F_{\text{climb},i}(t) = m_v g \sin \alpha_i(t). \tag{3.8}$$

Additionally, to obtain the traction force from the driving data, the motor torque $M_{\text{motor},i}(t)$ is multiplied by the gear ratio $j(t)$ to find the wheel torque, which in conjunction with the wheel radius r_{wheel} to see the traction force $F_{\text{trac},i}(t)$

$$F_{\text{trac},i}(t) = \frac{M_{\text{motor},i}(t) j(t)}{r_{\text{wheel}}}. \tag{3.9}$$

By subtracting the climbing force $F_{\text{climb},i}(t)$ from the traction force $F_{\text{trac},i}(t)$, the sum of resistive forces can be approximated. In the last preprocessing step, the data is trimmed by cutting a specific amount of samples from the beginning and end of each segment to remove possible non-steady state segments. Finally, for each segment i, the time-series measurements are averaged, while statistics like the standard deviation are calculated. By doing this, each constant speed segment becomes one data point consisting of a mean resistance force and a corresponding velocity. A quadratic model is fitted on this data while allowing for outliers to obtain the road load coefficients f_0, f_1, and f_2. The comparison of the fitted quadratic resistance model to resistance models obtained from lab tests works in the same way as with the coast-down approach. Differences in the resistance models obtained from driving data and lab data are quantified using the RMSE over valid velocity ranges.

Table 3.5: Design Parameters for Road Load Coefficient Estimation using Constant Speed Approach.

ID	Design Parameter	Description	Unit
1	Speed Threshold	Maximum allowed variance in velocity for constant speed segments	$\mathrm{km\,h^{-1}}$
2	Minimum Average Speed	Minimum average velocity for a segment to be considered	$\mathrm{km\,h^{-1}}$
3	Steering Angle Limit	Outer Limit of allowed steering angle range	°
4	Min Segment Length	Minimum amount of samples for a segment to be considered	-
5	Smoothing kwargs	Method and parameters for time domain smoothing	-
6	Trim Length	Amount of Data to cut from beginning and end	s
7	Outlier Threshold	Number of standard deviations to consider as outliers	-

3.3.2 Efficiency Map Estimation

To determine the efficiency map of the vehicle, the drivetrain efficiency $\eta_{\text{drivetrain}}$ has to be obtained over the full range of engine operating points across all combinations of rotational speed and torque. The efficiency is estimated for the whole drivetrain, including the high-voltage battery, the power electronics, the electric motor, and the transmission. The efficiency map is estimated for both gears as the transmission has two different transmission ratios and, hence, two different efficiencies. The data processing pipeline to build this efficiency map is depicted in Figure 3.6. It follows the general procedure model of the KDD process and thus also

encompasses preprocessing steps to improve the data quality. The design parameters and effectiveness of these preprocessing steps are evaluated in the sensitivity analysis. Table 3.6 summarizes the design parameters for the efficiency map estimation.

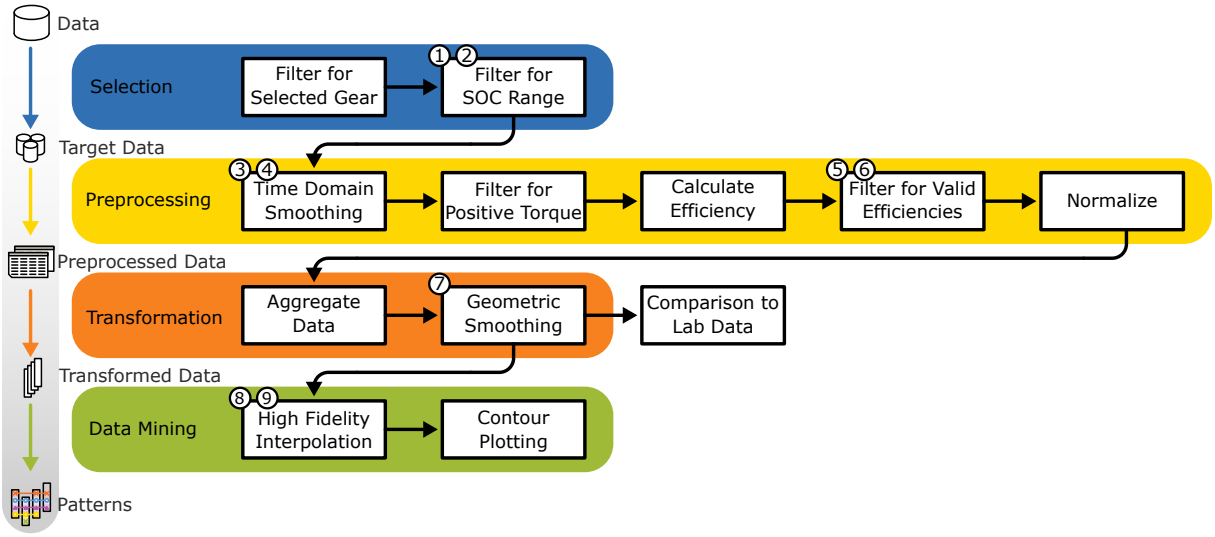

Figure 3.6: Efficiency Map Estimation Pipeline.

After loading the data, the first step is to select the relevant target data. This includes filtering for the correct selected gear and positive torque values, as this investigation only focuses on the drivetrain's efficiency in accelerating the vehicle. Furthermore, the data is filtered to only include sections where the car is within a specific SOC region, as Kropiwicki and Gawlas [39] deduced from their experiment that the efficiency of the drivetrain is dependent on the SOC of the battery. This concludes the data selection step.

The target data is then preprocessed to improve its quality. Initially, time-domain smoothing is performed. This is done to remove potential noise from the signals, possibly introduced by the signal acquisition process. Possible filters include the Savitzky-Golay filter, the moving average filter, and the exponential moving average filter. Each filter has its own set of parameters evaluated in the sensitivity analysis. Another design parameter in this step is the signals on which to apply this filter. The next step is to analytically determine the momentary drivetrain efficiency from the electrical, mechanical, and auxiliary power after Equation 2.13.

The now-known efficiency is again filtered between a specific range to remove outliers and non-valid data points. The following preprocessing step is to normalize the torque and motor rotational speed signals, as their absolute scale varies substantially, which would skew the results of subsequent interpolation steps. The normalization is done by dividing the signals by their respective maximum values.

The preprocessed data is then aggregated from all the time-series measurements and transformed into a 2D domain, where the x-axis represents the rotational speed and the y-axis represents the torque. On this domain, a final geometric smoothing is applied to once more catch outliers and to smooth the efficiency map, as the efficiency of the drivetrain is expected to be a continuous function of the rotational speed and the torque [4, p. 279]. Two-dimensional smoothing filters implemented and evaluated in the sensitivity analysis include inverse distance weighting, gaussian filter, grid-based interpolation, and ML regressors.

If comparisons to the lab test data are desired, the measurements are compared to the lab data at this stage. To do this, for each efficiency value from the dynamometer test, the closest efficiency values in the normalized torque-rotational speed domain are aggregated to form the comparison value. The comparison is made at this stage, as until now, the efficiency values are still the actual measurements from the road, and there are no inter- or extrapolated values. Differences between the lab test data and the real driving data-based efficiency map are quantified by the mean absolute error and the RMSE. These metrics are then

used to evaluate the quality of the efficiency map and are calculated as

$$\text{MAE} = \frac{1}{n}\sum_{i=1}^{n}|\eta_{\text{lab},i} - \eta_{\text{drive},i}|, \tag{3.10}$$

$$\text{RMSE} = \sqrt{\frac{1}{n}\sum_{i=1}^{n}(\eta_{\text{lab},i} - \eta_{\text{drive},i})^2}, \tag{3.11}$$

where $\eta_{\text{lab},i}$ is the efficiency value from the lab test and $\eta_{\text{drive},i}$ is the efficiency value from the driving data-based efficiency map. The number of comparison points is denoted by n. The efficiency measurements taken during the lab test determine the number of comparison points. As it takes considerable time to take dynamometer measurements for a two-dimensional domain, the number of comparison points is limited by laboratory tests. If the efficiency is tested using on-road driving data, the measurements are more continuous and cover a wider area of the torque-motor speed domain. It is, therefore, likely to resolve a higher fidelity efficiency map from the driving data than from the lab test data.

Hence, a last step is included in the data mining section of the efficiency map estimation pipeline, which interpolates the efficiency map to a high-fidelity grid before presenting the results in a contour plot.

Table 3.6: Design Parameters for Efficiency Map Estimation.

ID	Design Parameter	Description	Unit
1	SOC Limit Low	Lower limit of the SOC range to filter for	%
2	SOC Limit High	Upper limit of the SOC range to filter for	%
3	Smoothing kwargs	Method and parameters for time domain smoothing	-
4	Columns to Smooth	Columns to apply smoothing to	-
5	Efficiency Limit Low	Lower limit of the efficiency range to filter for	%
6	Efficiency Limit High	Upper limit of the efficiency range to filter for	%
7	Geom Smoothing Kwargs	Method and parameters for geometric smoothing	-
8	High Fidelity Grid Range	Range of the high fidelity grid	-
9	High Fidelity Grid Spacing	Spacing of the high fidelity grid	-

3.3.3 Gear Strategy Estimation

The gear strategy estimation algorithm aims to quantify the vehicle's gear selection strategy. The findings of Feng et al. [28], Wang et al. [29], and Ngo [30] indicate that this strategy typically depends on the engine's current operating point and the requested torque. Based on these insights, the objective is to identify a decision boundary—within the velocity-torque, velocity-power, and velocity-accelerator pedal domains—that characterizes when the vehicle shifts gears. Among the reviewed approaches, Ngo's [30] methodology is most suitable for the present task, as it clusters gear change instances before fitting a linear model to find the gear change thresholds. This approach forms the basis of the current gear strategy estimation algorithm, augmented by several additional processing steps and options to evaluate potential improvements. The gear strategy estimation pipeline incorporates several variable design parameters like the other algorithms. These parameters undergo a sensitivity analysis to determine a suitable combination and to examine whether the added steps enhance the results. The overall gear strategy estimation pipeline is depicted in Figure 3.7, and the associated design parameters are summarized in Table 3.7. The design parameter ID is indicated in the table and Figure 3.7, showing the specific step in the pipeline where each parameter is applied.

As indicated by the Porsche Taycan Handbook [61], the vehicle has different gear strategies across the three distinct drive modes: Efficiency, Normal, and Sport. In Efficiency mode, the vehicle always prioritizes gear two, while in Normal and Sport mode, the vehicle shifts gears based on the current operating point of the

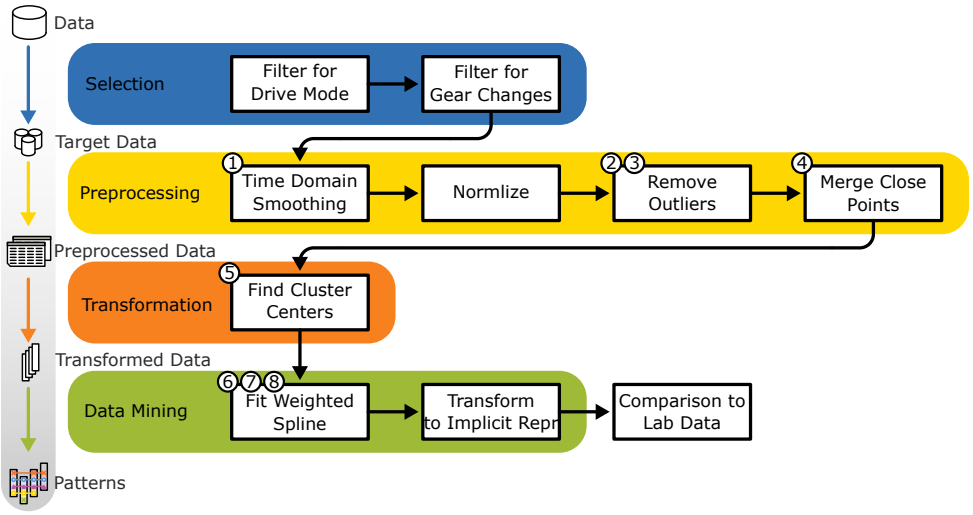

Figure 3.7: Gear Strategy Estimation Pipeline.

engine. Thus, the Efficiency mode doesn't have a particular gear change threshold. The gear strategy has to be estimated separately for the Normal and Sport drive modes, which is why the first step of the data selection process involves filtering the driving data for the correct drive mode. The next step is to mark the gear change moments in the time-series driving data before extracting them from the time-series to form the target dataset.

The preprocessing starts with an option to perform time-domain smoothing, which can be done using a moving average, an exponential moving average, or a Savitzky-Golay filter. The next step commences with a normalization step, where the velocity, torque, mechanical power, and accelerator pedal signals are normalized to a range between zero and one. This is done to ensure that the signals are on the same scale and to prevent the subsequent clustering algorithms from being biased toward signals with a higher absolute value. Afterward, an outlier removal filter powered by the DBSCAN-method is applied to the target dataset. This algorithm was chosen because of its intrinsic capability to handle outliers as well as its ability to detect clusters of arbitrary shape [53], which is essential because the cluster of non-outliers is expected to be a long and slim line-shaped object that may be non-convex. The last preprocessing step is to merge data points in close proximity to homogenize the density of data points along the decision boundary.

After preprocessing, k-means clustering is applied to the individual gear changes. The medoid of each resulting cluster is then computed, providing a simplified representation that may be more amenable to spline fitting.

To obtain the decision boundary, the Least-Squares Univariate Spline method is applied to both the cluster medioids and the individual data points using a weighted approach, allowing the prioritized closeness to either the data points or the cluster medioids. Other parameters that can be adjusted in this step include the spline degree and the number of knots. The splines are parametrized to quantify the similarity between the fitted line and the ground-truth data using the RMSE and to evaluate the quality of the decision boundary.

Table 3.7: Design Parameters for Gear Strategy Estimation.

ID	Design Parameter	Description	Unit
1	Smoothing kwargs	Method and parameters for time domain smoothing	-
2	Outlier Detection Epsilon	Epsilon Radius for DBSCAN	-
3	Outlier Detection Min Samples	Minimum number of samples for a DBSCAN cluster	-
4	Close Points Merge Threshold	Radius for merging datapoints	-
5	Number of Clusters	Number of clusters for k-means clustering	-
6	Spline Order	Degree of the spline to fit	-
7	Number of Knots	Number of knots for the spline	-
8	Fit Emphasis	Weighting of the samples for the spline fitting	-

3.4 Framework for Simulation of Driving Cycles

To quantify the differences between the vehicle parameters estimated from the driving data and the lab test data, a simulation of the driving cycle is performed, as that incorporates all three results: The RLCs to simulate the force required to overcome the drag forces for a given velocity profile, the gear strategy to determine the operating points of the drivetrain and the efficiency map to simulate the drive train losses for each operating point. The simulation is parametrized with both the vehicle parameters estimated using the new, on-road methodology and using the vehicle parameters obtained from the lab tests. The simulation is then run for given velocity profiles, with the total energy consumption being the output. The total energy consumption is then compared between the two sets of vehicle parameters to determine the differences in the energy consumption between the two sets of vehicle parameters. The general procedure is described in the following section.

The first intermediary goal is to find the traction Force F_{trac} required to follow the velocity profile $v(t)$, which is after Equation 2.1, the sum of the aerodynamic drag F_{air}, the rolling resistance F_{roll}, the climbing resistance F_{climb}, and the inertial force F_{acc}. As the climbing resistance is independent of the vehicle parameters, a driving cycle with no slope is assumed. With the aerodynamic drag and the rolling resistance being summarized to the F_{drag} term, the main equation of forces 2.1 hence becomes:

$$F_{\text{trac}}(t) = F_{\text{drag}}(t) + F_{\text{inertial}}(t). \tag{3.12}$$

The inertial force $F_{\text{acc}}(t)$ is derived from the total mass of the vehicle and the rotational mass equivalent m_{rot}, with the acceleration numerically found $\dot{v}(t)$ after equation 2.11

$$F_{\text{acc}}(t) = (m_v + m_{\text{rot}})\dot{v}(t). \tag{3.13}$$

The combined drag force $F_{\text{drag}}(v)$ is approximated by the quadratic polynomial model described by the RLCs f_0, f_1, and f_2:

$$F_{\text{drag}}(t) = f_0 + f_1 v(t) + f_2 v(t)^2. \tag{3.14}$$

The known traction force $F_{\text{trac}}(t)$ is then used to calculate the torque at the wheel $M_{\text{wheel}}(t)$ by multiplying it with the wheel radius r_{wheel} (Equation 2.2):

$$M_{\text{wheel}}(t) = F_{\text{trac}}(t) r_{\text{wheel}}. \tag{3.15}$$

With the formulated gear strategy, alongside the gear ratios j_1 and j_2, the torque at the engine $M_{\text{motor},j}(t)$ can be calculated for each gear j:

$$M_{\text{motor},j}(t) = \frac{M_{\text{traction}}(t)}{j_g}. \tag{3.16}$$

Similarly, the engine rotational speed $\omega_j(t)$ can be calculated as the product of the gear ratio j_g, wheel radius r_{wheel}, and the velocity $v(t)$:

$$\omega_j(t) = \frac{v(t)}{r_{\text{wheel}}} j_g. \tag{3.17}$$

The next step to obtain the total energy consumption is to calculate the mechanical power $P_{\text{mech},j}(t)$ in dependence of the gear j:

$$P_{\text{mech},j}(t) = M_{\text{motor},j}(t) \omega_j(t). \tag{3.18}$$

The efficiency map allows to obtain drivetrain efficiency η_j in dependence of the already known engine torque $M_{\text{motor},j}(t)$ and the engine rotational speed $\omega_j(t)$. The electrical power $P_{\text{elec},j}(t)$ can then be calculated by reversing Equation 2.13, dividing the momentary mechanical power by the associated drivetrain efficiency:

$$P_{\text{elec},j}(t) = \frac{P_{\text{mech},j}(t)}{\eta_j\big(M_{\text{motor},j}(t),\, \omega_j(t)\big)}. \tag{3.19}$$

The electrical power $P_{\text{elec},j}(t)$ is then integrated over the driving cycle to obtain the total electrical energy consumption E_{elec}:

$$E_{\text{elec}} = \sum_t P_{\text{elec},g}(t)\, \Delta t \quad \longrightarrow \quad \text{kW h} \tag{3.20}$$

The total energy consumption E_{elec} is then compared between the two sets of vehicle parameters to determine the differences in the energy consumption between the two sets of vehicle parameters. The efficiency maps have only been obtained for positive torque values, so the simulation is only run for positive torque values. Therefore, regenerative braking is not considered in this simulation. As the goal is to compare the energy consumption between the two sets of vehicle parameters, the omission of regenerative braking is acceptable.

4 Design Parameter Tuning and Evaluation

This chapter presents the sensitivity analysis of the design parameters for the three algorithms: the road load coefficient estimation algorithm, the efficiency map estimation algorithm, and the gear strategy estimation algorithm. The primary goal of this analysis is to evaluate how variations in the design parameters affect the performance and accuracy of the algorithms. Many of these parameters are associated with filtering processes, leading to a recurring tradeoff between the quantity of data retained and its overall quality. Striking the right balance is essential to ensure the algorithms remain robust and efficient.

To achieve this, the sensitivity analysis employs a structured approach combining the methodology of the GSA with a ANOVA analysis. This sequential approach is used to refine the design parameter search space, starting from an initial heuristic estimate encompassing a domain knowledge-based range of values.

It is important to note that the parameter configuration yielding the lowest loss is not automatically selected, which could lead to overfitting [60]. Instead, the chosen parameters aim to reduce the variance of results, enhancing the robustness and stability of the algorithms. Additional methods, such as pair plots, identify interactions between design parameters and ensure a well-informed selection process.

Moreover, the number of tested values for each parameter must be carefully considered. Adding too many values significantly increases the number of combinations in the grid search, which can become computationally prohibitive. For instance, testing more than a million parameter combinations requires excessive execution time with the available hardware and is thus avoided. A balanced approach is taken to explore the parameter space thoroughly while maintaining computational feasibility.

The selection process begins with determining whether a parameter significantly influences the algorithm's results using the statistical framework of the ANOVA method. For parameters found to have a significant impact, further analysis is conducted to understand the nature of this influence. This enables the identification of design parameters that ensure the algorithms are reliable and efficient across various scenarios.

4.1 Parameter Tuning for Road Load Coefficient Estimation

In this work, two distinct methods for obtaining the RLCs are implemented, each requiring its own set of design parameters to be investigated. Based on the WLTP standard, the first method involves accelerating before setting the vehicle in neutral and allowing it to coast down, measuring the resistance to motion. The second method, initially proposed by Komnos et al. [31], uses cruise control to maintain the vehicle at a constant speed, enabling the measurement of the power required to sustain that speed. Both approaches are analyzed independently to determine robust design parameters specific to each method.

For each design parameter, a range of values is defined based on reasonable, domain knowledge-based estimates for the respective parameter. A comprehensive grid search is conducted across all possible combinations of these parameters, assessing each parameter's individual influence and potential interactions between them. A loss function is calculated against ground truth values to quantify the impact of the design parameters. In both RLC estimation methods, the ground truth values are derived from laboratory

measurements conducted by Rosenberger et al. [18], who determined the RLCs under controlled conditions for all suspension settings over a defined range of velocity of the vehicle under study.

The real-world driving data for this sensitivity analysis was recorded in the vehicle's low suspension setting. Therefore, the loss computed for the sensitivity analysis is calculated relative to Rosenberger's measurements for the same suspension configuration [18]. Precisely, the loss is calculated using the RMSE between the resistance models derived from laboratory RLCs and those obtained from the coast-down method with driving data from public roads. The RMSE is restricted to the velocity range standard for both the lab-based and public road-based measurements.

The grid search results are initially analyzed using the ANOVA method to evaluate the significance of each design parameter's sensitivity to the RMSE. Subsequent visual analyses, including boxplots and pair plots, are employed to further explore the individual effects of each parameter and the interactions between parameters, providing deeper insights into their influence on the results.

4.1.1 Coastdown Method: Parameter Tuning and Evaluation

Table 4.1, provides an overview over the coastdown method's design parameters, alongside their respective ranges for the parameter grid search.

Table 4.1: Design parameters and tested value range for the coastdown method.

ID	Design Parameter	Tested Values	Unit
1	Steering Angle Limit	1, 3, 10	°
2	Smoothing kwargs	MA5, MA20, MA50, MA100; EMA0.03, EMA0.05, EMA0.1, EMA0.2, EMA0.4; SG3_5, SG5_5, SG3_25, SG5_25, SG3_50, SG5_50, SG3_100, SG5_100	-
3	Speed Signal	Raw CAN, Pitch-Corrected CAN, Raw GPS, Pitch-Corrected GPS	-
4	Trim Length	1, 3, 5, 10	s
5	Derivative Lower Limit	-0.5, -0.4, -0.3, -0.2	$\mathrm{km\,h^{-1}\,sample^{-1}}$
6	Derivative Upper Limit	-0.01, 0, 0.01, 0.02, 0.03, 0.04	$\mathrm{km\,h^{-1}\,sample^{-1}}$
7	Bucket Size	2, 4, 6, 10, 15	-
8	Outlier Threshold	None, 0.5, 1	Std Dev

The first design parameter is the *steering angle limit*, which determines which steering angle is acceptable for a coastdown segment. Tested values include one degree, three degrees, and ten degrees. Anything above that is considered a curve and thus unsuitable for coastdown measurements. The next design parameter is the smoothing method alongside its configuration, further called *smoothing kwargs*. The tested smoothing methods include the moving average filter, the exponential moving average filter, and the Savitzky-Golay filter. The parameter ranges for each filter were chosen to provide enough samples to average out potential noise while not being too long to distort the signal. The moving average filter was tested with window sizes of 5, 20, 50, and 100 samples. The exponential moving average filter was tested with smoothing factor α of 0.03, 0.05, 0.1, 0.2, and 0.4. The Savitzky-Golay filter was tested with window sizes of 5, 25, 50, and 100 with polynomial degrees of 3, and 5. Another design parameter is the *speed signal* for the coastdown method. Possible values here include the raw speed signal obtained by the CAN-logger, the pitch corrected speed signal obtained by the CAN-logger, the raw GPS speed signal, and the pitch corrected GPS speed signal. This design parameter thus not only captures the influence of using GPS measurements over CAN measurements and the influence of pitch correction. Additionally, every segment can be trimmed at the beginning and end of the segment to remove any disturbances that may have been introduced through non-steady-state behavior. The tested values for the trim length in seconds include 1, 3, 5, and 10. The next design parameter is the *bucket size*, which determines the size of the buckets in which the coastdown segments are divided. The

tested values for the bucket size include 2, 4, 6, 10, and 15 $\mathrm{km\,h^{-1}}$. A further design parameter is the lower and upper limit for the time derivative of the coastdown segment. This parameter is used to filter out segments that include a jump in the speed signal, which may arise due to measurement errors or other sudden disturbances on the road. The tested values for the lower limit include -0.5, -0.4, -0.3, and -0.2. These values are numerical derivatives of the speed signal, so they are given in $\mathrm{km\,h^{-1}\,sample^{-1}}$. This range was chosen to be around the expected maximum slope in vehicle coast down, as any slopes significantly higher than the theoretical maximum should be considered incorrect measurements and should thus be filtered out. The tested values for the upper limit include -0.01, 0, 0.01, 0.02, 0.03, and 0.04. This range was chosen to be around zero, as any values above zero mean that the vehicle is accelerating, which should not happen during a coastdown and thus may indicate a faulty or disturbed measurement. The last investigated design parameter is the outlier threshold of the curve fitting algorithm. This parameter gives a limit in standard deviations. If a data point is further away from the fitted curve than the outlier threshold, it is considered an outlier and is thus removed from the curve fitting process, which obtains the final model. The tested values for the outlier threshold include None, 0.5, and 1. To understand the influence of the design parameters on the results, the ANOVA method is used to determine the significance of the design parameters. These results are given in Figure 4.1.

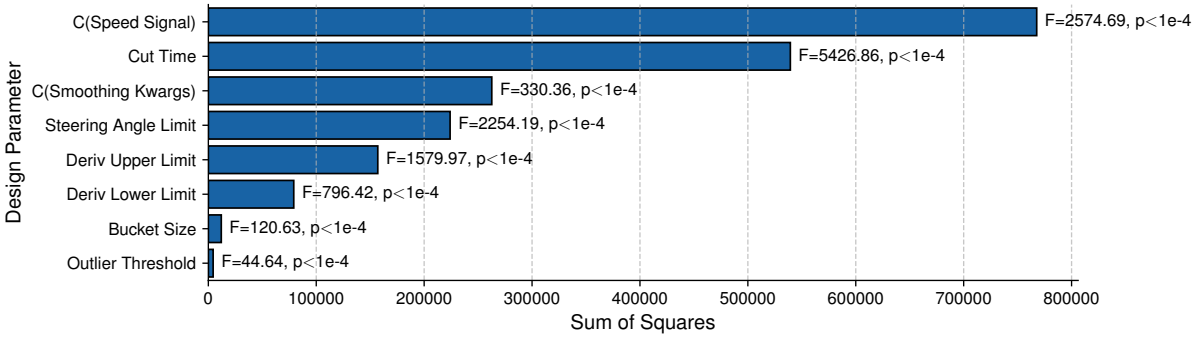

Figure 4.1: ANOVA results for the effect of design parameters on the RMSE in the coastdown method.

The results of the ANOVA reveal which design parameters have the most significant impact on the sensitivity of the coastdown method, as measured by the RMSE. The parameter with the most significant influence is the *cut time*, exhibiting the highest F-statistic of 5426.86 and the largest sum of squares (5.39×10^5), indicating that variations in this parameter contribute substantially to changes in the RMSE. Similarly, the *steering angle limit* and *derivative upper limit* are also highly influential, with F-statistics of 2254.19 and 1579.97, respectively, and p-values below 0.05. These results suggest that these parameters must be tuned with the utmost care, as even minor adjustments could have a pronounced effect on the model's output.

In contrast, parameters such as the *outlier threshold* and *bucket size* show more minor, though still statistically significant, effects with F-values of 44.64 and 120.63 and the sum of squares of 4.44×10^3 and 1.20×10^4, respectively. While these parameters influence the RMSE, their impact is less pronounced and can be considered secondary regarding sensitivity.

The *speed signal* and *smoothing kwargs* are categorical parameters, and their high sum of squares (7.68×10^5 and 2.63×10^5, respectively) reflects their broad impact on the RMSE. For example, the high F-statistic of 2574.69 for *speed signal* underscores its critical role in determining model accuracy. A larger F-statistic generally indicates that the variation in the parameter explains a more substantial proportion of the variability in the RMSE. Similarly, a higher sum of squares shows that the parameter's impact spans a broader range of the observed variance.

These findings indicate that the parameters that require the most careful tuning are which *speed signal* to use and the filtering-related design parameters like the *cut time*, the *steering angle limit*, and the *derivative*

upper limit, albeit showing that all other design parameters like the function fitting related parameters like the *bucket size*, and the *outlier threshold* also significantly influence the results. The next step is to investigate the interactions between the design parameters to understand why they shape the results as they do.

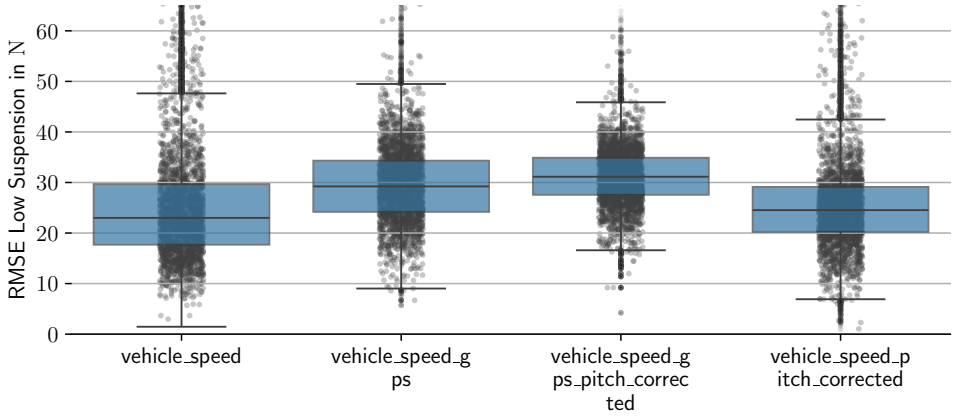

Figure 4.2: Boxplots of aggregated RMSE values for different speed signals in the coastdown method.

Figure 4.2 shows the results of all runs aggregated by which speed signal was used. It can be seen that the pitch correction of both the CAN and GPS speed signal decreases the spread of the results, indicating that the pitch correction reduces the variance of the measurements and thus increases the robustness of the algorithm. Comparing the speed signals obtained by CAN against the GPS-obtained signals show that the results from runs where the GPS based vehicle speed recording was used show both a lower IQR as well as a lower variance, which indicates that these measurements are less prone to noise and more robust in general.

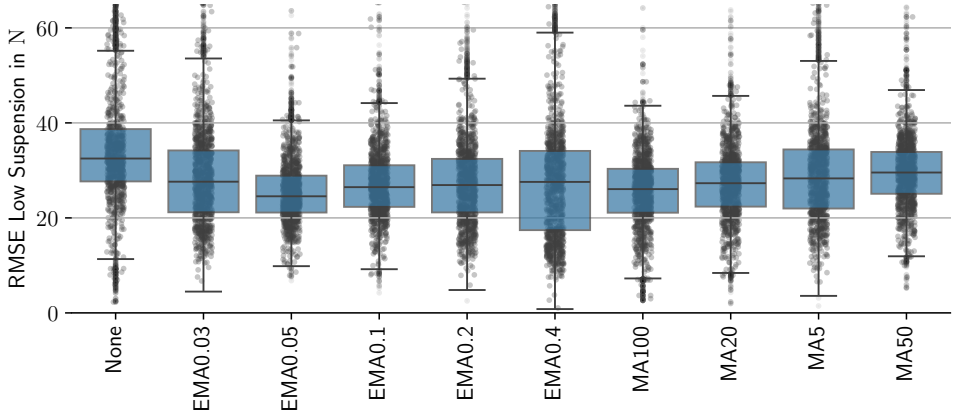

Figure 4.3: Boxplots of aggregated RMSE values for variation in time-domain smoothing configurations in the coastdown method.

The tested time-domain smoothing methods include the moving average and exponential moving average filters. Figure 4.3 shows the results of all runs aggregated by the smoothing method used. Immediately apparent is that all tested smoothing methods reduce the RMSE compared to no smoothing. When assessing the IQR between the different smoothing methods, it becomes apparent that the filter parameter significantly

influences the results' robustness. As the variance and IQR of the RMSE steadily decreases with increasing window size for the tested moving average filters, it can be concluded that larger window sizes are effective in reducing the noise in the speed signal without distorting the signal itself. The exponential moving average filter also shows a similar trend, with both the median RMSE and the IQR decreasing with decreasing smoothing factor, which means more weight is given to samples further in the past. This trend, though, only holds until $\alpha = 0.05$. For $\alpha = 0.03$, the IQR sharply increases again, indicating that the actual signal is distorted too much.

The filtering-related threshold parameters are the *cut time*, the *steering angle limit*, the *derivative upper limit*, and the *derivative lower limit*. Figure 4.4 provides insight into the parameter search space by aggregating the results of all runs into the distinct parameter combinations and showing them in the pair plots. The color indicates the mean RMSE of all runs with a particular combination of design parameters.

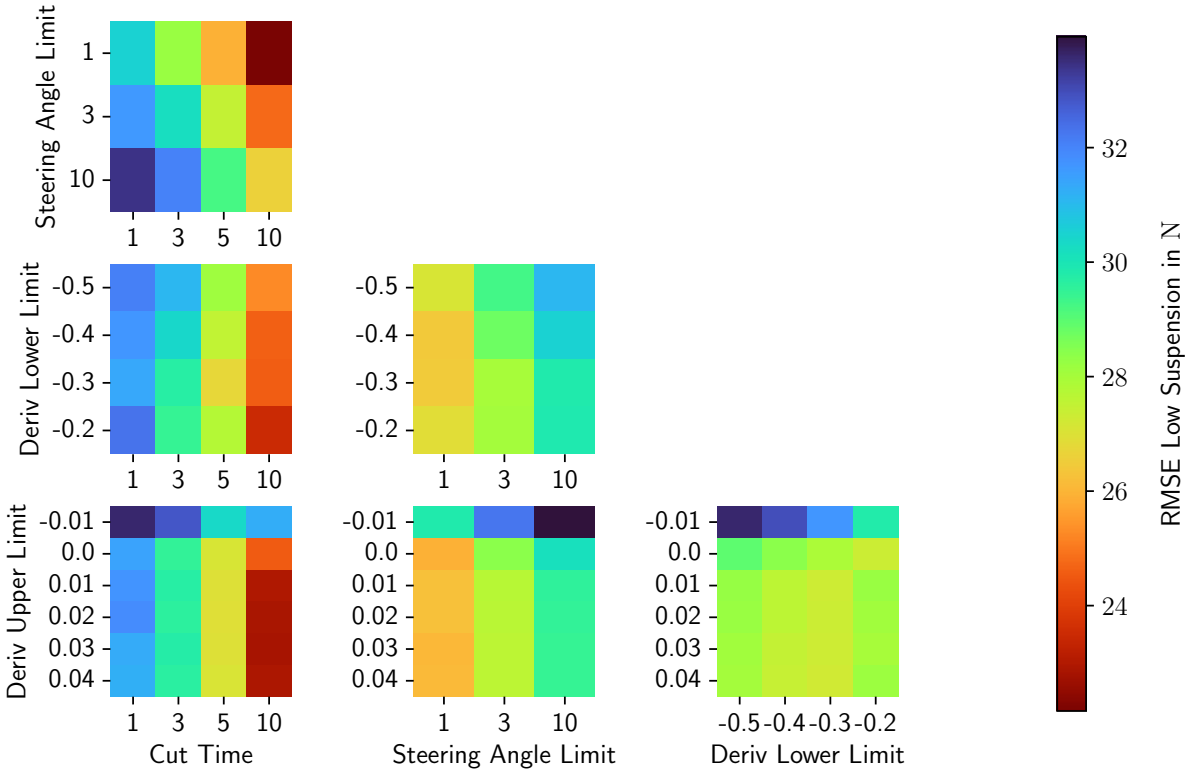

Figure 4.4: Pairplots showing interactions among filter-related design parameters and their effects on RMSE in the coastdown method.

As expected from the ANOVA analysis, the *cut time* has the most significant influence on the RMSE. A clear trend of higher cut times leads to lower RMSE values. Based on this trend, it has been decided to omit the lower cut times. This could indicate that the non-steady-state behavior of the vehicle is filtered out more effectively with higher trim lengths at the beginning and end of the countdown segment. Also, very short stub segments are increasingly removed with higher cut times, leading to more accurate results. These higher trim times may also be necessary with the longer smoothing windows, as the smoothing windows can distort the signal at the beginning and end of the segment. Even though the highest cut time of 10 seconds provides the lowest RMSEs, it is decided to use a cut time of 5 seconds as this provides a lower IQR spread while also preserving more data to fit the model to, which may be of importance for use-cases where the number of valid coastdown segments is limited. The *steering angle limit* also shows a clear trend of more aggressive filtering being more effective across all combinations in terms of mean RMSE and IQR. This confirms the assumption that for a coastdown segment to be valid, the vehicle should not be in a curve. Regarding the *derivative upper limit* again, the grid search confirms the intuitive assumption that the vehicle should not be

accelerating during a coastdown. This can be seen in the data that if all runs that have a positive derivative are filtered out, the RMSE decreases. Interestingly, the RMSE decreases even further when a slight positive derivative of $0.01\,\mathrm{km\,h^{-1}\,sample^{-1}}$ is allowed; this could be due to averaging effects over multiple segments in the same velocity range. Similarly, for the *derivative lower limit*, the results confirm the assumption that the vehicle should not be decelerating above a specific plausible rate. For the top speed of the vehicle of around $230\,\mathrm{km\,h^{-1}}$, a deceleration of $\approx -0.3\,\mathrm{km\,h^{-1}\,sample^{-1}}$ is observed. The grid search results confirm that if the coastdown segments are filtered out by that threshold, the RMSE decreases.

The last set of design parameters are the function fitting related parameters, the *outlier threshold*, and the *bucket size*.

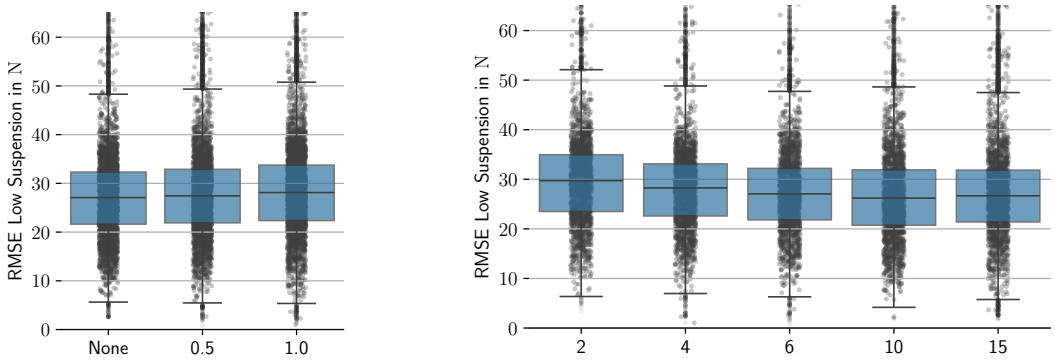

(a) Boxplots of aggregated RMSE values for variations in the outlier threshold in the coastdown method.

(b) Boxplots of aggregated RMSE values for variations in bucket size for curve fitting in the coastdown method.

Figure 4.5: Boxplots of aggregated RMSE values for variations in curve fitting related design parameters in the coastdown method.

The *outlier threshold* is a parameter that determines how far a data point can be from the fitted curve to be considered an outlier and thus be removed from the curve fitting process. The results in Figure 4.5a show that the outlier threshold does not strongly influence the results. As not allowing for any outliers leads to the lowest variance and IQR of the results, it can be concluded that the curve fitting algorithm is robust against outliers. The *bucket size* determines the size of the quantization buckets given in $\mathrm{km\,h^{-1}}$. This parameter achieves the lowest IQR with a bucket size of 6. This optimum in the middle of the range indicates a tradeoff between too-small and too-large bucket sizes. Too small bucket sizes may not benefit from averaging effects over multiple segments in the same velocity range. At the same time, bucket sizes that are too large might provide too few points for the curve-fitting algorithm to fit a model.

Table 4.2: Selected design parameters for the coastdown method after parameter tuning.

ID	Design Parameter	Selected Value	Unit
1	Steering Angle Limit	1	°
2	Speed Signal	Pitch-Corrected GPS Speed	-
3	Smoothing kwargs	EMA0.05	-
4	Derivative Lower Limit	-0.3	$\mathrm{km\,h^{-1}\,sample^{-1}}$
5	Derivative Upper Limit	0	$\mathrm{km\,h^{-1}\,sample^{-1}}$
6	Trim Length	5	s
7	Bucket Size	6	-
8	Outlier Threshold	None	Std Dev

The final set of design parameters that have been chosen is presented in Table 4.2. For the *speed signal*, the pitch corrected GPS recorded speed signal is preferred if available because of its superior robustness. The most effective time-domain *smoothing kwargs* is chosen to be the exponential moving average with a smoothing factor of $\alpha = 0.05$. Selected for its effectiveness in reducing measurement noise while not distorting the signal. The filtering-related parameters are chosen to be on the more aggressive side of the tested spectrum, with a cut time of $5\,s$ and a steering angle limit of $1\,°$. For the derivative limits, the physical limits of the vehicle and the coastdown application are chosen, which means that the *derivative lower limit* is set to $-0.3\,\mathrm{km\,h^{-1}\,sample^{-1}}$ as the vehicle should not decelerate faster than this even at maximum velocity, and the *derivative upper limit* is set to $0\,\mathrm{km\,h^{-1}\,sample^{-1}}$ as the vehicle should not accelerate during a coastdown. By enforcing these limits, it is assumed that coastdown segments containing derivative values outside this range are either disturbed or contain faulty measurements. The function fitting related parameters are chosen strictly based on which values lead to the lowest process variance, which is an *outlier threshold* of None, meaning no points are removed from the curve fitting process and a *bucket size* of $6\,\mathrm{km\,h^{-1}}$.

4.1.2 Constant Speed Method: Parameter Tuning and Evaluation

The other method to obtain the RLCs is the constant speed method demonstrated by Komnos et al. [31]. This method is based on the idea that the force required to overcome all resistive forces at a certain speed can be obtained by setting the vehicle to cruise control while measuring the average torque to maintain this speed [31]. This method has also been implemented using the same framework for comparison. Thus, the design parameters of this approach must also be analyzed for sensitivity and effect. The design parameters, alongside their selected ranges of parameters, are summarized in Table 4.3.

Table 4.3: Design parameters and tested value ranges for the constant speed method.

ID	Design Parameter	Tested Values	Unit
1	Speed Threshold	1, 2, 4, 8	$\mathrm{km\,h^{-1}}$
2	Minimum Average Speed	2, 4, 10	$\mathrm{km\,h^{-1}}$
3	Steering Angle Limit	1, 3, 5, 10	°
4	Min Number of Samples	10, 20, 40	sample
5	Smoothing kwargs	MA5, MA20, MA50, MA100; EMA0.03, EMA0.05, EMA0.1, EMA0.2, EMA0.4	–
6	Trim Length	None, 1, 4, 8	s
7	Outlier Threshold	None, 0.5, 1	Std Dev

As the algorithm automatically detects segments of constant speed from the driving data, a threshold value has to be provided to determine when a segment is considered constant speed. This threshold is called *speed threshold* and provides a range given in $\mathrm{km\,h^{-1}}$. The tested values for the speed threshold include 1, 2, 4, and 8. The range of the *speed threshold* was chosen with a lower bound of $1\,\mathrm{km\,h^{-1}}$, reflecting the assumption that the cruise control system is unlikely to regulate vehicle velocity with finer granularity than this. Additionally, the speed signal itself is likely not recorded with an accuracy exceeding $1\,\mathrm{km\,h^{-1}}$. The upper bound of $8\,\mathrm{km\,h^{-1}}$ represents a relatively wide corridor that is at the limit of what might reasonably be considered "constant speed." Nevertheless, this upper value is included to assess whether the method remains viable under such conditions and to explore the potential benefits of averaging effects that might arise from the longer segments identified with a larger threshold. Another related design parameter is the *minimum number of samples* for an identified segment of constant speed to be considered. As the recorded data is from on-road driving, many disturbances are present. Thus, the minimum number of samples should be assumed to be high enough to obtain a reliable average torque value. The tested values for the minimum number of samples include 10, 20, and $40\,\mathrm{sample}$. With a samplerate of $10\,\mathrm{Hz}$, this corresponds to 1, 2, and $4\,s$, respectively. Another design parameter related to disturbance rejection is a segment's *minimum average speed* to be considered valid. With very low speeds, the air and rolling resistance are very low; thus,

the disturbances and non-steady state behavior have a comparatively large influence on the results. The tested values for the minimum average speed include 2, 4, and $10\,\mathrm{km\,h^{-1}}$. The remaining design parameters overlap with the coastdown method. These include the *steering angle limit*, the *time-domain smoothing method and parameters*, the *outlier threshold*, and the *trim length*. For the *steering angle limit* the tested values include $1\,°$, $3\,°$, $5\,°$, and $10\,°$. The *time-domain smoothing method and parameters*, summarized as *smoothing kwargs*, include the moving average filter with window sizes of 5, 20, 50, and $100\,\mathrm{sample}$, and the exponential moving average filter with smoothing factors of α of 0.03, 0.05, 0.1, 0.2, and 0.4. The *outlier threshold* in the curve fitting algorithm is set to None, 0.5, and 1 standard deviations. The *trim length* was set to None, 1, 4, and $8\,\mathrm{s}$.

After the grid search has been conducted, the results are analyzed using the ANOVA method to determine the significance of the design parameters. The results of the ANOVA analysis are shown in Figure 4.6.

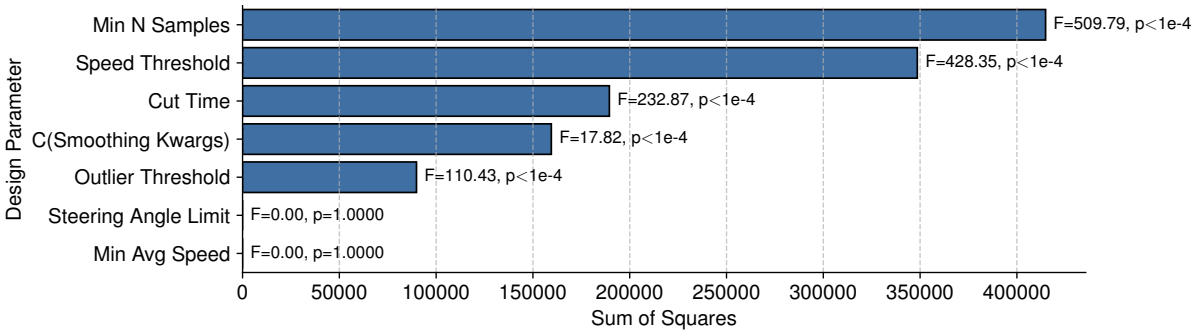

Figure 4.6: ANOVA results for the effect of design parameters on RMSE in the constant speed method.

The results of the ANOVA analysis show that neither the *steering angle limit* nor the *minimum average speed* has a significant influence on the results. This could be due to other filter criteria making these redundant. The *minimum number of samples* exhibits the strongest effect, as indicated by its large F-value and extremely low p-value, followed closely by *speed threshold* and *cut time*, which are likewise highly significant. Additionally, both the *outlier threshold* and the *smoothing kwargs* show clear statistical significance. Consequently, these parameters should be carefully tuned to optimize performance, while ignoring or removing *steering angle limit* and *minimum average speed* could simplify the filtering process without compromising the overall results.

Starting with the most significant design parameter, the *minimum number of samples* for a segment to be considered valid, the figure 4.7a shows the results aggregated over the tested options. This design parameter, which enforces a minimum number of samples for a segment, could be important because the average torque value is calculated for all samples in a segment. If a segment contains sufficiently many samples, the average torque value is more likely to represent the actual torque required to maintain the speed averaging out the disturbances. The results show that the IQR and variance decrease with longer segments, indicating that the average torque value is more reliable with more samples.

The *speed threshold* parameter variation results presented in Figure 4.7b clearly show that allowing only for segments that follow a more narrow width of less than one $\mathrm{km\,h^{-1}}$ around the target speed leads to the most robust results. This indicates that the constrained to a more narrow band enforces the algorithm to only consider segments very close to a target speed, which may effectively filter out disturbances and non-steady state behavior.

The grid search results for the *trim length* parameter are shown in Figure 4.8a. Again, there is a highly significant influence of the *trim length* on the results, with a visible trend of decreasing RMSE, IQR, and variance with increasing trim length up to the value of $4\,\mathrm{s}$, with larger values demonstrating an increase in variance again. This indicates that the segments are more reliable with a trim length of $4\,s$ seconds, as the

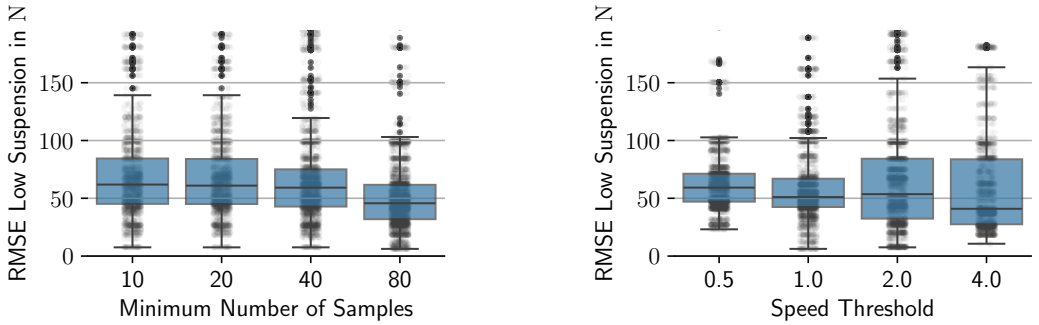

(a) Boxplots of aggregated RMSE values for variations in the minimum number of samples in the constant speed method.

(b) Boxplots of aggregated RMSE values for different speed thresholds in the constant speed method.

Figure 4.7: Boxplots of aggregated RMSE values for variations in the minimum number of samples and speed threshold in the constant speed method.

disturbances at the beginning and end of the segment are filtered out effectively while not removing too much data.

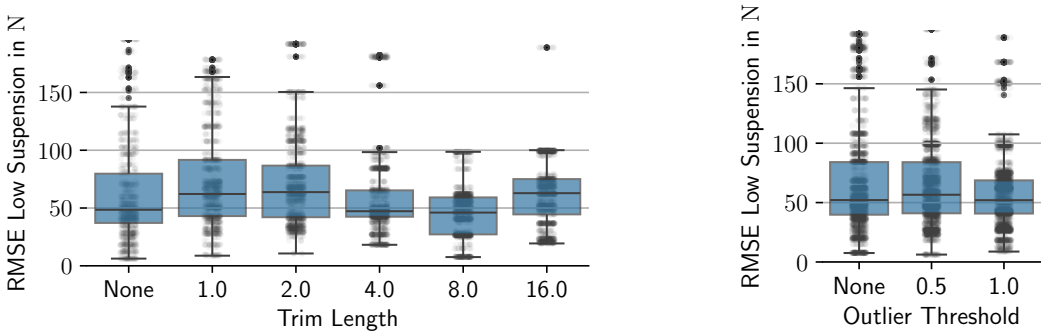

(a) Boxplots of aggregated RMSE values for different trim lengths in the constant speed method.

(b) Boxplots of aggregated RMSE values for various outlier thresholds in the constant speed method.

Figure 4.8b shows that the algorithm benefits from allowing for outliers in the curve fitting process. Omitting points that are more than 0.5 standard deviations away from the fitted curve leads to a lower variance in results than not allowing for any outliers. This indicates that the data may be noisy, and disregarding outliers leads to a more robust fit. This trend even continues for an outlier threshold of 1 standard deviation, which means that if only more extreme outliers are removed from the curve fitting process, the results have become less spread.

While some *smoothing kwargs* didn't influence the results visibly from not applying filtering at all, some others, mainly the moving average and the Savitzky-Golay filters with a large window size, show a clear trend of decreasing IQR and variance. This could indicate that filtering in the time domain effectively reduces noise in the speed signal, which is beneficial for the curve fitting process. The results are shown in Figure 4.9.

Each design parameter in Table 4.4 was selected to balance robustness and practical feasibility based on the ANOVA findings and subsequent boxplot analyses. The *speed threshold* is set to $1\,\mathrm{km\,h^{-1}}$ because

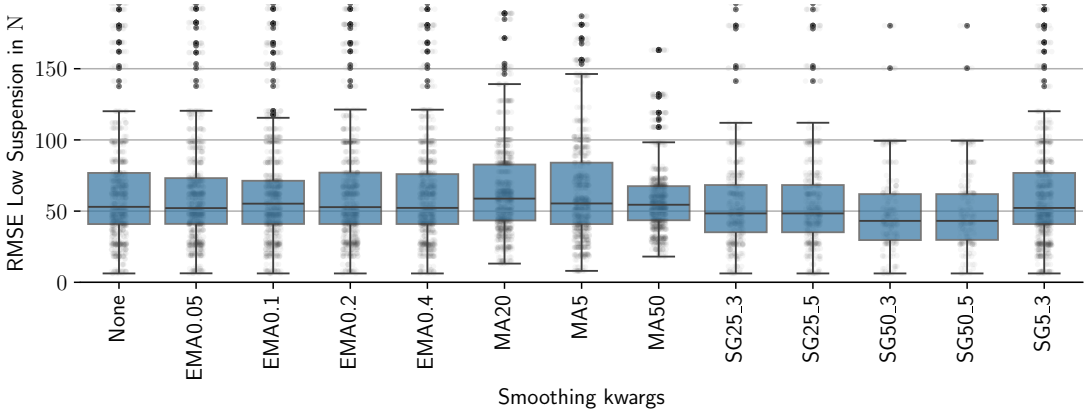

Figure 4.9: Boxplots of aggregated RMSE values for multiple time-domain smoothing configurations in the constant speed method.

Table 4.4: Selected design parameters for the constant speed method after parameter tuning.

ID	Design Parameter	Selected Value	Unit
1	Speed Threshold	1	$\mathrm{km\,h^{-1}}$
2	Minimum Average Speed	2	$\mathrm{km\,h^{-1}}$
3	Steering Angle Limit	10	°
4	Min n of Samples	80	sample
5	Smoothing kwargs	MA80	–
6	Trim Length	4	s
7	Outlier Threshold	1	Std Dev

allowing only a very narrow deviation around the target speed yielded the most consistent and least variable torque estimates, broader thresholds introduced noticeable increases in variance and RMSE. The *minimum number of samples* is raised to 80 (equivalent to eight seconds at a $10\,\mathrm{Hz}$ sampling rate), as larger segment lengths consistently showed reduced variance in the average torque, leading to more stable and reliable results. Both the *minimum average speed* and the *steering angle limit* were found statistically insignificant, so the largest or least restrictive values ($0\,\mathrm{km\,h^{-1}}$ and $10\,°$, respectively) were chosen to retain as many segments as possible without adversely affecting the outcome. A more lenient *outlier threshold* of 1 standard deviation was selected because the results indicated that discarding only the most extreme outliers provided an optimal balance between removing spurious data points and preserving valid measurements. Finally, a *trim length* of $4\,s$ was chosen as it minimized transient effects at the beginning and end of each speed segment while avoiding overly aggressive data reduction. The *smoothing kwargs* with large window sizes have proven effective for this use-case, with a moving average with a window size of 80 providing robust results.

4.2 Parameter Tuning for Efficiency Map Estimation

The efficiency map estimation algorithm's design parameters are summarized in Table 4.5. Each parameter's range of reasonable values is defined based on previous works and domain knowledge. A grid search is performed on all possible combinations of these parameters to investigate how each parameter influences the results and to identify potential interactions between the parameters. The RMSE is used as the loss function to measure the influence of the design parameters. The ground truth efficiency map is obtained from the laboratory-based dynamo measurements from Rosenberger [18]. The RMSE is calculated between the estimated efficiency map and the ground truth efficiency map. The grid search results are then analyzed using the ANOVA method to determine the significance of the design parameters.

Table 4.5: Design parameters and tested value ranges for the efficiency map estimation algorithm.

ID	Design Parameter	Tested Values	Unit
1	SOC Limit Lower	0, 10, 20, 30, 40	%
2	SOC Limit Upper	60, 70, 80, 90, 100	%
3	Smoothing kwargs	None, MA3, MA5, MA7, MA10, EMA0.4, EMA0.6, EMA0.8, SG5_1, SG10_1, SG15_1, SG5_3, SG10_3, SG15_3, SG10_5, SG15_5	-
4	Columns To Smooth	All, Mechanical, Electrical	-
5	Efficiency Limit Lower	0, 0.02, 0.04, 0.06, 0.08, 0.1, 0.15, 0.2, 0.25, 0.3, 0.35, 0.4	-
6	Efficiency Limit Upper	0.95, 0.96, 0.97, 0.98, 0.99, 1	-
7	Two-Dimensional Smoothing kwargs	None, GF1_50, GF1_100, GF2_50, GF2_100, GF3_50, GF3_100, GD_linear, GD_nearest, GD_cubic, IDW_0.8_10, IDW_0.8_20, IDW_1_10, IDW_1_20, IDW_1.5_10, IDW_1.5_20, IDW_2_10, IDW_2_20, IDW_3_20, RF50_5, RF50_10, RF100_5, RF100_10, RF200_5, RF200_10	-

The design parameters investigated for this algorithm include the *efficiency limit lower* and *efficiency limit upper* bounds of the efficiency map. The motivation for assessing these bounds is to ensure that the efficiency map remains within a physically realistic range, as values outside the interval $[0, 1]$ are impossible. It is hypothesized that fine-tuning the bounds beyond the physical extremes may enhance the overall accuracy of the efficiency map. This arises from the observation that, during vehicle operation, practical efficiency values may deviate from theoretical limits and fall within a narrower range. For example, Konzept et al. state that the lower bound for vehicle efficiencies is often approximately $48\,\%$ [65]. Thus, the tested range for the lower efficiency limit is set between 0 and 0.4.

Similarly, the upper bound requires careful consideration, as achieving the theoretical maximum of $100\,\%$ efficiency is practically unattainable due to inherent system losses. The upper limit is explored within the range of 0.95 to 1.

Inspired by the results of Kropiwnicki and Gawlas, which demonstrated that the SOC significantly influences the drivetrain efficiency in regenerative mode [39], the investigation considers the correlation between the vehicle's SOC and the battery's voltage, which may, in turn, affect the overall efficiency. Therefore, the *lower SOC limit* and *upper SOC limit* are examined. The heuristically chosen range for the lower SOC limit is set between $0\,\%$ and $40\,\%$, while the upper limit ranges from $60\,\%$ to $100\,\%$.

The efficiency map algorithm is executed across all combinations of these four design parameters, with each run's results logged and compared against Rosenberger's ground truth efficiency map to calculate the RMSE between the estimated and true efficiency maps. The sensitivity analysis focuses not on minimizing the RMSE but rather on understanding how the design parameters influence the RMSE of the efficiency map estimation algorithm. Statistical analysis using the ANOVA method is applied to quantify this influence. Additionally, pair plots between the design parameters and the RMSE are used to visualize the relationships and identify potential interactions among the parameters.

Figure 4.10 presents the statistical analysis of the influence of the lower and upper SOC bounds, as well as the efficiency limits, on the RMSE of the efficiency map estimation algorithm. A p-value of less than 0.05 is considered significant, and all four tested design parameters meet this criterion. However, an assessment of the F-values reveals that, although all design parameters significantly influence the RMSE, the *efficiency limit lower* exerts the most significant influence by a substantial margin. This finding indicates that particular care must be taken when selecting this parameter.

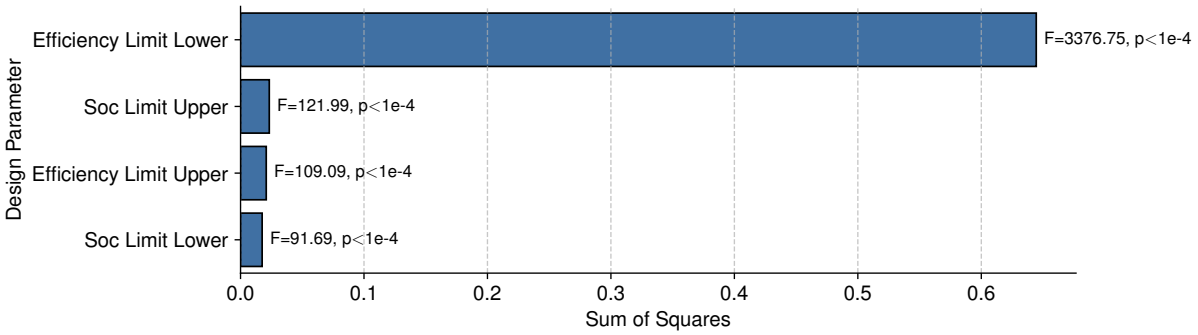

Figure 4.10: ANOVA results showing the effect of lower/upper efficiency and SOC limits on RMSE in the efficiency map estimation algorithm.

While the statistical significance test provides insights into the sensitivity of the results to each parameter, it does not offer information about potential interactions between the parameters. To address this, pairplots are employed to visualize the relationships between the design parameters and the RMSE of the efficiency map estimation algorithm. Figure 4.11 presents the pairplots of the design parameters and the RMSE. The color indicates the mean RMSE of all runs with a particular combination of design parameters. These pair plots reveal how the different design parameters interact and influence the RMSE.

As all four parameters effectively act as thresholds that filter out data outside their respective ranges, the influence of reducing the data amount by narrowing the ranges must be considered. As seen in Figure 4.11a, the *efficiency limit lower* exerts a significant influence on the RMSE, with a clear trend favoring higher values. The *efficiency limit upper* also shows a tendency toward higher values, though its impact is less pronounced. An interesting observation regarding the lower limit is that the RMSE decreases when more data is filtered out. This suggests that, despite the reduction in data, the accuracy improves, likely because the quality of the retained data increases with a higher lower limit. This aligns with the notion that the drivetrain rarely

operates at efficiencies below 48 % [65], implying that efficiency values measured in the very low range may correspond to noisy or erroneous data.

For the *efficiency limit upper*, the RMSE increases as the limit is raised, but this increase does not become significant above 98 %. This indicates that excessively low upper limits may exclude valid data, which is critical for generating an accurate efficiency map.

The pairplot of the SOC limits in Figure 4.11b shows that narrowing either the *upper or lower SOC* limit reduces the accuracy of the efficiency map estimation algorithm. This behavior aligns with the hypothesis that reducing the amount of data leads to decreased accuracy, not because the SOC has a substantial impact but due to the reduction in available data. This finding supports the observations of Rosenberger [18], who concluded that the SOC does not significantly influence vehicle efficiency.

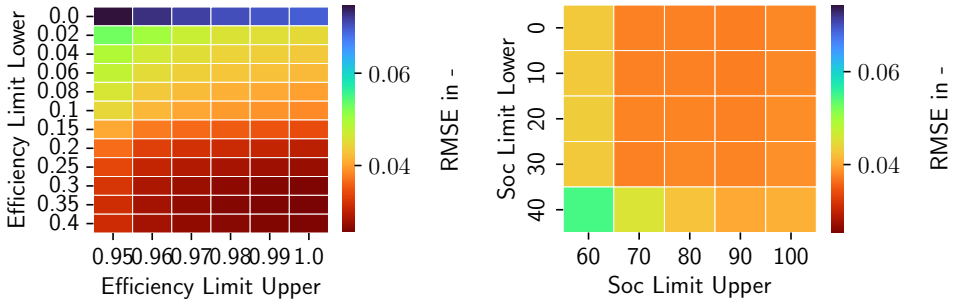

(a) Pairplot illustrating the effect of lower/upper-efficiency limits on RMSE in the efficiency map estimation algorithm.

(b) Pairplot illustrating the effect of lower/upper SOC limits on RMSE in the efficiency map estimation algorithm.

Figure 4.11: Pairplots illustrating the effect of filtering design parameters on RMSE in the efficiency map estimation algorithm.

The next set of design parameters, whose influence on the resulting efficiency map is determined, is the set of smoothing-related design parameters. These include the time-domain smoothing method and parameters, summarized as *smoothing kwargs*. Another design parameter is the signal to which this smoothing is applied. As each signal is stored in a column, the design parameter *columns to smooth* is introduced. Lastly, different methods to smooth the resulting two-dimensional efficiency map are considered and summarized as *two-dimensional smoothing kwargs*.

Tested time-domain smoothing methods include the moving average filter, the exponential moving average filter, as well as the Savitzky-Golay filter. The parameter ranges for each filter were chosen to provide enough samples to average out potential noise while not being too long to distort the signal. The moving average filter was tested with window sizes of five, seven, and ten samples, corresponding to a period of 0.5, 0.7, and $1\,\mathrm{s}$, respectively, with a sampling frequency of $10\,\mathrm{Hz}$. The exponential moving average filter was tested with smoothing factor α of 0.4, 0.6, and 0.8. The Savitzky-Golay filter was tested with window sizes of five, ten, and fifteen samples, with polynomial orders of one, three, and five, respectively.

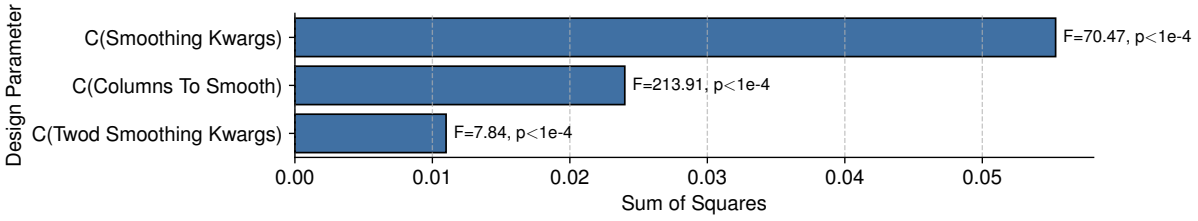

Figure 4.12: ANOVA results for the effect of smoothing-related parameters on RMSE in the efficiency map estimation algorithm.

Figure 4.12 illustrates the results of the ANOVA analysis, highlighting the influence of smoothing-related design parameters on the RMSE of the efficiency map estimation algorithm. Among the tested parameters, the *Smoothing kwargs* exhibited the highest impact, as evidenced by its large F-value. This result underscores the significant role of time-domain smoothing methods and their associated configurations in mitigating noise and shaping the efficiency map. Notably, this parameter is applied at the very beginning of the data processing pipeline, directly influencing the raw input data and propagating its effects through all subsequent processing stages. This early position likely amplifies its overall impact compared to the *Two-Dimensional Smoothing kwargs*, which are applied at the end of the pipeline to refine the already processed efficiency map.

The *columns to smooth* parameter, representing the selection of signals for smoothing, showed the second-highest impact, indicating that careful selection of which signals to smooth substantially influences the overall accuracy of the algorithm. While *Two-Dimensional Smoothing kwargs* had a relatively minor effect, their statistical significance suggests they should still be fine-tuned to ensure an accurate and visually coherent efficiency map. These findings validate the choice of smoothing-related parameters as critical design factors in efficiency map estimation and highlight the importance of considering the position of these parameters within the processing pipeline when interpreting their impact. To closer understand how each parameter influences the results, boxplots that summarize the RMSE values for each parameter are presented in Figures 4.13, 4.14a, and 4.15.

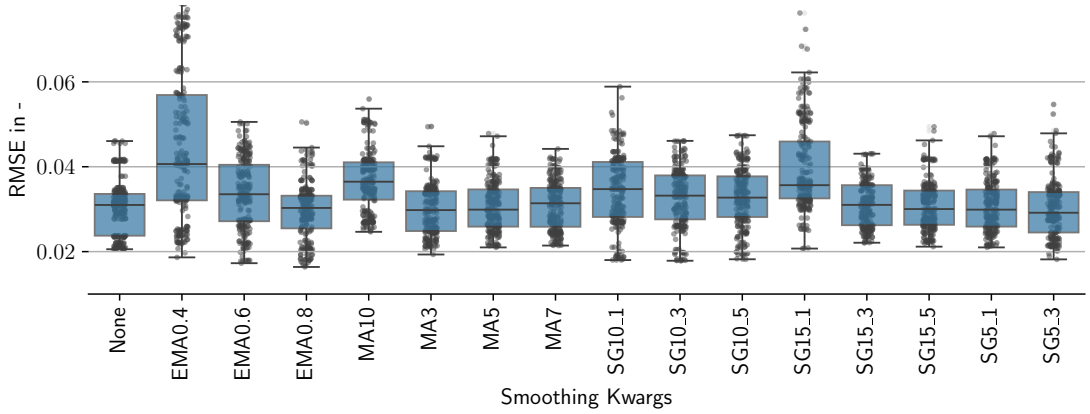

Figure 4.13: Boxplots of aggregated RMSE values for various time-domain smoothing configurations in the efficiency map estimation algorithm.

Investigating the influence of the time-domain smoothing method and parameters on the efficiency map estimation algorithm, the boxplots in Figure 4.13 show that not all configurations are equally effective, with some being substantially worse than not applying filtering at all. This indicates that the results can easily be distorted by using the wrong smoothing method or parameters. The moving average filter, marked with "MA" in the boxplots, shows a clear trend of increasing RMSE with larger window sizes, with the smallest tested window size of three samples being not only the most effective but also the only configuration that on average outperforms no smoothing significantly. The same behavior can also be observed for the exponential moving average filter, indicated with "EMA" in the boxplots. It can be seen that smaller smoothing factors are less effective, with the most minor tested factor of 0.4 being the least effective and the largest factor of 0.8 performing the best both in median and variance. This resembles the same observation of the moving average filter, where the smallest window size was the most effective, as larger smoothing factors effectively decrease the window size as less weight is given to old samples. For the investigated Savitzky-Golay filter

configurations, indicated with "SG" in the boxplots, with the first number representing the window size and the second number the polynomial order, it can again be observed that the window size significantly impacts the results. Other than for the moving average and exponential moving average filters, there is no clear trend of increasing window size leading to worse results except for the polynomial order of one. The polynomial order of one, which represents a piecewise linear fit, generally performs worse than the higher orders, which could be attributed to the fact that the efficiency map is not linear; thus, a linear fit cannot capture the underlying structure of the data. The polynomial order of three and five show similar results, with the order of five having a slightly higher median RMSE. The configuration with a short window size of five samples and a polynomial order of three performs the best in terms of median RMSE. Still, it has a comparably low variance while reaching the lowest RMSE of all Savitzky-Golay filter configurations.

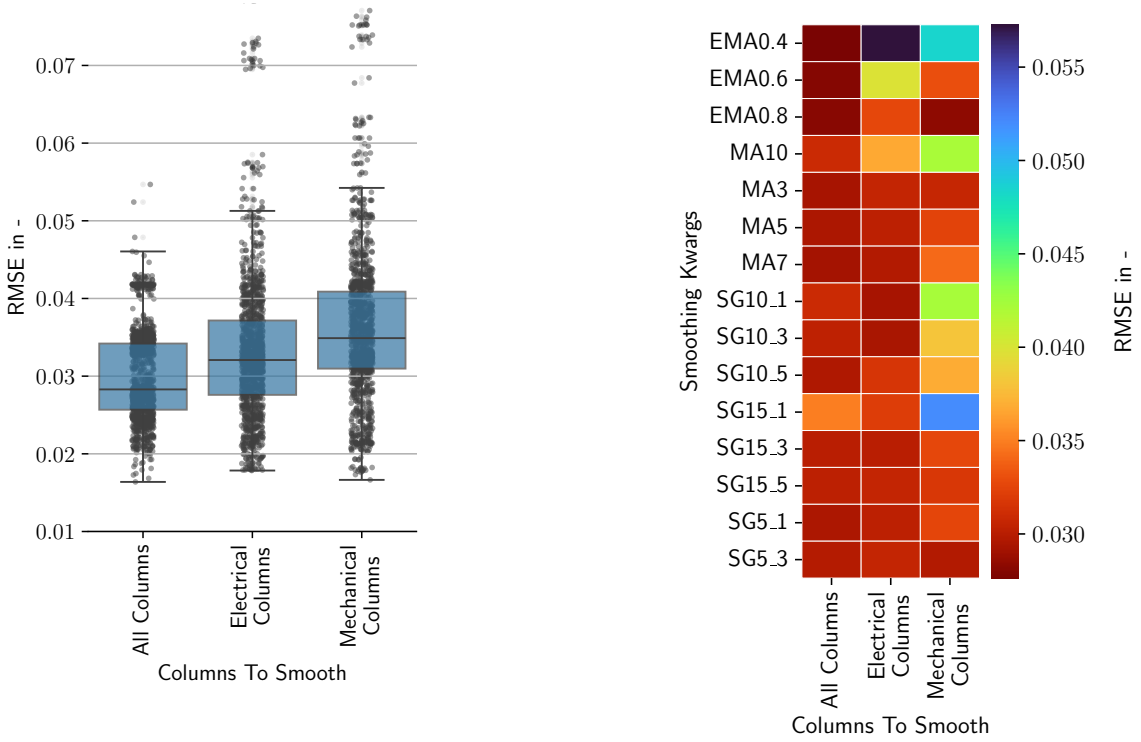

(a) Boxplots of aggregated RMSE values illustrating which columns to smooth in the efficiency map estimation algorithm.

(b) Pairplot illustrating interactions between smoothing configurations and columns to smooth in the efficiency map estimation algorithm.

Figure 4.14: Boxplots and pair plot illustrating the effect of smoothing configurations and columns to smooth on RMSE in the efficiency map estimation algorithm.

A related design parameter to the time-domain smoothing configuration is the selection of which columns to apply the smoothing to. The signals have been clustered into three logical groups: The columns that contain electrical signals, the columns that contain mechanical signals, and the columns that contain all efficiency map-related signals. The significance of this parameter, which is indicated by its high F-value in the ANOVA analysis depicted in Figure 4.12, is further supported by the boxplots in Figure 4.14a. The boxplots show that the configuration of applying smoothing to all columns performs the best, with the lowest median RMSE and the lowest variance alongside the lowest absolute RMSE. The configuration of applying smoothing to the electrical signals performs the second best, with a higher median RMSE and variance, but still outperforms the configuration of applying smoothing to the mechanical signals. This may indicate that the electrical signals are more noise-prone and thus benefit more from smoothing. As this design parameter is highly related to the

time-domain smoothing configuration, possible interactions are captured by the pairplot in Figure 4.14b. This representation shows that the configuration of applying smoothing to all columns is generally more effective than the other configurations, with the configuration of applying smoothing to the electrical signals performing the second best. Particularly apparent from this representation is that the combination of applying smoothing to all signals is particularly effective when using an exponential moving average filter.

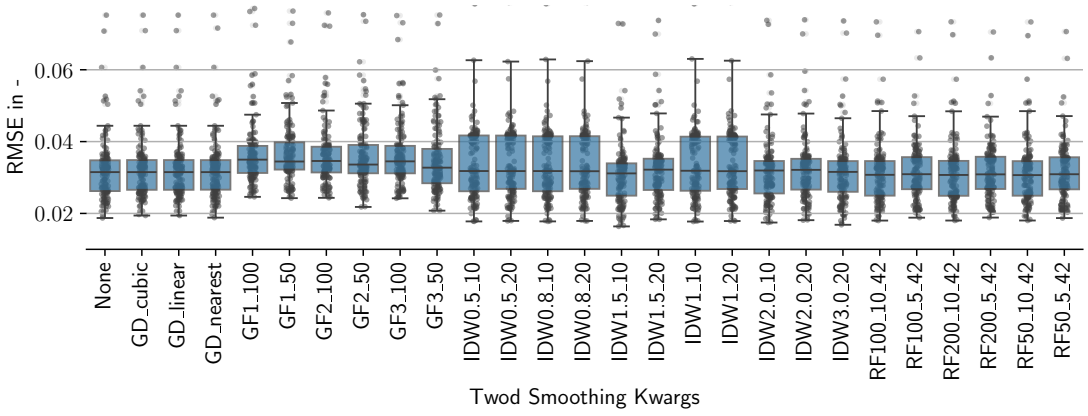

Figure 4.15: Boxplots comparing different two-dimensional smoothing configurations in the efficiency map estimation algorithm.

Figure 4.15 gives an overview of the aggregated results of each tested two-dimensional surface smoothing method. No clear trend can be observed from the boxplots, as the results are very similar across all tested configurations, varying slightly in IQR range as well as median RMSE. This confirms the ANOVA analysis, which showed that the two-dimensional smoothing configuration has a comparably low impact on the results. In conjunction with experimentation, domain knowledge is used to decide on a smoothing configuration. The Gaussian filter, while providing good smoothing in the center of the map, was not applied to data points close to the edge where the filter would have to extrapolate. It is thus not further considered. The grid data interpolation-based smoothing methods are also not considered further as they are prone to outliers, which can strongly influence the interpolation results locally. While providing excellent smoothing, the Random Forrest regression methods tend to introduce vertical and horizontal lines into the map due to the tree-based decision criteria acting as split statements on the axes. The Inverse Distance Weighting method is free of all mentioned shortcomings and provides robust results. Using a power of 0.8 and a number of 20 neighbors, the method provides good smoothing while not distorting the data due to inverse distance weighting being a local method that does not extrapolate. The number of neighbors is set to 20 to provide enough data points to be robust against outliers.

Table 4.6: Selected design parameters for the efficiency map estimation algorithm after parameter tuning.

ID	Design Parameter	Selected Value	Unit
1	SOC Limit Lower	10	%
2	SOC Limit Upper	90	%
3	Smoothing kwargs	EMA0.8	-
4	Columns To Smooth	All	-
1	Efficiency Limit Lower	0.4	-
2	Efficiency Limit Upper	1	-
7	Two-Dimensional Smoothing kwargs	IDW0.8_20	-

The final set of design parameters for the efficiency map estimation algorithm is summarized in Table 4.6. The selected values were chosen based on their ability to balance accuracy and robustness while maintaining the integrity of the efficiency map. For the *efficiency limit lower*, the value was set to 0.4, reflecting a cutoff for filtering out data in an unrealistic efficiency range. At the same time, the upper bound of 1 avoids excluding valid data at high efficiencies. The *SOC limits* were kept at minimal with an almost full range of $10\,\%$ to $90\,\%$, ensuring the least loss of data while confirming the hypothesis that SOC has a negligible direct influence on the algorithm's accuracy [18], and simultaneously removing the most extreme data points.

The time-domain *smoothing kwargs* was selected to use the exponential moving average (EMA0.8), as this configuration provided the best balance between reducing noise and preserving signal fidelity. The *columns to smooth* were set to "All" to maximize noise reduction across all signals, particularly benefiting the electrical signals, which are more susceptible to noise. For the *two-dimensional smoothing kwargs*, the Inverse Distance Weighting method with a power of 0.8 and 20 neighbors (IDW0.8_20) was selected, as it ensures robust, localized, and axes indifferent smoothing without introducing distortions or extrapolations at the map edges.

4.3 Parameter Tuning for Gear Strategy Estimation

To quantify the gear change strategy of the test vehicle, driving data is recorded in both the Normal drive mode and the Sport drive mode. Using unsupervised data mining techniques, a decision boundary is derived that aims to formulate the gear change strategy for each drive mode. Again, ground truth values for the gear change strategy have been measured under lab conditions on a rolling dynamo by Rosenberger [18]. Using a parametric RMSE, the difference between the gear strategy model derived from driving data and the model from lab data. This metric is used to quantify the impact of the design parameters presented in Table 4.7.

Table 4.7: Design parameters and tested value ranges for the gear strategy estimation algorithm.

ID	Design Parameter	Tested Values	Unit
1	Smoothing kwargs	None, EMA0.4, EMA0.6, EMA0.8, MA3, MA5, MA7	-
2	Outlier Detection Epsilon	0.025, 0.05, 0.1, 0.125	-
3	Outlier Detection Min Samples	2, 3, 4	-
4	Close Points Merge Threshold	0.0005, 0.001, 0.005, 0.01, 0.025, 0.05	-
5	Number of Clusters	5, 6, 7, 8	-
6	Spline Order	1, 2, 3	-
7	Number of Knots	3, 5, 7, 9	-
8	Fit Emphasis	0.1, 0.3, 0.5, 0.7, 0.9	-

The gear strategy estimation algorithm's design parameters and their respective ranges are summarized in Table 4.7. The parameters are selected based on domain knowledge, insights from the raw data, and literature. As with all previous algorithms, a grid search is performed to investigate the influence of each parameter on the results. With the results being a decision boundary, the resulting lines are parametrized to allow for a quantitative comparison using the RMSE metric. The RMSE is calculated between the estimated and ground truth gear strategies, obtained from dynamometer-based laboratory measurements from Rosenberger [18]. The grid search results are then analyzed using the ANOVA method to determine the significance of the design parameters. As always, it is investigated whether time-domain smoothing can improve the results. Different *smoothing kwargs* include the moving average filter with window sizes of three, five, and seven samples and the exponential moving average filter with smoothing factors α of 0.4, 0.6, and 0.8, alongside the option of performing no smoothing at all. Savitzky-Golay filter configurations are not tested for the gear strategy estimation algorithm as they require window sizes larger than the polynomial order. They generally do not perform optimally if used with very short window sizes [45]. These ranges were chosen with

a comparatively short window size and smoothing factor to avoid distorting the signal, which is of particular importance for the gear strategy estimation algorithm, as the gear change moments are instantaneous and distorting the signals too much in an effort to reduce noise could in this algorithm quicker than for the others lead to the loss of the underlying structure of the data. The mechanism to remove erroneous gear change data from the dataset is done by DBSCAN clustering. This algorithm has to be configured with two design parameters [53]. This includes an epsilon radius, subsequently called *outlier detection epsilon*, and a minimum number of samples, subsequently called *outlier detection min samples*. The epsilon radius is tested with values of 0.025, 0.05, 0.1, and 0.125. As this outlier detection happens in the normalized torque-speed domain, no unit is associated with it other than the interpretation as a percent of the respective maximum value. The minimum number of samples is tested with values of 2, 3, and 4, as with the amount of gear change moments that can be expected in the dataset, a higher number of samples is not likely to be necessary to form an inlier cluster. The *close points merge threshold* is tested with values of 0.0005, 0.001, 0.005, 0.01, 0.025, and 0.05, also given in percent of the respective maximum value. If two points are closer to each other than this threshold, they are merged into one averaged point. To further simplify the data to a few key characteristic points, Ngo [30] proposed to cluster the data into a few key points using the k-means algorithm. This method requires the *number of clusters* to be specified [52], which is tested with values of 5, 6, 7, and 8, as it can be expected that this amount of clusters can effectively capture the characteristics of a gear change threshold. The spline interpolation is used to fit a curve between the key points, which is parametrized by the *spline order*, for which the linear spline and the quadratic and cubic spline are tested. In addition, another key parameter for the spline interpolation is the *number of knots*, which determines the number of control points and, subsequently, the number of spline segments. The number of knots is tested with values of 3, 5, 7, and 9, as the results of Ngo [30] have shown that a higher number of knots is usually not required to describe gear change decision boundaries. The *fit emphasis* parameter is used to weigh the importance of fitting the spline to the cluster centers versus the data points themselves. A fit emphasis of above 0.5 will put more weight on the cluster centers, while a fit emphasis of below 0.5 will put more weight on the data points themselves. The parameter is tested with values of 0.1, 0.3, 0.5, 0.7, and 0.9 to cover the full range of possible values.

The first iteration of the gear strategy design parameter grid search has shown that the *smoothing kwargs* even with the shortest window size of three samples, significantly distorts the gear change moments, which can also be seen in Figure 4.16, where all tested methods perform worse in terms of variance and median parameteric-RMSE, than applying no smoothing. This is likely because the gear change moments are instantaneous, and a time-domain smoothing method distorts the underlying structure of the data. Due to this large effect on the results, this parameter would strongly influence a subsequent ANOVA investigation, so it is decided not to further investigate the time-domain smoothing configuration.

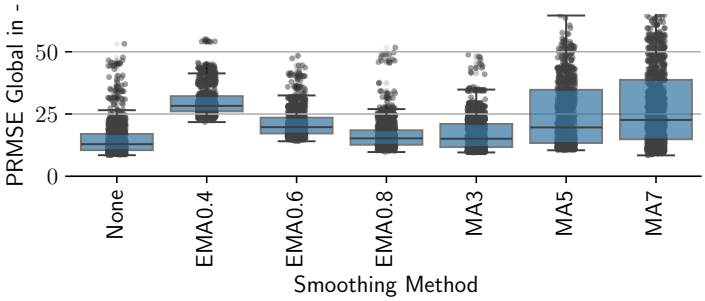

Figure 4.16: Boxplots of aggregated parametric RMSE values for different time-domain smoothing configurations in the gear strategy estimation algorithm.

For the remaining gear strategy estimation algorithm design parameter grid search results, the ANOVA analysis is presented in Figure 4.17. The analysis shows that all design parameters significantly impact the results, with a p-value below the significance threshold. The largest influence on the results is exerted by the *close points merge threshold*, closely followed by *fit emphasis*. The remaining design parameters influence the result significantly less, starting with the spline fitting related parameters *spline order*, and *number of knots*. The outlier detection parameters *outlier detection epsilon* and *outlier detection min samples* don't exercise a strong albeit still significant influence. The least influential parameter is the clustering parameter *number of clusters*. It has to be noted a low F-value does not automatically correspond to low importance of this processing step, as a lower F-value compared to other design parameters could also indicate that the selected range of values for this parameter is already spread narrowly around a robust value.

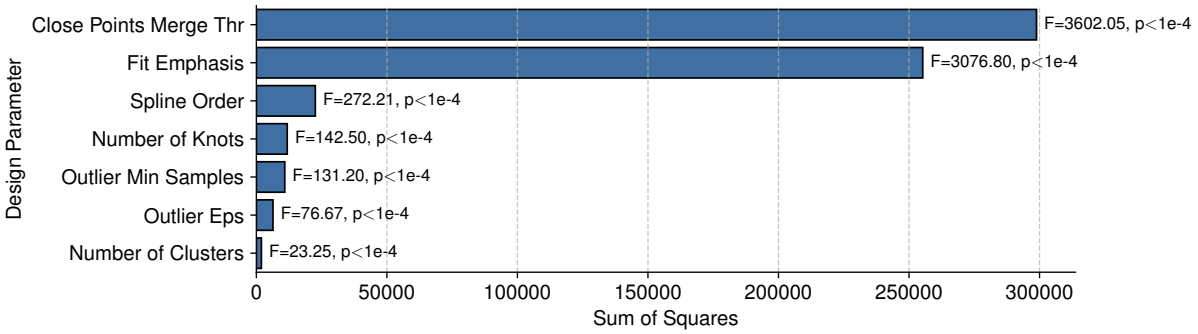

Figure 4.17: ANOVA results showing the effect of design parameters on the parametric RMSE in the gear strategy estimation algorithm.

The option to merge close points is evaluated using the *close points merge threshold* parameter. This feature was introduced to assess the impact of consolidating similar data points into a single averaged point, thereby reducing the complexity of the decision boundary and evening out the density of points along it. As the ANOVA analysis indicates, this parameter has a relatively large influence on the results. Figure 4.18 shows that most tested values yield similar performance, except for the value of 0.05, which exhibits a significantly higher IQR and median parametric RMSE. This suggests that merging points further apart than $2.5\,\%$ of the respective maximum value leads to a loss of relevant information. Consequently, the value of 0.05 is excluded from further consideration and is likely responsible for the high F-value observed for this parameter. At the other extreme, with a threshold of 0.0005, the median and IQR decrease until reaching the outlier value of 0.05. This trend suggests that allowing some merging of close points can be beneficial, provided excessive merging is avoided. The final design parameter of 0.005 was selected, as it not only yields the lowest IQR among the tested values but also maintains a sufficient margin from the excessive merging threshold. This ensures robustness for datasets where the optimal threshold may be slightly lower while retaining the benefits of merging close points.

Varying the fit emphasis parameter produces the results shown in Figure 4.19. Looking at the variances for the distributions of the aggregated results, it can be observed that starting from a high emphasis on the cluster medioids (0.9), the variance decreases with increasing emphasis on the original data, up to a value of 0.3. The value of 0.1 shows an increase in variance again, which may indicate that the decision boundary is described most robustly by a spline that is fitted to the individual gear change data points with a fit emphasis of 0.3, which still allows for some incentive to fit the spline to the cluster medioids, which as experimentation has shown provides a good tradeoff between the general shape of the decision boundary which is described best by the cluster centers and the local structure, especially in corner cases, which is described best by the data points themselves. This design parameter may be particularly sensitive to the quality of the data. Experimentation with noisy data sets has shown that if the individual gear change data points are scattered with much noise around the actual decision boundary, a higher fit emphasis on the cluster medioids may be

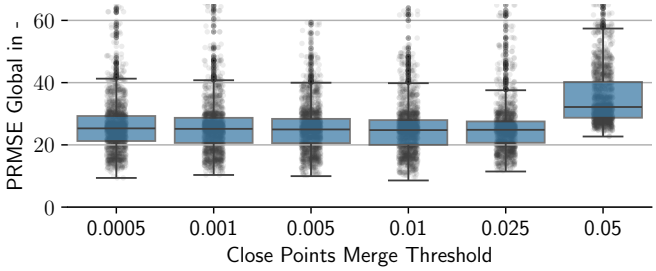

Figure 4.18: Boxplots of aggregated parametric RMSE values for variations in the close-points merge threshold in the gear strategy estimation algorithm.

beneficial to describe the general shape of the decision boundary. A conservative choice would be 0.5, which weighs both the cluster medioids and the data points equally. Though it is assumed that data is available of high quality, the value of 0.3 is chosen for its lowest variance and IQR.

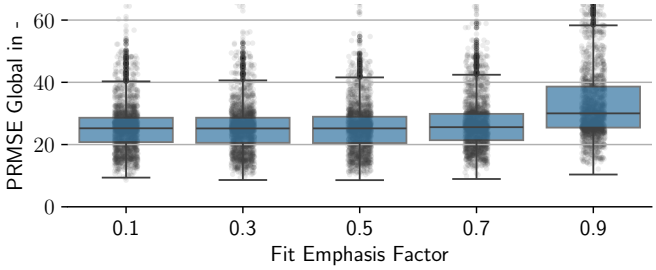

Figure 4.19: Boxplots of aggregated parametric RMSE values for variations in fit emphasis in the gear strategy estimation algorithm.

The next most significant set of design parameters pertains to spline fitting, beginning with the *spline order*. The results of varying the spline order are illustrated in Figure 4.20b. The lowest IQR and variance are observed for a spline order of 2, suggesting that quadratic splines perform most consistently in capturing the decision boundary. Experiments with cubic and higher spline orders indicate that, to prevent overfitting, an increased density of data points and cluster medoids would be required. A higher data density is deliberately avoided, as it would contradict the objective of minimizing the effort needed for vehicle parameter extraction while offering only negligible improvements in the approximation of the gear change decision boundary. Further testing with quadratic splines confirms that they yield robust results and appear more reliable than linear splines, they still frequently overshoot the decision boundary in corner geometries. In contrast, when provided with a sufficient number of knots, linear splines offer a favorable balance between preserving the overall shape of the decision boundary and accurately capturing local structures, particularly in corners. The superior performance of the linear spline is further supported by the findings of Ngo [30], who also performed gear strategy estimation using linear splines.

The impact of varying the *number of knots* is depicted in Figure 4.20a. The lowest variance is observed for a configuration of three knots, while the lowest IQR corresponds to five knots. This suggests the decision boundary is optimally described using a spline with three to five knots. A visual examination of the results indicates that five knots interact well with the selected spline order. This approach aligns with the methodology

of Ngo [30], who also refrained from employing a higher number of knots to model gear change decision boundaries.

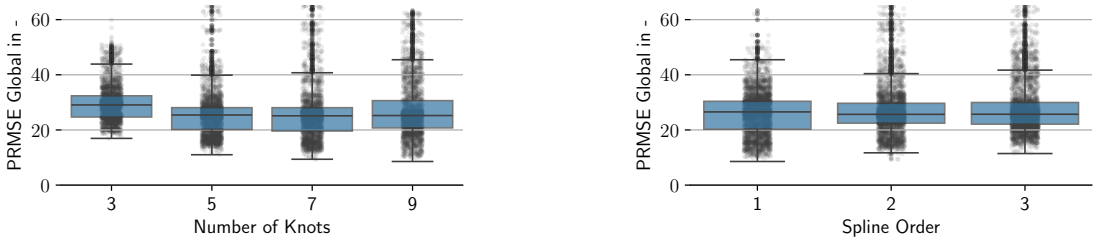

(a) Boxplots of all aggregated RMSE values for variation in the number of knots for the gear strategy estimation algorithm.

(b) Boxplots of aggregated parametric RMSE values for different spline orders in the gear strategy estimation algorithm.

Figure 4.20: Boxplots of aggregated parametric RMSE values for variations in spline fitting parameters in the gear strategy estimation algorithm.

The results of variation in the *outlier epsilon* design parameter are shown in Figure 4.21a. It is immediately apparent that there is an evident change after the epsilon value of 0.05. This indicates choosing a proximity radius of $10\,\%$ or more falsely labels inliers as noise, as everything above this threshold vastly increases the variance and IQR. Using this insight, the lowest values of 0.1 and above are ruled out. As there is no striking difference between the remaining tested values, the value that provides the lowest IQR is chosen, which is the value of 0.05.

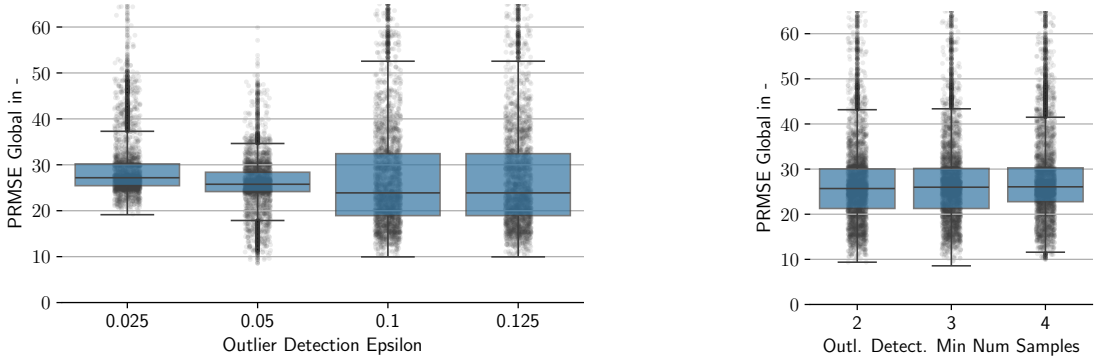

(a) Boxplots of aggregated parametric RMSE values for variations in outlier detection epsilon in the gear strategy estimation algorithm.

(b) Boxplots of aggregated parametric RMSE values for variations in outlier detection minimum samples in the gear strategy estimation algorithm.

Figure 4.21: Boxplots of aggregated parametric RMSE values for variations in outlier detection parameters in the gear strategy estimation algorithm.

The results of the other outlier detection parameter, the *outlier detection min samples*, are shown in Figure 4.21b. It can be observed that the value that provides the lowest IQR and variance is the value of 4. The value selected for both outlier filtering-related parameters highly depends on the amount and quality of the collected gear change data. Experimentation with previous worse datasets has shown that if the data is more noisy, a higher epsilon value is required to filter out the noise. At the same time, a lower number of minimum samples should be selected to form an inlier cluster if the data is more sparse. The chosen design

parameters are as such a good fit for gear change datasets of similar density, which in our case are 63 gear changes in the Normal drive mode and 65 gear changes in the Sport drive mode distributed evenly over the available power band.

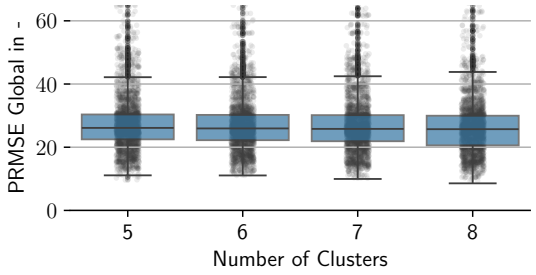

Figure 4.22: Boxplots of aggregated parametric RMSE values for different numbers of clusters in the gear strategy estimation algorithm.

Interestingly, the number of clusters assigned to the data to capture their underlying structure has a similarly low impact. The results of the variation in the number of clusters are shown in Figure 4.22. It can be observed that the value of 5 provides the lowest variance and IQR, which may indicate that the decision boundary is best described by five clusters in between the anchored start and end points of the decision boundary. This is supported by the approach of Ngo [30], who also assigned five clusters to the data to capture the underlying structure of the data. The generally low impact of this parameter may also indicate that the data is well distributed among the decision boundary because the clustering is supposed to simplify the representation of the data, which is possibly only required if the data is not well distributed and or noisy. Similarly, the result from the *fit emphasis* parameter, which said that fitting the spline more strongly to the direct data than to the cluster centers, also supports this notion of the clustering simplification being less relevant when the actual data already describes the decision boundary well. The fine-tuning results for the old noisy dataset can be found in Appendix C. These results showed that the clustering method was more important for robust results.

Table 4.8: Selected design parameters for the gear strategy estimation algorithm after parameter tuning.

ID	Design Parameter	Selected Value	Unit
1	Smoothing kwargs	None	-
2	Outlier Detection Epsilon	0.05	-
3	Outlier Detection Min Samples	4	-
4	Close Points Merge Threshold	0.005	-
5	Number of Clusters	5	-
6	Spline Order	1	-
7	Number of Knots	4	-
8	Fit Emphasis	0.3	-

Table 4.8 provides an overview of the final design parameters chosen based on the grid search results and subsequent ANOVA analysis. Time-domain smoothing is omitted because gear changes are instantaneous events that become overly distorted by moving average or exponential moving average filters. An outlier detection epsilon of 0.05 is selected, as smaller proximity radii risk falsely labeling inliers as noise, while larger values do not provide a significant advantage. The minimum sample requirement for outlier detection is 4, ensuring stable cluster formation without discarding too many valid data points. The choice of these parameters is particularly dependent on the density and quality of the dataset, with higher noise levels requiring a higher epsilon and a lower sample requirement. The close points merge threshold is set to 0.005, as it balances simplifying the decision boundary while retaining essential structural details, especially relevant

when working with well-distributed, high-quality data. The selected number of clusters, 5, aligns with findings from the literature and effectively represents the data structure without unnecessary abstraction. This choice may become more critical if data quality is lower. A linear spline (spline order 1) with four knots is chosen to maintain a balance between preserving the overall decision boundary shape and accurately capturing local features, particularly in corner geometries. Finally, a fit emphasis of 0.3 is selected, as it provides the lowest variance and IQR, ensuring that the spline remains closely aligned with the actual gear change data while still benefiting from cluster-based generalization. Notably, this choice assumes a high-quality dataset, as noisier data would require a higher fit emphasis to stabilize the decision boundary.

5 Results and Discussion

Building on the parameter selection and evaluation process outlined in Chapter 4, this chapter presents the results of the algorithms using the final set of design parameters and compares them against laboratory measurements. The performance of each algorithm is analyzed, highlighting areas where they performed well and identifying aspects that did not meet expectations. Additionally, the findings are contextualized within the broader landscape of existing research, drawing comparisons with similar studies. In the same order as the algorithms were presented in the previous chapters, the results of both road load coefficient estimation algorithms, the efficiency map estimation algorithm, and the gear strategy estimation algorithm are presented. Next, the parameters determined through laboratory- and on-road-based methods are used to parametrize a vehicle model. Both resulting models are then applied to simulate several driving cycles. In addition to the individual differences in parameters, this simulation integrates all intermediary results, making it possible to assess how each deviation affects overall energy consumption predictions in a driving cycle.

5.1 Road Load Coefficient Estimation

In this section, the results of the road load coefficient estimation algorithms are presented. As both algorithms output a set of RLCs that define a drag force model in dependence on the vehicle speed, they are compared against the same set of measurements conducted under laboratory conditions from Rosenberger et al. [18]. As the suspension setting of the vehicle under study influences its drag characteristics, a separate set of RLCs was measured for each suspension level. Different constraints in the vehicle software and test conditions limit the velocity range at which the measurements could be conducted for each suspension level [18]. Table 5.1 shows the velocity range for each suspension level. To compare the force model obtained from on-road driving data with the force model obtained from laboratory measurements, the RMSE between the two force models is calculated. The RMSE is calculated for the velocity range on which the measurements were conducted. As the RLCs are also given by the Certificate of Conformity (CoC) [66] and by the EPA [67], additional comparisons against these drag models are conducted.

Table 5.1: Velocity range for each suspension level.

Suspension Level	Lower Velocity Limit	Upper Velocity Limit
Very Low	$15\,\mathrm{km\,h^{-1}}$	$160\,\mathrm{km\,h^{-1}}$
Low	$15\,\mathrm{km\,h^{-1}}$	$160\,\mathrm{km\,h^{-1}}$
Medium	$15\,\mathrm{km\,h^{-1}}$	$160\,\mathrm{km\,h^{-1}}$
High	$15\,\mathrm{km\,h^{-1}}$	$95\,\mathrm{km\,h^{-1}}$

5.1.1 Coastdown Method

The coastdown method plays a critical role as a popular approach in estimating RLCs by utilizing driving data. This section delves into the results derived from applying this method across varying suspension levels,

enabling the comparison of the force models with laboratory measurements. The discussion will also highlight the influence of test conditions and vehicle-specific parameters on the outcomes. The results are presented in the following order: first, the results for the dataset, which was recorded in drive mode Normal with IMU data, are presented. Subsequently, the results for the datasets recorded under the very low, low, and medium suspension levels are presented. Finally, the algorithm is applied to the dataset from Rosenberger et al. [3], which was recorded with a VW ID.3.

Drive Mode Normal with IMU Data

Initially, the results for a dataset that have been recorded with IMU data are presented. This dataset was recorded in drive mode Normal, which is of importance because, in this drive mode, the vehicle automatically lowers itself from medium to low suspension level at speed above $65\,\mathrm{km\,h^{-1}}$ [61]. The availability of the IMU data allows to perform pitch correction. Figure 5.1a shows all coastdown segments, as they have been recorded during the total of $8.18\,\mathrm{h}$ of driving tests over $528.36\,\mathrm{km}$. It shows 259 coastdown segments, with each segment representing an individual segment from the driving data where the neutral gear was engaged and the vehicle was coasting. In total, $97\,654$ data points are included in these segments, which with a sample rate of $10\,\mathrm{Hz}$ amounts to a total duration of $2.7\,\mathrm{h}$. It can be seen that the raw coastdown segments cover the full range of vehicle speeds from $230\,\mathrm{km\,h^{-1}}$ to $0\,\mathrm{km\,h^{-1}}$. The coastdown segments are then processed as described in Section 3.3.1, with the design parameters from Section 4.1.1. The processed coastdown segments are shown in Figure 5.1b. After processing 180 segments consisting of $68\,391$ data points remain, representing a reduction of $29.96\,\%$ in the amount of data. The pitch-correction effect is visible as some of the segment's slope has been changed. Similarly, the smoothing and filtering impact is visible as choppy segments have been smoothed out, and outliers like sudden increases in speed have been removed. The processed segments still cover the full range of vehicle speeds.

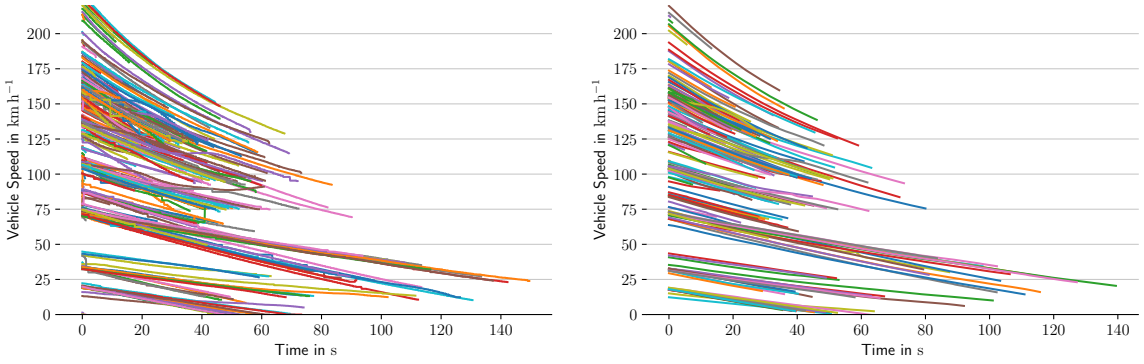

(a) Raw Coastdown Segments.

(b) Processed Coastdown Segments.

Figure 5.1: Comparison of Raw and Processed Coastdown Segments for Drive Mode Normal with Pitch Correction.

The results from transforming the coastdown segments from time-domain to velocity-domain are shown in Figure 5.2. The blue line represents the connected mean values of all aggregated coastdown segments for a specific vehicle speed. The corresponding variance to each mean value is shown as a shaded area around the blue line, representing the standard deviation. The red line represents the fitted quadratic model to the mean values. Table 5.2 shows the RLCs that describe this quadratic model alongside the RMSE between the fitted model and the drag models obtained under lab conditions. It can be observed that the fitted model agrees most with the drag model obtained under medium suspension conditions with a RMSE of $23.77\,\mathrm{N}$, closely followed by the drag model obtained under low suspension conditions with a RMSE of $23.94\,\mathrm{N}$. The loss against the very low suspension level is significantly higher, which aligns with the expectation of the vehicle operating in the medium and low suspension level during the measurements.

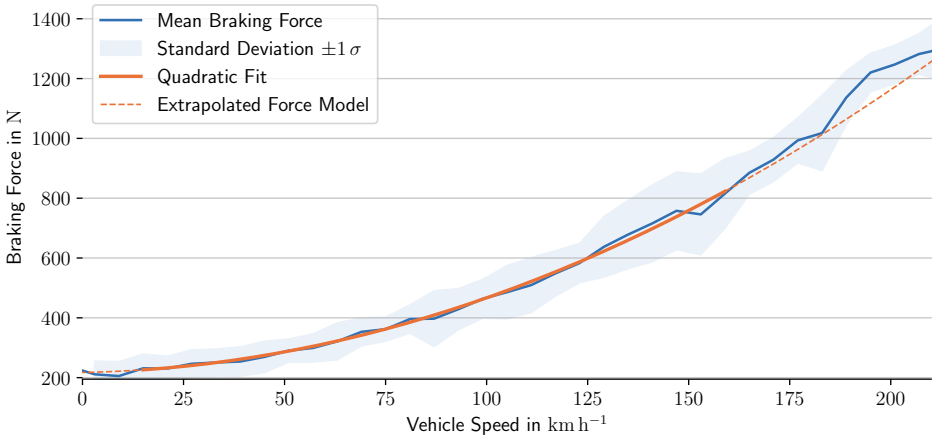

Figure 5.2: Mean Braking Force over Vehicle Speed for Pitch Corrected Drive Mode Normal with Fitted Quadratic Model.

Table 5.2: Results across all suspension levels for the coastdown analysis.

RLCs			**RMSEs**				
f_0	f_1	f_2	Very Low Susp.	Low Susp.	Medium Susp.	CoC	EPA
217.2016	0.2631	0.0223	38.19	23.94	**23.77**	45.83	89.67

The model fit was constrained to the velocity range of the lab measurements. The on-road measurements were also conducted at a higher speed, as visible from the further extension of the blue line compared to the red line's extension, representing the quadratic fit. The model fit is, therefore, only valid for the velocity range of the lab measurements for comparability reasons. As the Autobahn allows to also take measurements on public roads at top speeds, where the drag characteristics are even more pronounced due to the quadratic nature of aerodynamic drag, a possibly even more accurate model could be obtained by extending the velocity range of the model fit, if no comparability to lab measurements is required. Furthermore, the pitch correction demonstrated its effectiveness by reducing the mean standard deviation over the velocity range from 112.23 N to 73.86 N.

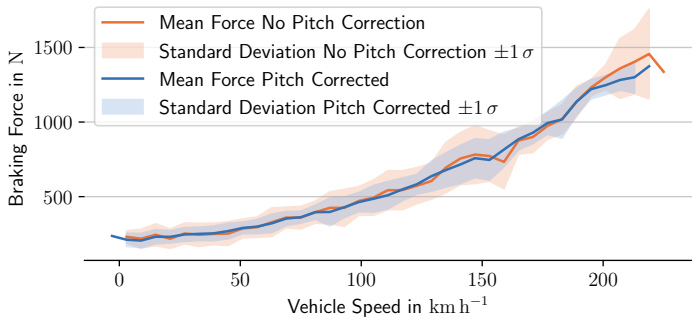

Figure 5.3: Mean Braking Force over Vehicle Speed for Drive Mode Normal with and without Pitch Correction.

As visible from Figure 5.3, the pitch correction successfully reduces the variance, while simultanously making the mean values align closer to a parabola.

Very Low Suspension Level

The subsequent section analyses that assess the road load coefficients for different suspension levels are conducted with the same design parameters as the previous analysis. Still, the pitch correction is not applied as no IMU data is available. Figure 5.4a shows the again shows the raw coastdown segments used for the subsequent analysis. A total of 459 coastdown segments were extracted from the driving data, which are made of $210\,189$ data points. From this pool of driving data, a total of $6.65\,\mathrm{h}$ covering $364.47\,\mathrm{km}$ was driving in the very low suspension setting. After processing and filtering the segments for ones where the very low suspension level was set, 206 segments with $81\,254$ data points remain, which equate to $2.26\,\mathrm{h}$. The processed segments are shown in Figure 5.4b. Comparing both figures, it can be seen that the processing has removed segments that contain faulty data, like sudden increases or sharp drops in speed. Also, the smoothing and omission of short stub segments are apparent. When recording this data, the suspension level was manually set in the vehicle settings, which allows to overrride the default behaviour of the vehicle to automatically lower itself from medium to low suspension level at speeds above $65\,\mathrm{km\,h^{-1}}$ [61]. The processed segments from the very low suspension level thus still cover the full range of vehicle speeds.

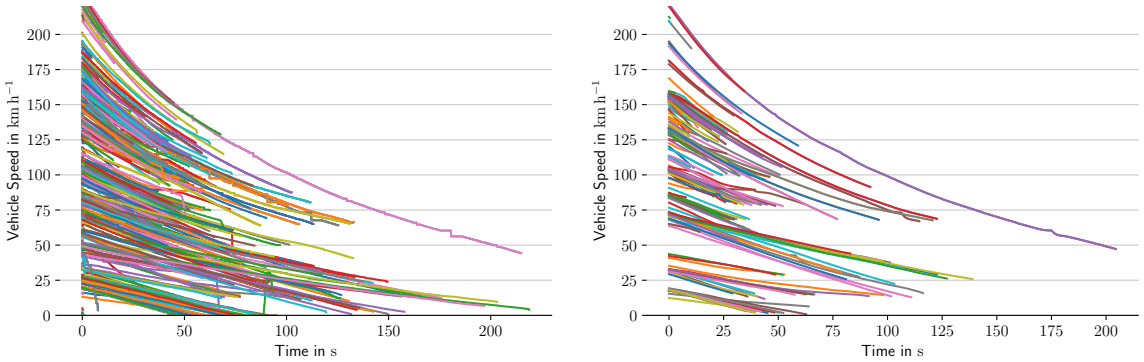

(a) Raw Coastdown Segments. (b) Processed Coastdown Segments.

Figure 5.4: Comparison of Raw and Processed Coastdown Segments for Very Low Suspension Level.

The domain transformed measurements depicted in Figure 5.5 show the mean braking force over vehicle speed for the very low suspension level. The corresponding RLCs and the RMSEs are shown in Table 5.3. Interestingly, the lowest RMSE is against the lab measurements for the medium suspension setting with $18.15\,\mathrm{N}$. It would have been expected to have the lowest RMSE against the lab measurements for the very low suspension setting, which is significantly higher with $44.36\,\mathrm{N}$.

Table 5.3: Results across very low suspension levels for the coastdown analysis.

RLCs			**RMSEs**				
f_0	f_1	f_2	Very Low Susp.	Low Susp.	Medium Susp.	CoC	EPA
185.5536	1.2479	0.0163	44.36	27.01	**18.15**	83.23	130.25

Assessing the standard deviation, it becomes apparent that the variance in the data is fairly consistent up to a vehicle speed of $150\,\mathrm{km\,h^{-1}}$ where the variance sharply increases and the mean braking force decreases. Looking at the segments from Figure 5.4b at the velocity range in question shows that the segments start out with a lower slope than expected, which explains the lower braking force in this region. This could indicate that the trim duration was too short for the vehicle to reach a stable coasting state, and the segments could still include non-steady state behavior. This could be because when performing these measurements on public roads, the neutral gear was engaged quicker after the acceleration phase than for other runs. As the curve fit is also constrained to the region of the lab measurements, the model fit just barely includes the

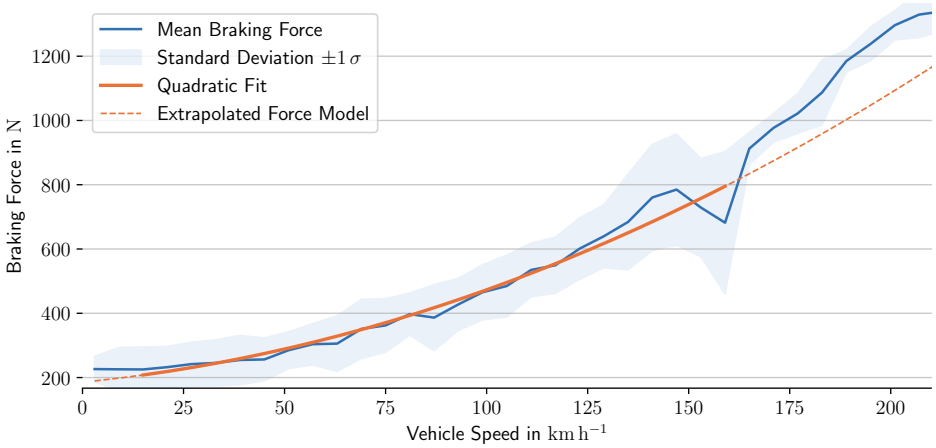

Figure 5.5: Mean Braking Force over Vehicle Speed for Very Low Suspension Level with Fitted Quadratic Model.

region of increased variance, which is why it likely underestimates the braking force in this region, as visible from the higher recorded braking forces than what the extrapolated model would suggest in the region of above $150\,\mathrm{km\,h^{-1}}$. Extending the model fit to higher speeds could provide a more accurate model for this region, with a higher quadratic term to account for the increased aerodynamic drag at higher speeds.

Low Suspension Level

This paragraph applies identical processing steps as in previous assessments but focuses on data exclusively recorded under the low suspension setting, which equals to $2.75\,\mathrm{h}$ of driving a distance of $212.65\,\mathrm{km}$. From the same pool accross all suspension levels of 459 coastdown segments consisting of $210\,189$ data points as before, now shown in Figure 5.6a, 93 segments with $39\,832$ data points remain after applying all filter conditions, including filtering for low suspension level, processing steps, and keeping only segments with the low suspension setting. This equals do $1.1\,\mathrm{h}$ of coasting in low suspension level. The processed segments are shown in Figure 5.6b. The processed segments from the low suspension level still cover the full range of vehicle speeds. The RLCs that best describe the domain-transformed coastdowns for the low suspension

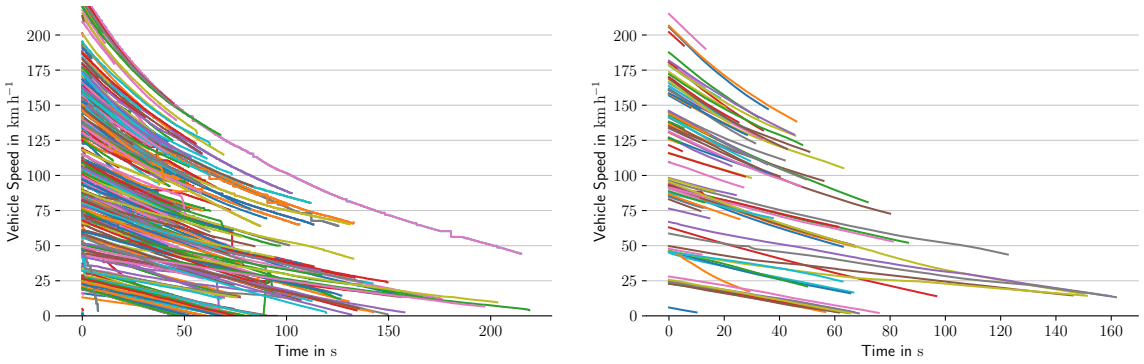

(a) Raw Coastdown Segments.

(b) Processed Coastdown Segments.

Figure 5.6: Comparison of Raw and Processed Coastdown Segments for Low Suspension Level.

setting are given alongside the RMSEs in Table 5.4. The RMSE against the lab measurements for the low suspension setting is $34.31\,\mathrm{N}$. This value being the lowest RMSE against the lab measurements for the low suspension setting is expected.

Table 5.4: Results across low levels for the coastdown analysis.

RLCs			RMSEs				
f_0	f_1	f_2	Very Low Susp.	Low Susp.	Medium Susp.	CoC	EPA
243.3028	0.0372	0.0223	48.71	**34.31**	36.31	55.67	101.74

The strong overlap of the extrapolated force model and the on-road measurements, visible in Figure 5.7, indicates that the fit constraint to the lab measurement's range didn't change the model significantly. The variance in the data is fairly consistent and uniform over the whole velocity range, which indicates that the vehicle was in a mostly stable coasting state during the measurements and that the selected combination of design parameters provides robust results for the measurements under the low suspension setting.

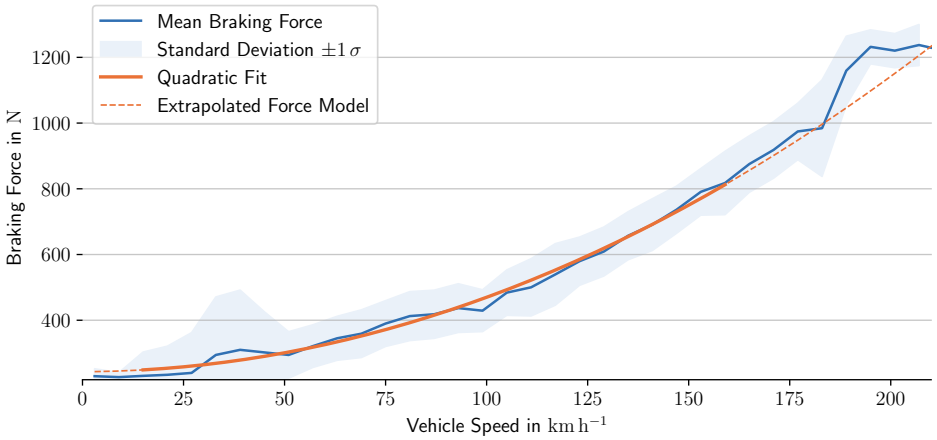

Figure 5.7: Mean Braking Force over Vehicle Speed for Low Suspension Level with Fitted Quadratic Model.

Medium Suspension Level

This section presents the results of coastdown experiments conducted specifically under the medium suspension setting, offering a clear comparison with both the outcomes for other suspension levels and the laboratory-derived drag models. In Medium suspension setting, a total duration of $3.34\,\mathrm{h}$ of driving a distance of $117.65\,\mathrm{km}$ was recorded. In this analysis, identical data processing steps, as described previously, are applied to ensure consistency, enabling a robust assessment of the method's performance under medium suspension conditions. The raw coastdown segments for the pool of coastdown segments are shown in Figure 5.8a. From the original pool of 459 coastdown segments accross all suspension levels consisting of $210\,189$ datapoints, 43 segments with $31\,702$ data points remain after applying all processing steps and keeping only segments with the medium suspension setting. This is equivalent to $0.6\,\mathrm{h}$ of coasting. The processed segments are shown in Figure 5.8b. As the vehicle automatically lowers itself beyond vehicle speeds of $110\,\mathrm{km\,h^{-1}}$, no segments with medium suspension are available above this speed. This behaviour persists even if the suspension level is manually set to medium suspension level.

Using the processed coastdown segments, the mean braking force over vehicle speed for the medium suspension setting is shown in Figure 5.9. The corresponding RLCs and the RMSEs are given in Table 5.5. The RMSE against the lab measurements for the medium suspension setting is $16.81\,\mathrm{N}$, with the second lowest being the RMSE against the lab measurements for the low suspension setting with $33.47\,\mathrm{N}$, and the other RMSEs being significantly higher. This apparent difference between the RMSE-values, with the observation that the RMSE against medium is the lowest, indicates that the on-road measurements conducted

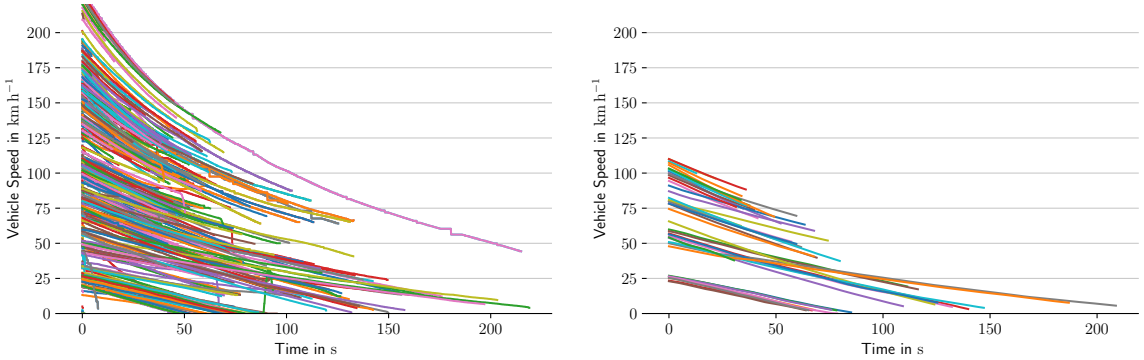

(a) Raw Coastdown Segments. (b) Processed Coastdown Segments.

Figure 5.8: Comparison of Raw and Processed Coastdown Segments for Medium Suspension Level.

with the medium suspension setting are best described by the laboratory-obtained drag model obtained under medium suspension conditions.

Table 5.5: Results across medium suspension levels for the coastdown analysis.

RLCs			**RMSEs**				
f_0	f_1	f_2	Very Low Susp.	Low Susp.	Medium Susp.	CoC	EPA
172.4174	1.7238	0.0121	57.52	33.47	**16.61**	132.05	179.34

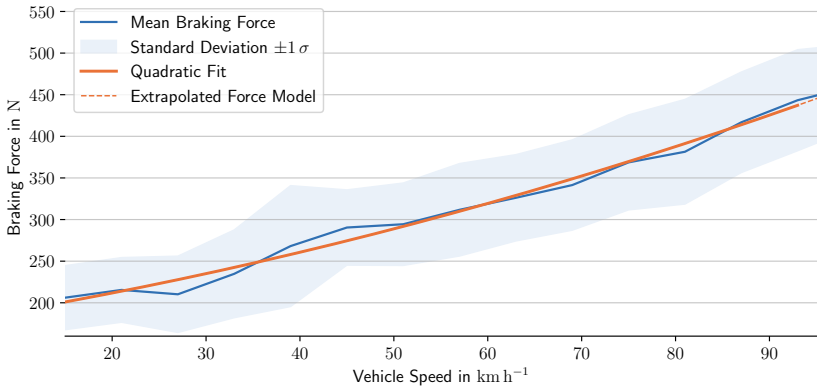

Figure 5.9: Mean Braking Force over Vehicle Speed for Medium Suspension Level with Fitted Quadratic Model.

Assessing the obtained RLCs and the fitted force model in Figure 5.9, it becomes evident that the fitted model exhibits pronounced linear characteristics. This is reflected in both the relatively large value of f_1 and the visibly linear shape of the model. This behavior can be attributed to the constrained range of the model fit, which extends only up to $95\,\mathrm{km\,h^{-1}}$. Since the quadratic term becomes more influential at higher speeds, which are absent in this range, the linear term naturally plays a more dominant role. Additionally, the data variance remains fairly consistent across the velocity range, suggesting that the vehicle maintained a predominantly stable coasting state during the measurements. This consistency indicates that the chosen design parameters effectively produce reliable results for the medium suspension setting.

VW ID.3

As coastdown measurements have also been conducted on public roads using a VW ID.3 by Rosenberger et al. [3], the available data can be fed into the coastdown method. By applying the algorithm with design parameters that have been fine-tuned for robustness based on coastdown measurements from the Porsche Taycan, this application could serve as a validation step to demonstrate the generalizability of the method with the selected parameters.

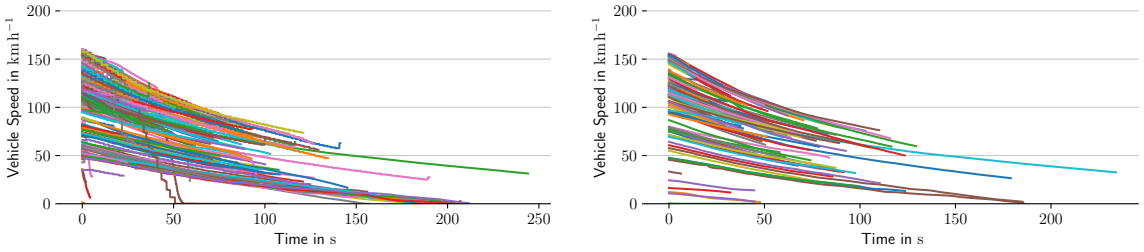

(a) Raw Coastdown Segments of VW ID.3 from [18].

(b) Processed Coastdown Segments of VW ID.3.

Figure 5.10: Comparison of Raw and Processed Coastdown Segments for VW ID.3.

Figure 5.10a shows the raw coast segments extracted from the time-series driving data. It illustrates 205 coastdown segments, comprising 139 360 data points. The vehicle is limited to a maximum speed of $160\,\mathrm{km\,h^{-1}}$, reflected in the segments' velocity range. Further, the raw plot includes segments unsuitable for analysis for different reasons, including non-steady-state behavior, choppy data, and accelerations and decelerations outside the expected range for a natural coastdown. After processing the segments, 125 segments consisting of 68 968 data points remain, as shown in Figure 5.10b. The processed segments exhibit a smoother and more consistent behavior, which indicates that the selected smoothing and filtering configuration is also effective for the VW ID.3 data.

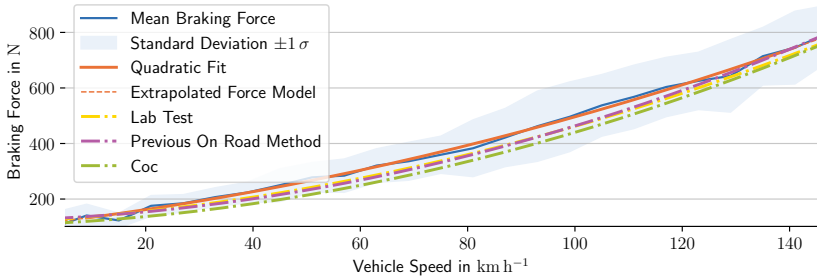

Figure 5.11: Mean Braking Force over Vehicle Speed for VW ID.3 with Fitted Quadratic Model and Other Models.

The processed coastdown segments from Figure 5.10b, aggregated, domain transformed and fitted using the same method as for the Porsche Taycan data, are shown in Figure 5.11. This graph also includes the quadratic models derived from Rosenberger et al. [3] both under laboratory conditions and also under on-road conditions, alongside the model described by the RLCs from the CoC. When comparing the fitted model to the others, it is visible that all models agree well in regions of high and low speed, with only the middle-velocity region being estimated higher by the fitted model. This behavior of the fitted model estimating a higher braking force in the middle-velocity region can also be seen in the comparatively large linear term of $f_1 = 2.276\,\mathrm{N\,h\,km^{-1}}$. The RMSEs between the fitted model and the others are given in Table 5.6. The RMSE against the lab measurements for the VW ID.3 is $26.24\,\mathrm{N}$, with the difference to the on-road measurements is $26.37\,\mathrm{N}$. This comparison has to be taken with caution as the RLCs from the lab measurements are not guaranteed to be free from confounding factors like wind speed and direction. Also, it has to be noted that the

difference in a more pronounced drag in the middle-velocity region compared to the models described by the RLCs from the previous method is likely stemming from the different implementation of the data processing pipeline.

Table 5.6: Results of ID.3 Coastdown Analysis with losses against other models.

RLCs			**RMSEs**		
f_0	f_1	f_2	Lab Conditions	On-Road Conditions	CoC
110.127	2.276	0.016	**26.24**	26.37	45.95

Nevertheless, in most regions, the derived force models agree well with the other models, which indicates that the implemented method is generalizable to other vehicles and that the selected design parameters are robust.

Coastdown Method Discussion

The results of the coastdown analyses, summarized in Table 5.7 underscore key considerations for selecting design parameters and interpreting outcomes under various test conditions. A balance must be struck between the quantity and quality of the data collected, particularly when performing measurements on public roads, where disturbances such as varying road surface conditions, wind effects, and aerodynamic interactions with other vehicles are more pronounced. These disturbances can introduce noise into the dataset, yet their impact may be mitigated by collecting a larger volume of data, assuming these disturbances follow a Gaussian distribution. Increased data volume can aid in averaging out such effects, thereby enhancing the reliability of the results.

Table 5.7: Coastdown results over all suspension levels.

	RLCs			**Losses against Lab Tests**			**Other Losses**	
Susp. Setting	f_0	f_1	f_2	Very Low	Low	Medium	CoC	EPA
Normal, PC	217.2016	0.2631	0.0223	38.19	23.94	**23.77**	45.83	89.67
Very Low	185.5536	1.2479	0.0163	44.36	27.01	**18.15**	83.23	130.25
Low	243.3028	0.0372	0.0223	48.71	**34.31**	36.31	55.67	101.74
Medium	172.4174	1.7238	0.0121	57.52	33.47	**16.61**	132.05	179.34

The discrepancy between the lab measurements and the on-road measurements could be caused by several factors, which are limited by the constraints of the methods. Neither the lab measurements nor the on-road measurements include wind speed and direction correction. For example, the discrepancy of the very low suspension measurements having not the lowest loss between each other could be caused by a number of factors among the unquantified wind speed and direction in both measurements or the absence of IMU data for the on-road measurements and a slope could also skew other traffic participants.

The effectiveness of the chosen design parameters is evident across all examined suspension levels. For instance, the parameters have proven robust when applied to both datasets with numerous coastdown segments, as in the Normal drive mode case, and those with fewer segments, such as the medium suspension level dataset. This adaptability highlights the versatility of the methodology in varying data availability scenarios.

Notably, data quality and availability differences across suspension levels must be accounted for, especially when IMU data is absent. The pitch correction enabled by IMU data significantly reduces variance by addressing vehicle slope disturbances, as demonstrated by the reduction in mean standard deviation for the Normal drive mode with pitch correction dataset. While the methodology is effective without pitch correction,

leveraging IMU, data is strongly recommended in cases where only a limited number of segments are available, as it improves the data quality and compensates for environmental factors inherent to public road measurements.

A comparison of results across suspension levels and their corresponding laboratory measurements reveals further insights. The correlation between the fitted models and lab-based drag measurements aligns most closely for medium and low suspension settings, where the RMSE values are lowest against their respective lab data. Interestingly, this pattern does not hold for the very low suspension setting, suggesting that additional factors, such as dynamic behavior during coasting, may influence the results in that case. These observations highlight the interplay between on-road measurement variability and the processing algorithm's ability to produce results consistent with controlled laboratory conditions.

The constrained velocity range of the model fit also plays a significant role in shaping the fitted force model. The linear term dominates for medium suspension due to the limited speed range, as higher velocities, where the quadratic term becomes more influential, are absent. This relationship is further supported by the observed trend across all suspension levels: quadratic terms gain prominence when the velocity range of the fit extends to higher speeds, capturing the effects of aerodynamic drag.

The results from the VW ID.3 coastdown analysis further underscore the robustness of the coastdown method and the selected design parameters. The fitted model aligns well with the laboratory and on-road measurements, with the RMSE values indicating a similarly strong agreement for this vehicle as for the Porsche Taycan. This consistency across different vehicle models highlights the methodology's generalizability and the design parameters' adaptability to varying test conditions and vehicle characteristics.

5.1.2 Constant Speed Method

This section explores the constant speed method as a complementary approach to RLC estimation, enabling a comparative evaluation with the coastdown method. The method involves analyzing vehicle behavior at steady velocities. Figure 5.12a illustrates the raw extracted constant speed driving segments, comprising 203 segments and 55 761 data points. After applying the processing steps described in Section 3.3.1, 115 segments with 27 780 data points remain, corresponding to 46.3 min of driving data. The processed data, shown in Figure 5.12b, demonstrates the removal of non-steady-state sections at the segment boundaries and short, irrelevant stub segments, as well as the overall smoothing effect, among other processing outcomes.

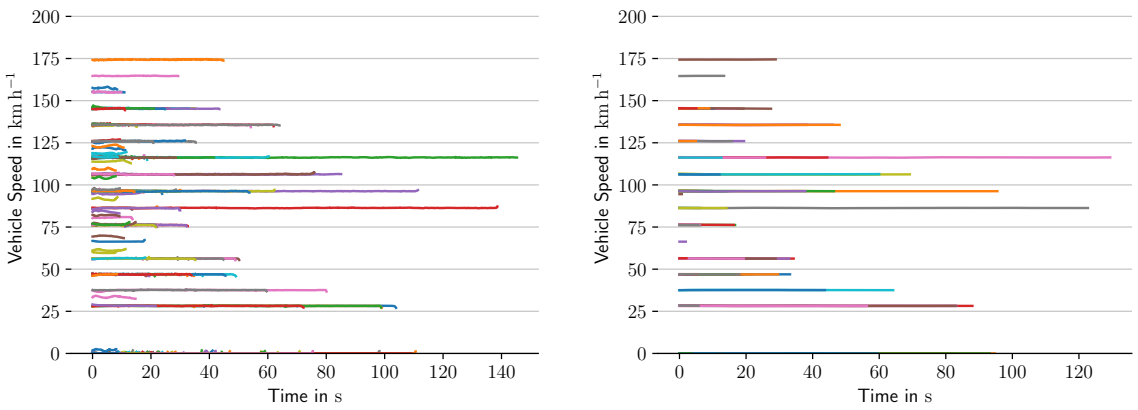

(a) Raw Constant Speed Segments.

(b) Processed Constant Speed Segments.

Figure 5.12: Comparison of Raw and Processed Constant Speed Segments.

Each processed segment is converted into a data point in the velocity domain, as shown in Figure 5.13. A quadratic model is fitted to these data points, represented by the red curve in the figure. Despite notable variability in the data, particularly a wide spread of points at identical velocities, the fitted model captures the general trend effectively. This variability aligns with observations from Komnos et al. [31], who emphasized the importance of accommodating outliers in data fitting to enhance robustness. This principle was similarly validated during the design parameter fine-tuning phase.

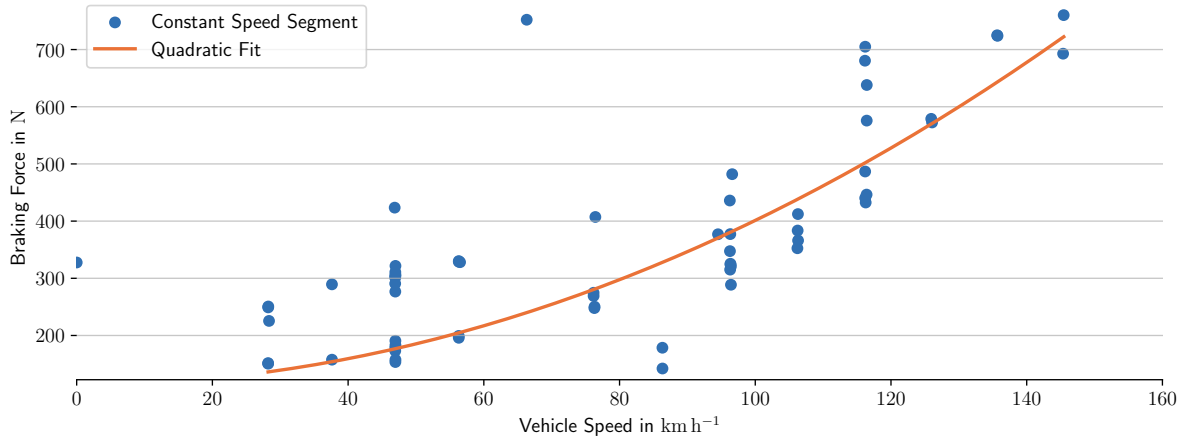

Figure 5.13: Mean Braking Force over Vehicle Speed for Constant Speed Method with Fitted Quadratic Model.

Table 5.8 presents the RLCs derived from the fitted model. Notably, the linear coefficient f_1 is determined to be zero, which deviates from the typical expectation that drag force comprises constant, linear, and quadratic velocity dependencies.

Table 5.8: Results across all suspension levels for the coastdown analysis.

RLCs			**RMSEs**				
f_0	f_1	f_2	Very Low Susp.	Low Susp.	Medium Susp.	CoC	EPA
113.3626	0.0000	0.0288	60.30	**52.16**	84.09	89.77	87.62

The constant speed data primarily comprises measurements from the "very low" ($56.96\,\%$), "low" ($31.01\,\%$), and "medium" ($12.03\,\%$) suspension levels. Correlating these proportions with the RMSE values in Table 5.8, the lowest RMSE of $52.12\,\mathrm{N}$ occurs at the "low" suspension level, followed by $60.30\,\mathrm{N}$ at "very low" and $84.09\,\mathrm{N}$ at "medium." While a partial alignment is observed between the prevalence of data and the RMSE, it is not strictly consistent, as the most substantial dataset is associated with "very low" suspension, yet the lowest RMSE occurs for "low" suspension.

Some of the observed variability in the data could be attributed to the calculation method for the required force to maintain constant speed, which is based on engine torque. This approach does not account for transmission inefficiencies and drivetrain losses, which vary between gears. Consequently, this oversight contributes to the broader spread of measurements and the higher RMSE values compared to the coastdown method. In essence, the "drag" measured at the engine shaft omits several influential factors, which probably impact the accuracy of the RLC estimates. To reduce the large observed spread of mean braking forces at identical velocities, the data collection process could be refined to account for more confounding factors, such as road surface quality. Nevertheless, this method also proved effective in estimating RLCs, even if compared to the coastdown method, it exhibits higher variability and RMSE values compared to the lab measurements.

5.1.3 Discussion of Road Load Coefficient Estimation

This section synthesizes the results obtained from the methodologies used to estimate RLCs. By comparing the RLCs derived from on-road testing, laboratory measurements, and official documentation such as the EPA and CoC models, key insights into the strengths and limitations of the approaches are revealed. These findings are contextualized, specifically emphasizing suspension level effects, environmental influences, and the implications for different speed ranges.

The methodology for merging RLCs across suspension levels, as introduced by Rosenberger et al. [18], was used to create a compound model representing the default drive mode, where the vehicle automatically adjusts its suspension level based on speed. The approach involves dividing the velocity range into distinct regions based on the active suspension level and subsequently merging the corresponding force models.

The middle suspension model is applied from the lowest speeds ($15\,\mathrm{km\,h^{-1}}$) up to the transition speed ($65\,\mathrm{km\,h^{-1}}$) and the lowered suspension model is used for speeds above $65\,\mathrm{km\,h^{-1}}$, as this suspension level activates automatically at higher speeds [61, p. 267].

In the overlapping region ($65\,\mathrm{km\,h^{-1}}$ to $95\,\mathrm{km\,h^{-1}}$), both force models are evaluated, and their RMSE is calculated to $2.17\,\mathrm{N}$. The combined dataset, consisting of forces from both suspension levels across their respective ranges, is then fitted to a quadratic model. This process ensures a smooth transition between the models and provides a unified representation of the drag characteristics for the normal drive mode.

Figure 5.14 illustrates the resulting combined model alongside the combined model from the lab test and the combined models from EPA and CoC. Notably, this compound model aligns closely with the EPA and CoC data for speeds below $100\,\mathrm{km\,h^{-1}}$, validating the merging process.

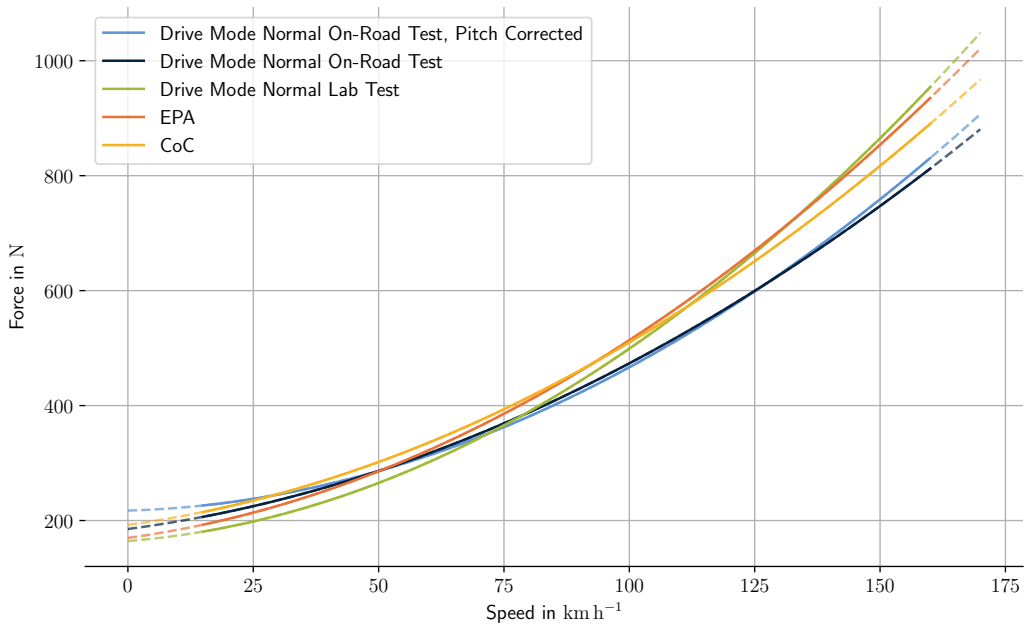

Figure 5.14: Comparison of RLC Models for Normal Drive Mode.

The compound model for the normal drive mode, derived using on-road testing, aligns closely with the EPA and CoC models for speeds below $100\,\mathrm{km\,h^{-1}}$, as shown in Figure 5.14. This agreement demonstrates that the proposed methodology is capable of producing reliable RLCs for urban driving scenarios, where vehicles typically operate at lower speeds. At higher speeds ($100\,\mathrm{km\,h^{-1}}$ and above), however, the compound on-road model predicts lower drag than both the EPA and CoC models, as well as the laboratory-derived model.

This deviation highlights the challenges of quantifying aerodynamic drag under real-world conditions, where variables such as wind and vehicle interactions can significantly affect results. While these differences may impact accuracy for high-speed applications, the methodology remains highly suitable for urban driving assessments.

A detailed analysis of suspension-specific RLCs provides further insights into the on-road testing methodology. Figures 5.15a, 5.15b, and 5.15c compare the fitted models for the very low, low, and medium suspension levels against laboratory measurements. Across all suspension levels, the following trends are observed:

Compared to laboratory results, on-road measurements consistently predict higher drag forces at low speeds. This could be attributed to unquantified environmental factors such as rolling resistance variations due to road surface quality or temperature differences.

In contrast, at speeds above $100\,\mathrm{km\,h^{-1}}$, the on-road tests predict lower drag than laboratory measurements. This discrepancy is likely due to reduced aerodynamic drag caused by drafting effects (e.g., trailing vehicles on highways) or systematic differences in test conditions, such as wind.

The standard deviation in on-road data is consistently higher than that in laboratory tests. This is expected as public road conditions introduce additional variability in factors such as wind direction, road surface texture, and vehicle dynamics.

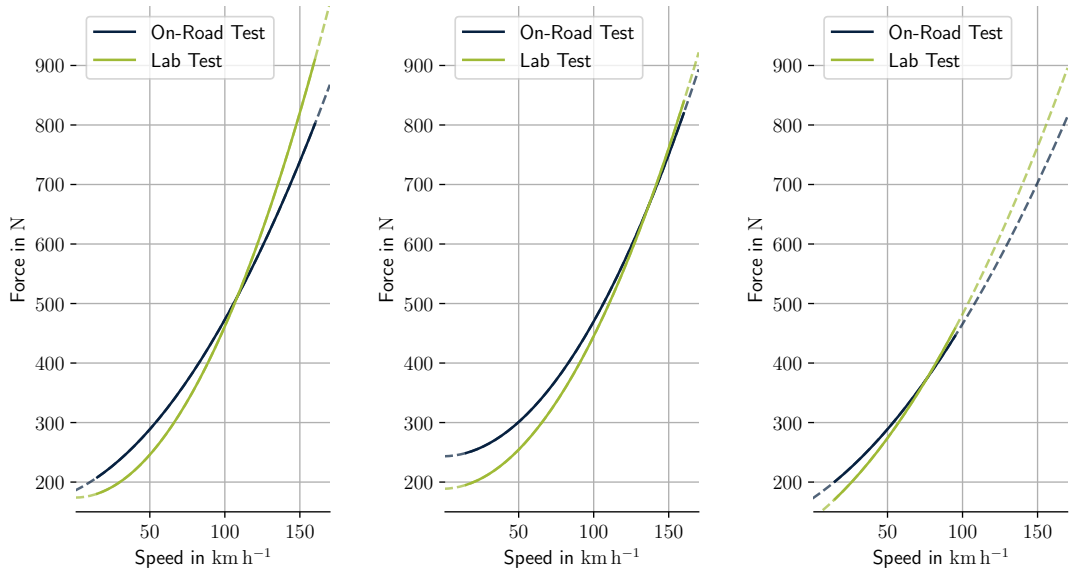

(a) Very Low Suspension Level. (b) Low Suspension Level. (c) Medium Suspension Level.

Figure 5.15: Comparison of Fitted RLC Models for Different Suspension Levels.

The absence of detailed environmental data (e.g., temperature, wind speed/direction, and road texture) during on-road testing likely contributed to the observed variability. This observation is shared by Batra [41]. Future studies should explicitly incorporate environmental sensors or record such factors to refine the results. As noted in the coastdown results, sparse data at high speeds introduces challenges in accurately capturing the quadratic nature of aerodynamic drag. Expanding the dataset with more measurements at higher velocities would enhance the robustness of the fitted models. The consistent underestimation of drag at high speeds could also stem from systematic differences in data acquisition techniques or sensor accuracy. For instance, errors in calculating vehicle resistance based on engine torque (in the constant speed method) may propagate into the results.

The results demonstrate that on-road testing is a viable alternative to laboratory-based methods for estimating RLCs. While laboratory tests provide higher precision and controlled conditions, on-road testing is

significantly more cost-effective and representative of real-world scenarios. The on-road approach aligns closely with official drag models for urban driving conditions, making it an effective and practical solution. However, targeted refinements—such as addressing environmental factors and improving data density at high speeds—could further enhance the methodology's accuracy and broaden its applicability.

Table 5.9: RLC values categorized by test source.

Source	RLC Type	f_0	f_1	f_2
On-road Tests Coastdown	Very Low Suspension	185.6	1.248	0.01626
	Low Suspension	243.3	0.037	0.02228
	Medium Suspension	172.4	1.724	0.01208
	Drive Mode Normal	185.2	1.156	0.01727
	Drive Mode Normal - Pitch Corrected	217.2	0.263	0.02232
On-road Tests Constant Speed	All Suspension Levels	113.4	0.000	0.02880
Lab Tests	Very Low Suspension	173.9	0.005	0.02871
	Low Suspension	188.7	0.064	0.02500
	Medium Suspension	138.4	1.981	0.01456
	Drive Mode Normal	164.3	0.698	0.02649
Third-party Values	CoC Values	192.4	1.200	0.01976
	EPA Values	169.7	1.200	0.02240

While the on-road testing results did not perfectly align with those obtained under laboratory conditions, an outcome that was somewhat expected due to uncontrollable real-world factors, it can be concluded that on-road derivation of RLCs is a viable alternative to laboratory-based methods. The new method's generalizability and the robustness of its design parameters were demonstrated by applying it to a different vehicle, the VW ID.3. Notably, the coastdown method yielded lower variability and reduced RMSE values compared to the constant-speed method. Nevertheless, the constant-speed method remained effective, and its more straightforward test-drive procedure on public roads makes it even more accessible.

5.2 Efficiency Map Estimation

This section presents the generated efficiency maps for different vehicle configurations, comparing them to benchmark data from laboratory tests [18]. Key findings are discussed, emphasizing discrepancies, patterns, and potential implications for further optimization. The results of the processing pipeline from Section 3.3.2 with the selected design parameters given in Section 4.2 are presented for both gears of the Porsche Taycan, the vehicle under study. The total duration of driving data recordings for the efficiency map estimation is $12.52\,\mathrm{h}$ with a covered distance of $1086.38\,\mathrm{km}$. Notably, not all of this data was used exclusively for the efficiency map estimation, but also for the constant speed RLC investigation as well as the gear strategy estimation. Furthermore, the generalizability of the methodology is assessed by applying it to driving data from the VW ID.3.

5.2.1 Porsche Taycan Gear One

Rosenberger et al. [18] conducted laboratory tests to measure the efficiency map of the Porsche Taycan in first gear. This was done by using a rolling dynamometer to put the vehicle into specific operating points while measuring electrical and mechanical power. A grid of discrete operating points was measured, which was used to draw the contour plot presented in Figure 5.16a. It shows the efficiency of the electric drivetrain in gear one as a function of torque and engine speed. The efficiency map derived from $3.95\,\mathrm{h}$ on-road

driving data covering a distance of 134.25 km with the methodology described in Section 3.3.2 is shown in Figure 5.16b. The efficiency maps are limited to the domain where both dynamometer and driving data are available. The low torque high RPM region is not covered by the driving data, as the vehicle changes to second gear before reaching this region. On the dynamo this region is reachable, if the vehicle is put into dynamometer mode. Lastly the small gaps between the covered area and the axes are due to the limitations of the discrete dynamometer measurements, which don't extend into this region, which is on the other hand still covered by the driving data.

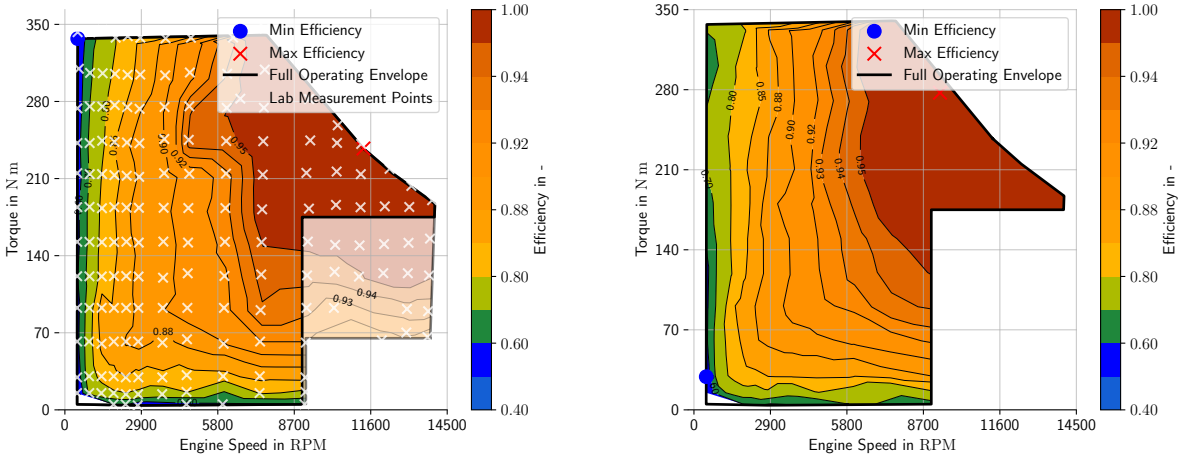

(a) Efficiency map for Porsche Taycan Gear One derived from Dynamo data. Data from Rosenberger [3].

(b) Efficiency map for Porsche Taycan Gear One derived from driving data.

Figure 5.16: Efficiency maps for Porsche Taycan Gear One derived from (a) dynamometer data and (b) driving data.

It is immediately apparent that the general shape of the efficiency map derived from driving data matches the efficiency map derived from dynamometer data closely, with the same general trends of low efficiency with about 40 % at low torques and engine speeds, and high efficiency with more than 95 % at high combinations of high torques and engine speeds. As indicated by the figures, the point of maximum efficiency generally also matches, with the efficiency map derived from driving data showing the point of maximum efficiency inside the region. In contrast, the efficiency map derived from dynamometer data shows the maximum efficiency point at the edge of the operating domain. According to Doppelbauer, the point of maximum efficiency is generally not at the edge of the operating domain but inside of it [8, p.279], which would indicate that the efficiency map derived from driving data is more accurate in this regard. For the point of lowest efficiency, both maps estimate it at the lowest possible engine speeds. Still, the efficiency map derived from driving data estimates it at low torques, while the efficiency map derived from dynamometer data estimates it at high torques. Another observable difference is that the isolines of efficiency of the dynamometer obtained map follow more straight lines in axes directions, while the isolines of the driving data obtained map are more curved and smooth. This could be because the dynamometer data was measured at specific operating points, while the driving data was measured at a continuous range of operating points. Therefore, the isolines of the dynamometer obtained map are more jagged and less smooth than the isolines of the driving data obtained map. To compare both maps, both figuratively and quantitatively, the continuous measurements from the driving data-based map have been assigned to the closest operating point of the dynamometer data grid-based map before calculating the average for all data points that have been assigned to the same operating grid point. This allows to create a difference map, which is shown in Figure 5.17. Moreover, using these differences, the mean absolute difference and the RMSE between them can be calculated to quantify the difference between the two efficiency maps. The mean absolute difference between the efficiency map derived from driving data and the efficiency map derived from dynamometer data is 1.96% . The RMSE between the two efficiency maps is 3.73% . Interestingly, both the points of maximum over- and underestimation are in regions

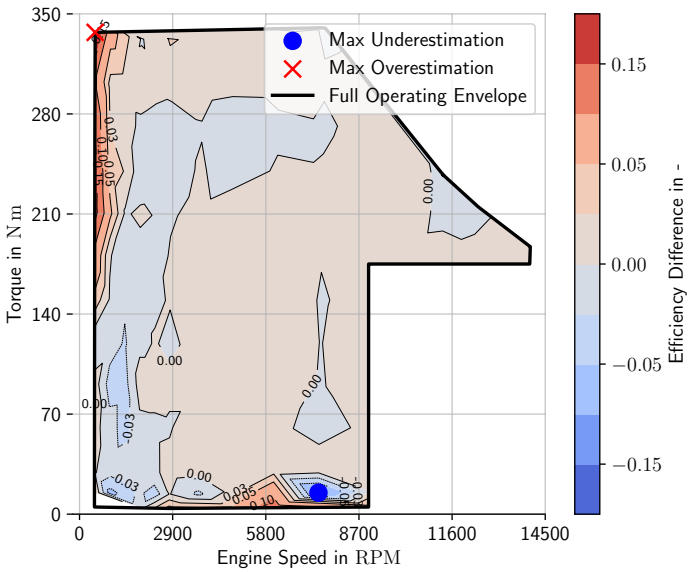

Figure 5.17: Difference between the efficiency map derived from driving data and the efficiency map derived from dynamo data.

of low torque and engine speed, while in the regions further away, the difference is a lot lower, with most areas deviating not more than $\pm 2.5\,\%$. At the same time, the regions close to the axes differ by as much as $\pm 12.5\,\%$. This is likely due to the inherent higher density of contour lines in these regions, which makes the difference more pronounced. The overall difference between the two maps is relatively low, indicating that the methodology effectively estimates efficiency maps from driving data.

5.2.2 Porsche Taycan Gear Two

Rosenberger et al. [18] also measured the efficiency map of the Porsche Taycan in second gear by manually setting the vehicle into specific operating points on a dynamometer. The efficiency map derived from this controlled test is shown in Figure 5.18a. Unlike in real-world driving, the dynamometer setup allows testing beyond the indicated operating domain, particularly in the region of lower engine speeds. However, as this region is inaccessible in real-world driving conditions in gear two, the dynamometer data was constrained to match the indicated operating domain, which was constructed using driving data. The efficiency map derived from $8.28\,\mathrm{h}$ driving data covering a distance of $952.02\,\mathrm{km}$ is shown in Figure 5.18b. Again the area of both efficiency maps is constrained to the region where both dynamometer and driving data are available. The low RPM region is not covered by the driving data, as the vehicle changes to first gear, when approaching low engine speeds. In contrast, the dynamometer data covers this region, as the vehicle can be put into dynamometer mode to reach these regions.

The general shape of the efficiency map derived from driving data closely resembles the efficiency map obtained from dynamometer data, with similar trends observed across both maps. At very low torque levels, a key difference arises: the dynamometer-based map shows efficiency dropping as low as $40\,\%$, while the driving data-based map only estimates a minimum efficiency of $60\,\%$ in the same region. The point of globally lowest efficiency is estimated in the same torque range on both maps; however, the driving data-based map positions this point at a lower engine speed compared to the dynamometer-based map. According to Doppelbauer [8, p.279], theoretical efficiency maps of PMSM generally predict the point of lowest efficiency closer to the location observed on the dynamometer map. This suggests that the dynamometer-derived map aligns more closely with theoretical expectations for this characteristic.

In contrast, the point of maximum efficiency aligns very closely between the two maps, both in terms of its location within the operating domain and the maximum efficiency value. Consistent with the observations in gear one, the isolines of efficiency derived from driving data are smoother and deviate less from the general trends, while the dynamometer-based map exhibits more abrupt transitions and isolines that follow axis directions more closely. This distinction can be attributed to the continuous range of operating points captured in driving data instead of the discrete grid of operating points used in the dynamometer test, which introduces interpolation artifacts and irregularities. To further analyze the differences between the two maps, a difference map was generated using the same methodology as described in Section 3.3.2. The difference map is shown in Figure 5.19.

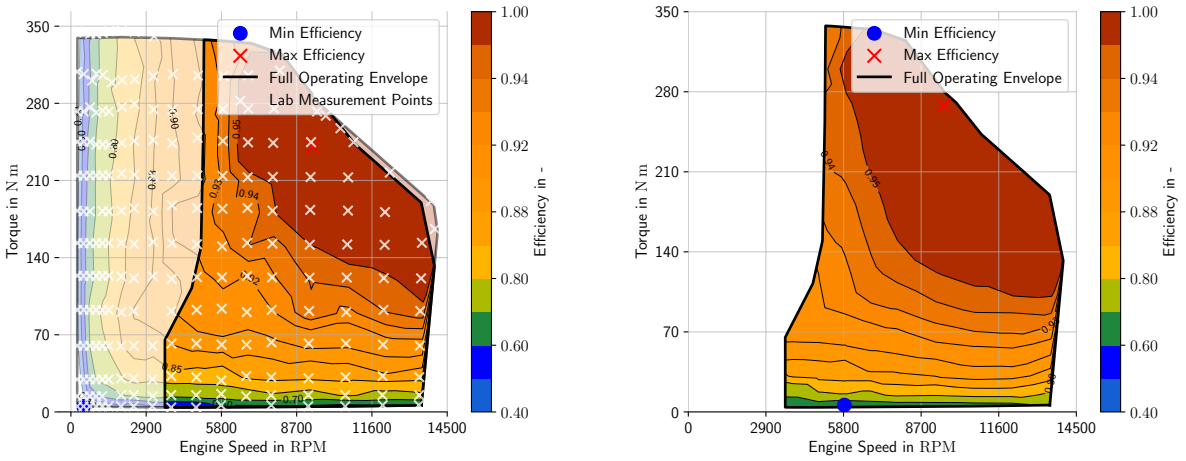

(a) Efficiency map for Porsche Taycan gear two derived from Dynamo data. Data from Rosenberger [18].

(b) Efficiency map for Porsche Taycan gear two derived from driving data.

Figure 5.18: Efficiency maps for Porsche Taycan gear two derived from (a) dynamometer data and (b) driving data.

The difference map reveals that, as in gear one, the largest over- and underestimation regions are concentrated near areas of high isoline density, typically near the axes. However, due to the exclusion of very low engine speed regions (which are inaccessible in gear two during real driving), the magnitude of these differences is less pronounced than in gear one results. The high-density regions of torque close to the RPM axis show the most significant differences, but the remainder of the operating domain exhibits relatively small deviations. Notably, large regions of the map show differences of less than $\pm 2.5\,\%$, while areas near the edges of the operating domain demonstrate slightly larger deviations, with a maximum observed difference of $\pm 15\,\%$.

The mean absolute difference and RMSE between the two efficiency maps are 1.64% and 2.58%, respectively. Both values are lower than those observed in gear one, likely due to the constrained operating domain for gear two, which excludes the region of very low engine speeds. This constrained domain reduces the potential for data acquisition and interpolation differences, leading to closer alignment between the two maps.

The overall low discrepancy between the efficiency maps confirms that the methodology for deriving efficiency maps from driving data is both reliable and effective. These results, combined with the gear one findings, further support the validity of the driving-data-based approach for efficiency estimation, particularly for real-world vehicle operations.

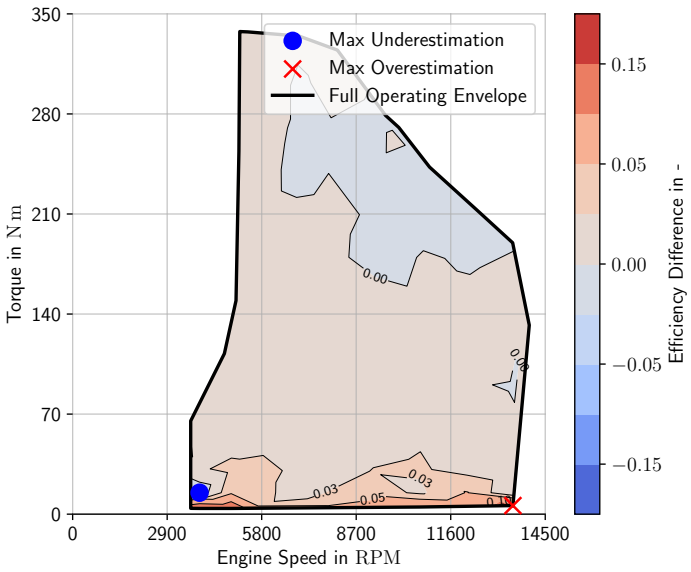

Figure 5.19: Difference between the efficiency map derived from driving data and the efficiency map derived from dynamo data for Gear Two.

5.2.3 VW ID.3

To validate the generalizability of the design parameter selection across different vehicle configurations, the methodology was applied to driving data from the VW ID.3. This vehicle was chosen as Rosenberger et al.[3] conducted laboratory tests to measure its efficiency map, allowing for a direct comparison between dynamometer-based and driving-data-based maps. The efficiency map derived from dynamometer data is shown in Figure5.20a, while the efficiency map derived from driving data is shown in Figure 5.20b.

As observed in the Porsche Taycan results, the general shape of the efficiency map derived from driving data closely matches that of the dynamometer-based map, with similar trends across both. The regions of minimum efficiency are consistent along the edges of the operating domain, with both maps predicting these values at the lowest possible engine speeds. However, as in the Porsche Taycan second gear results, the maps differ in their torque predictions for minimum efficiency. The dynamometer-based map places this point at high torque values, whereas the driving-data-based map estimates it at low torque. This discrepancy may occur due to this region's high density of contour lines, highlighting the need for further investigation into low-torque regions during on-road testing.

A notable artifact is observed in the dynamometer-based map: a region of exceptionally high efficiency (above $95\,\%$) between $5000\,\mathrm{min}^{-1}$ and $6000\,\mathrm{min}^{-1}$, at torque values between $50\,\mathrm{N\,m}$ and $60\,\mathrm{N\,m}$. This artifact is absent in the driving-data-based map, likely due to a gap in on-road driving data that did not sufficiently cover this specific operating range. Supplementary plots in Appendix A.13a illustrate this gap, where the absence of driving data in this region is clearly visible.

A difference map was generated to further analyze these differences, shown in Figure 5.21. The mean absolute difference and the RMSE between the two efficiency maps were also calculated for quantitative assessment.

The difference map exhibits the same pattern observed in the Porsche Taycan results, with low differences in regions farther from the axes and the largest deviations occurring near the axes, where isoline density is highest. However, in the case of the VW ID.3, these deviations are less pronounced. The largest overestimation is $7.5\,\%$, and the largest underestimation is $5\,\%$, which are smaller than the discrepancies observed for

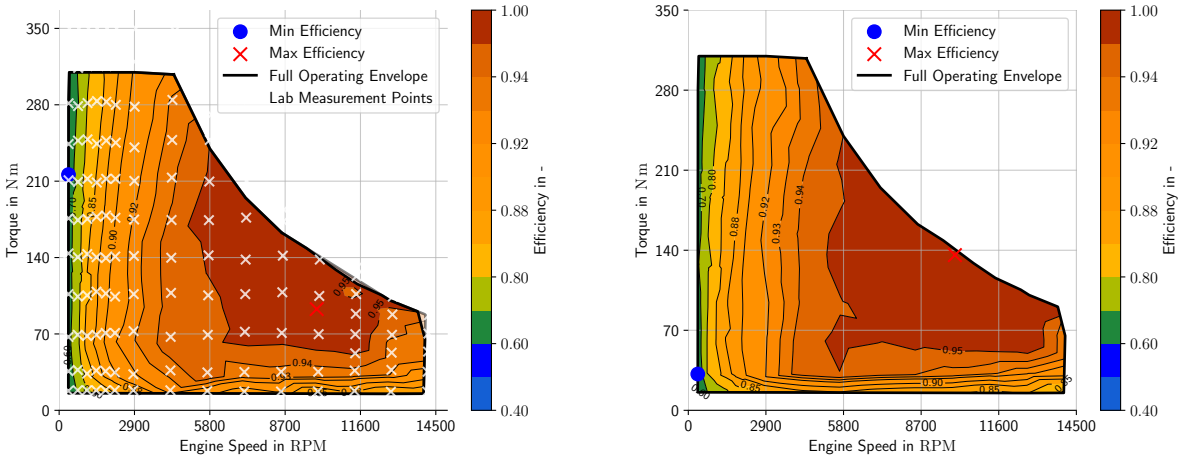

(a) Efficiency map for VW ID.3 derived from dynamo data. Data from Rosenberger [3].

(b) Efficiency map for VW ID.3 derived from driving data.

Figure 5.20: Efficiency maps for VW ID.3 derived from (a) dynamometer data and (b) driving data.

both gears of the Porsche Taycan. Large portions of the map exhibit differences within $\pm 2.5\,\%$, highlighting the overall accuracy of the driving-data-based approach.

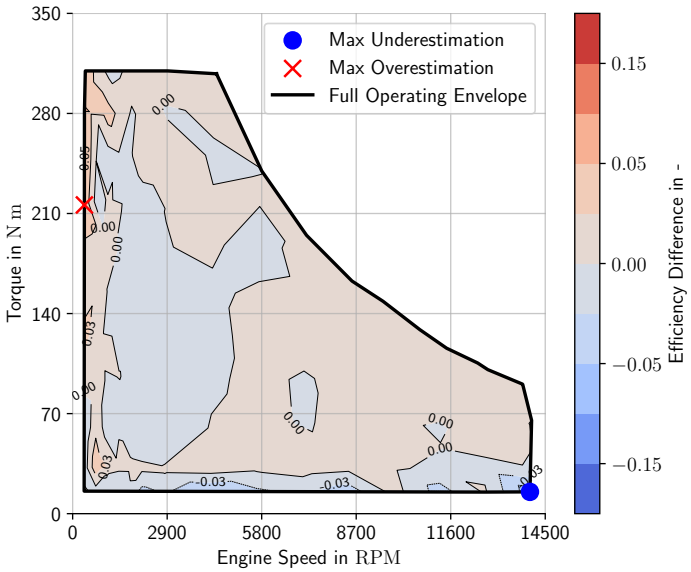

Figure 5.21: Difference between the efficiency map derived from driving data and the efficiency map derived from dynamo data for VW ID.3.

The calculated mean absolute difference of 0.92% and RMSE of 1.43% are both lower than those observed for the Porsche Taycan. This result further proves that the methodology effectively estimates efficiency maps from driving data across different vehicle configurations. Notably, these results were achieved despite the design parameter fine-tuning being performed exclusively on Porsche data, indicating that the methodology is generalizable to other vehicle types.

5.2.4 Discussion of Efficiency Map Estimation

The results across all analyzed configurations, summarized in Table 5.10, Porsche Taycan in gear one and gear two, and VW ID.3, demonstrate the effectiveness of the proposed methodology in deriving efficiency

maps from driving data. A key finding is that the general shape and trends of efficiency maps derived from driving data align closely with those obtained from dynamometer data. This validates the capability of the driving-data-based approach to provide accurate efficiency estimates without requiring the controlled conditions of a dynamometer.

Table 5.10: Mean absolute difference and RMSE between efficiency maps derived from driving data and dynamo data for different vehicle configurations.

Vehicle Configuration	Mean Absolute Difference	RMSE
Porsche Taycan Gear One	1.96%	3.73%
Porsche Taycan Gear Two	1.64%	2.58%
VW ID.3	0.92%	1.43%

The driving-data-based efficiency maps for the Porsche Taycan in both gear one and gear two showed similar levels of accuracy when compared to dynamometer-based maps. The VW ID.3 results further confirmed the methodology's robustness, achieving the lowest mean absolute difference and RMSE among all tested configurations.

Across all maps, the largest discrepancies were consistently observed near the axes (low-speed and low-torque regions). These regions are particularly important for urban driving, where vehicles frequently operate under such conditions. While the overall differences between maps are low, targeted improvements in these regions could enhance the accuracy of real-world driving simulations.

The smoother isolines observed in the driving-data-based maps indicate a higher fidelity representation of real-world driving conditions. In contrast, the dynamometer-based maps exhibit jagged transitions and iso-lines going along axes' directions, likely due to interpolation artifacts from their grid-based data collection method.

Three main advantages from the driving data-based approach are evident: practical efficiency, continuous data range, and greater realism. Driving data can be collected in a much shorter time and with less effort than setting up and running tests on a dynamometer. Real-world driving captures a continuous range of operating points, avoiding the need for interpolation artifacts inherent to dynamometer data. The driving-data-based approach inherently reflects real-world conditions, accounting for transient effects and varying operating environments that dynamometer tests may not replicate.

Despite its advantages, the driving-data-based approach faces challenges in ensuring comprehensive coverage of the operating domain. Unlike the systematic testing of specific operating points on a dynamometer, driving data lacks real-time feedback to indicate whether all critical regions have been sufficiently sampled. This limitation could be mitigated by incorporating live feedback systems to guide the driver toward underrepresented operating points, reducing data collection time while maintaining coverage.

The largest discrepancies between the two approaches were observed in low-speed, low-torque regions, which are critical for urban driving scenarios. Improving accuracy in these regions should be a priority, as they represent a significant portion of real-world driving conditions. Nevertheless, the observed differences, even in these regions, remain within acceptable tolerances for most practical applications.

The consistent accuracy of the driving-data-based methodology across different vehicle configurations (Porsche Taycan and VW ID.3) highlights its generalizability. While the design parameter fine-tuning was performed exclusively on Porsche data, the approach demonstrated strong performance on the VW ID.3, underscoring its applicability to other vehicles with minimal adaptation.

5.3 Gear Strategy Estimation

Gear strategy estimation offers important insights into the dynamic behavior of multi-gear drivetrains by identifying thresholds for gear changes, which is required if the simulation of vehicles with multiple gears is to be done. This section discusses the derived gear change strategies, comparing results from on-road tests with controlled dynamometer data. The analysis focuses on upshift strategies, representing the thresholds at which the vehicle transitions from first to second gear. It is important to note that downshift strategies, which follow independent rules not based on torque and speed, are not depicted in the same plots as upshift strategies.

Figures 5.22a and 5.22b illustrate the comparison of gear change thresholds derived from on-road tests and dynamometer tests for the Porsche Taycan in Normal and Sport drive modes, respectively. The total duration of the data recorded in Normal drive mode is $0.74\,\mathrm{h}$, covering a distance of $35.36\,\mathrm{km}$. In Sport drive mode, the total duration is $1.30\,\mathrm{h}$, covering a distance of $58.68\,\mathrm{km}$. The green lines indicate the gear change thresholds derived by Rosenberger et al. [18] through precise dynamometer testing, while the blue lines show the thresholds derived from on-road tests using the method described in Section 3.3.3.

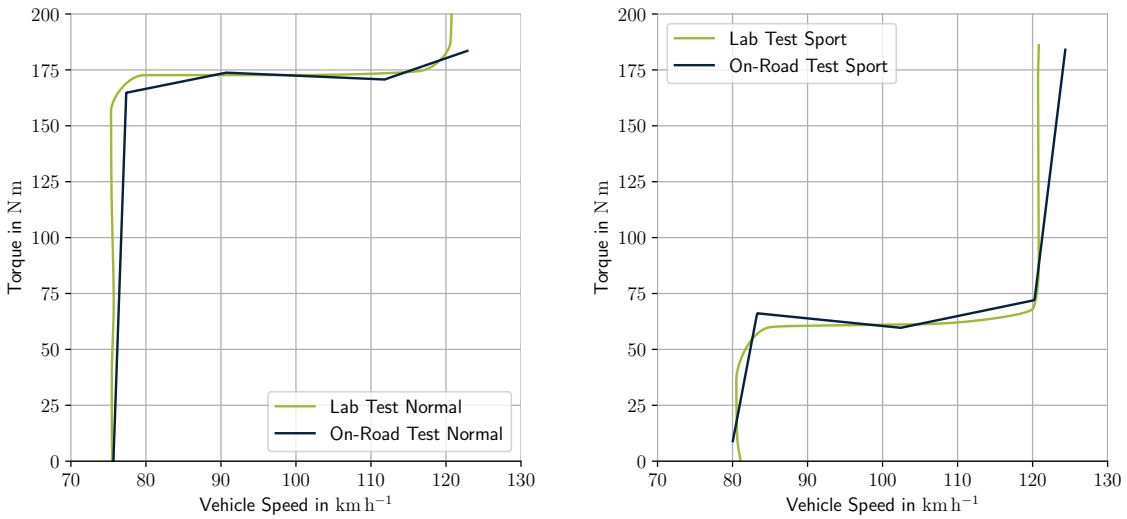

(a) Comparison of Gear Change Strategies derived from On Road Test vs Dynamo Test in Normal Drive Mode.

(b) Comparison of Gear Change Strategies derived from On Road Test vs Dynamo Test in Sport Drive Mode.

Figure 5.22: Comparison of Gear Change Strategies derived from On Road Test vs Dynamo Test in Normal and Sport Drive Modes.

Figure 5.22a shows the gear change strategy for Normal drive mode. The gear change threshold derived from on-road tests successfully identifies the horizontal threshold at $75\,\mathrm{km\,h^{-1}}$ for the torque range of $0\,\mathrm{N\,m}$ to $175\,\mathrm{N\,m}$, closely matching the dynamometer-derived threshold. Beyond this point, the threshold is expected to transition vertically at $120\,\mathrm{km\,h^{-1}}$, the maximum speed achievable in first gear. However, due to the sparse availability of real driving data in this region, the algorithm did not fit the vertical transition as accurately as desired. Nevertheless, the derived threshold remains geometrically close to the dynamometer-based result. The comparison between on-road driving data derived gear strategies compared to dynamo derived gear strategies in the vehicle speed power domain can be found in Figure A.25.

To quantify these differences, both curves were parametrized, enabling the computation of the RMSE between them. The calculated RMSE for Normal drive mode is 13.45 .

Figure 5.22b illustrates the gear change strategy for Sport drive mode. In this mode, the upshift threshold is delayed to higher speeds, with the first vertical line starting at $80\,\mathrm{km\,h^{-1}}$ instead of $75\,\mathrm{km\,h^{-1}}$, a difference that is correctly captured by the on-road data-derived approach. Additionally, the horizontal threshold is shifted toward lower torque values to extend the use of the first gear in sport mode, which is again accurately identified by both dynamometer and on-road tests. Beyond $80\,\mathrm{km\,h^{-1}}$, the threshold rises to the speed limit of $120\,\mathrm{km\,h^{-1}}$, with minimal differences between the two approaches in this region.

The RMSE for Sport mode is 9.96 , and the average RMSE across both modes is 11.70 .

The combined gear domains for Normal and Sport modes are visualized in Figure 5.23. These domains illustrate how the upshift strategies are adjusted to accommodate different driving modes, with sport mode allowing for higher speeds and lower torque thresholds in first gear compared to normal mode to extend the range of operating points where first gear is used, as it allows for higher wheel torque.

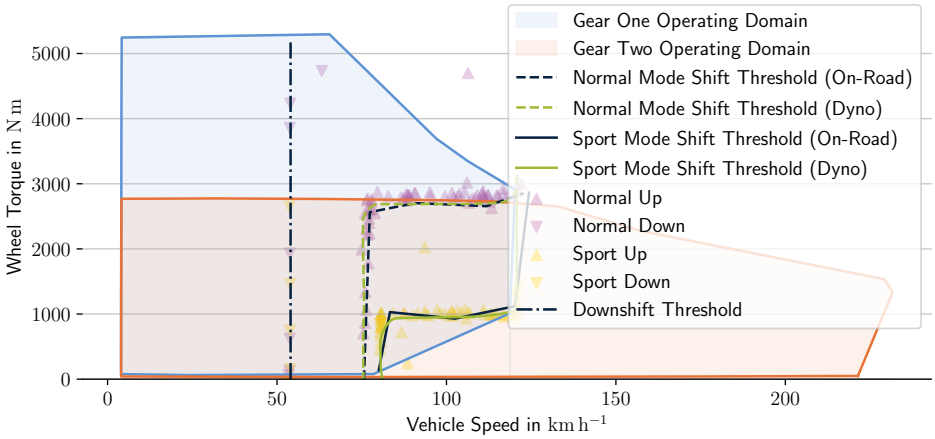

Figure 5.23: Gear Domains for Porsche Taycan in Normal and Sport Drive Modes.

Visual exploration of the data has shown, that the strategy of the vehicle to shift from second to first gear, is mainly dependent from the vehicle velocity and brake pedal activation. If the vehicle decelerates freely, downshifts happen at $54\,\mathrm{km\,h^{-1}}$. Activating the brakepedal can delay the downshift. The $54\,\mathrm{km\,h^{-1}}$ threshold is also visible in some of the individual downshifts visible in Figure 5.23. This behaviour is valid for both Sport and Normal drive modes. Together with the upshift strategies, the downshift strategy forms a hysteretic behaviour, which is typical for automatic transmissions [30].

5.3.1 Discussion of Gear Strategy Estimation

The results demonstrate that the proposed methodology effectively estimates gear change strategies from real driving data, closely matching dynamometer-based results. However, certain limitations and areas for improvement were observed.

As shown in Figures 5.22a and 5.22b, vertical transitions in the gear change threshold are only approximate. This is a known limitation of the spline-based methodology, as perfectly vertical lines would require an infinite slope, which is mathematically infeasible. Consequently, the derived thresholds "cut corners" slightly in regions where a sharp vertical transition is expected. This effect could be mitigated by increasing the density of driving data or using higher-order splines.

The accuracy of the derived gear change thresholds is heavily dependent on the density of driving data. Sparse data near the upper-speed limits of first gear ($120\,\mathrm{km\,h^{-1}}$ to $125\,\mathrm{km\,h^{-1}}$) led to slight deviations

from the expected vertical transitions. This limitation highlights the importance of sufficient data collection in critical regions.

With higher data density, employing higher-order splines or linear splines with more segments may be feasible, enabling a more accurate representation of gear change strategies. This would be particularly beneficial in capturing the sharp transitions at the boundaries of gear domains. However, the effort of collecting more data should probably outweigh the improvement in accuracy that can be achieved by using higher-order splines. Adhering to the outlined goal of reducing the effort and complexity of vehicle parameter estimation, the current methodology strikes a balance between accuracy and practicality.

The methodology effectively captured the differences between Normal and Sport drive modes, accurately identifying the delayed upshift thresholds and extended gear domains in sport mode. This demonstrates the adaptability of the proposed approach to different driving scenarios. The close agreement between on-road and dynamometer-derived strategies underscores the validity of the driving-data-based approach. Despite the inherent challenges of real-world data collection, the methodology reliably estimated gear change thresholds with minimal deviation.

The results suggest that the real-driving-data approach is a viable alternative to labor-intensive dynamometer testing. In addition to being more representative of real-world conditions, this approach offers significant time and cost savings. However, targeted efforts to collect denser data in critical regions, potentially with live feedback to the driver, could further enhance the accuracy and reliability of this methodology.

5.4 Quantification of Parameter Differences by Simulation of Driving Profile

To further validate the proposed methodology, the vehicle parameters derived from Rosenberger et al. [18] and those obtained from on-road driving data were used to parameterize a simulation model. These parameters include the gear shift strategy, efficiency maps, and the RLC models representing drag forces. The simulation model was employed to estimate the energy consumption for a given velocity profile, as described in Section 3.4. Both the gear strategy and the RLCs were adjusted accordingly to simulate different driving modes. Vehicle parameter agnostic energy-consuming factors, such as the auxiliary power consumption like the air conditioning or the road slope, were not considered in this simulation as they would affect both cases equally.

As outlined in the Handbook [61], the Porsche adjusts its suspension setting to the 'low' level in Sport mode. Consequently, the RLCs corresponding to the 'low' suspension setting was utilized for the Sport mode simulation. For the Normal drive mode, the RLCs were selected to reflect the suspension behavior of the vehicle in Normal mode. Additionally, the gear strategy was adapted to match the distinct driving characteristics of each mode.

The simulation results indicate that the cumulative energy consumption across all driving cycles deviates by no more than $6.5\,\%$ between the laboratory-derived and on-road driving data-derived vehicle parameters. Notably, the majority of the percentage deviations are negative for driving cycles with less high-speed driving, signifying that the simulated energy consumption based on driving lab-derived parameters is lower than that estimated using on-road-derived parameters for low-speed driving heavy cycles. Furthermore, in Sport mode, the difference has a generally smaller value, signifying that the simulated energy consumption based on driving lab-derived parameters is generally lower than that estimated using on-road-derived parameters.

Specific time-series data from the simulations are analyzed to better understand these discrepancies. A comparison of the estimated drag forces, efficiency, and gear shift strategy reveals that the gear strategy

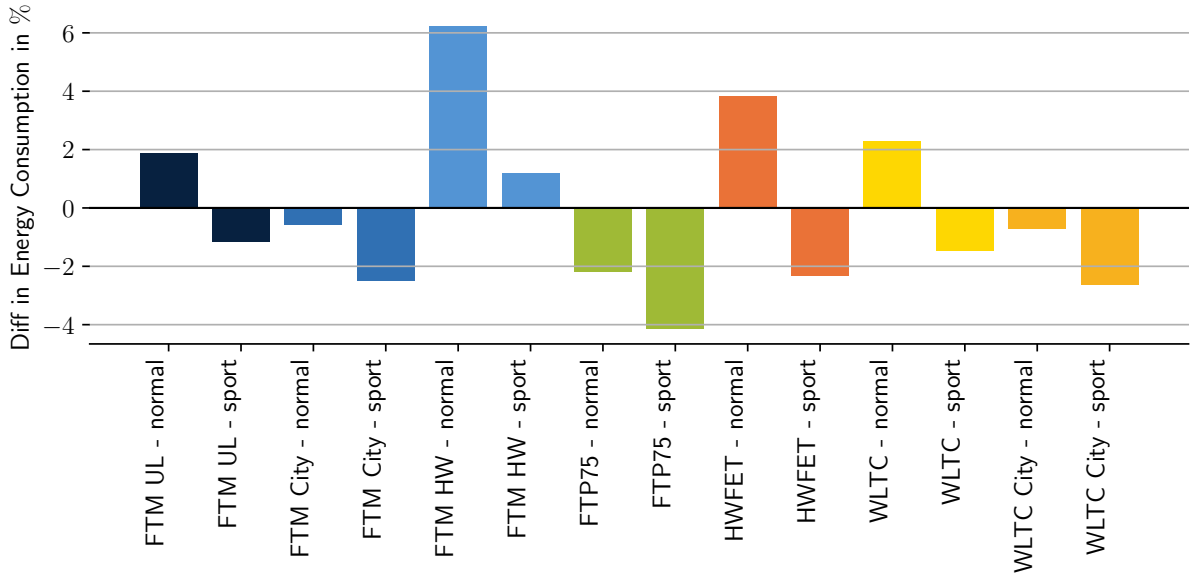

Figure 5.24: Comparison of Simulated Driving Profiles using Laboratory-Derived and On-Road Driving Data-Derived Vehicle Parameters.

exhibits the highest similarity between the two parameter sources. In contrast, efficiency differences are more pronounced than those observed in the gear strategy but remain smaller than the variations in estimated drag forces.

A noteworthy trend is observed in the drag models: On-road driving data-derived parameters predict higher drag at low speeds and lower drag at high speeds than laboratory-derived parameters. This trend is reflected in the simulation results, where only the driving cycles with extended high-speed sections exhibit a positive percentage difference, indicating that the total cumulative energy consumption estimated using the lab-derived parameter model exceeds that of the laboratory parameter model. Specifically, it is the Future Transport Mobility (FTM) highway, the Highway Fuel Economy Test (HWFET), the Worldwide harmonized Light-duty vehicles Test Cycle (WLTC), and the FTMUL, which extend enough into higher speed sections to result in higher energy consumption by the lab-obtained parameter model. This observation aligns with Figure 5.25, which depicts the simulated drag forces for the WLTC in normal drive mode and illustrates that at higher speeds, the on-road driving data-derived drag models predict lower resistance than those based on laboratory parameters. This behavior is additionally visible in the difference in drag force models depicted in Figure 5.15.

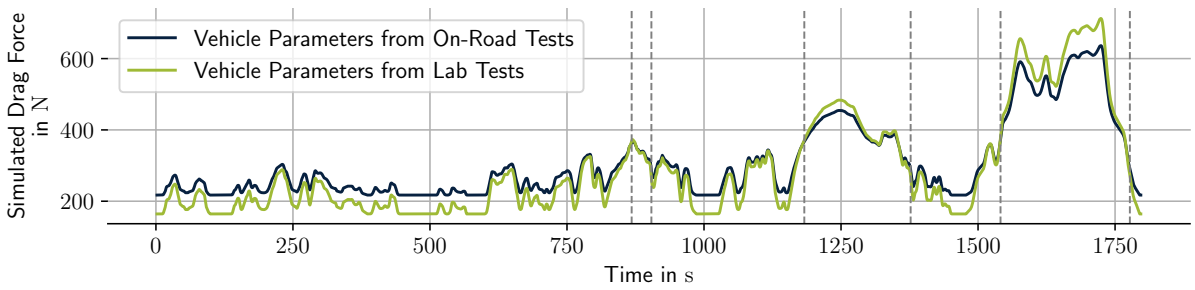

Figure 5.25: Comparison of Driving Resistance for the WLTC Cycle in Normal Mode.

The general trend of Sport mode exhibiting a smaller/more negative percentage difference can also be attributed mainly to the drag models. Since the Sport mode utilizes the 'low' suspension setting, the RLCs governing the drag force models change. The parameters from 'low' differ more significantly at lower speeds,

despite their alignment at higher speeds, compared to the 'normal' parameters. Given that all driving cycles contain low-speed segments of varying durations, this discrepancy further amplifies the observed deviations in energy consumption estimates in Sport mode.

The difference in predicted drivetrain efficiency between the efficiency maps derived from laboratory and on-road driving data is less pronounced than the differences in drag forces. Still, it contributes to the overall discrepancies in energy consumption estimates. Figure 5.26 shows the difference in drivetrain efficiency for the Federal Test Procedure (FTP)75 cycles in Normal mode, read from both efficiency maps. The simulation results confirm the same observations from Section 3.3.2, where the maps match really well in the regions of high efficiency but differ more in the areas of low efficiency, especially in regions of low torque or engine speed. As city driving cycles generally contain more low-speed, low-torque areas, the differences in efficiency maps impose a larger impact on the energy consumption estimates for these cycles, which is evident when observing that the absolute differences of the city version of both the WLTC and the FTM cycle are larger than those of the higher speed versions.

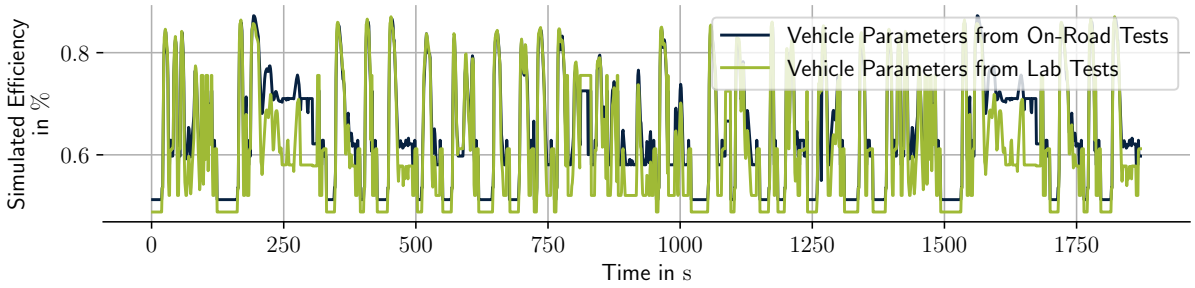

Figure 5.26: Comparison of Drivetrain Efficiency for the FTP75 Cycle in Normal Mode.

The gear shift strategy exhibits the highest similarity between laboratory and on-road driving data-derived parameters and has the least impact on the energy consumption estimates. Even though the gear shift strategy threshold line does not match perfectly, in practice, the vehicle traverses these differences relatively quickly, which is why the impact on total energy consumption is relatively low. Figure 5.27 shows the predicted gear for both the on-road driving data-derived and laboratory-derived shift strategy for the FTMUL cycle in Sport mode. This cycle is chosen as it contains the most gear changes of all simulated cycles. The figure shows that the gear changes are generally well captured by the on-road driving data-derived shift strategy, with only minor deviations in the exact timing of the gear changes. As these timing differences are relatively small, the impact on the total energy consumption is also relatively small.

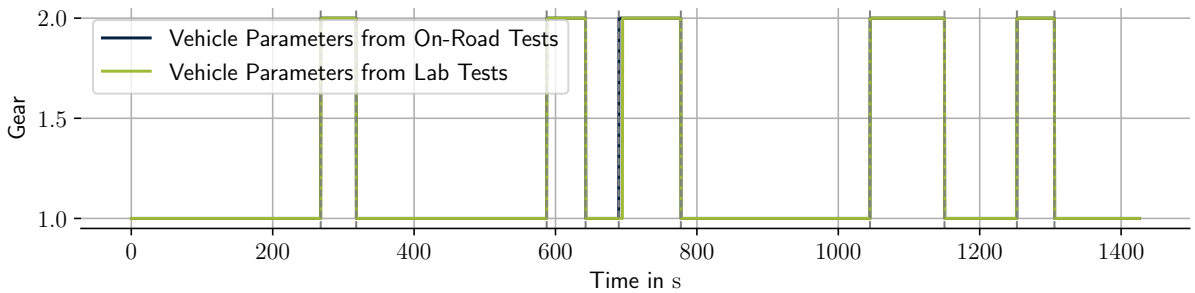

Figure 5.27: Comparison of Gear Shift Strategy for the FTM UL Cycle in Sport Mode.

The presented figures have been selected as examples to illustrate the general trends observed in the simulation results. The complete set of simulation time-series data is provided in Appendix B.

The influence of each parameter on the energy consumption was also quantified by running the simulation with only one parameter varied while the others were kept constant. The detailed results can be found in Appendix B.1. The mean absolute differences between the energy consumption estimates using laboratory-derived and on-road driving data-derived parameters when varying only singular vehicle parameters are given in Table 5.11.

Table 5.11: Average absolute percentage difference in energy consumption for each varied parameter.

Varied Parameter	Avg. Abs. Diff
All	2.36 %
Efficiency Map	1.88 %
Gear Strategy	0.01 %
RLC	3.44 %

The results from the individual parameter variations confirm the observations made in the time-series data analysis. The drag force models have the most significant impact on the energy consumption estimates, followed by the drivetrain efficiency maps. The gear shift strategy has a negligibly small impact, as the differences in the gear shift strategy are relatively small and as the gear change happens momentarily while the other parameters have a continuous impact on the energy consumption.

5.5 Effort Comparison of Laboratory and On-Road Parameter Estimation

The primary objective of the proposed methodology is to reduce the overall effort required for automotive benchmarking by comparing the time investment involved in laboratory-based and on-road parameter estimation. Effort is estimated based on the time required to collect and evaluate data for each parameter estimation method. A key advantage of the new KDD-based end-to-end on-road methodology is its ability to perform near-instantaneous evaluation, thereby reducing the total hours needed for parameter estimation across all three investigated vehicle characteristics.

Table 5.12: Effort Comparison of Laboratory and On-Road Parameter Estimation. Laboratory test durations from [18].

Description	Duration Laboratory Test	Duration On-Road Test
RLC		
Data Collection	15 h	28 h
Evaluation	40 h	<1 h
Total	55 h	29 h
Efficiency Map		
Data Collection	35 h	13 h
Evaluation	20 h	<1 h
Total	55 h	14 h
Gear Strategy		
Data Collection	27 h	2 h
Evaluation	15 h	<1 h
Total	42 h	3 h

Although Table 5.12 provides a direct comparison of laboratory and on-road durations, these numbers should be interpreted with caution. In the case of RLC measurements, for example, the on-road data collection time includes constant-speed method data collection as well as coastdown segment data collection, whereas the laboratory-based approach only covers coastdown measurements. Another important consideration is

that some on-road data was recorded once but used by multiple parameter estimation algorithms, effectively decreasing the total time invested in data collection. Furthermore, the laboratory tests were conducted solely to derive vehicle parameters for the Porsche Taycan, while the on-road tests supported the development of a generalized methodology for vehicle parameter extraction. As a result, more on-road data was gathered than strictly necessary for the Taycan alone in order to fine-tune the algorithms.

Despite these considerations, the time savings of the on-road methodology are already evident. In practice, the data collection process could be further optimized by more targeted measurements, which could further reduce the required on-road testing time. Nevertheless, the results in Table 5.12 clearly demonstrate the potential for substantial reductions in both data collection and evaluation effort by using the on-road approach.

6 Conclusion

This chapter summarizes the methods and results of this study and discusses potential future improvements. The developed framework successfully estimates key vehicle parameters, road load coefficients, drivetrain efficiency maps, and gear strategy using real on-road driving data. The findings highlight the advantages of this approach over traditional laboratory testing and pave the way for further enhancements.

6.1 Summary of Utilized Methods

This work presents a framework for estimating key vehicle parameters, road load coefficients, drivetrain efficiency maps, and gear strategy using real on-road driving data. The methodology incorporates a structured sensitivity analysis to optimize algorithm parameters and minimize estimation errors, ensuring robustness and generalizability. A key advantage of this approach is its reliance on real-world data rather than expensive laboratory tests, making independent vehicle benchmarking more accessible.

6.2 Summary of Results

The developed methods produced results closely matching laboratory measurements, demonstrating their practical viability. The end-to-end KDD approach was successfully implemented, automating the data processing workflow and extracting vehicle parameters from raw driving data without manual intervention. However, it must be noted that the laboratory measurements used for validation do not represent absolute ground truth. Consequently, the RMSEs reported indicate deviations between real-driving-data-based and laboratory-based results rather than the absolute accuracy of the real-driving-data-based estimations.

The RLC estimation algorithms successfully estimated plausible RLCs. The coastdown-based method, applied across all suspension levels of the Porsche Taycan, showed a correlation with laboratory-obtained RLCs, yielding RMSEs of $16.61\,\mathrm{N}$ for the medium suspension level, $34.41\,\mathrm{N}$ for the low suspension level, and $44.36\,\mathrm{N}$ for the very low suspension level. The pitch correction effectively reduced the mean standard deviation from $112.23\,\mathrm{N}$ to $73.86\,\mathrm{N}$. Generalizability was demonstrated by applying the coastdown method to VW ID.3 data, resulting in an RMSE of $26.24\,\mathrm{N}$. The constant-speed method, tested on the Porsche Taycan, produced an RMSE of $52.16\,\mathrm{N}$, a larger deviation than the coastdown method but with the advantage of a simpler data collection process.

The efficiency map estimation algorithms also showed good agreement with laboratory measurements. The RMSE for the efficiency map estimation of the Porsche's first gear is $3.73\,\%$, with a mean absolute difference of $1.96\,\%$. The second gear efficiency map yielded a RMSE of $2.58\,\%$, and a mean absolute difference of $1.64\,\%$. Generalizability was confirmed by applying the estimation method to the VW ID.3, resulting in an RMSE of $1.64\,\%$ and a mean absolute difference of $0.92\,\%$. Across all efficiency maps, near-perfect

agreement was observed in the high torque and speed regions, with deviations occurring primarily near the axes.

The derived gear change strategy also exhibited a high degree of accuracy and strong agreement with laboratory results. The simulation of driving cycles, which integrates all three algorithms, showed good alignment with laboratory measurements, with a mean absolute deviation in estimated cumulative energy consumption of $2.35\,\%$ over seven different simulated driving cycles in both Normal and Sport drive modes. This validates the overall framework. The simulation further revealed that the influence of gear strategy on energy consumption was minimal, whereas differences in efficiency maps contributed more significantly, particularly in low-speed and urban cycles, where the vehicle frequently operates at the efficiency map's boundaries, leading to the largest deviations. The RLC estimation exhibited the greatest influence on overall simulation results.

A key advantage of this framework is its ability to reduce testing effort and improve efficiency by repurposing data for multiple estimation tasks. This was demonstrated by reducing the time required to derive parameters from weeks for comprehensive laboratory tests, to days for on-road methods, eliminating the need for expensive measurement equipment, closed test tracks, or rolling dynamometers. Data reusability was also confirmed: the same driving data used for gear strategy estimation contributed to drivetrain efficiency mapping, and coastdown test data was repurposed for other estimation algorithms. Additionally, the constant-speed method provides an alternative to the coastdown method, enabling the derivation of road load coefficients from cruise-controlled driving data, thereby allowing data collection as a byproduct of routine vehicle operation. These findings emphasize the efficiency and cost-effectiveness of the proposed approach, especially for real-world applications where access to laboratory facilities is limited.

6.3 Future Work

While this study demonstrates the feasibility and reduced effort of real-driving-data-based parameter estimation, several areas for improvement remain.

Since BEVs utilize regenerative braking, future work should integrate recuperation effects into the efficiency map estimation. This would provide a more comprehensive understanding of vehicle energy consumption. Recuperation was excluded from this study due to the lack of laboratory data for the negative torque region. However, as the recorded driving data already includes recuperation events, this extension should be straightforward, requiring only a method for validating the negative torque region.

For efficiency maps, the highest deviations between real-driving-data-based and laboratory-based results occurred in regions with high isoline density. Future research should focus on improving accuracy in these areas, both for dynamometer and real-driving-data-based methods, to strengthen validation of the proposed approach.

Incorporating IMU measurements, particularly vehicle inclination, improved measurement quality by directly addressing a major confounding factor in RLC estimation. However, the IMU sensor used in this study exhibited inconsistent behavior, occasionally producing unusable data. Additionally, the separate setup required for the IMU sensor increased data collection complexity, counteracting the goal of reducing effort. Future work should explore alternative methods for road inclination estimation, such as using GPS-based altitude measurements, as proposed by Komnos et al. [31]. Leveraging the vehicle's internal GPS sensor could eliminate the need for additional hardware and simplify data collection.

To further streamline on-road benchmarking, an online implementation of this framework could be developed. A real-time capable version of the proposed algorithms could process data as it is collected, providing

continuously updated vehicle parameter estimations with uncertainty quantification. This could also include a driver guidance system to enhance data quality, suggesting optimal torque and speed combinations, and maneuvers for improved efficiency map coverage or recommending cruise-control activation at specific speeds to enhance RLC estimation. This guided approach could further reduce benchmarking effort.

Finally, the framework's generalizability should be further evaluated by applying it to additional vehicle models and powertrains. This would provide insights into the adaptability of the algorithms to different vehicle architectures and help identify potential limitations. The framework's modularity facilitates easy integration of new vehicle models, making it well-suited for comparative studies.

List of Figures

List of Tables

Bibliography

[1] European Court of Auditions, „The EU's Response to the "Dieselgate" Scandal," 2019.

[2] M. Budinski. „*Why Simulation Is the Cornerstone of Autonomous Vehicle Development*," https://htec.com/6-reasons-why-you-should-use-simulation-in-autonomous-vehicle-software-development/. 2024. [Visited on 10/21/2024].

[3] N. Rosenberger, P. Rosner, P. Bilfinger, J. Schöberl, O. Teichert, et al., „Quantifying the State of the Art of Electric Powertrains in Battery Electric Vehicles: Comprehensive Analysis of the Tesla Model 3 on the Vehicle Level," *World Electric Vehicle Journal*, vol. 15, no. 6, p. 268, 2024, DOI: 10.3390/wevj15060268. [Visited on 09/05/2024].

[4] H. Tschöke, *Elektrifizierung des Antriebsstrangs: Grundlagen - vom Mikro-Hybrid zum vollelektrischen Antrieb*, Berlin, Heidelberg, Springer Berlin Heidelberg, 2019, ISBN: 978-3-662-60355-0 978-3-662-60356-7. DOI: 10.1007/978-3-662-60356-7. [Visited on 09/29/2024].

[5] L. Guzzella and A. Sciarretta, *Vehicle Propulsion Systems: Introduction to Modeling and Optimization*, Berlin, Heidelberg, Springer Berlin Heidelberg, 2013, ISBN: 978-3-642-35912-5 978-3-642-35913-2. DOI: 10.1007/978-3-642-35913-2. [Visited on 10/23/2024].

[6] A. Kampker, *Elektromobilität: Grundlagen einer Fortschrittstechnologie*, Berlin, Heidelberg, Springer Berlin Heidelberg, 2024, ISBN: 978-3-662-65811-6 978-3-662-65812-3. DOI: 10.1007/978-3-662-65812-3. [Visited on 02/05/2025].

[7] M. Trzesniowski, *Antrieb*, Wiesbaden, Springer Fachmedien Wiesbaden, 2019, ISBN: 978-3-658-26697-4 978-3-658-26698-1. DOI: 10.1007/978-3-658-26698-1. [Visited on 02/05/2025].

[8] M. Doppelbauer, *Grundlagen der Elektromobilität: Technik, Praxis, Energie und Umwelt*. vol. Doppelbauer, Wiesbaden, Springer Fachmedien Wiesbaden, 2020, ISBN: 978-3-658-29729-9 978-3-658-29730-5. DOI: 10.1007/978-3-658-29730-5. [Visited on 09/29/2024].

[9] H.-H. Braess, *Vieweg Handbuch Kraftfahrzeugtechnik*, Wiesbaden, Springer Fachmedien Wiesbaden, 2013, ISBN: 978-3-658-01690-6 978-3-658-01691-3. DOI: 10.1007/978-3-658-01691-3. [Visited on 02/06/2025].

[10] H. Wallentowitz and A. Freialdenhoven, *Strategien zur Elektrifizierung des Antriebsstranges*, Wiesbaden, Vieweg+Teubner Verlag, 2011, ISBN: 978-3-8348-1412-8 978-3-8348-9910-1. DOI: 10.1007/978-3-8348-9910-1. [Visited on 10/21/2024].

[11] M. Mitschke and H. Wallentowitz, *Dynamik der Kraftfahrzeuge*, Wiesbaden, Springer Fachmedien Wiesbaden, 2014, ISBN: 978-3-658-05067-2 978-3-658-05068-9. DOI: 10.1007/978-3-658-05068-9. [Visited on 10/21/2024].

[12] T. Schütz, *Fahrzeugaerodynamik: Basiswissen für das Studium*, Wiesbaden, Springer Fachmedien Wiesbaden, 2016, ISBN: 978-3-658-12817-3 978-3-658-12818-0. DOI: 10.1007/978-3-658-12818-0. [Visited on 10/21/2024].

[13] U. Nations. „*Worldwide Harmonized Light Vehicles Test Procedure*," 2014.

[14] A. L. GmbH. „*Global Vehicle Benchmarking and Technology Scouting*,“ https://www.avl.com/en/engineering/vehicle-engineering/vehicle-development/global-vehicle-benchmarking-and-technology-scouting. 2025. [Visited on 07/02/2025].

[15] L. Nicoletti, S. Mayer, M. Brönner, F. Schockenhoff and M. Lienkamp, „Design Parameters for the Early Development Phase of Battery Electric Vehicles,“ *World Electric Vehicle Journal*, vol. 11, no. 3, p. 47, 2020, DOI: 10.3390/wevj11030047. [Visited on 02/07/2025].

[16] E. Roshandel, A. Mahmoudi, S. Kahourzade and W. L. Soong, „Efficiency Maps of Electrical Machines: A Tutorial Review,“ *IEEE Transactions on Industry Applications*, vol. 59, no. 2, pp. 1263–1272, 2023, DOI: 10.1109/TIA.2022.3210077. [Visited on 02/07/2025].

[17] D. Goßlau. „“Fahrzeugmesstechnik”,“ in: *Fahrzeugmesstechnik*. Wiesbaden: Springer Fachmedien Wiesbaden, 2020, pp. 217–235. ISBN: 978-3-658-28478-7 978-3-658-28479-4. DOI: 10.1007/978-3-658-28479-4_17. [Visited on 02/07/2025].

[18] N. Rosenberger and M. Lienkamp, „Quantifying the State of the Art of Electric Powertrains in Battery Electric Vehicles: Comprehensive Analysis of the 800 V and Two-Speed Transmission Technology of the Porsche Taycan,“ 2025.

[19] R. Ahlawat. „*Estimation of Road Load Parameters via On-road Vehicle Testing*,“ Cologne, 2013.

[20] N. E. Ligterink, „Correction Algorithms for WLTP Chassis Dynamometer and Coast-down Testing,“ TNO, 2014.

[21] C. R. (EU), „Commission Regulation (EU) 2017/1151 of 1 June 2017 Supplementing Regulation (EC) No 715/2007 of the European Parliament and of the Council on Type-Approval of Motor Vehicles with Respect to Emissions from Light Passenger and Commercial Vehicles (Euro 5 and Euro 6) and on Access to Vehicle Repair and Maintenance Information, Amending Directive 2007/46/EC of the European Parliament and of the Council, Commission Regulation (EC) No 692/2008 and Commission Regulation (EU) No 1230/2012 and Repealing Commission Regulation (EC) No 692/2008 (Text with EEA Relevance),“ 2017.

[22] H. Ferreira, C. M. Rodrigues and C. Pinho, „Impact of Road Geometry on Vehicle Energy Consumption and CO2 Emissions: An Energy-Efficiency Rating Methodology,“ *Energies*, vol. 13, no. 1, p. 119, 2019, DOI: 10.3390/en13010119.

[23] A. Rajagopalan and G. Washington, „Intelligent Control of Hybrid Electric Vehicles Using GPS Information,“ in *Future Car Congress*, 2002, pp. 2002–01–1936, DOI: 10.4271/2002-01-1936.

[24] A. Ferrara and M. E. Regolin, „Vehicle Dynamics Control in MAGV: Forces Estimation and Motion Planning Methods,“ 2019.

[25] A. Falai, „Data Driven Techniques for On-board Performance Estimation and Prediction in Vehicular Applications,“ 2023.

[26] R. Karlsson, U. Hammarström, H. Sörensen and O. Eriksson, „Road Surface Influence on Rolling Resistance,“ 2011.

[27] A. Swift, „Calculation of Vehicle Aerodynamic Drag Coefficients from Velocity Fitting of Coastdown Data,“ *Journal of Wind Engineering and Industrial Aerodynamics*, vol. 37, no. 2, pp. 167–185, 1991, DOI: 10.1016/0167-6105(91)90071-4. [Visited on 01/23/2025].

[28] J. Feng, D. Qin, Y. Liu, D. Sun and Z. Guo, „Data-Driven Cloud-Based Intelligent Gear-Shift Decision Strategy of Vehicle Considering Driving Behavior and Environment,“ *Journal of Cleaner Production*, vol. 429, p. 139558, 2023, DOI: 10.1016/j.jclepro.2023.139558. [Visited on 10/23/2024].

[29] L. Wang, X. Xu, Q. Su, Y. Song, H. Wang, et al., „Automatic Gear Shift Strategy for Manual Transmission of Mine Truck Based on Bi-LSTM Network,“ *Expert Systems with Applications*, vol. 209, p. 118197, 2022, DOI: 10.1016/j.eswa.2022.118197. [Visited on 10/23/2024].

[30] D. D. Ngo. „*Gear Shift Strategies for Automotive Transmissions*,“ 2012. DOI: 10.6100/IR735458. [Visited on 10/14/2024].

[31] D. Komnos, S. Broekaert, N. Zacharof, L. Ntziachristos and G. Fontaras, „A Method for Quantifying the Resistances of Light and Heavy-Duty Vehicles under in-Use Conditions,“ *Energy Conversion and Management*, vol. 299, p. 117810, 2024, DOI: 10.1016/j.enconman.2023.117810. [Visited on 10/10/2024].

[32] C. Dépature, W. Lhomme, A. Bouscayrol, L. Boulon, P. Sicard, et al., „Characterisation of the Electric Drive of EV: On-road versus Off-road Method,“ *IET Electrical Systems in Transportation*, vol. 7, no. 3, pp. 215–222, 2017, DOI: 10.1049/iet-est.2016.0060. [Visited on 09/05/2024].

[33] C. Depature, W. Lhomme, A. Bouscayrol, P. Sicard and L. Boulon, „Efficiency Map of the Traction System of an Electric Vehicle from an On-Road Test Drive,“ in *2014 IEEE Vehicle Power and Propulsion Conference (VPPC)*, 2014, pp. 1–6, ISBN: 978-1-4799-6783-4. DOI: 10.1109/VPPC.2014.7007056. [Visited on 10/10/2024].

[34] R. Delbridge, J. Lowe and N. Oliver, „The Process of Benchmarking: A Study from the Automotive Industry,“ *International Journal of Operations & Production Management*, vol. 15, no. 4, pp. 50–62, 1995, DOI: 10.1108/01443579510083604. [Visited on 10/09/2024].

[35] N. Wassiliadis, M. Steinsträter, M. Schreiber, P. Rosner, L. Nicoletti, et al., „Quantifying the State of the Art of Electric Powertrains in Battery Electric Vehicles: Range, Efficiency, and Lifetime from Component to System Level of the Volkswagen ID.3,“ *eTransportation*, vol. 12, p. 100167, 2022, DOI: 10.1016/j.etran.2022.100167. [Visited on 10/09/2024].

[36] B. Šarkan, T. Skrúcaný, Š. Semanová, R. Madleňák, A. Kuranc, et al., „VEHICLE COAST-DOWN METHOD AS A TOOL FOR CALCULATING TOTAL RESISTANCE FOR THE PURPOSES OF TYPE-APPROVAL FUEL CONSUMPTION,“ *Scientific Journal of Silesian University of Technology. Series Transport*, vol. 98, pp. 161–172, 2018, DOI: 10.20858/sjsutst.2018.98.15. [Visited on 09/05/2024].

[37] G. Oh, D. J. Leblanc and H. Peng, „Vehicle Energy Dataset (VED), A Large-Scale Dataset for Vehicle Energy Consumption Research,“ *IEEE Transactions on Intelligent Transportation Systems*, vol. 23, no. 4, pp. 3302–3312, 2022, DOI: 10.1109/TITS.2020.3035596. [Visited on 09/05/2024].

[38] O. Mısır and M. Akar, „Efficiency and Core Loss Map Estimation with Machine Learning Based Multivariate Polynomial Regression Model,“ *Mathematics*, vol. 10, no. 19, p. 3691, 2022, DOI: 10.3390/math10193691. [Visited on 09/05/2024].

[39] J. Kropiwnicki and T. Gawłas, „Evaluation of the Energy Efficiency of Electric Vehicle Drivetrains under Urban Operating Conditions,“ *Combustion Engines*, 2023, DOI: 10.19206/CE-169492. [Visited on 09/05/2024].

[40] Y. Singh, A. Jayakumar and G. Rizzoni, „Data-Driven Estimation of Coastdown Road Load,“ in *WCX SAE World Congress Experience*, 2024, pp. 2024–01–2276, DOI: 10.4271/2024-01-2276. [Visited on 09/05/2024].

[41] M. Batra, J. McPhee and N. L. Azad, „Parameter Identification for a Longitudinal Dynamics Model Based on Road Tests of an Electric Vehicle,“ in *Volume 3: 18th International Conference on Advanced Vehicle Technologies; 13th International Conference on Design Education; 9th Frontiers in Biomedical Devices*, 2016, V003T01A026, ISBN: 978-0-7918-5013-8. DOI: 10.1115/DETC2016-59732. [Visited on 09/05/2024].

[42] U. Fayyad, G. Piatetsky-Shapiro and P. Smyth, „From Data Mining to Knowledge Discovery in Databases,“ 1996.

[43] O. Maimon and L. Rokach, „Introduction to Knowledge Discovery in Databases,“ in *Data Mining and Knowledge Discovery Handbook*, O. Maimon and L. Rokach, ed. New York: Springer-Verlag, 2005, pp. 1–17, ISBN: 978-0-387-24435-8. DOI: 10.1007/0-387-25465-X_1. [Visited on 11/19/2023].

[44] A. Alami and F. Belmajdoub, „Noise Reduction Techniques in Adas Sensor Data Management: Methods and Comparative Analysis,“ *International Journal of Advanced Computer Science and Applications*, vol. 15, no. 8, 2024, DOI: 10.14569/IJACSA.2024.0150868. [Visited on 02/03/2025].

[45] Abraham. Savitzky and M. J. E. Golay, „Smoothing and Differentiation of Data by Simplified Least Squares Procedures.“ *Analytical Chemistry*, vol. 36, no. 8, pp. 1627–1639, 1964, DOI: 10.1021/ac60214a047. [Visited on 01/20/2025].

[46] R. Schafer, „What Is a Savitzky-Golay Filter? [Lecture Notes],“ *IEEE Signal Processing Magazine*, vol. 28, no. 4, pp. 111–117, 2011, DOI: 10.1109/MSP.2011.941097. [Visited on 02/03/2025].

[47] D. Shepard, „A Two-Dimensional Interpolation Function for Irregularly-Spaced Data,“ in *Proceedings of the 1968 23rd ACM National Conference On* -, 1968, pp. 517–524, DOI: 10.1145/800186.810616. [Visited on 02/05/2025].

[48] R. C. Gonzalez and R. E. Woods, *Digital Image Processing*, Fourth edition, global edition, New York, Pearson, 2017, ISBN: 978-0-13-335672-4 978-1-292-22307-0 978-1-292-22304-9.

[49] T. M. Mitchell, *Machine Learning*, (McGraw-Hill Series in Computer Science), Nachdr., New York, McGraw-Hill, 1997, ISBN: 978-0-07-042807-2 978-0-07-115467-3.

[50] C. M. Bishop, *Pattern Recognition and Machine Learning*, (Information Science and Statistics), New York, Springer, 2006, ISBN: 978-0-387-31073-2.

[51] L. Breiman, „Random Forests,“ *Machine Learning*, vol. 45, no. 1, pp. 5–32, 2001, DOI: 10.1023/A:1010933404324. [Visited on 04/30/2024].

[52] J Macqueen, „Some Methods for Classification and Analysis of Multivariate Observations,“ 1967.

[53] M. Ester, H.-P. Kriegel and X. Xu, „A Density-Based Algorithm for Discovering Clusters in Large Spatial Databases with Noise,“ 1996.

[54] A. Ram, A. Sharma, A. S. Jalal, A. Agrawal and R. Singh, „An Enhanced Density Based Spatial Clustering of Applications with Noise,“ in *2009 IEEE International Advance Computing Conference*, 2009, pp. 1475–1478, ISBN: 978-1-4244-2927-1. DOI: 10.1109/IADCC.2009.4809235. [Visited on 02/04/2025].

[55] D. C. Montgomery, *Design and Analysis of Experiments*, Ninth edition, Hoboken, NJ, John Wiley & Sons, Inc, 2017, ISBN: 978-1-119-11347-8 978-1-119-29936-3 978-1-119-32093-7.

[56] J. Bergstra, J. Bergstra, Y. Bengio and Y. Bengio, „Random Search for Hyper-Parameter Optimization,“ 2012.

[57] A. Saltelli, *Global Sensitivity Analysis: The Primer*, Chichester, England Hoboken, NJ, John Wiley, 2008, ISBN: 978-0-470-05997-5 978-0-470-72518-4 978-0-470-72517-7. DOI: 10.1002/9780470725184.

[58] L. Ståhle and S. Wold, „Analysis of Variance (ANOVA),“ *Chemometrics and Intelligent Laboratory Systems*, vol. 6, no. 4, pp. 259–272, 1989, DOI: 10.1016/0169-7439(89)80095-4. [Visited on 02/05/2025].

[59] I. Goodfellow, Y. Bengio and A. Courville, *Deep Learning*, (Adaptive Computation and Machine Learning), Cambridge, Mass, The MIT press, 2016, ISBN: 978-0-262-03561-3.

[60] P. Probst, A.-L. Boulesteix and B. Bischl, „Tunability: Importance of Hyperparameters of Machine Learning Algorithms,“ 2019.

[61] Porsche AG, „Taycan Handbuch,“ 2020.

[62] Porsche AG. „*The Powertrain: Pure Performance*,“ Apr. 2019. [Visited on 10/03/2024].

[63] Porsche AG. „*The Technology behind the New Porsche Taycan*,“ 2020. [Visited on 10/25/2024].

[64] F. Küçükay, *Grundlagen der Fahrzeugtechnik: Antriebe, Getriebe, Energieverbrauch, Bremsen, Fahrdynamik, Fahrkomfort*, Wiesbaden, Springer Fachmedien Wiesbaden, 2022, ISBN: 978-3-658-36726-8 978-3-658-36727-5. DOI: 10.1007/978-3-658-36727-5. [Visited on 12/10/2024].

[65] A. Konzept, B. Reick, A. Kaufmann, R. Hermanutz and R. Stetter, „Battery Electric Vehicle Efficiency Test for Various Velocities,“ *Vehicles*, vol. 4, no. 1, pp. 60–73, 2022, DOI: 10.3390/vehicles4010004. [Visited on 12/16/2024].

[66] Porsche AG. „*Certificate of Conformity*,“ 2022.

[67] United States Environmental Protection Agency. „*Data on Cars Used for Testing Fuel Economy: 2022 Test Car List Data*,“ 2022.

Appendix

A Pipeline Insights

A.1 Efficiency Map Estimation

A.1.1 Porsche Taycan Gear One

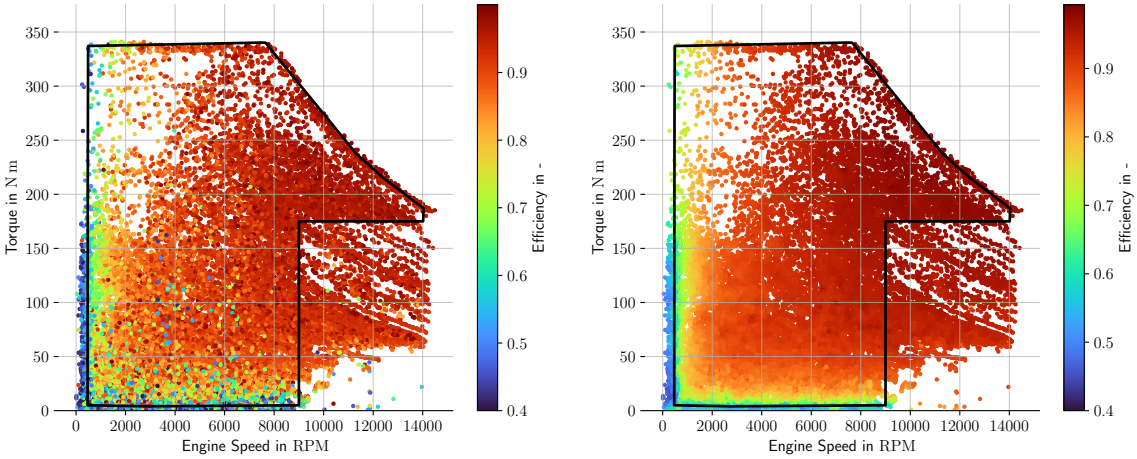

(a) Preprocessed Individual Datapoints for Gear One

(b) Smoothed Individual Datapoints for Gear One

Figure A.1: Efficiency Map Individual Datapoints for Gear One

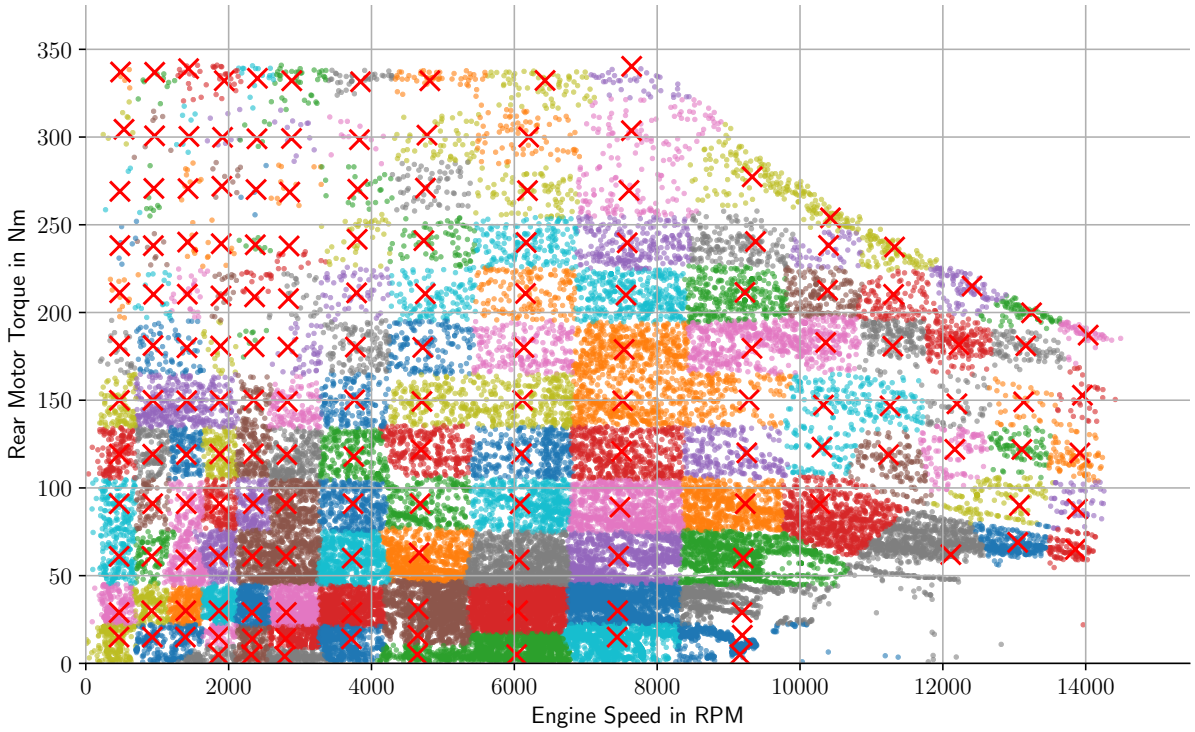

Figure A.2: Efficiency Map Difference Calculation Cluster Assignment for Gear One

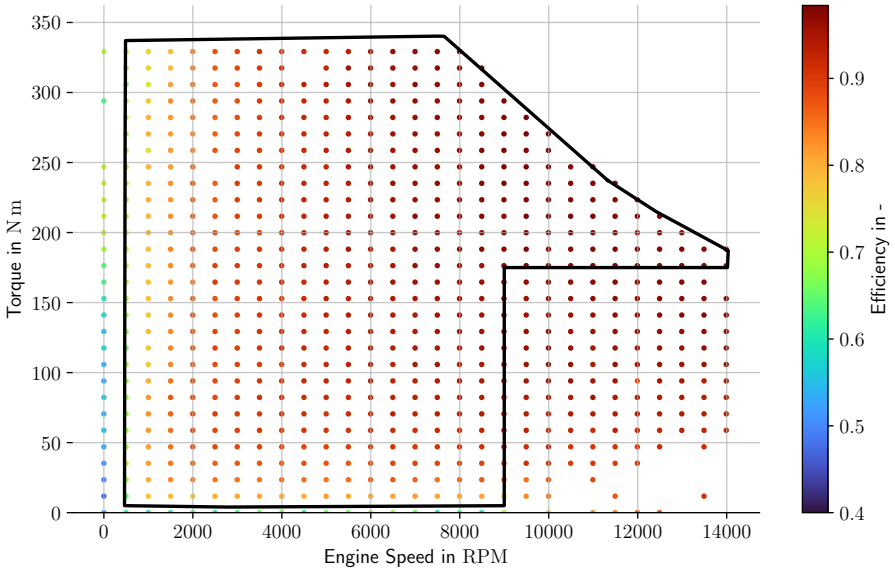

Figure A.3: Efficiency Map Quantized Datapoints for Gear One

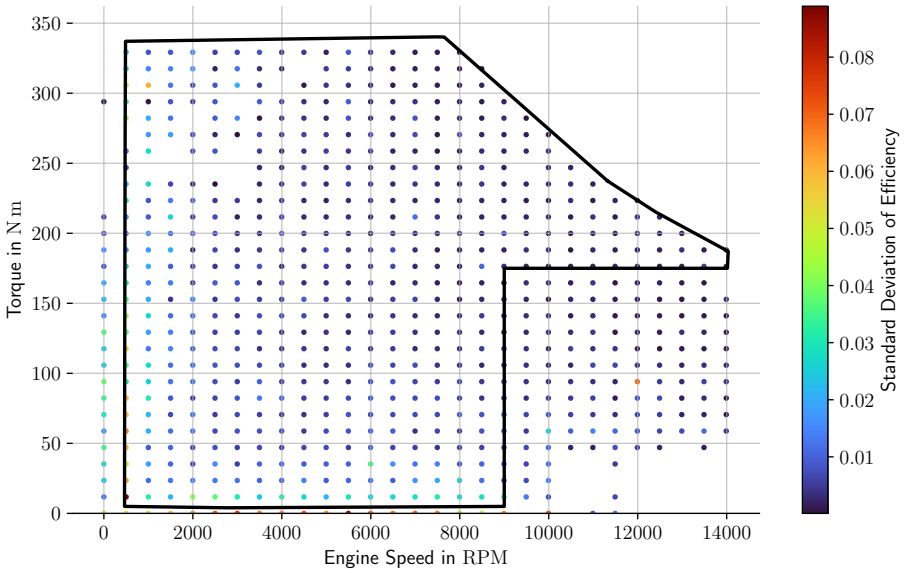

Figure A.4: Efficiency Map Quantized Datapoints Standard Deviation for Gear One

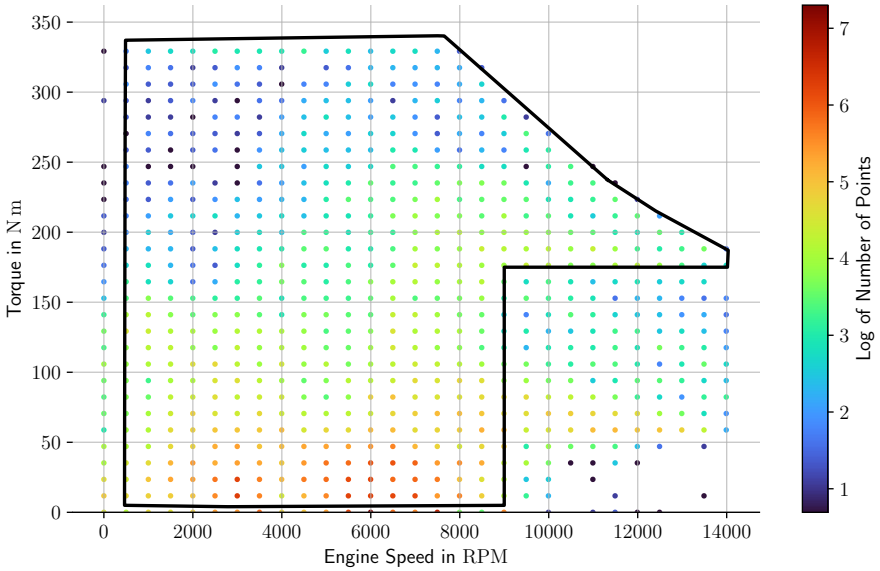

Figure A.5: Efficiency Map Quantized Datapoints Number of Points for Gear One

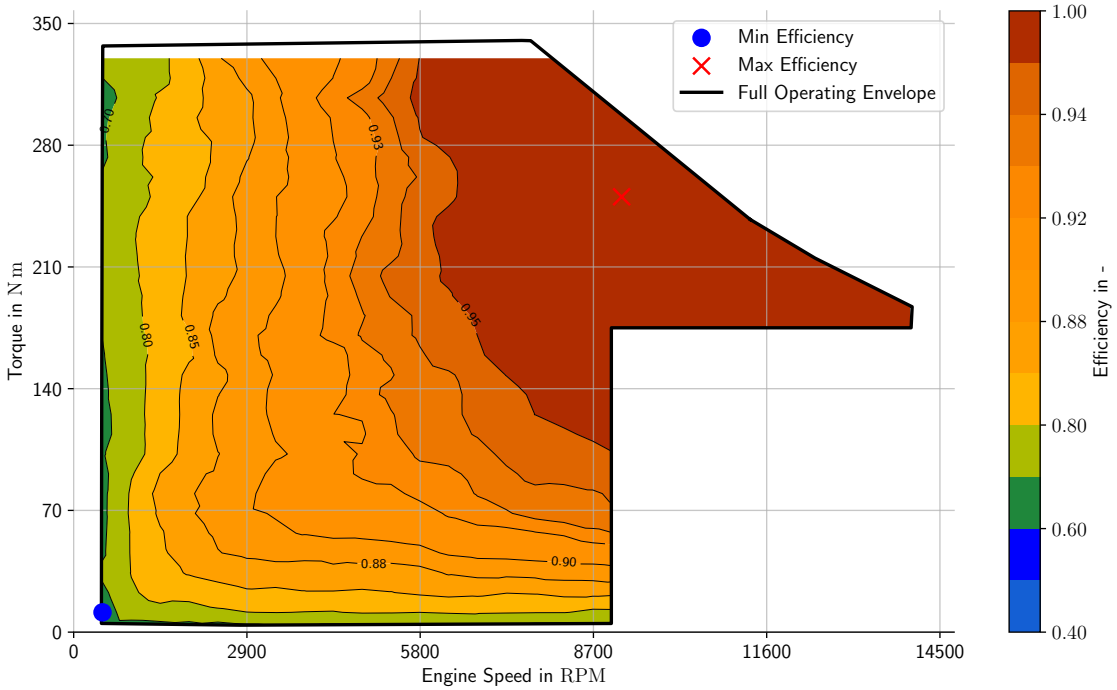

Figure A.6: Efficiency Map Interpolated High Fidelity Contourplot for Gear One

A.1.2 Porsche Taycan Gear Two

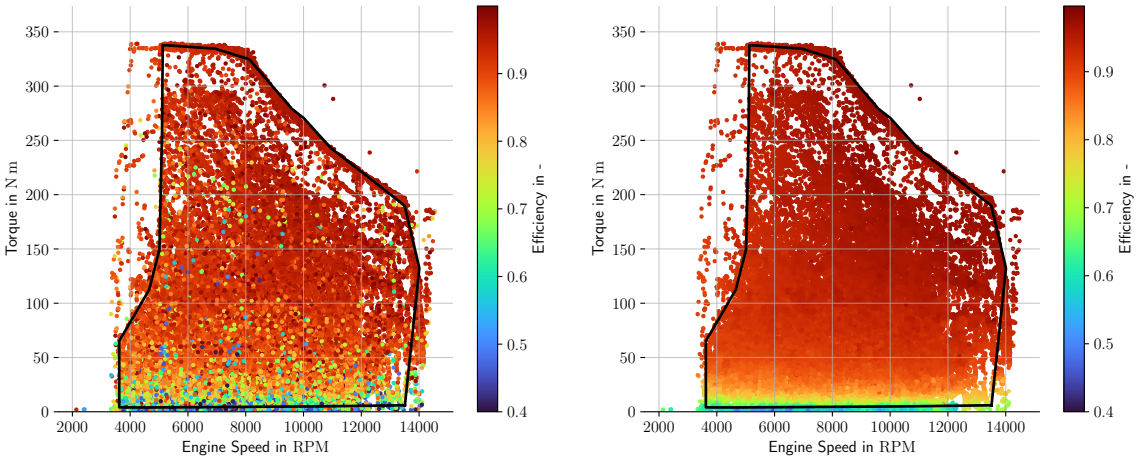

(a) Preprocessed Individual Datapoints for Gear Two

(b) Smoothed Individual Datapoints for Gear Two

Figure A.7: Efficiency Map Individual Datapoints for Gear Two

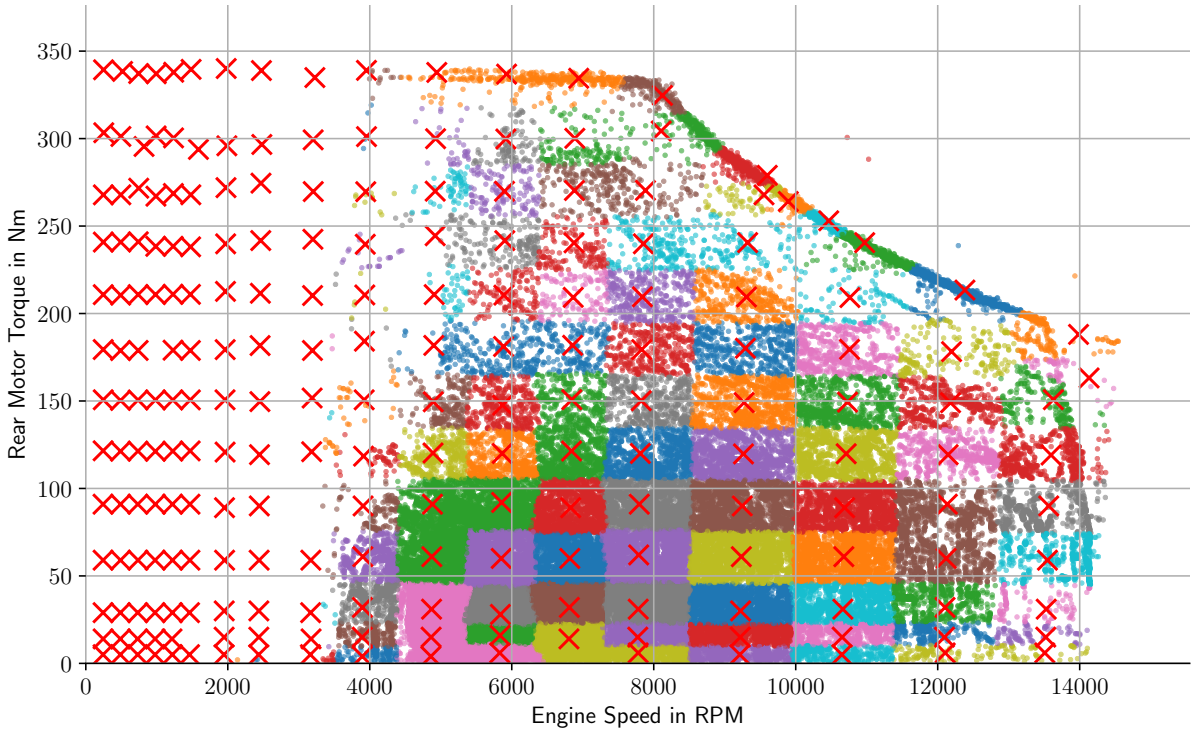

Figure A.8: Efficiency Map Difference Calculation Cluster Assignment for Gear Two

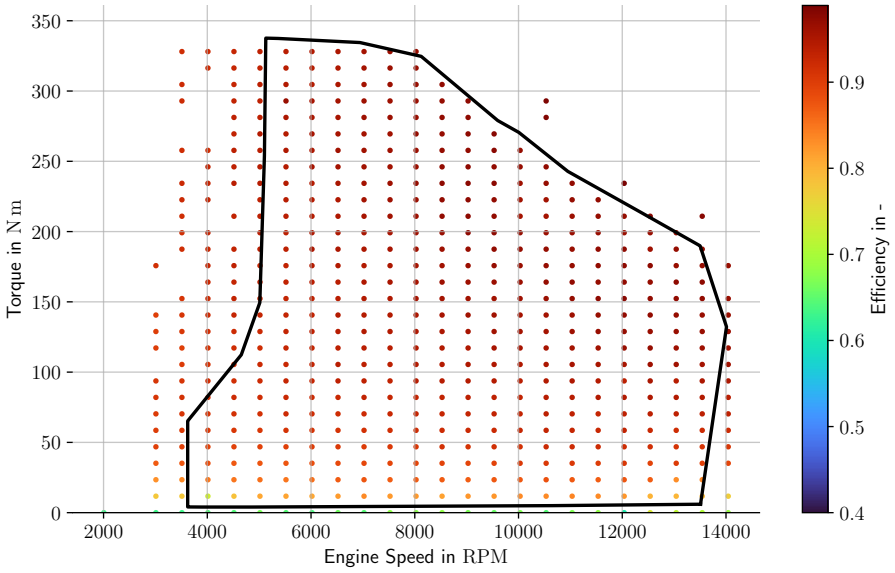

Figure A.9: Efficiency Map Quantized Datapoints for Gear Two

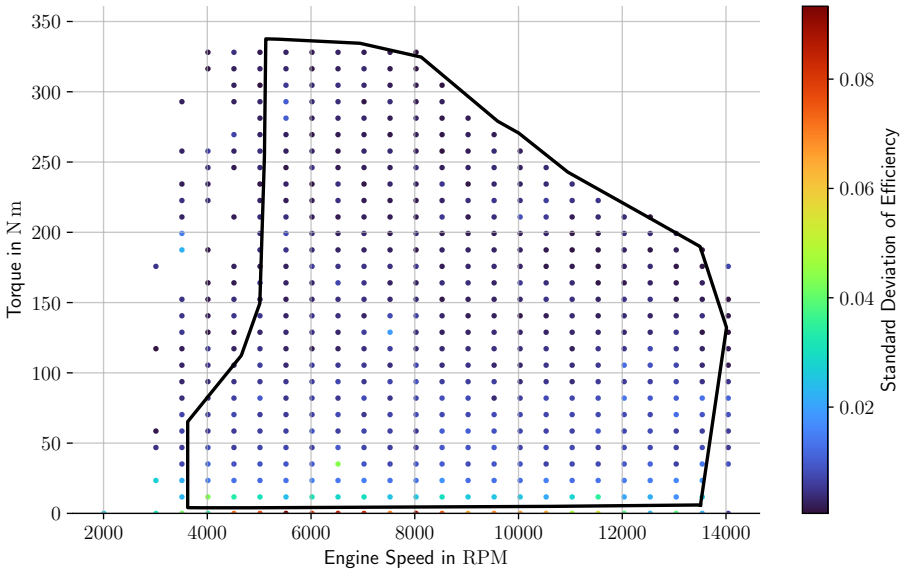

Figure A.10: Efficiency Map Quantized Datapoints Standard Deviation for Gear Two

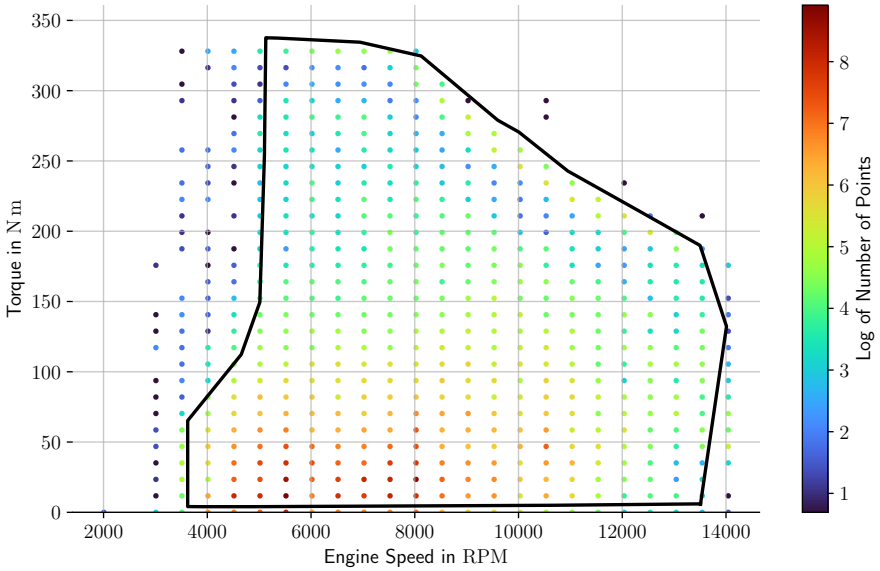

Figure A.11: Efficiency Map Quantized Datapoints Number of Points for Gear Two

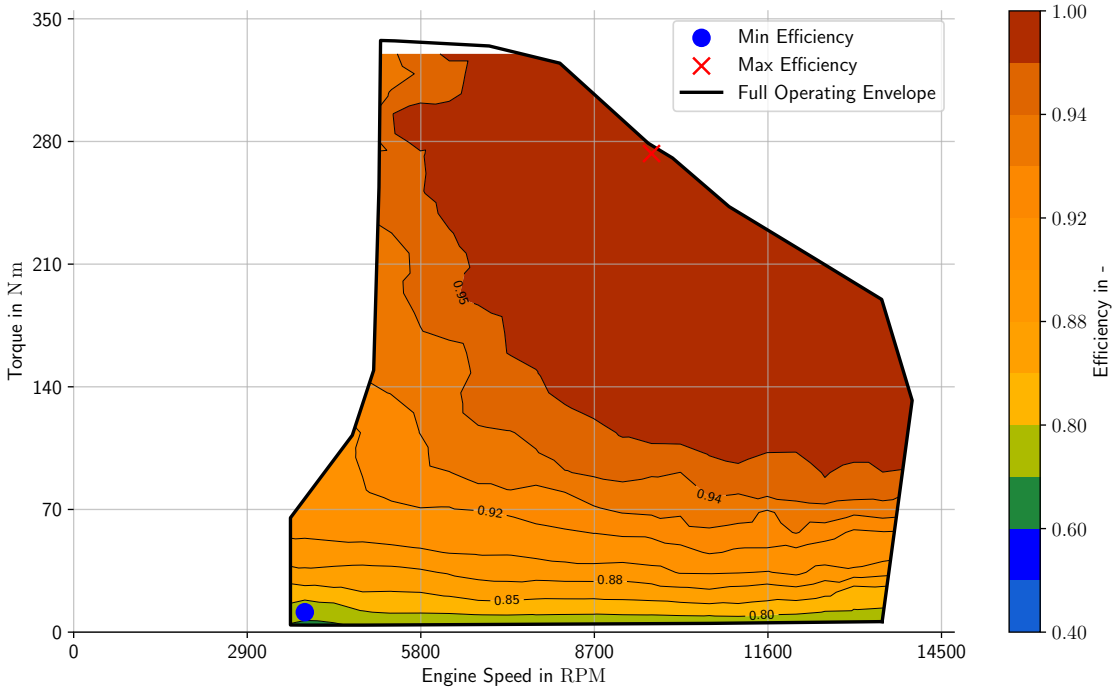

Figure A.12: Efficiency Map Interpolated High Fidelity Contourplot for Gear Two

A.1.3 VW ID.3

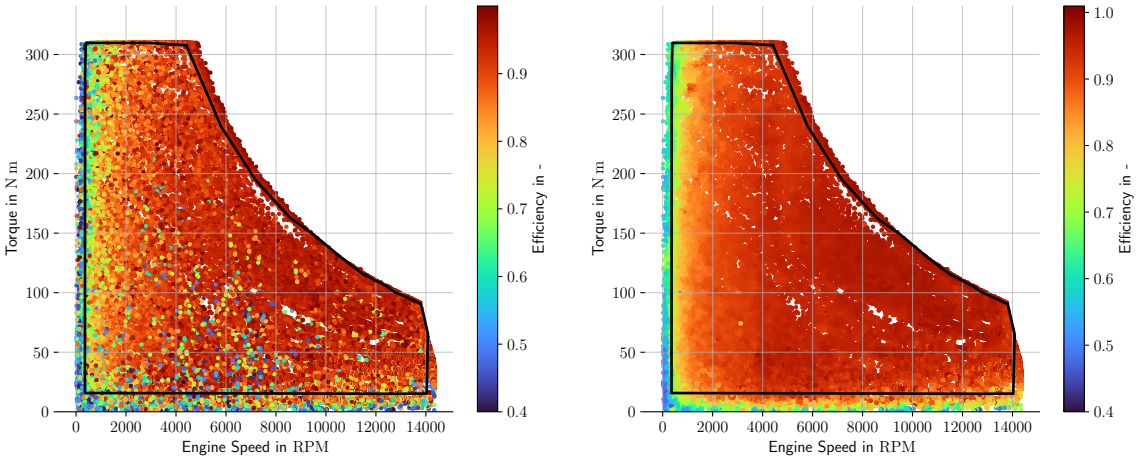

(a) Preprocessed Individual Datapoints for VW ID.3

(b) Smoothed Individual Datapoints for VW ID.3

Figure A.13: Efficiency Map Individual Datapoints for VW ID.3

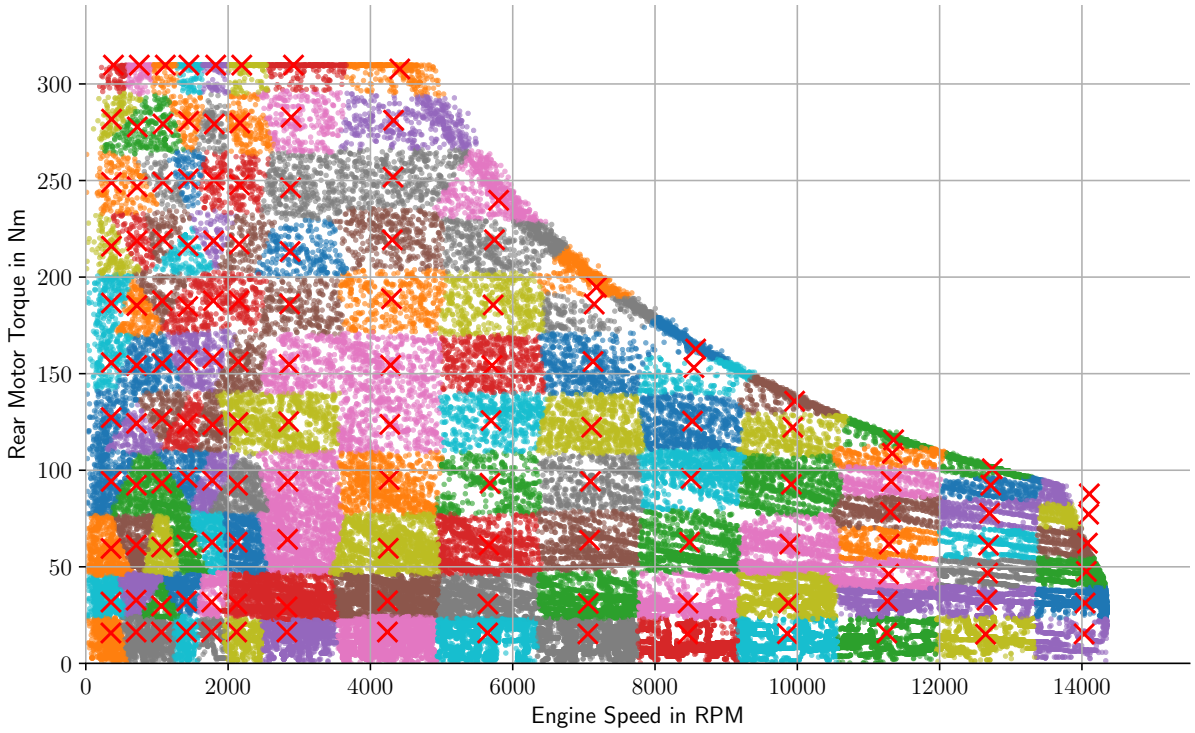

Figure A.14: Efficiency Map Difference Calculation Cluster Assignment for VW ID.3

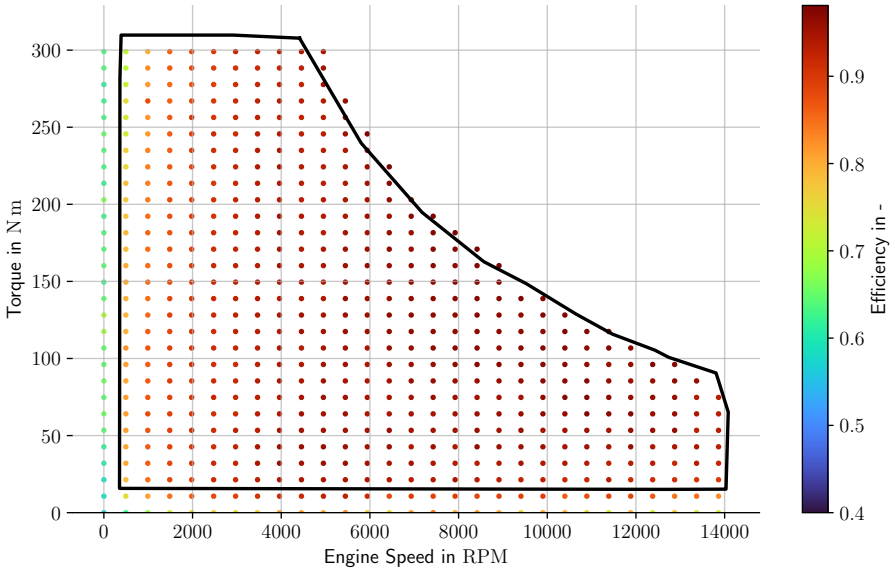

Figure A.15: Efficiency Map Quantized Datapoints for VW ID.3

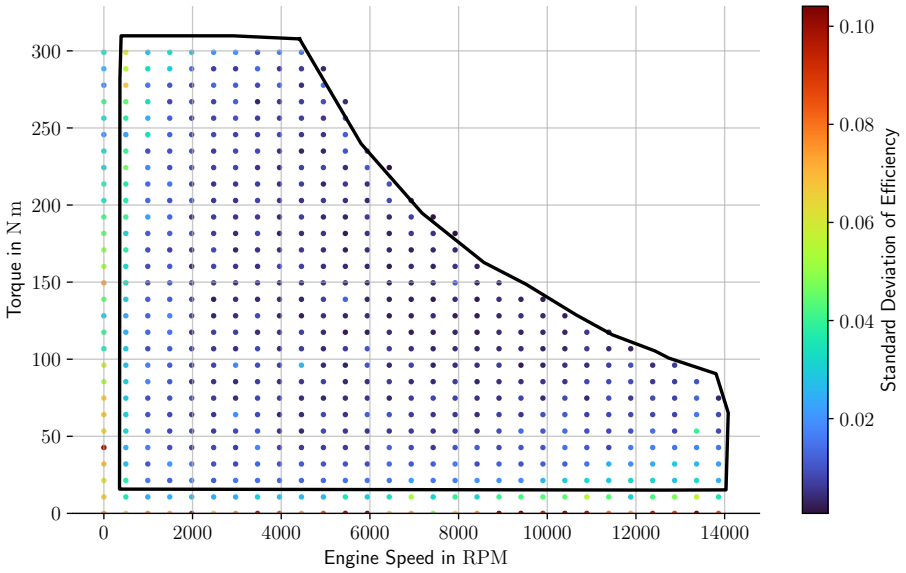

Figure A.16: Efficiency Map Quantized Datapoints Standard Deviation for VW ID.3

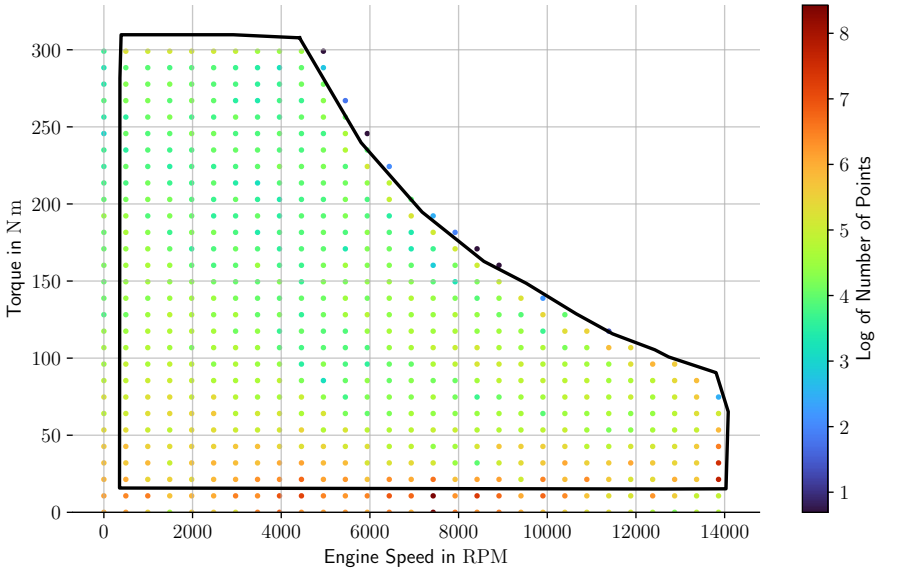

Figure A.17: Efficiency Map Quantized Datapoints Number of Points for VW ID.3

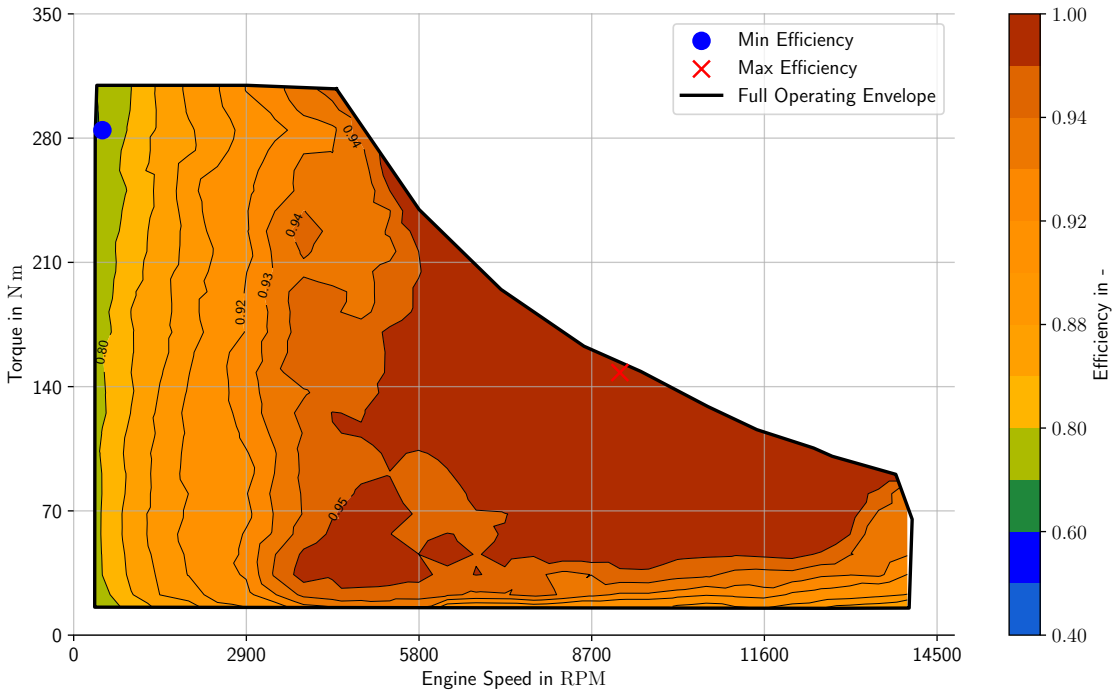

Figure A.18: Efficiency Map Interpolated High Fidelity Contourplot for VW ID.3

A.2 Gear Strategy Estimation with clean data

This section shows the intermediary steps for the gear strategy estimation algorithm with the better data set, which has also been used for the gear strategy part in the main text. The final results are presented in the main text, with this section providing additional insights.

Intermediary plots of the gear strategy shift up estimation process are shown in the following figures. The final results are presented in the main text.

Figure A.19 shows the raw unprocessed gear change points from the gear change testdrive data in three different domains: torque, accelerator pedal position, and power mechanical.

Figure A.20 and Figure A.22 show the detected outliers in the gear change points for the normal mode. The detected outliers are marked in red, and the outlier detection is done in the four dimensional space of torque, accelerator pedal position, power mechanical, and speed, hence the results are shown in three different subfigures.

Figure A.21 shows the preprocessed (merged) gear change points in the three different domains for the normal mode.

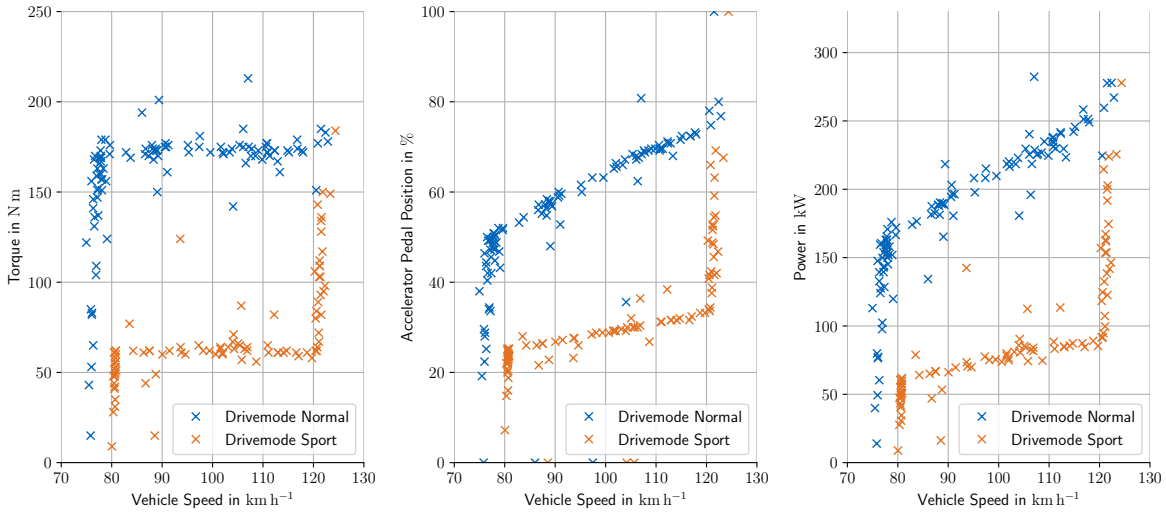

(a) Gear Change Points in Torque Domain

(b) Gear Change Points in Accelerator Pedal Domain

(c) Gear Change Points in Power Mechanical Domain

Figure A.19: Raw Gear Change Points for Sport and Normal Mode

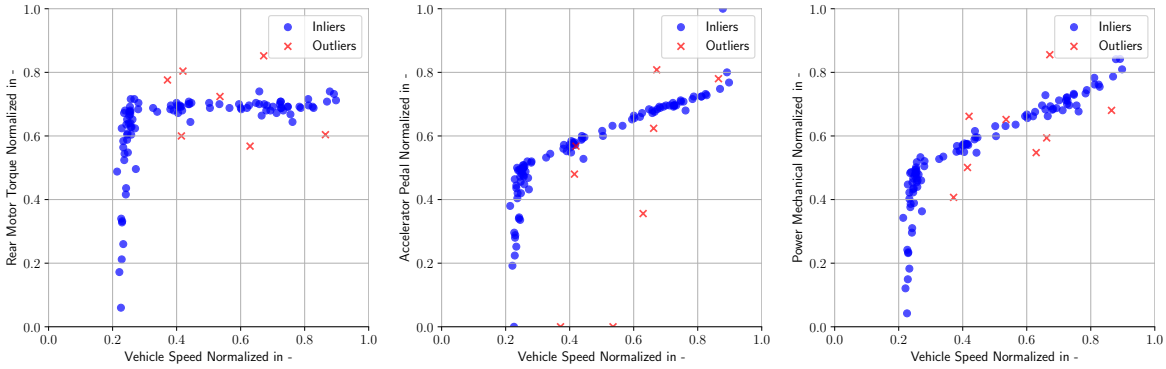

(a) Outliers in Torque Domain

(b) Outliers in Accelerator Pedal Domain

(c) Outliers in Power Mechanical Domain

Figure A.20: Outliers in Gear Change Points for Normal Mode

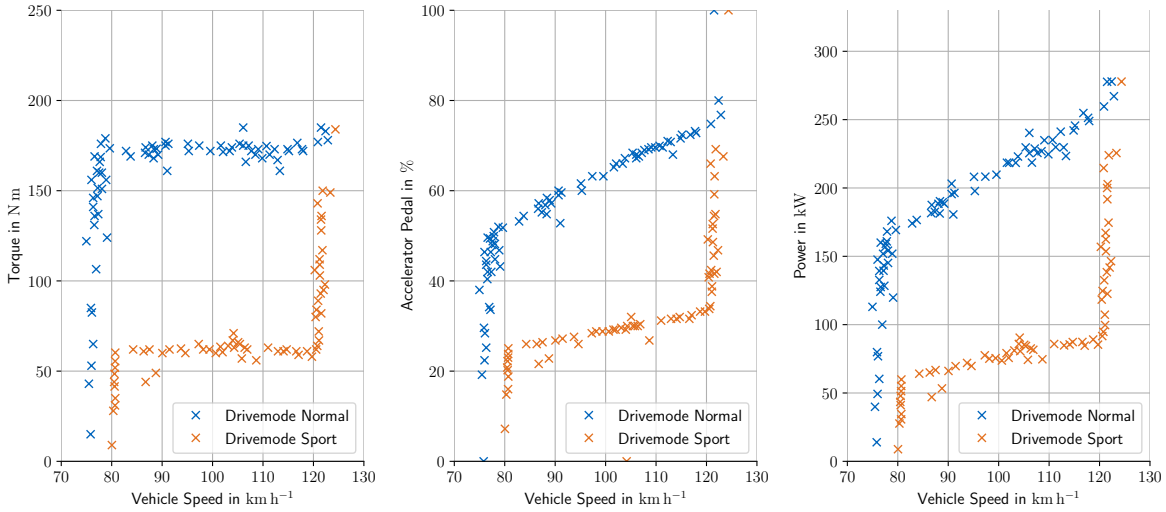

(a) Preprocessed Gear Change Points in Torque Domain

(b) Preprocessed Gear Change Points in Accelerator Pedal Domain

(c) Preprocessed Gear Change Points in Power Mechanical Domain

Figure A.21: Preprocessed Gear Change Points for Normal Mode

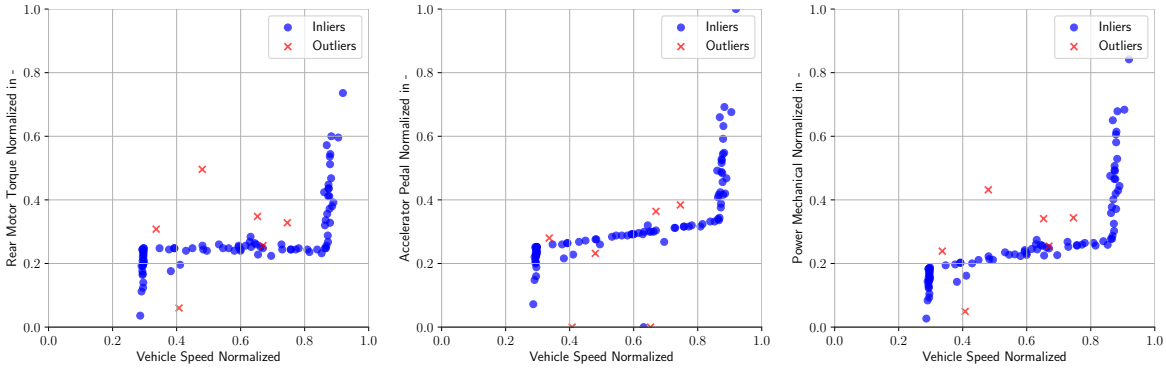

(a) Outliers in Torque Domain

(b) Outliers in Accelerator Pedal Domain

(c) Outliers in Power Mechanical Domain

Figure A.22: Outliers in Gear Change Points for Sport Mode

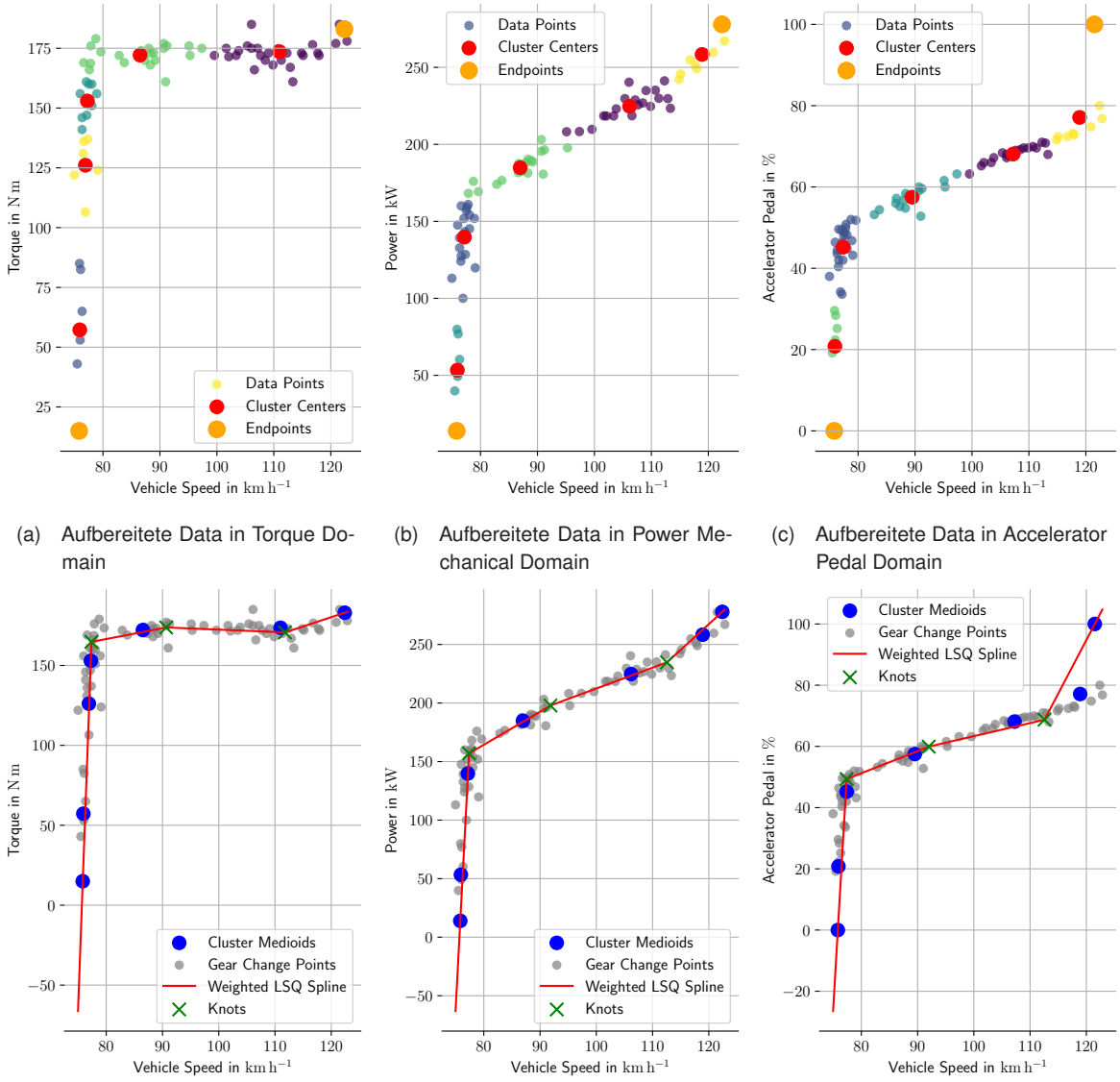

(a) Aufbereitete Data in Torque Domain

(b) Aufbereitete Data in Power Mechanical Domain

(c) Aufbereitete Data in Accelerator Pedal Domain

(d) Fitted Spline in Torque Domain

(e) Fitted Spline in Power Mechanical Domain

(f) Fitted Spline in Accelerator Pedal Domain

Figure A.23: Gear Strategy Shift Up Estimation for Normal Mode

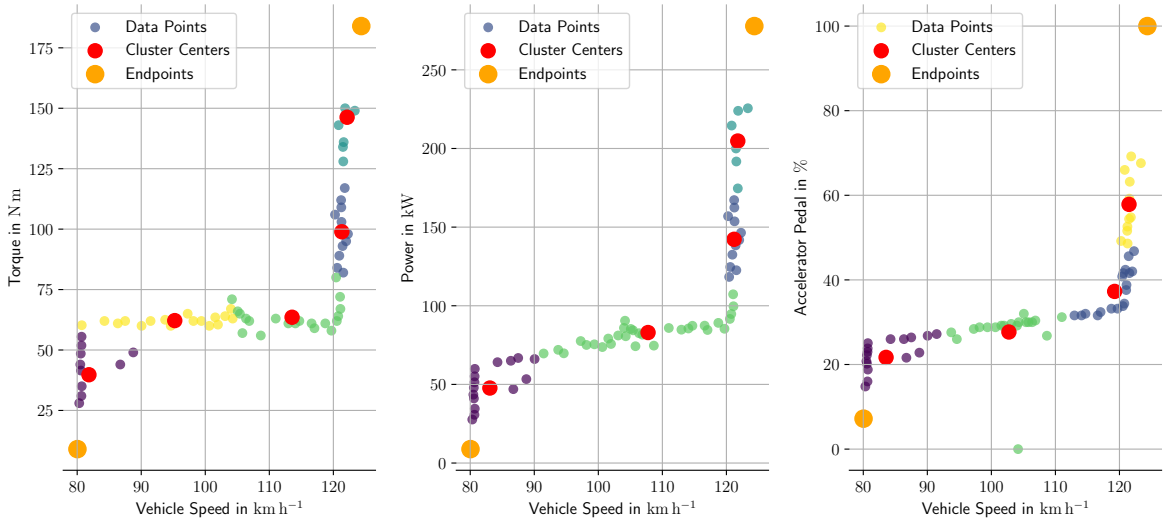

(a) Aufbereitete Data in Torque Domain

(b) Aufbereitete Data in Power Mechanical Domain

(c) Aufbereitete Data in Accelerator Pedal Domain

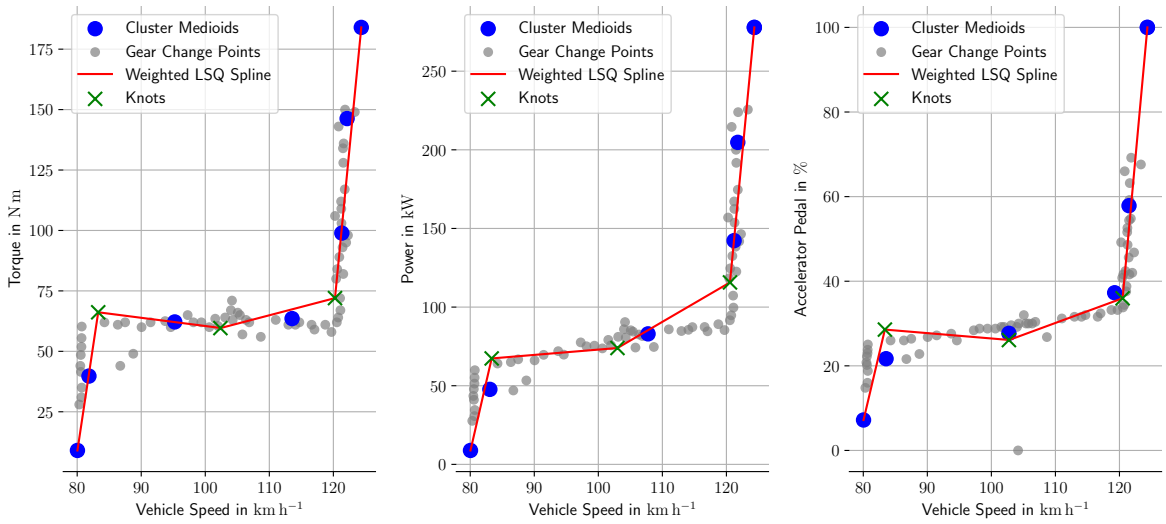

(d) Fitted Spline in Torque Domain

(e) Fitted Spline in Power Mechanical Domain

(f) Fitted Spline in Accelerator Pedal Domain

Figure A.24: Gear Strategy Shift Up Estimation for Sport Mode

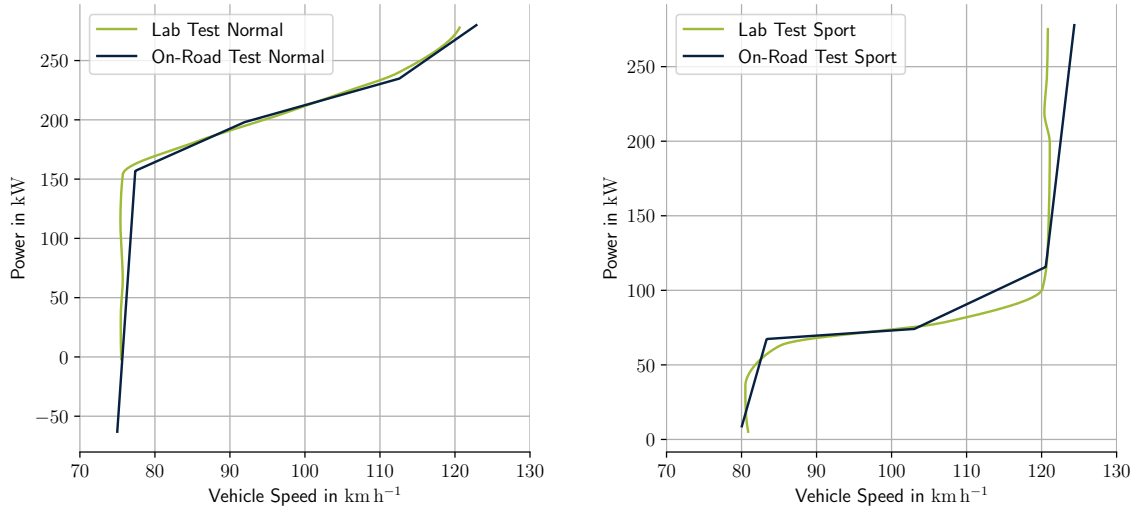

(a) Comparison of Gear Change Strategies derived from On Road Test vs Dynamo Test in Normal Drive Mode.

(b) Comparison of Gear Change Strategies derived from On Road Test vs Dynamo Test in Sport Drive Mode.

Figure A.25: Comparison of Gear Change Strategies in mechanical power domain derived from On Road Test vs Dynamo Test in Normal and Sport Drive Modes.

A.3 Gear Strategy Estimation with noisy data

This section shows the intermediary steps for the gear strategy estimation algorithm with the noisy previous data set. The final results are presented in the main text.

Intermediary plots of the gear strategy shift up estimation process are shown in the following figures. The final results are presented in the main text.

Figure A.26 shows the raw unprocessed gear change points from the gear change testdrive data in three different domains: torque, accelerator pedal position, and power mechanical.

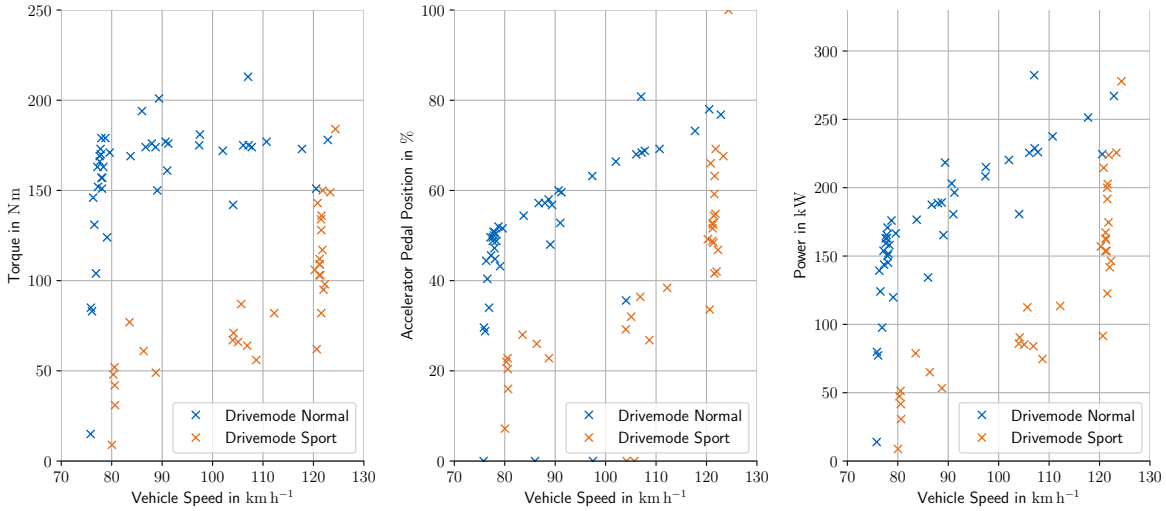

(a) Gear Change Points in Torque Domain

(b) Gear Change Points in Accelerator Pedal Domain

(c) Gear Change Points in Power Mechanical Domain

Figure A.26: Raw Gear Change Points for Sport and Normal Mode

Figure A.27 and Figure A.29 show the detected outliers in the gear change points for the normal mode. The detected outliers are marked in red, and the outlier detection is done in the four dimensional space of torque, accelerator pedal position, power mechanical, and speed, hence the results are shown in three different subfigures.

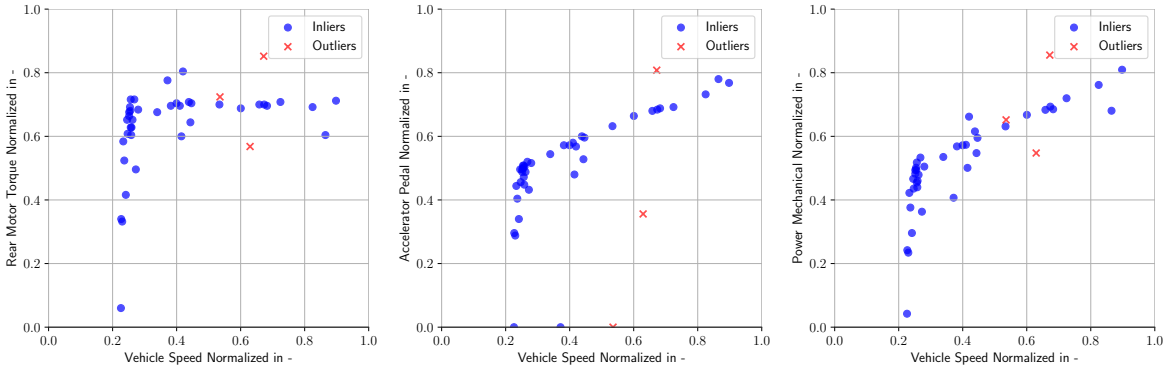

(a) Outliers in Torque Domain (b) Outliers in Accelerator Pedal Domain (c) Outliers in Power Mechanical Domain

Figure A.27: Outliers in Gear Change Points for Normal Mode

Figure A.28 shows the preprocessed (merged) gear change points in the three different domains for the normal mode.

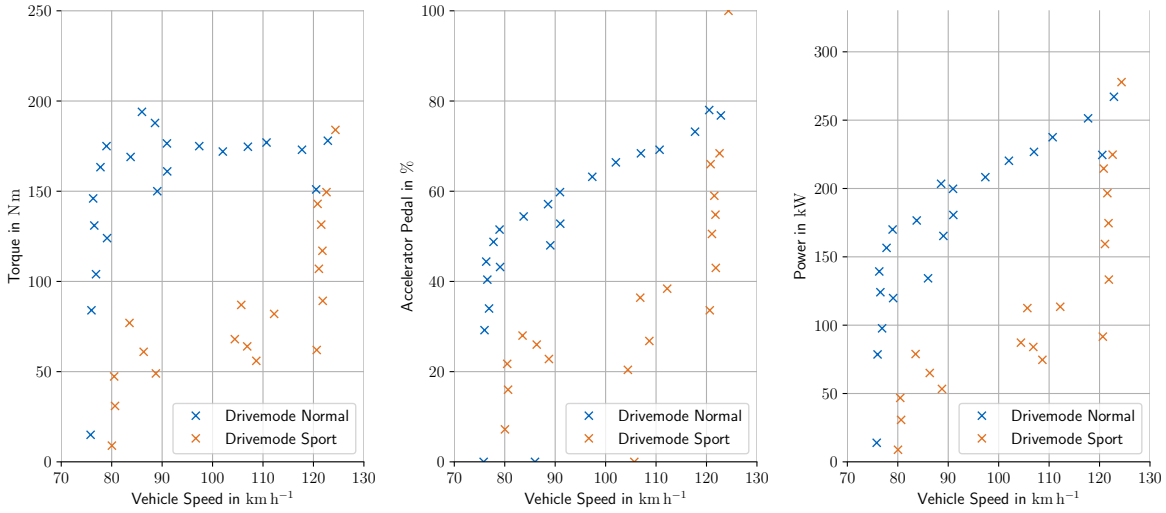

(a) Preprocessed Gear Change Points in Torque Domain (b) Preprocessed Gear Change Points in Accelerator Pedal Domain (c) Preprocessed Gear Change Points in Power Mechanical Domain

Figure A.28: Preprocessed Gear Change Points for Normal Mode

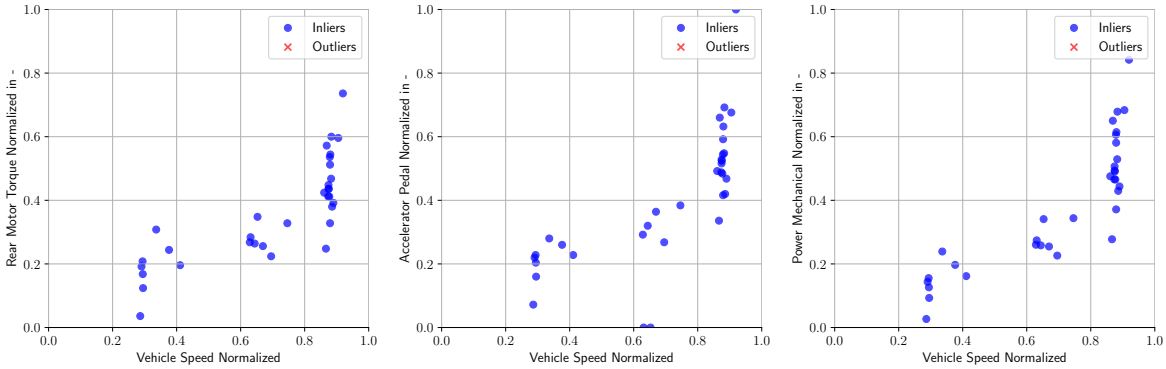

(a) Outliers in Torque Domain (b) Outliers in Accelerator Pedal Domain (c) Outliers in Power Mechanical Domain

Figure A.29: Outliers in Gear Change Points for Sport Mode

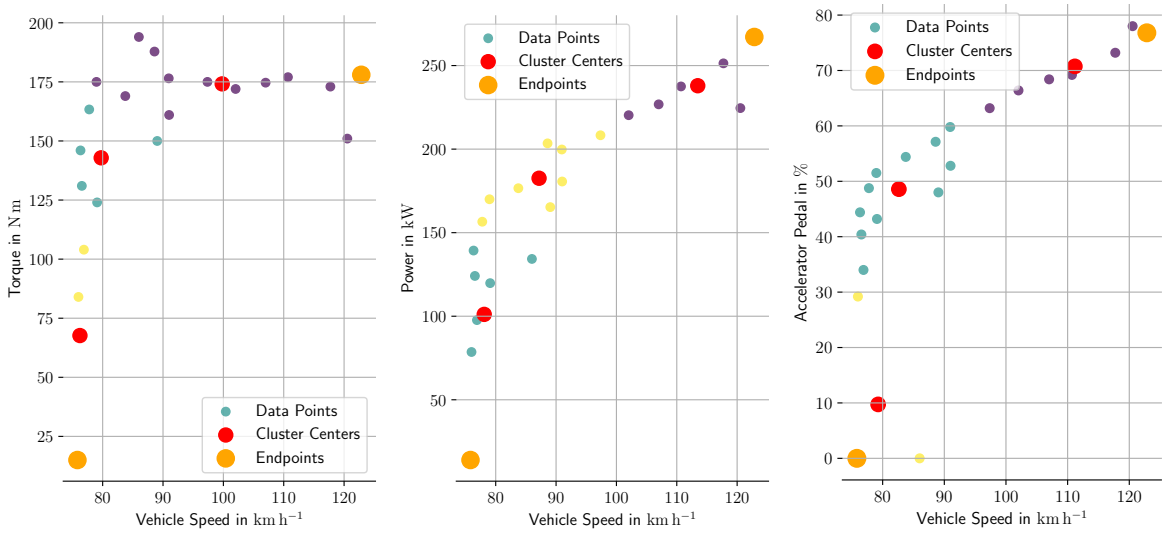

(a) Aufbereitete Data in Torque Domain (b) Aufbereitete Data in Power Mechanical Domain (c) Aufbereitete Data in Accelerator Pedal Domain

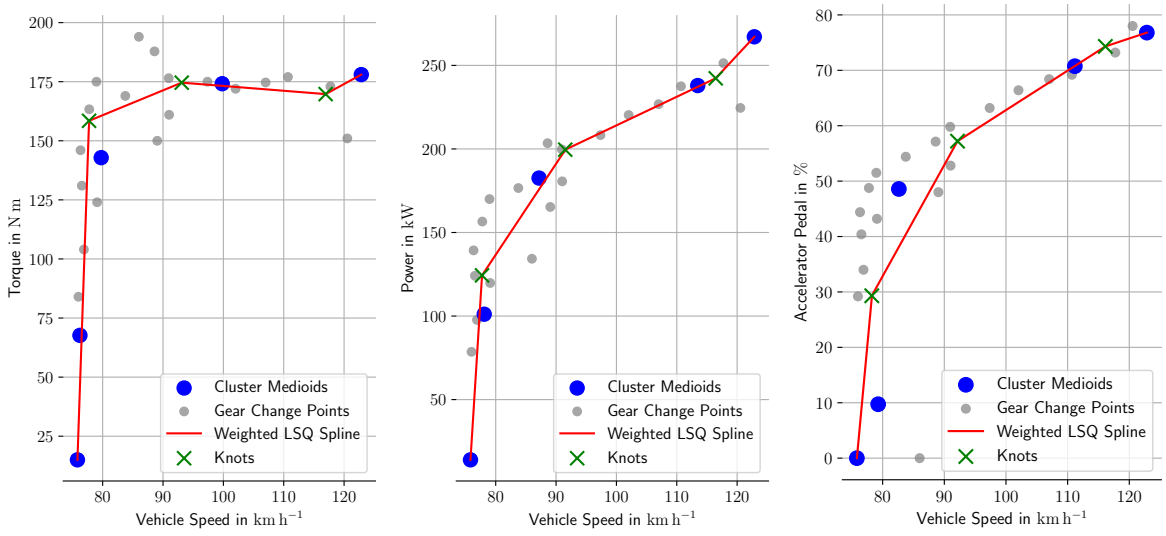

(d) Fitted Spline in Torque Domain (e) Fitted Spline in Power Mechanical Domain (f) Fitted Spline in Accelerator Pedal Domain

Figure A.30: Gear Strategy Shift Up Estimation for Normal Mode

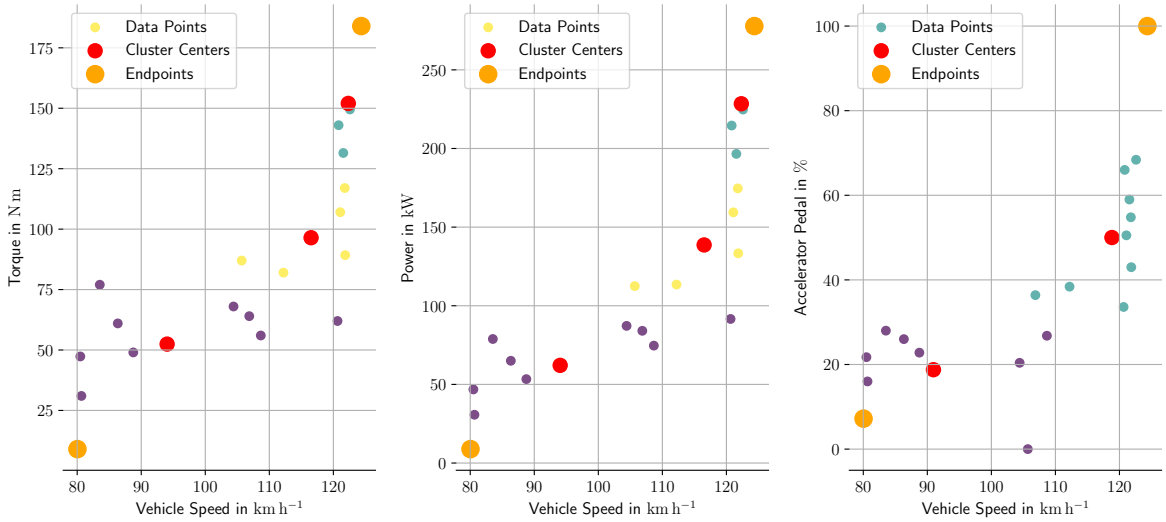

(a) Aufbereitete Data in Torque Domain

(b) Aufbereitete Data in Power Mechanical Domain

(c) Aufbereitete Data in Accelerator Pedal Domain

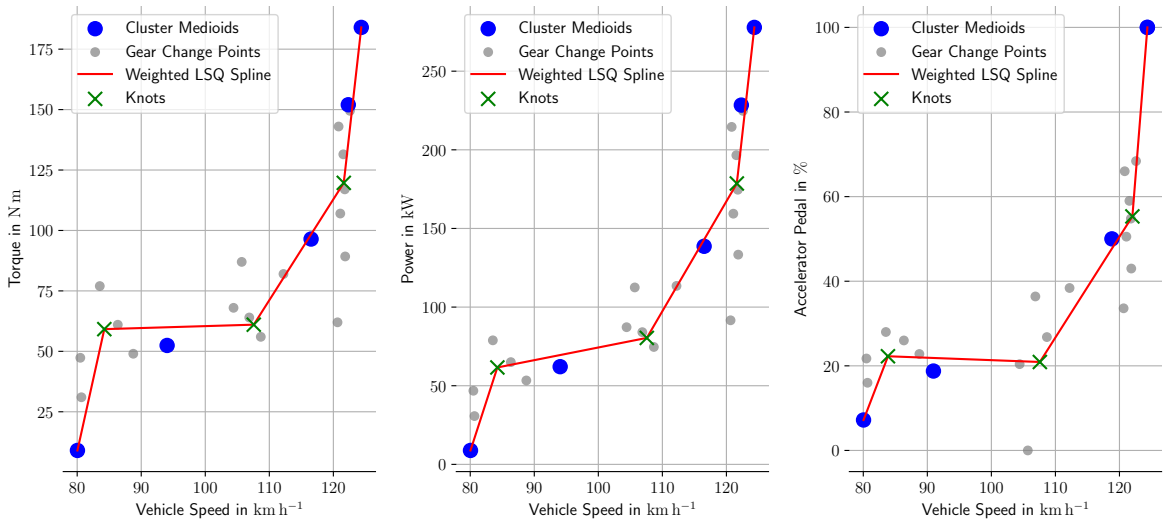

(d) Fitted Spline in Torque Domain

(e) Fitted Spline in Power Mechanical Domain

(f) Fitted Spline in Accelerator Pedal Domain

Figure A.31: Gear Strategy Shift Up Estimation for Sport Mode

B Simulation of Driving Cycles

B.1 Variation of Singular Parameters

In the default case, all three vehicle paramters (the efficiency map, the gear strategy, and the RLCs) are varied. It was also investigated how large the difference in cummulative energy consumption is when only one of the three parameters is varied. The results for each driving cycle and drive mode are shown in the following figures.

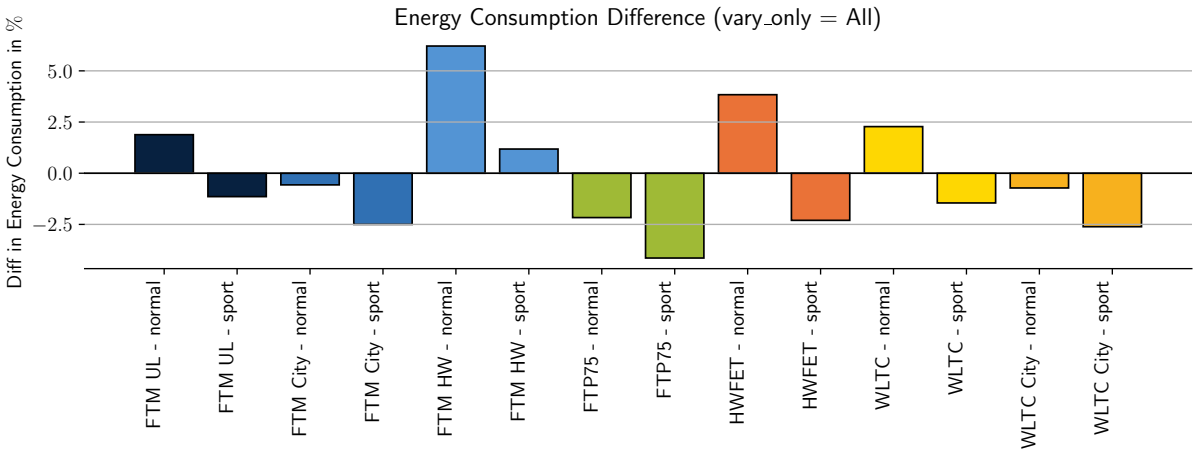

Figure B.1: Cumulative Energy Consumption Comparison for Varying All Parameters.

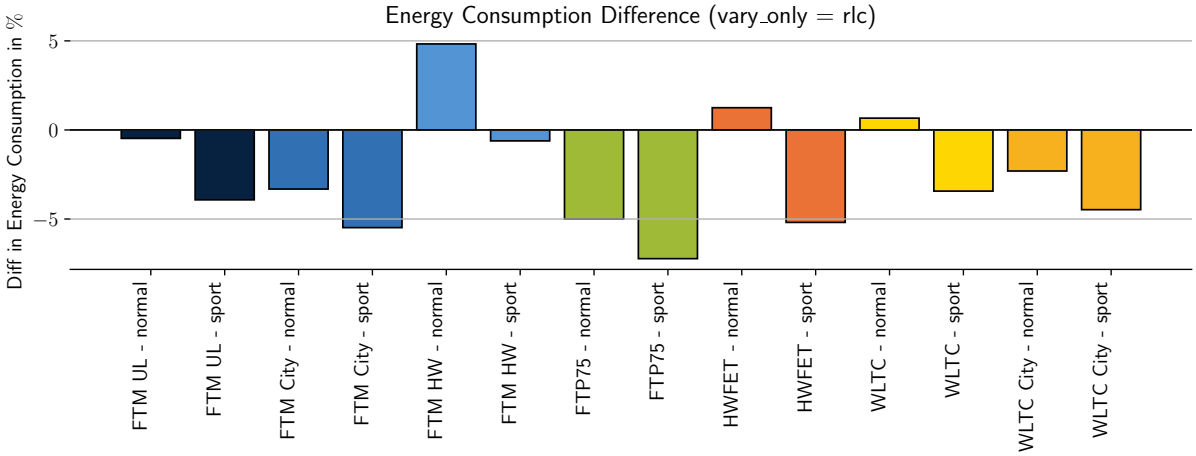

Figure B.2: Cumulative Energy Consumption Comparison for Varying Only the RLCs.

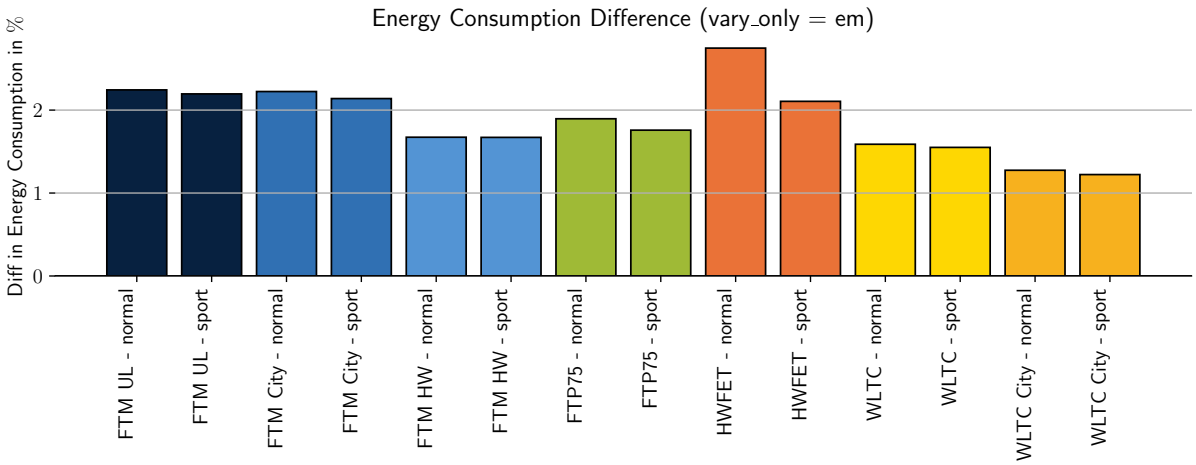

Figure B.3: Cumulative Energy Consumption Comparison for Varying Only the Efficiency Map.

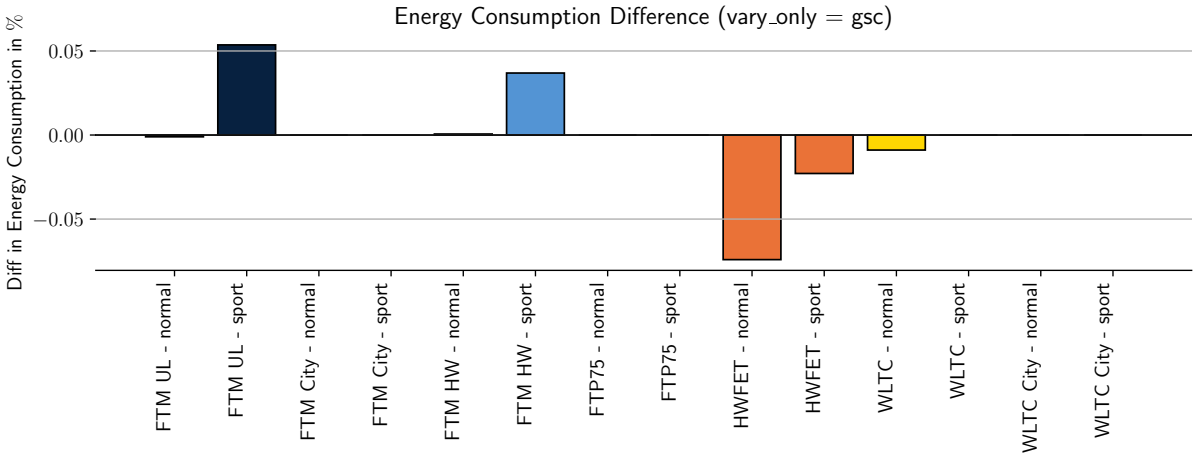

Figure B.4: Cumulative Energy Consumption Comparison for Varying Only the Gear Strategy

B.2 FTM Überland Cycle

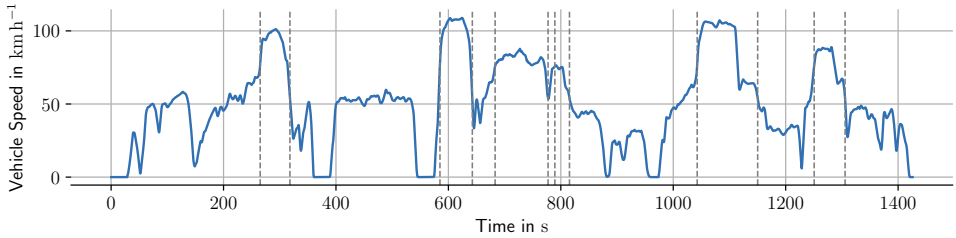

(a) Velocity Profile of the FTM_UL Cycle

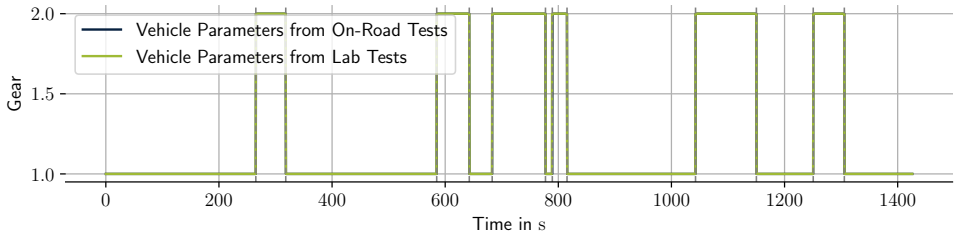

(b) Gear Selection Comparison for the FTM_UL Cycle with Normal Mode Gear Strategies

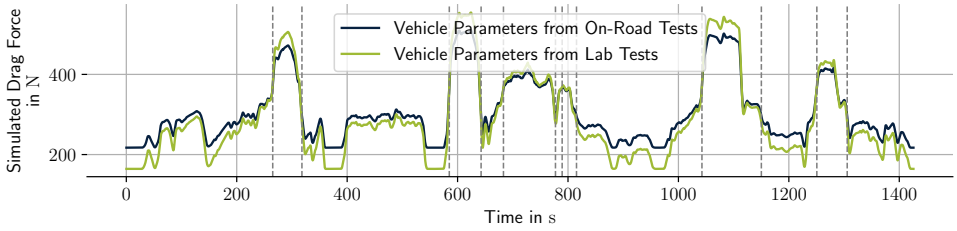

(c) Driving Resistance Comparison for the FTM_UL Cycle

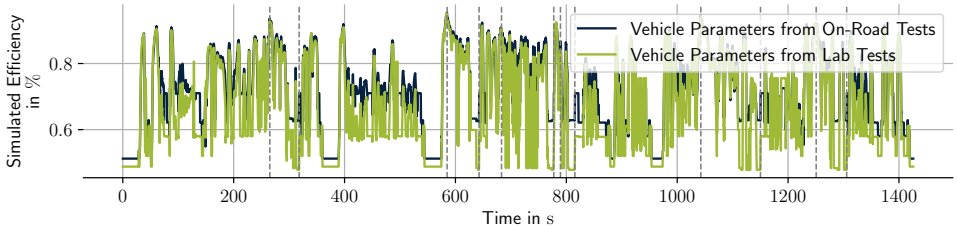

(d) Driving Efficiency Comparison for the FTM_UL Cycle

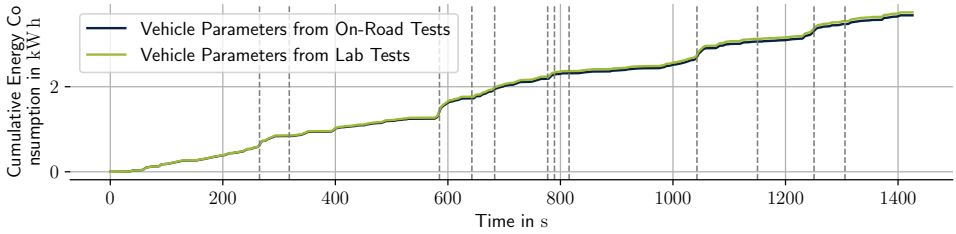

(e) Cumulative Energy Consumption Comparison for the FTM_UL Cycle

Figure B.5: Simulation Results for the FTM_UL Cycle in Normal Mode

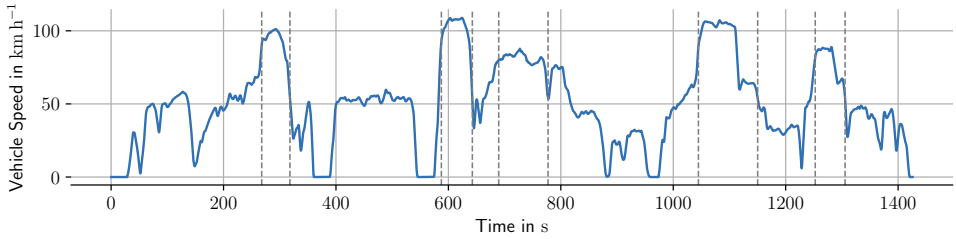

(a) Velocity Profile of the FTM_UL Cycle

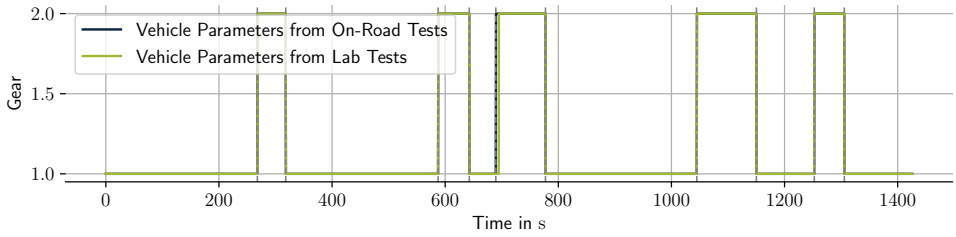

(b) Gear Selection Comparison for the FTM_UL Cycle with Sport Mode Gear Strategies

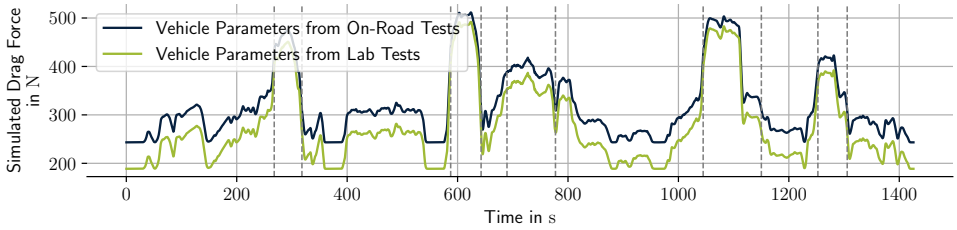

(c) Driving Resistance Comparison for the FTM_UL Cycle

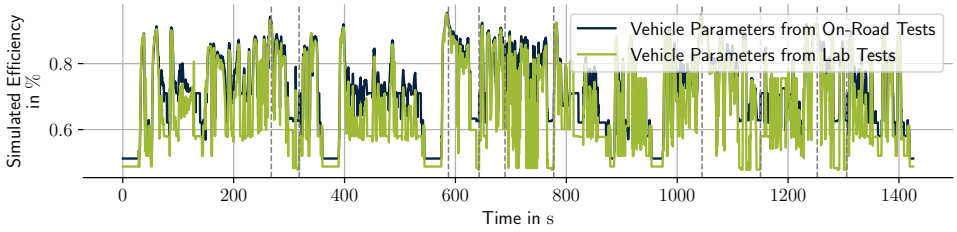

(d) Driving Efficiency Comparison for the FTM_UL Cycle

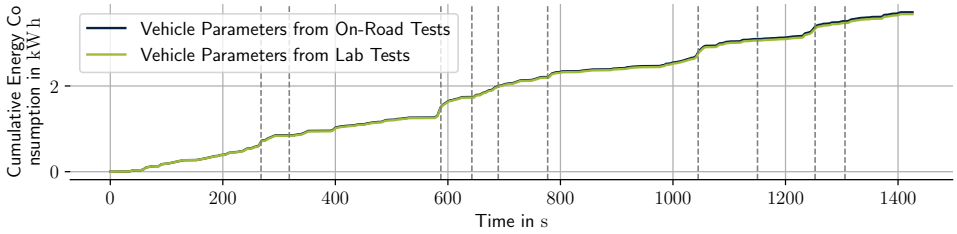

(e) Cumulative Energy Consumption Comparison for the FTM_UL Cycle

Figure B.6: Simulation Results for the FTM_UL Cycle in Sport Mode

B.3 FTM City Cycle

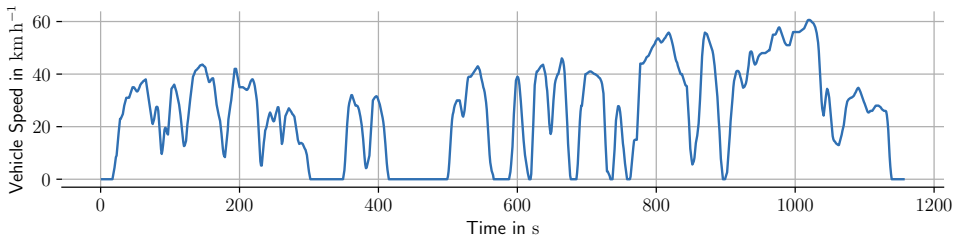

(a) Velocity Profile of the FTM_City Cycle

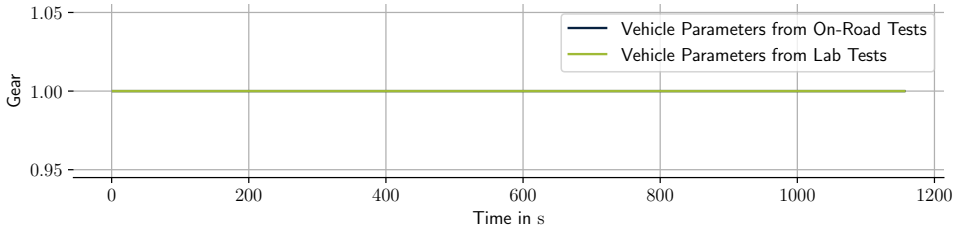

(b) Gear Selection Comparison for the FTM_City Cycle with Normal Mode Gear Strategies

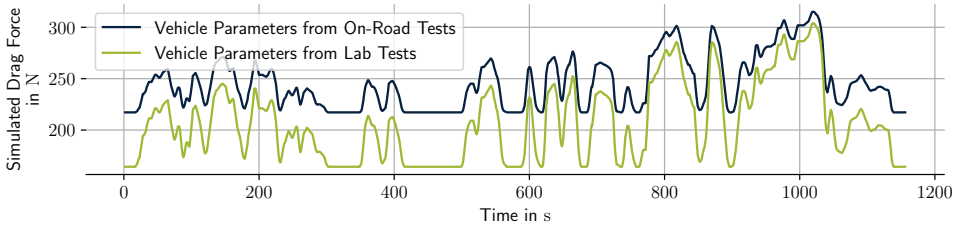

(c) Driving Resistance Comparison for the FTM_City Cycle

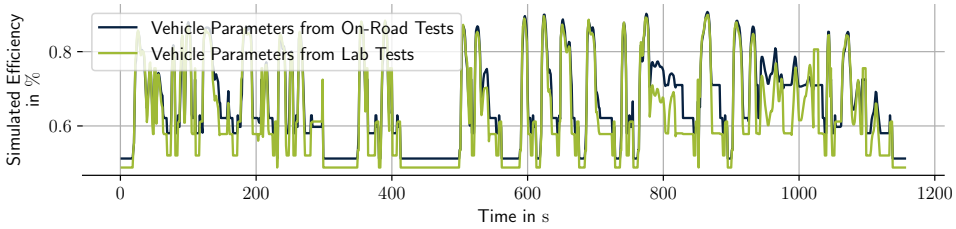

(d) Driving Efficiency Comparison for the FTM_City Cycle

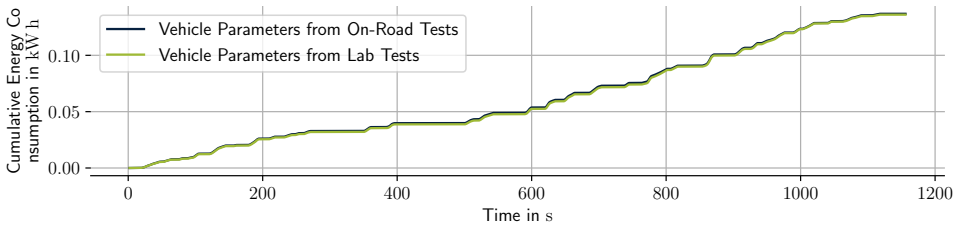

(e) Cumulative Energy Consumption Comparison for the FTM_City Cycle

Figure B.7: Simulation Results for the FTM_City Cycle in Normal Mode

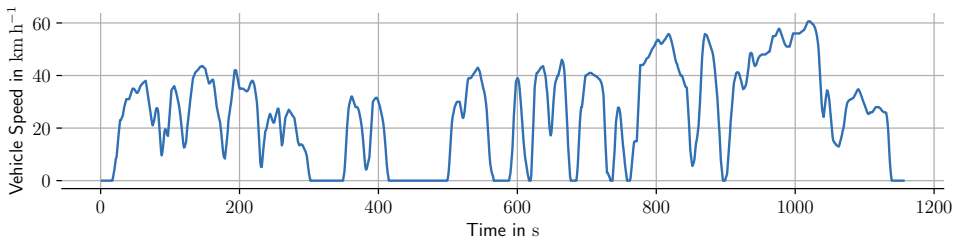

(a) Velocity Profile of the FTM_City Cycle

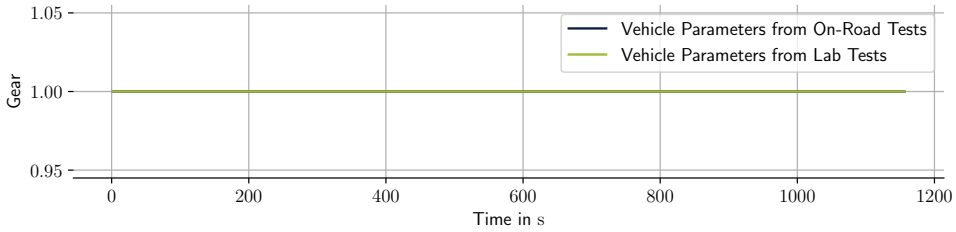

(b) Gear Selection Comparison for the FTM_City Cycle with Sport Mode Gear Strategies

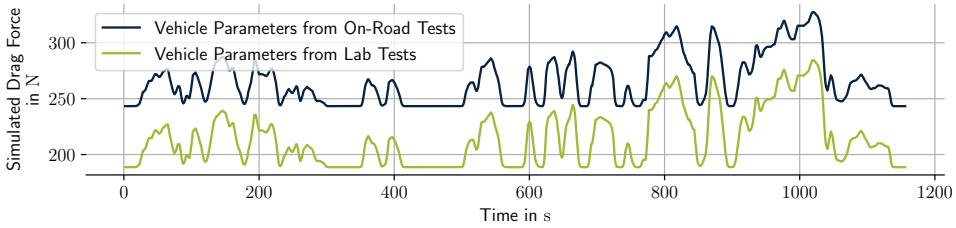

(c) Driving Resistance Comparison for the FTM_City Cycle

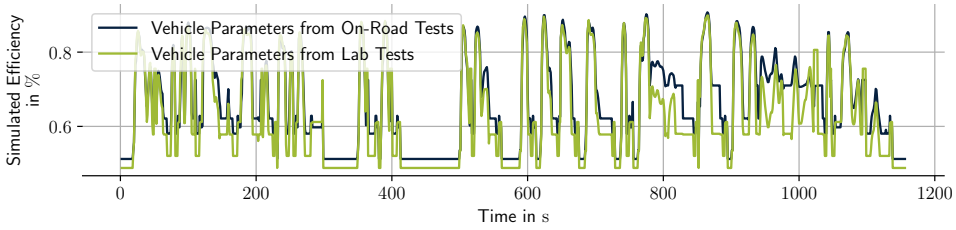

(d) Driving Efficiency Comparison for the FTM_City Cycle

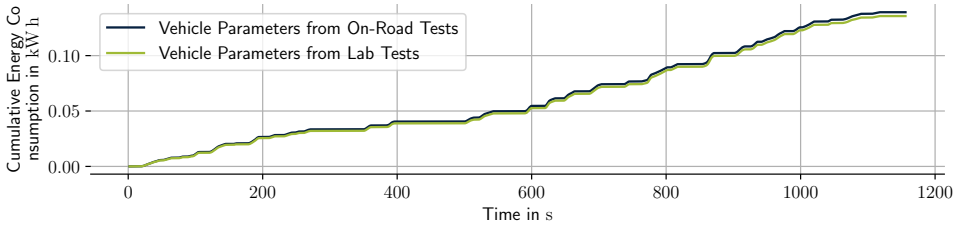

(e) Cumulative Energy Consumption Comparison for the FTM_City Cycle

Figure B.8: Simulation Results for the FTM_City Cycle in Sport Mode

B.4 FTM Highway Cycle

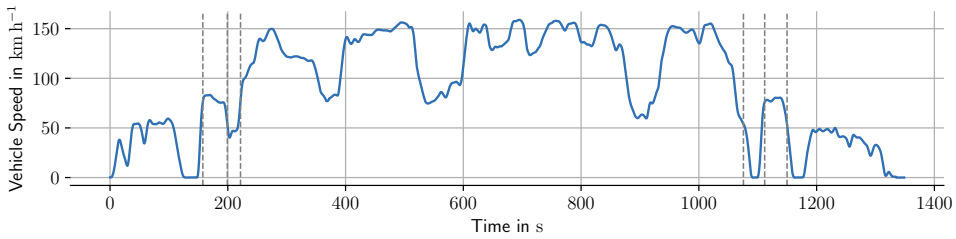

(a) Velocity Profile of the FTM_HW Cycle

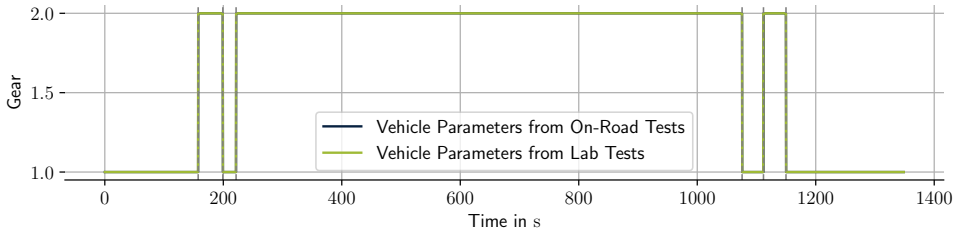

(b) Gear Selection Comparison for the FTM_HW Cycle with Normal Mode Gear Strategies

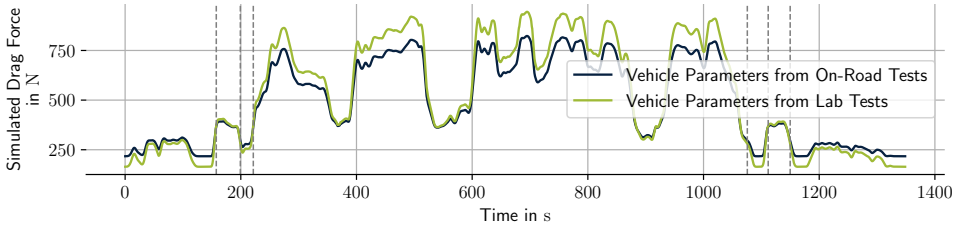

(c) Driving Resistance Comparison for the FTM_HW Cycle

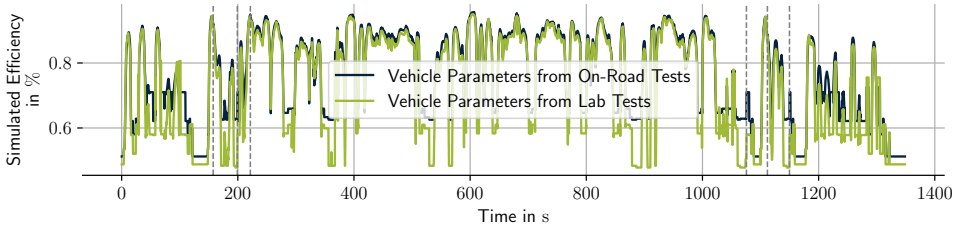

(d) Driving Efficiency Comparison for the FTM_HW Cycle

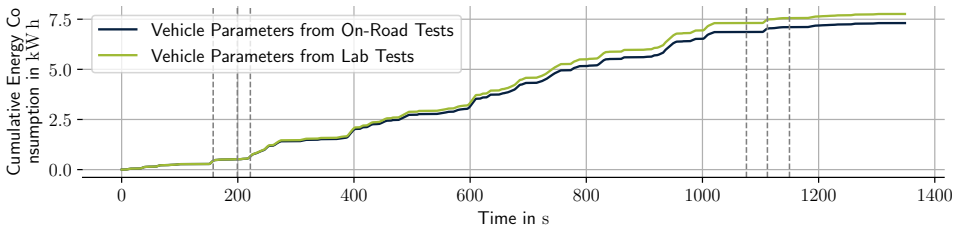

(e) Cumulative Energy Consumption Comparison for the FTM_HW Cycle

Figure B.9: Simulation Results for the FTM_HW Cycle in Normal Mode

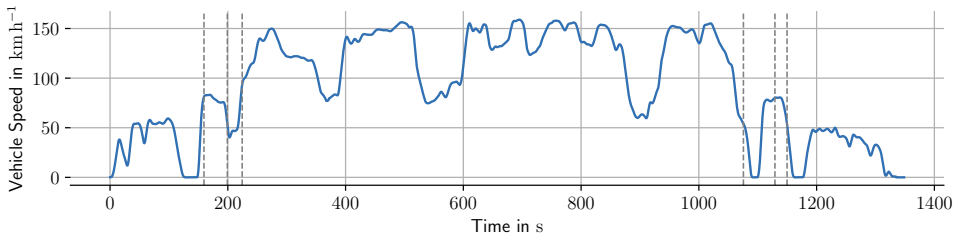

(a) Velocity Profile of the FTM_HW Cycle

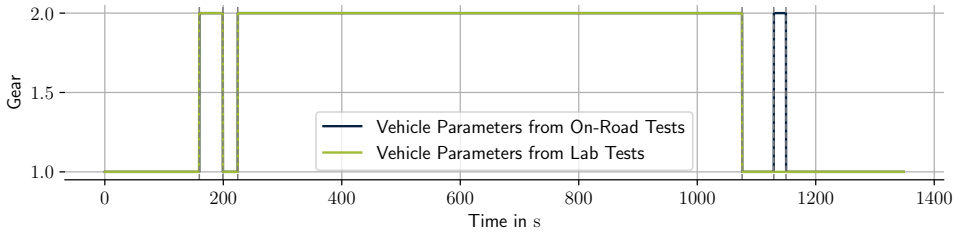

(b) Gear Selection Comparison for the FTM_HW Cycle with Sport Mode Gear Strategies

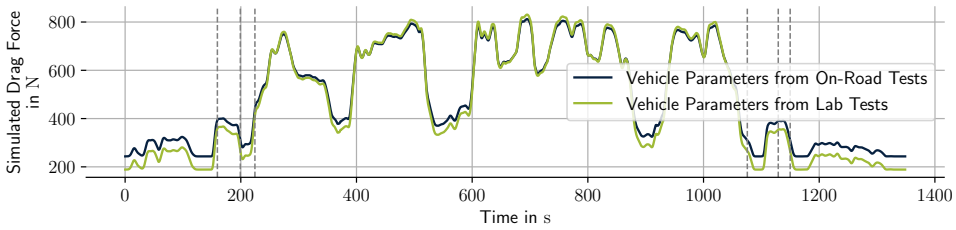

(c) Driving Resistance Comparison for the FTM_HW Cycle

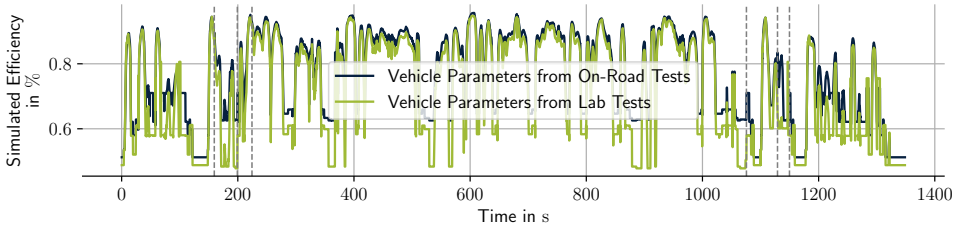

(d) Driving Efficiency Comparison for the FTM_HW Cycle

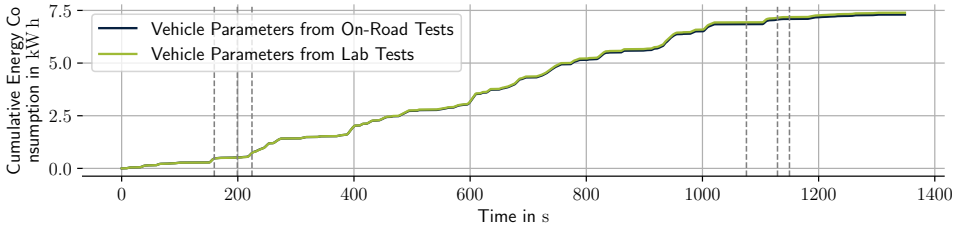

(e) Cumulative Energy Consumption Comparison for the FTM_HW Cycle

Figure B.10: Simulation Results for the FTM_HW Cycle in Sport Mode

B.5 FTP75 Cycle

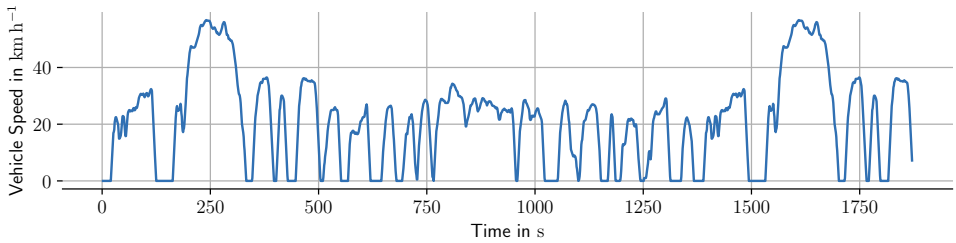

(a) Velocity Profile of the FTP75 Cycle

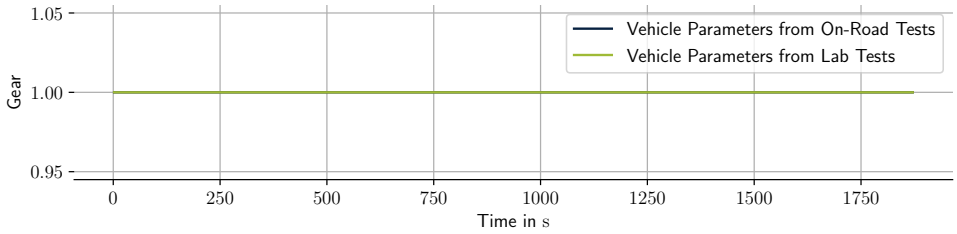

(b) Gear Selection Comparison for the FTP75 Cycle with Normal Mode Gear Strategies

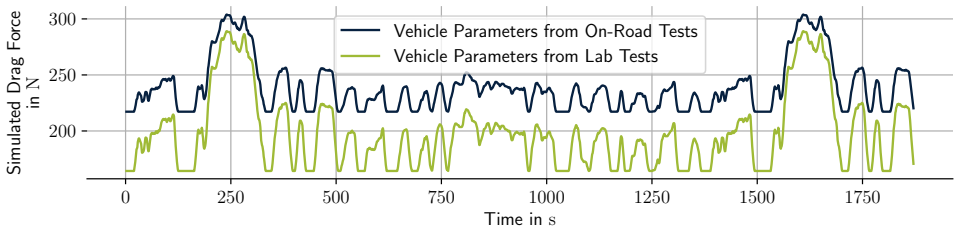

(c) Driving Resistance Comparison for the FTP75 Cycle

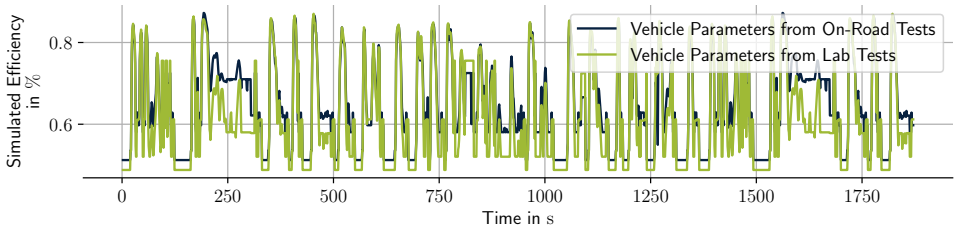

(d) Driving Efficiency Comparison for the FTP75 Cycle

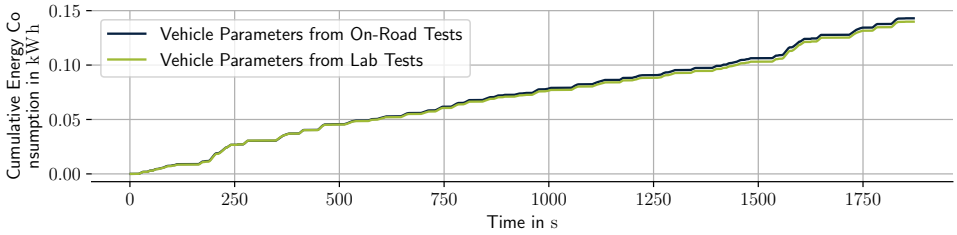

(e) Cumulative Energy Consumption Comparison for the FTP75 Cycle

Figure B.11: Simulation Results for the FTP75 Cycle in Normal Mode

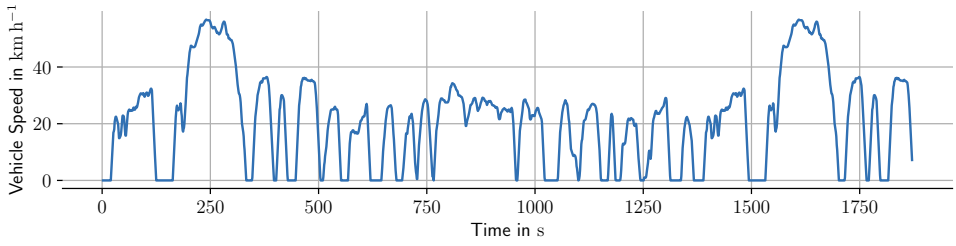

(a) Velocity Profile of the FTP75 Cycle

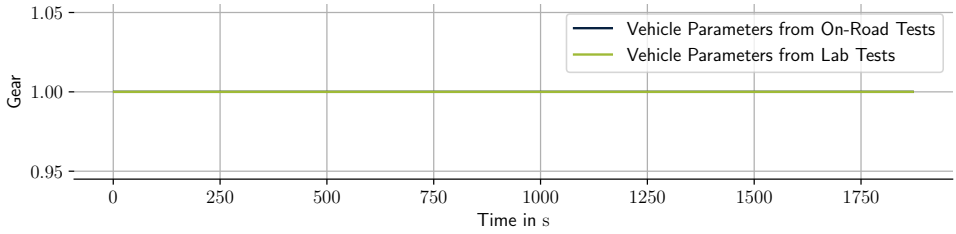

(b) Gear Selection Comparison for the FTP75 Cycle with Sport Mode Gear Strategies

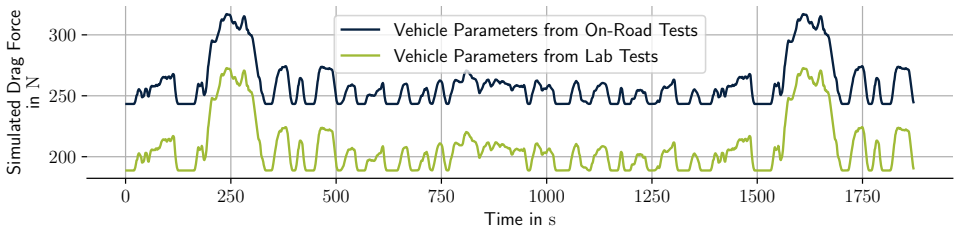

(c) Driving Resistance Comparison for the FTP75 Cycle

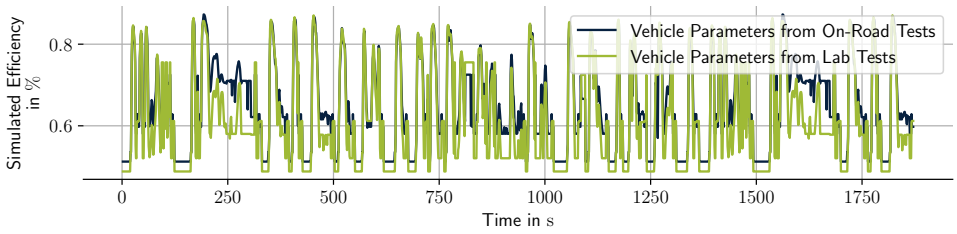

(d) Driving Efficiency Comparison for the FTP75 Cycle

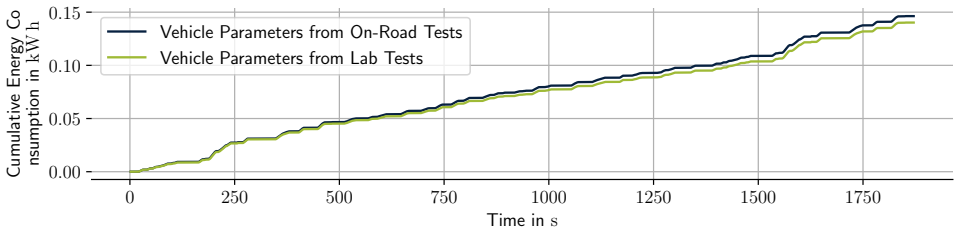

(e) Cumulative Energy Consumption Comparison for the FTP75 Cycle

Figure B.12: Simulation Results for the FTP75 Cycle in Sport Mode

B.6 HWFET Cycle

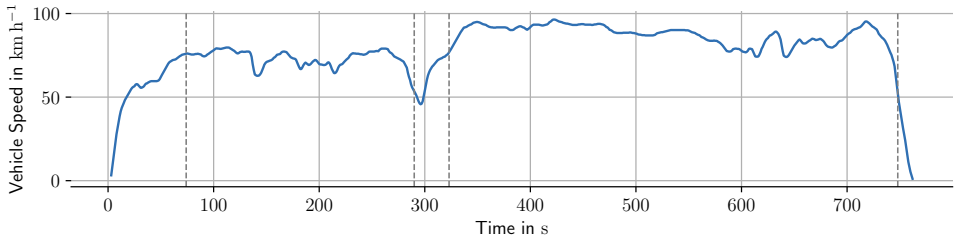

(a) Velocity Profile of the HWFET Cycle

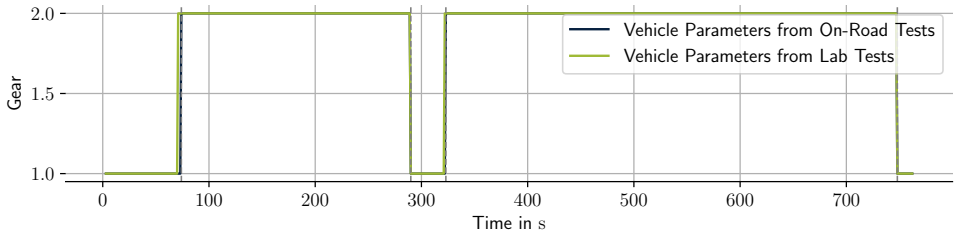

(b) Gear Selection Comparison for the HWFET Cycle with Normal Mode Gear Strategies

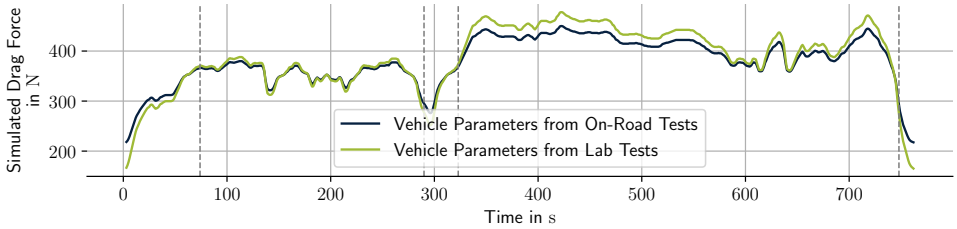

(c) Driving Resistance Comparison for the HWFET Cycle

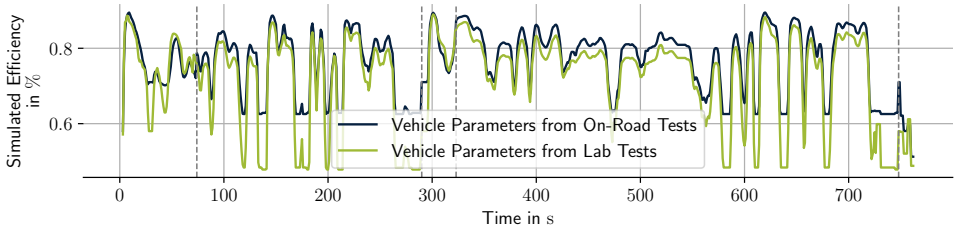

(d) Driving Efficiency Comparison for the HWFET Cycle

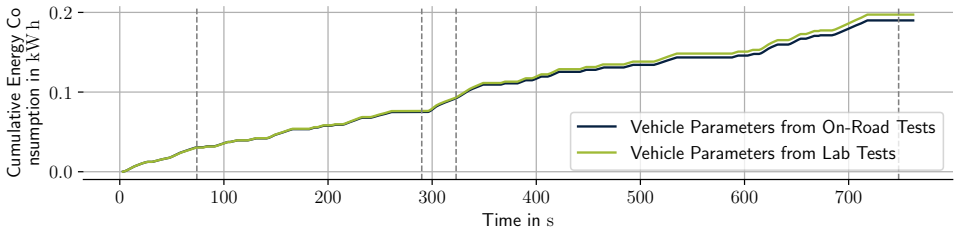

(e) Cumulative Energy Consumption Comparison for the HWFET Cycle

Figure B.13: Simulation Results for the HWFET Cycle in Normal Mode

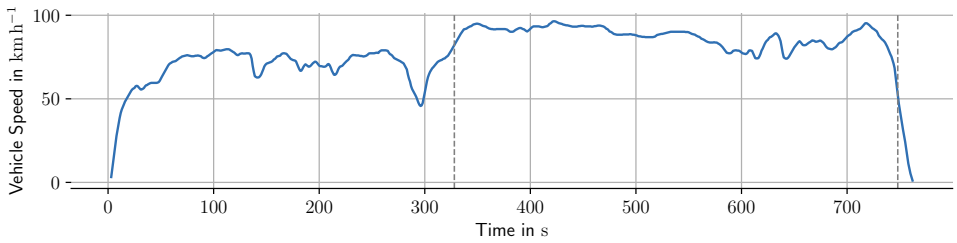

(a) Velocity Profile of the HWFET Cycle

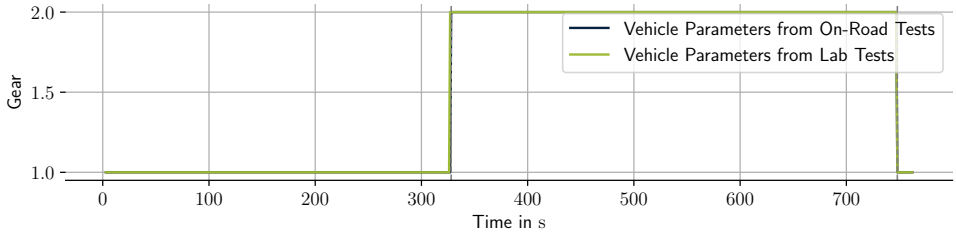

(b) Gear Selection Comparison for the HWFET Cycle with Sport Mode Gear Strategies

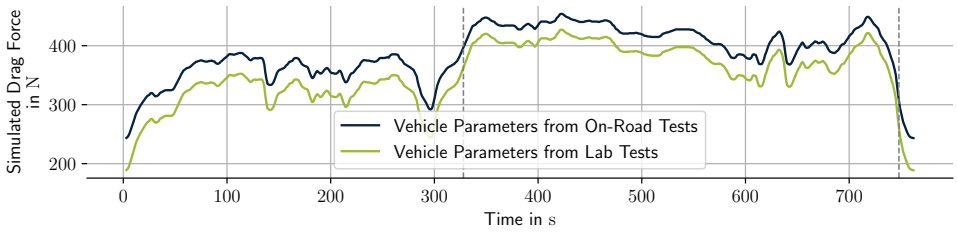

(c) Driving Resistance Comparison for the HWFET Cycle

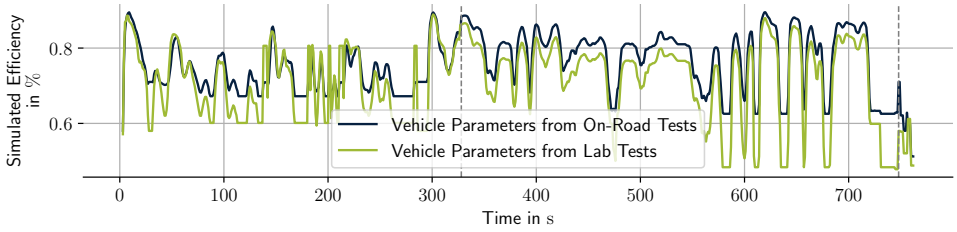

(d) Driving Efficiency Comparison for the HWFET Cycle

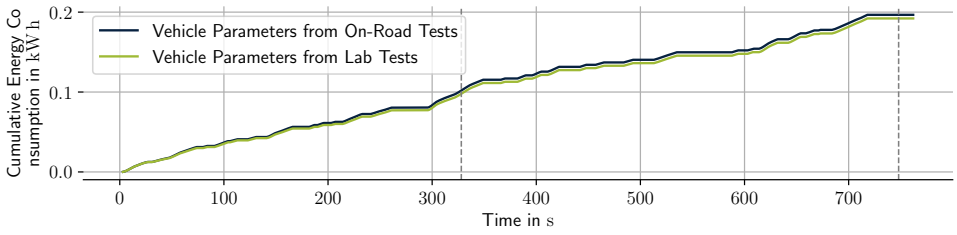

(e) Cumulative Energy Consumption Comparison for the HWFET Cycle

Figure B.14: Simulation Results for the HWFET Cycle in Sport Mode

B.7 WLTC Cycle

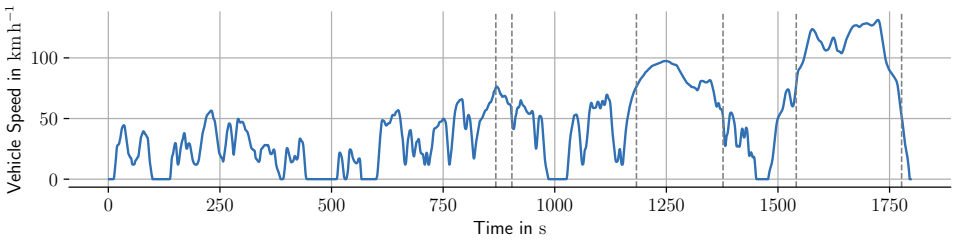

(a) Velocity Profile of the WLTC Cycle

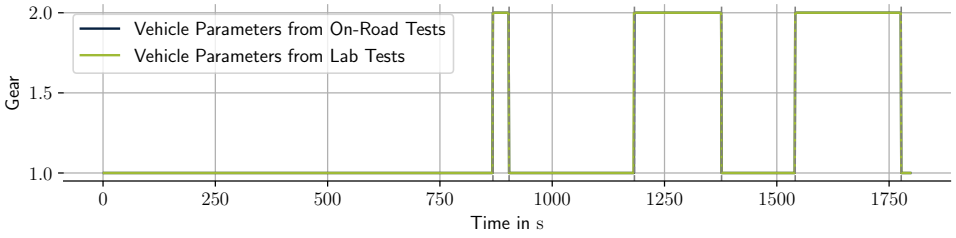

(b) Gear Selection Comparison for the WLTC Cycle with Normal Mode Gear Strategies

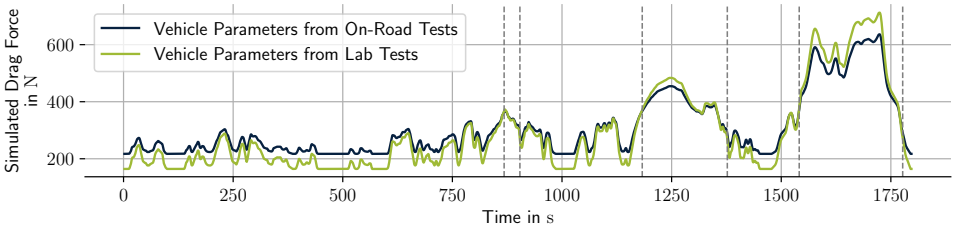

(c) Driving Resistance Comparison for the WLTC Cycle

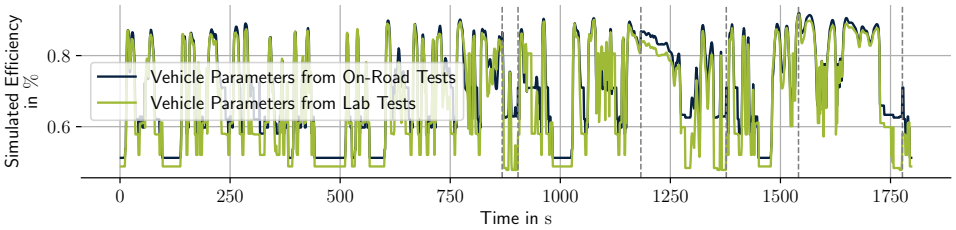

(d) Driving Efficiency Comparison for the WLTC Cycle

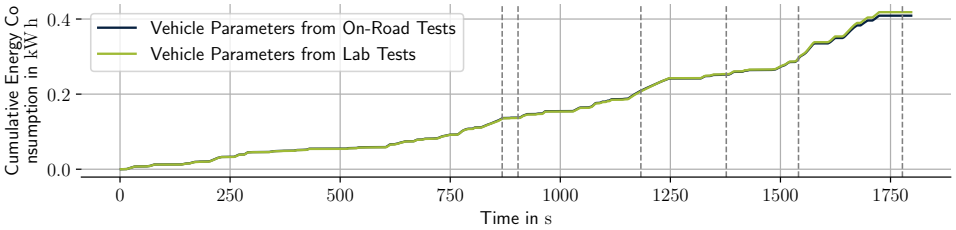

(e) Cumulative Energy Consumption Comparison for the WLTC Cycle

Figure B.15: Simulation Results for the WLTC Cycle in Normal Mode

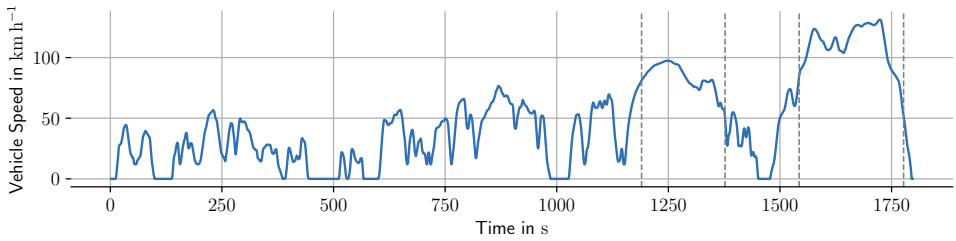

(a) Velocity Profile of the WLTC Cycle

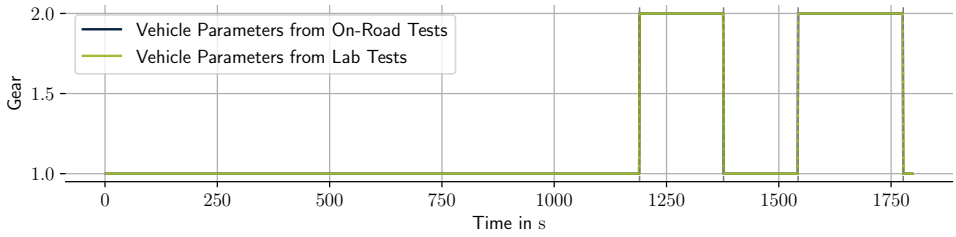

(b) Gear Selection Comparison for the WLTC Cycle with Sport Mode Gear Strategies

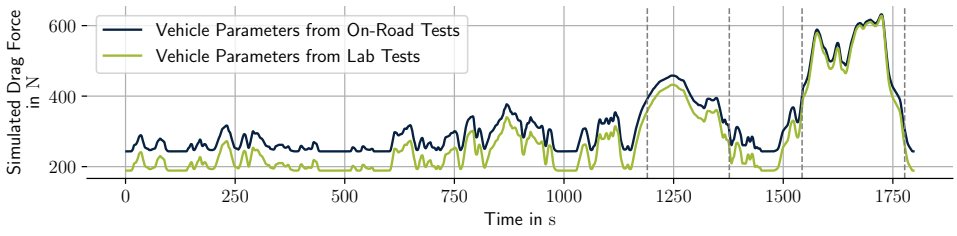

(c) Driving Resistance Comparison for the WLTC Cycle

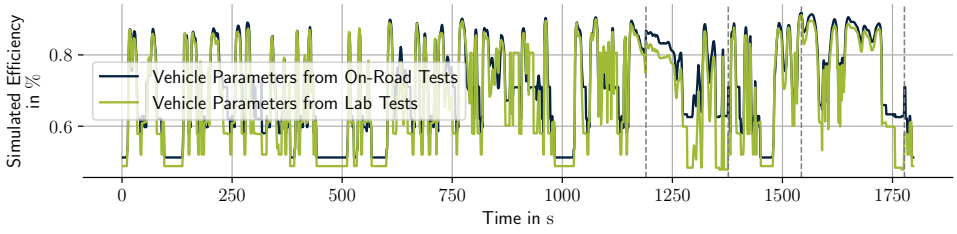

(d) Driving Efficiency Comparison for the WLTC Cycle

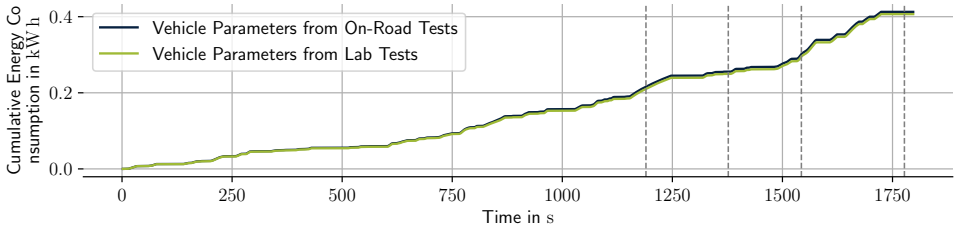

(e) Cumulative Energy Consumption Comparison for the WLTC Cycle

Figure B.16: Simulation Results for the WLTC Cycle in Sport Mode

B.8 WLTC City Cycle

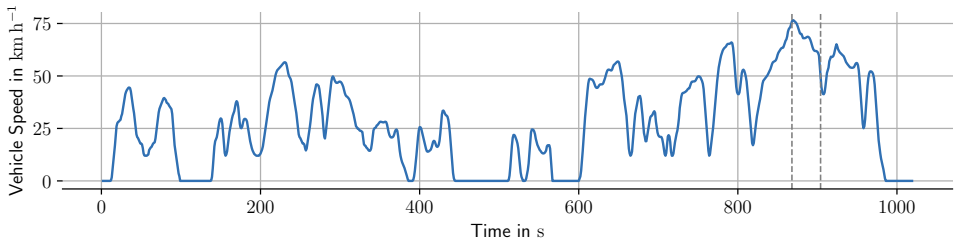

(a) Velocity Profile of the WLTC City Cycle

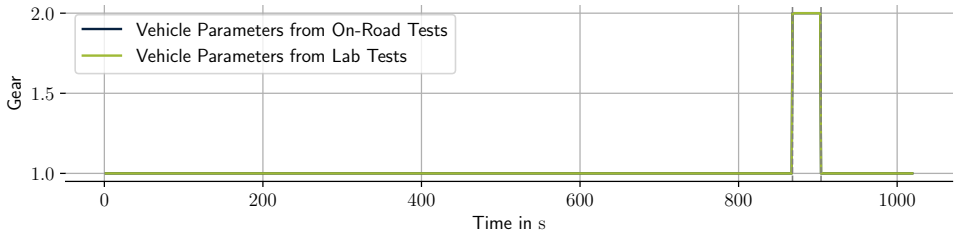

(b) Gear Selection Comparison for the WLTC City Cycle with Normal Mode Gear Strategies

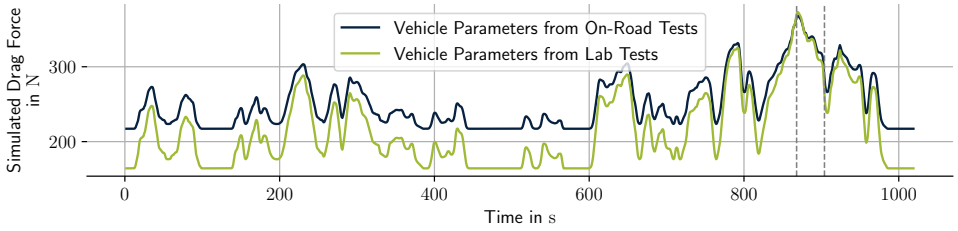

(c) Driving Resistance Comparison for the WLTC City Cycle

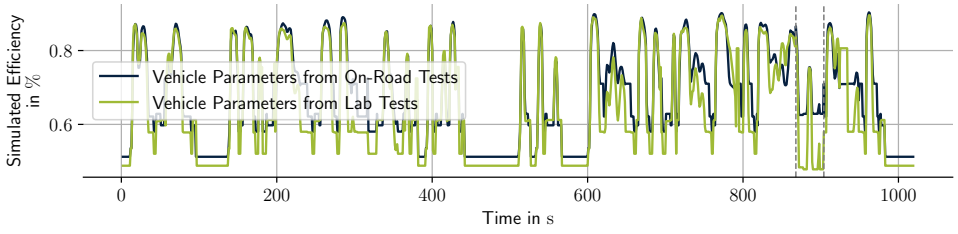

(d) Driving Efficiency Comparison for the WLTC City Cycle

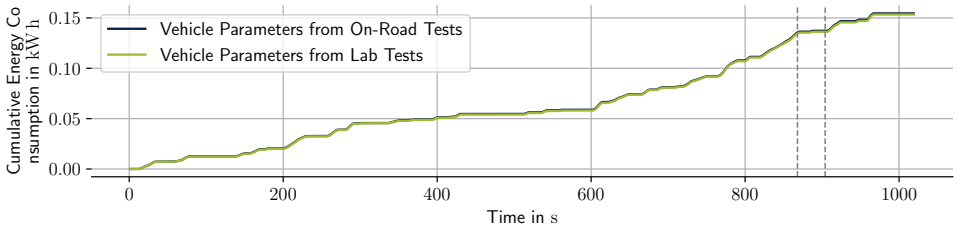

(e) Cumulative Energy Consumption Comparison for the WLTC City Cycle

Figure B.17: Simulation Results for the WLTC City Cycle in Normal Mode

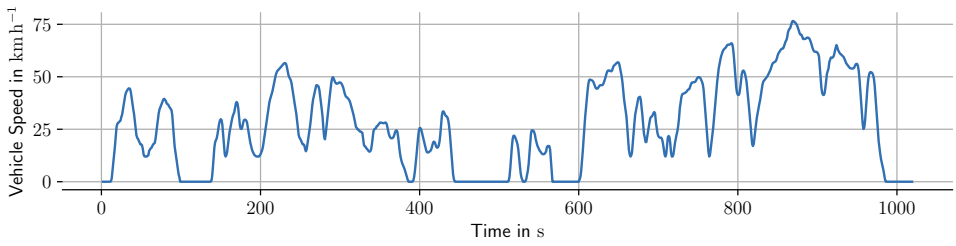

(a) Velocity Profile of the WLTC City Cycle

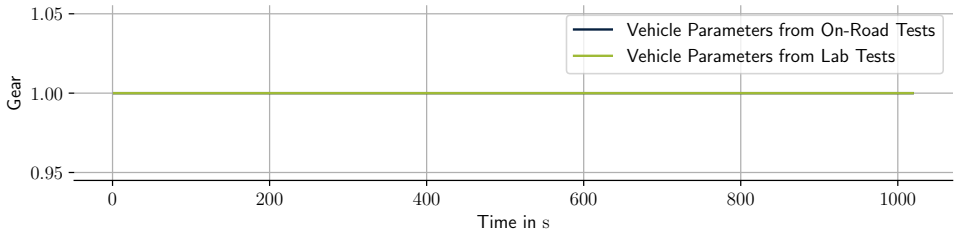

(b) Gear Selection Comparison for the WLTC City Cycle with Sport Mode Gear Strategies

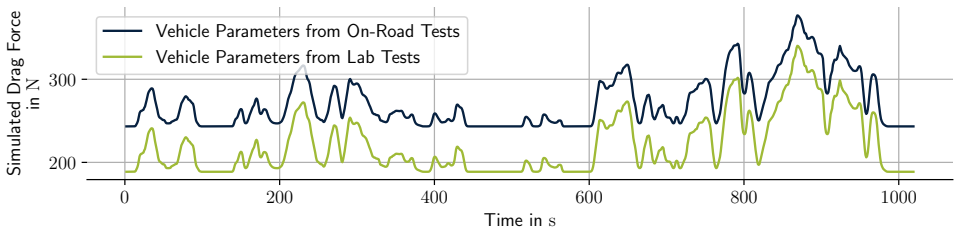

(c) Driving Resistance Comparison for the WLTC City Cycle

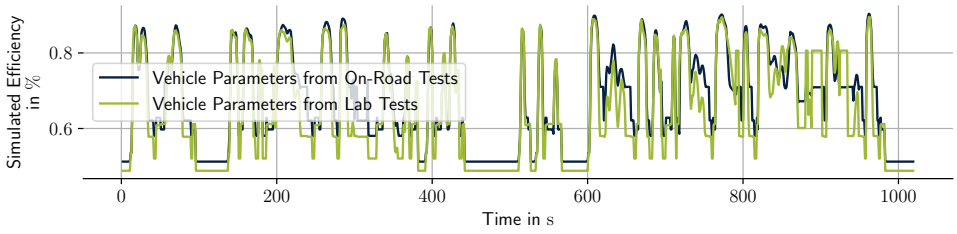

(d) Driving Efficiency Comparison for the WLTC City Cycle

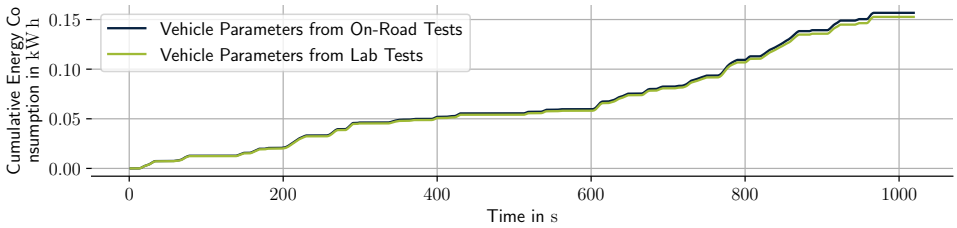

(e) Cumulative Energy Consumption Comparison for the WLTC City Cycle

Figure B.18: Simulation Results for the WLTC City Cycle in Sport Mode

C Parameter Fine-Tuning for Noisy Gear Change Strategy Data

As the vehicle under study was faulty and thus not drivable for a longer part of the timeframe used for this study, the available data for the gear strategy estimation was rather noisy and of not high quality. Nevertheless a parameter tuning was performed with the noisy data, which is presented in this appendix section. As the vehicle was repaired just in time, a higher quality dataset was recorded for the final investigation that made it into the thesis. Differences in selected design parameters that depend on the data quality are discussed in the main part of the thesis. The following section presents the previous results for the gear strategy estimation algorithm with noisy data.

To quantify the gear change strategy of the test vehicle, driving data is recorded in both the Normal drive mode and the Sport drive mode. Using unsupervised data mining techniques, a decision boundary is derived that aims to formulate the gear change strategy for each drive mode. Again, ground truth values for the gear change strategy have been measured under lab conditions on a rolling dynamo by Rosenberger [18]. Using a parametric RMSE, the difference between the gear strategy model derived from driving data and the model from lab data. This metric is used to quantify the impact of the design parameters presented in Table C.1.

Table C.1: Design parameters and tested value ranges for the gear strategy estimation algorithm. (Old)

ID	Design Parameter	Tested Values	Unit
1	Smoothing kwargs	None, EMA0.4, EMA0.6, EMA0.8, MA3, MA5, MA7	-
2	Outlier Detection Epsilon	0.05, 0.1, 0.125, 0.15, 0.175, 0.2	-
3	Outlier Detection Min Samples	2, 3, 4	-
4	Close Points Merge Threshold	0.01, 0.02, 0.03, 0.04, 0.05	-
5	Number of Clusters	3, 4, 5, 6	-
6	Spline Order	1, 2, 3	-
7	Number of Knots	3, 4, 5	-
8	Fit Emphasis	0.1, 0.3, 0.5, 0.7, 0.9	-

The gear strategy estimation algorithm's design parameters and their respective ranges are summarized in Table C.1. The parameters are selected based on domain knowledge, insights from the raw data, and literature. As with all previous algorithms, a grid search is performed to investigate the influence of each parameter on the results. With the results being a decision boundary, the resulting lines are parametrized to allow for a quantitative comparison using the RMSE metric. The RMSE is calculated between the estimated and ground truth gear strategies, obtained from dynamometer-based laboratory measurements from Rosenberger [18]. The grid search results are then analyzed using the ANOVA method to determine the significance of the design parameters. As always, it is investigated whether time-domain smoothing can improve the results. Different *smoothing kwargs* include the moving average filter with window sizes of three, five, and seven samples and the exponential moving average filter with smoothing factors α of 0.4, 0.6, and 0.8, alongside the option of performing no smoothing at all. Savitzky-Golay filter configurations are not tested for the gear strategy estimation algorithm as they require window sizes larger than the polynomial order. They generally do not perform optimally if used with very short window sizes [45]. These ranges were chosen with

a comparatively short window size and smoothing factor to avoid distorting the signal, which is of particular importance for the gear strategy estimation algorithm, as the gear change moments are instantaneous and distorting the signals too much in an effort to reduce noise could in this algorithm quicker than for the others lead to the loss of the underlying structure of the data. The mechanism to remove erroneous gear change data from the dataset is done by DBSCAN clustering. This algorithm has to be configured with two design parameters [53]. This includes an epsilon radius, subsequently called *outlier detection epsilon*, and a minimum number of samples, subsequently called *outlier detection min samples*. The epsilon radius is tested with values of 0.05, 0.1, 0.125, 0.15, 0.175, and 0.2. As this outlier detection happens in the normalized torque-speed domain, no unit is associated with it other than the interpretation as a percent of the respective maximum value. The minimum number of samples is tested with values of 2, 3, and 4, as with the amount of gear change moments that can be expected in the dataset, a higher number of samples is not expected to be necessary to form an inlier cluster. The *close points merge threshold* is tested with values of 0.01, 0.02, 0.03, 0.04, and 0.05, also given in percent of the respective maximum value. If two points are closer to each other than this threshold, they are merged into one averaged point. To further simplify the data to a few key characteristic points, Ngo [30] proposed to cluster the data into a few key points using the k-means algorithm. This method requires the *number of clusters* to be specified [52], which is tested with values of 3, 4, 5, and 6. The spline interpolation is used to fit a curve between the key points, which is parametrized by the *spline order*, for which the linear spline and the quadratic and cubic spline are tested. In addition, another key parameter for the spline interpolation is the *number of knots*, which determines the number of control points and, subsequently, the number of spline segments. The number of knots is tested with values of 3, 4, and 5, as the results of Ngo [30] have shown that a higher number of knots is usually not required to describe gear change decision boundaries. The *fit emphasis* parameter is used to weigh the importance of fitting the spline to the cluster centers versus the data points themselves. A fit emphasis of above 0.5 will put more weight on the cluster centers, while a fit emphasis of below 0.5 will put more weight on the data points themselves. The parameter is tested with values of 0.1, 0.3, 0.5, 0.7, and 0.9.

The first iteration of the gear strategy design parameter grid search has shown that the *smoothing kwargs* even with the shortest window size of three samples, significantly distorts the gear change moments, which can also be seen in Figure C.1, where all tested methods perform worse in terms of variance and median parameteric-RMSE, than applying no smoothing. This is likely because the gear change moments are instantaneous, and a time-domain smoothing method distorts the underlying structure of the data. Due to this large effect on the results, this parameter would strongly influence a subsequent ANOVA investigation, so it is decided not to further investigate the time-domain smoothing configuration.

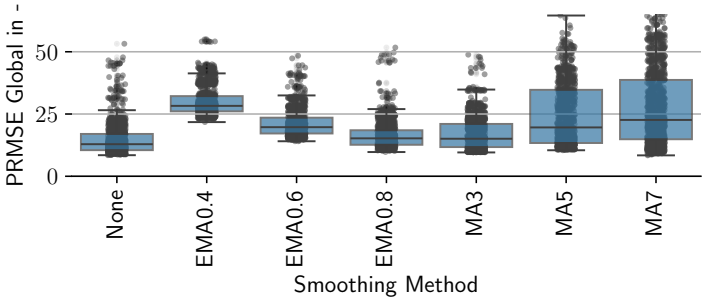

Figure C.1: Boxplots of aggregated parametric RMSE values for different time-domain smoothing configurations in the gear strategy estimation algorithm. (Old)

For the remaining gear strategy estimation algorithm design parameter grid search results, the ANOVA analysis is presented in Figure C.2. The analysis shows that all design parameters significantly impact the results, with a p-value below the significance threshold. The largest influence on the results is exerted by the *outlier detection epsilon*, which is expected as the outlier detection is the first step in the data processing pipeline and has a direct and substantial impact on the data. This implies that although the second outlier detection parameter, the *outlier detection min samples*, has a less pronounced effect on the results, the outlier detection must be tuned carefully to avoid overfitting the data while still removing erroneous data points. The following most important design parameters are the curve fitting related parameters *number of knots*, *spline order*, and *fit emphasis*, which are expected to have a significant impact on the results as they directly influence the decision boundary. The *number of clusters* and the *close points merge threshold* have a comparably more minor impact on the results. They must still be fine-tuned to ensure an accurate and robust decision boundary as they meet the significance criterion.

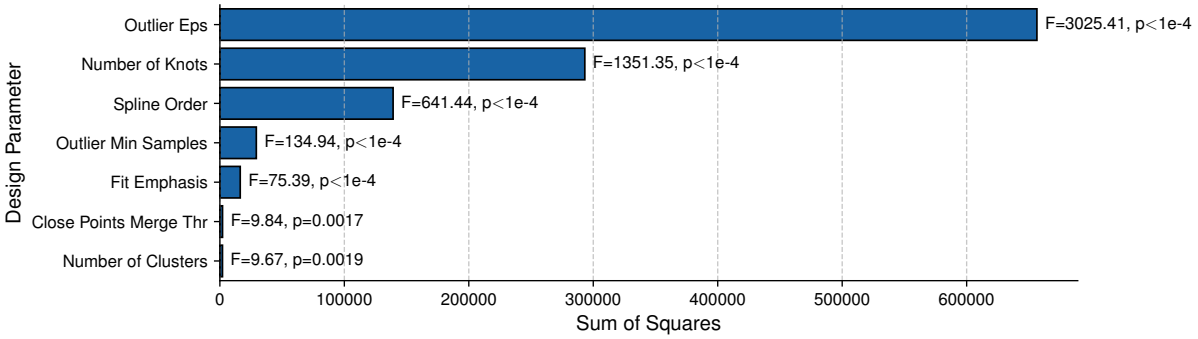

Figure C.2: ANOVA results showing the effect of design parameters on the parametric RMSE in the gear strategy estimation algorithm. (Old)

The results of variation in the *outlier epsilon* design parameter are shown in Figure C.3a. It is immediately apparent that there is an evident change after the epsilon value of 0.05. This indicates that only data points that deviate at least $10\,\%$ from others can confidently labeled as outliers, as everything below this threshold vastly increases the variance and median RMSE. Using this insight, the lowest value of 0.05 is ruled out. As there is no striking difference between the remaining tested values, the value that provides the lowest IQR is chosen, which is the value of 0.15.

The results of the other outlier detection parameter, the *outlier detection min samples*, are shown in Figure C.3b. It can be observed that the value that provides the lowest IQR and variance is the value of 2. This is likely due to the fact that the amount of gear change moments that can be expected in the dataset is comparably low. Thus, a higher number of samples is not likely to be necessary to form an inlier cluster.

The next most important set of design parameters is the spline fitting related parameters, starting with the *number of knots*. The results of the variation in the number of knots are shown in Figure C.4a. The lowest IQR and variance are observed for the value of 4, which may indicate that the decision boundary is best described by fitting a spline with four knots and, thus, also four segments. This fits the observation of Ngo [30] that a higher number of knots is usually not required to describe gear change decision boundaries.

The results of the variation in the spline order are shown in Figure C.4b. The lowest IQR and variance are observed for the value of 1, which may indicate that a linear spline best describes the decision boundary. Experimentation with the higher spline orders has also shown that for the splines to not overfit to the data with higher spline orders, the density of the data points would have to be increased, which is not feasible with the current dataset. The fact that the linear spline performs the best is also supported by the results of Ngo [30], who found that a linear spline is usually sufficient to describe gear change decision boundaries.

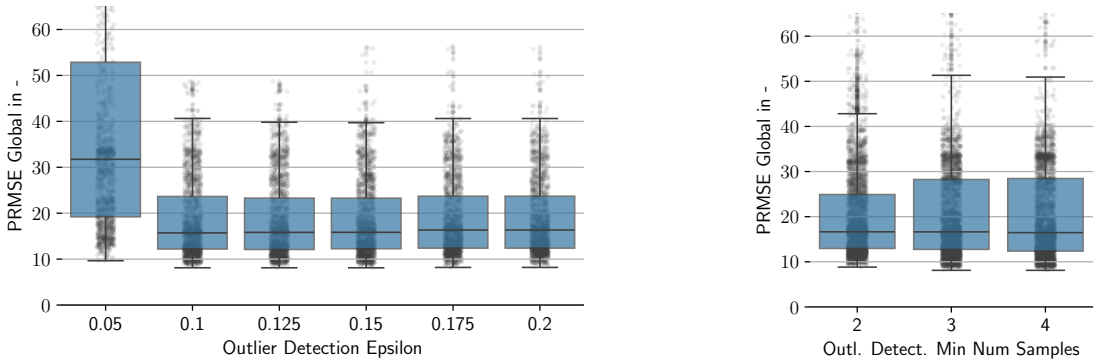

(a) Boxplots of aggregated parametric RMSE values for variations in outlier detection epsilon in the gear strategy estimation algorithm. (Old)

(b) Boxplots of aggregated parametric RMSE values for variations in outlier detection minimum samples in the gear strategy estimation algorithm. (Old)

Figure C.3: Boxplots of aggregated parametric RMSE values for variations in outlier detection parameters in the gear strategy estimation algorithm. (Old)

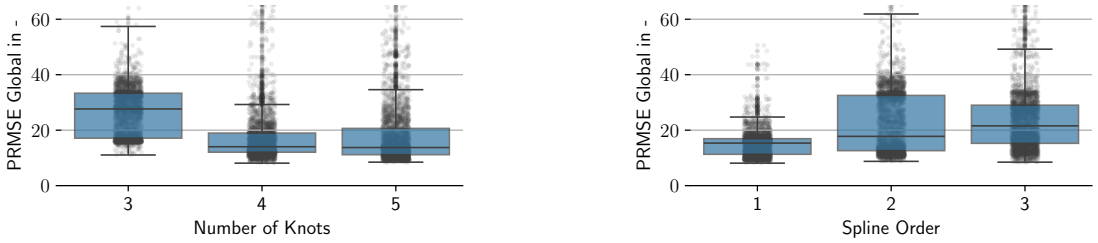

(a) Boxplots of all aggregated RMSE values for variation in the number of knots for the gear strategy estimation algorithm. (Old)

(b) Boxplots of aggregated parametric RMSE values for different spline orders in the gear strategy estimation algorithm. (Old)

Figure C.4: Boxplots of aggregated parametric RMSE values for variations in spline fitting parameters in the gear strategy estimation algorithm. (Old)

Varying the fit emphasis parameter produces the results shown in Figure C.5. Looking at the variances for the distributions of the aggregated results, it can be observed that starting from a high emphasis on the original data (0.1), the variance decreases with increasing emphasis on the cluster centers up to a value of 0.7. The value of 0.9 shows an increase in variance again, which may indicate that the decision boundary is described most robustly by a spline that is fitted to the cluster centers with a fit emphasis of 0.7, which still allows for some incentive to fit the spline to the data points themselves, which as experimentation has shown provides a good tradeoff between the general shape of the decision boundary which is described best by the cluster centers and the local structure, especially in corner cases, which is described best by the data points themselves.

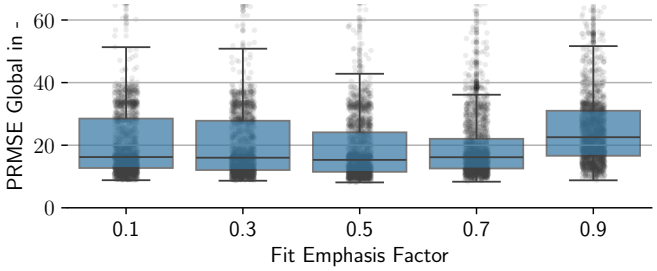

Figure C.5: Boxplots of aggregated parametric RMSE values for variations in fit emphasis in the gear strategy estimation algorithm. (Old)

The option to merge close points is tested with the *close points merge threshold* parameter. This option was implemented to test the effects of consolidating similar data points into one averaged point to reduce the complexity of the decision boundary. As the ANOVA has shown that this parameter has a comparatively low impact, the parameter is selected simply by choosing the value that provides the lowest IQR and variance, which is the value of 0.03.

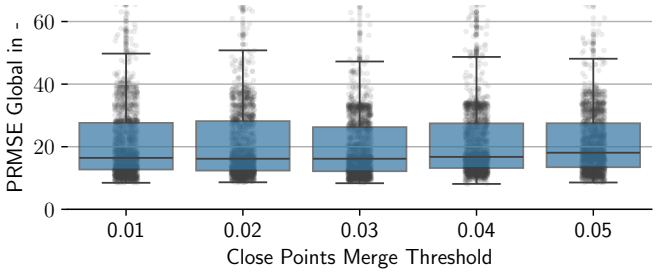

Figure C.6: Boxplots of aggregated parametric RMSE values for variations in the close-points merge threshold in the gear strategy estimation algorithm. (Old)

Interestingly, the number of clusters assigned to the data to capture their underlying structure has a similarly low impact. The results of the variation in the number of clusters are shown in Figure C.7. It can be observed that the value of 3 provides a visibly lower variance and IQR than the other tested values, which may indicate that the decision boundary is best described by three clusters in between the anchored start and end points of the decision boundary.

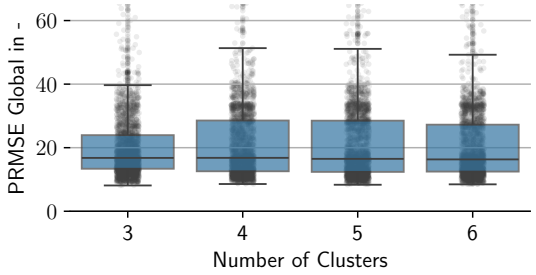

Figure C.7: Boxplots of aggregated parametric RMSE values for different numbers of clusters in the gear strategy estimation algorithm. (Old)

Table C.2: Selected design parameters for the gear strategy estimation algorithm after parameter tuning. (Old)

ID	Design Parameter	Selected Value	Unit
1	Smoothing kwargs	None	-
2	Outlier Detection Epsilon	0.15	-
3	Outlier Detection Min Samples	2	-
4	Close Points Merge Threshold	0.03	-
5	Number of Clusters	3	-
6	Spline Order	1	-
7	Number of Knots	4	-
8	Fit Emphasis	5	-

Table C.2 provides an overview of the final design parameters chosen based on the grid search results and subsequent ANOVA analysis. Time-domain smoothing is omitted because gear changes are instantaneous events that become overly distorted by moving average or exponential moving average filters. An outlier detection epsilon of 0.15 strikes a balance between removing highly deviant points and retaining genuine shifts while setting the minimum number of samples to 2 accounts for the relatively small number of gear-change events in the dataset. A close-point merge threshold of 0.03 helps consolidate only very similar data without obscuring critical shifts. Three clusters were found to best capture the main segments of the gear-change boundary, and using a linear spline avoids overfitting when data density is limited. Finally, the fit emphasis is chosen to ensure a suitable trade-off between adhering closely to the cluster centers and retaining sufficient sensitivity to individual data points, yielding a robust and interpretable decision boundary overall.